MAGNETOM Flash

Issue Number 73 · 2/2019
SPR Edition

siemens.com/magnetom-world

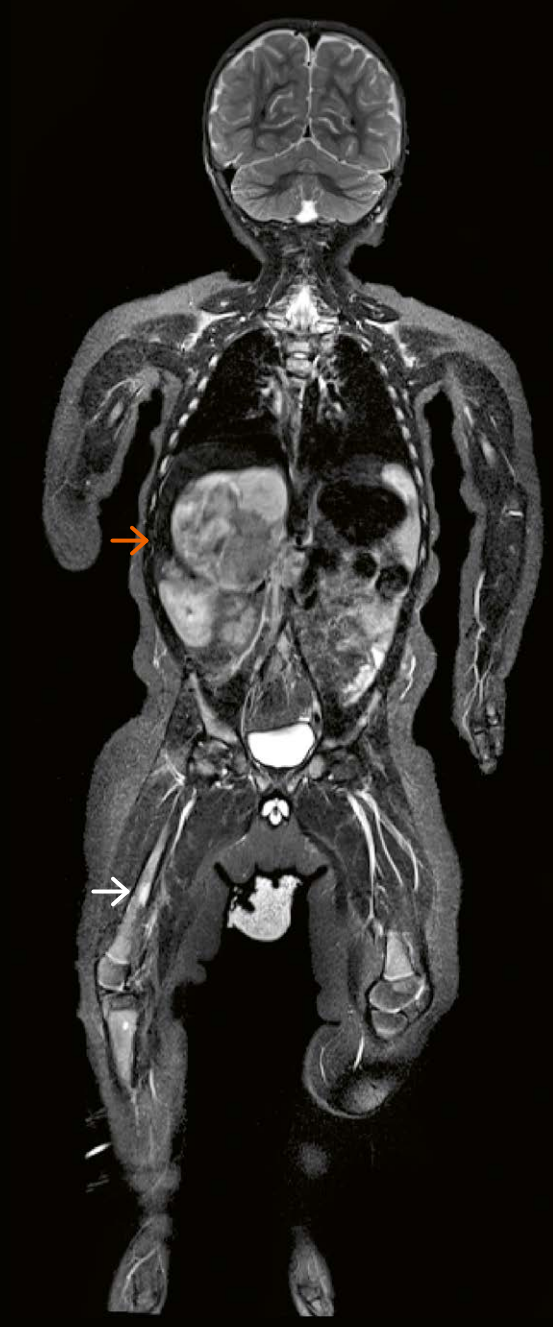

SIEMENS Healthineers

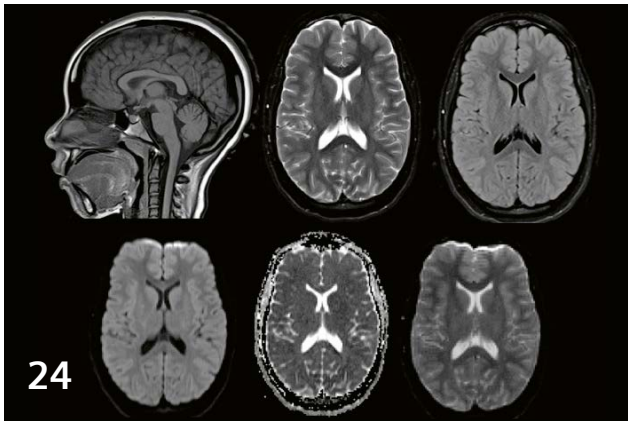

GOBrain 5-Minute MRI in children:
Reducing the need for sedation

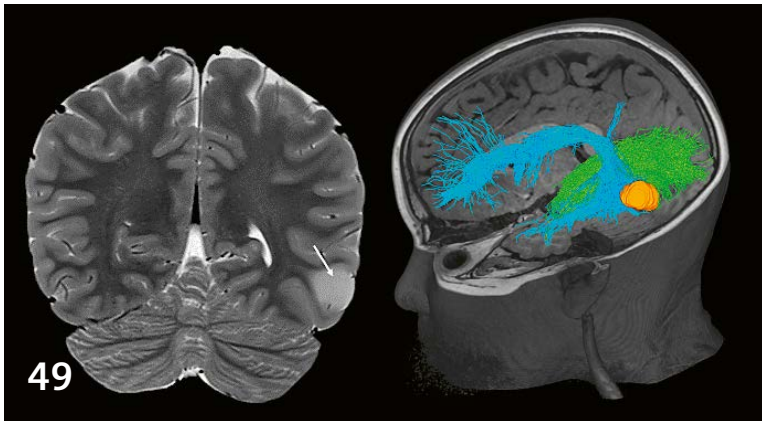

Advanced neuroimaging and pediatric epilepsy surgery

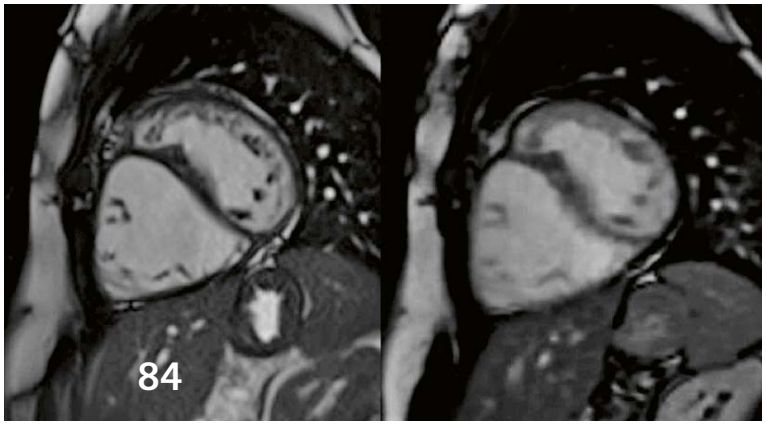

Compressed Sensing cardiac cine in children

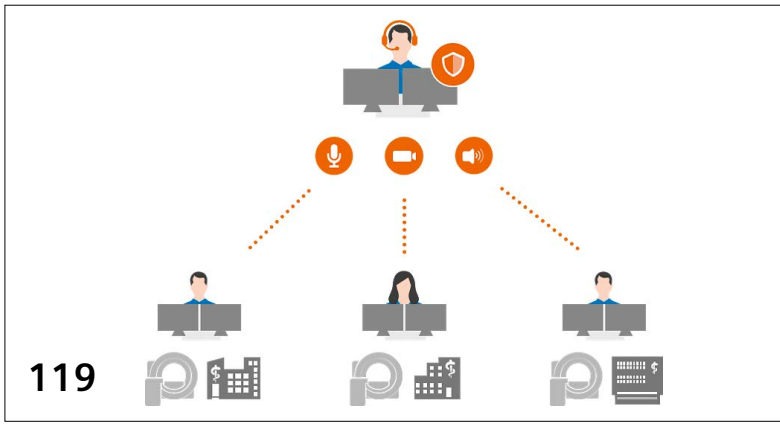

syngo Virtual Cockpit – remote scanning assistance and flexible workforce management

Body and MSK Imaging

Cardiovascular Imaging

Fetal MRI

Product News

Meet Siemens Healthineers

[1]MR scanning has not been established as safe for imaging fetuses and infants less than two years of age. The responsible physician must evaluate the benefits of the MR examination compared to those of other imaging procedures.
[2]Work in progress: the application is currently under development and is not for sale in the US and in other countries. Its future availability cannot be ensured.
[3]syngo.via Frontier is for research only, not a medical device. syngo.via Frontier MR Total Tumor Load is a released research prototype.
[4]syngo Virtual Cockpit is not commercially available in all countries. For regulatory reasons, its future availability cannot be guaranteed. Precondition: Expert-i enabled modality from Siemens Healthineers.

Paolo Tomà

Professor Paolo Tomà qualified in medicine at the University of Genoa in 1976. He trained in both radiology and pediatrics. Between 1980 and 1994 he worked as a radiologist in the Department of Imaging at the G. Gaslini Institute in Genoa, first as a registrar and later in a more senior position. From 1992 to 1994 he was Director of Ultrasound at the institute. Between 1995 and 2009 he was Director of Radiology, and from 2005 to 2009 he also held the position of Director of the Department of Imaging.

Dear readers and colleagues,

I am extremely honored to be invited as editor of this issue of Siemens Healthineers MAGNETOM Flash journal. As a radiologist, I have always believed that pediatric[1] magnetic resonance imaging (MRI) represents a very interesting and challenging field for radiologists as well as for physicists, engineers, and technicians. Like for adults, in children MRI is today performed in a variety of medical settings, including neurological, cardiac, thoracoabdominal, musculoskeletal, and oncological. Clinical MRI applications allow us to observe structural, functional, and chemical changes in patients and to identify biomarkers of specific diseases in their early stages, which can help us to better understand typical and atypical findings. Imaging pediatric patients normally requires a variety of specific and adaptable equipment, together with dedicated software and well-trained staff. The need for specialized technology arises from several challenges of pediatric MRI, which include anatomical, developmental, physiological, and behavioral issues.

A child's anatomy is smaller than that of an adult and changes rapidly during early growth [1]. The reduced size of pediatric structures makes it difficult to obtain adequate signal-to-noise ratio (SNR). As suggested by the literature [2], this obstacle may be mitigated by choosing a compromise between reduction of the field of view and reduction of spatial resolution, respectively, at the cost of decreased SNR and less informative images. As well as a compromising strategy, many manufacturers are adopting a customized approach with appropriate hardware, consisting of specialized coils sized to fit neonates and a narrow bore, which allows faster scans using higher gradient strength and slew rate.

It is far from simplistic to say that one of the major challenges in imaging pediatric patients is getting them to cooperate sufficiently for a diagnostic MRI study [3, 4], in the effort both to prevent motion artifacts and to obtain high-quality scans. Younger children are unable to cooperate, perform breath-holding, and frequently require sedation or general anesthesia to undergo MRI. Since sedation and anesthesia involve long-term neurocognitive effects, short-term risks related to the procedure, and require specialized staff, the chance to implement fast and motion-resistant MRI sequences is appealing [5, 6]. In the last few years, several approaches aimed at accelerating acquisition time have been developed, including parallel imaging, compressed sensing, non-Cartesian acquisition, and simultaneous multislice acquisition. Also, much has been done to ensure that parallel imaging methods reduce scan times, thus avoiding errors in coil sensitivity measurement. In this context, Wave CAIPIRINHA[2] has recently been introduced [7], which ensures the use of full 3D coil sensitivities to achieve high acceleration factors with small *g*-factor penalties and less SNR degradation. These very promising results have already been shown in adult acquisition data, but much still has to be done to extend clinical application to the pediatric population.

[1]MR scanning has not been established as safe for imaging fetuses and infants less than two years of age. The responsible physician must evaluate the benefits of the MR examination compared to those of other imaging procedures. Note: This disclaimer does not represent the opinion of the author.
[2]WIP, the product is currently under development and is not for sale in the U.S. and in other countries. Its future availability cannot be ensured.

Professor Tomà was appointed Professor of Pediatric Radiology at the University of Genoa's Radiology and Pediatric Postgraduate Schools in 1990. For the last 20 years, he has mentored, inspired, and led a strong and committed group of pediatric radiologists at the G. Gaslini Institute. He has held a similar position at the Bambino Gesù Hospital in Rome since 2010.

Internationally, he served as Vice-President of the European Society of Paediatric Radiology (ESPR) from 1999 to 2002, and as President from 2002 to 2003. He received the ESPR gold medal in 2016.

He has published over 200 papers in peer-reviewed journals, as well as book chapters and books.

Novel technologies for prospective motion correction are gaining consensus. The BioMatrix Kinetic Sensor, for example, uses an in-bore camera system and a marker on the patient's skin to track head movement and correct motion as slight as normal breathing, thus producing remarkably accurate MRI scans. The scan length is a key point not only for exam quality but also for children's safety. Naturally, increasing efforts should be made to develop innovative techniques that can help to accustom children to MRI exams. Today, many new devices can provide a play-based simulation of the full MRI experience, including a motion sensor and noise simulation, providing children with the skills to cope during the actual scan. Also, making MRI rooms less institutional with playful surroundings and in-bore experience can do much to help children fully trust MRI staff.

Acoustic noise of the MRI scan remains an important challenge and is a cause of major discomfort for the pediatric population [8, 9]. Involuntary patient movements, temporary hearing difficulties, and problems in communication between patient and operator are possible issues related to acoustic noise. Evidence from the literature suggests that reducing acoustic noise can increase patient comfort and their acceptance of the procedure, which improves image quality. Several countermeasures have been proposed but there is still much to be done before MRI can really be considered a "child-friendly" experience.

The brain undergoes a period of dramatic change in the first few years of life, as sulci become deeper and numerous, and water content decreases due to progressive myelination, producing gray versus white matter contrast improvement and connectivity enhancement. Consequently, brain tissue properties such as the longitudinal relaxation time (T1) and axial relaxation time (T2) differ significantly between children and adults. As myelination progresses, water diffusion within the white matter changes, creating differences at a microstructural level, thus posing a challenge for diffusion-weighted imaging (DWI) and diffusion-tensor imaging (DTI) [10–12]. Standard analysis techniques used for adult data are not directly applicable. The development of novel pipelines that deal directly with neonatal-specific issues, including high brain water content and reduced anisotropy, are necessary. Accelerating techniques have made it possible to introduce sequences such as Diffusion Kurtosis Imaging (DKI)[2] in a clinical setting, due to reduced acquisition time. DKI is a water diffusion technique based on a non-Gaussian water distribution model. DKI has shown great potential in exploring tissue complexity, and has produced promising results in adult glioma grading [13] (Fig. 1). Robust T1 and T2 mapping in both the brain and the rest of the body are valuable methods and are only starting to emerge in the clinical context of pediatric MRI, i.e., for monitoring brain maturation and measuring chronic liver disease over time [14]. The differences in frequency of biomedical signals between children and adults are another very sensitive issue to consider in clinical practice. Blood flow, pulse, and respiratory rates are faster in children than in adults, thus significantly affecting data from brain, cardiac, thoracic, and abdominal imaging. Cerebral blood flow (CBF) as measured by Arterial Spin Labeling (ASL) is particularly affected by physiological changes in blood flow. ASL is a low-SNR method and, even though higher mean CBF and blood flow velocity in the carotid arteries lead to a physiological improvement of SNR in children compared with healthy adults, the interpretation of pediat-

ric perfusion data is complex as it is dependent on age-related and sedation-related changes. Indeed, perfusion map templates for healthy children are extremely important to confine or broaden normal perfusion data.

In cardiac magnetic resonance (CMR), the infant heart rate (90–180 bpm) is higher than the average adult (60–100 bpm), resulting in a very short cardiac cycle. Moreover, the variability of cardiac frequency makes image reconstruction complex, since it affects temporal resolution and velocity measurements. Flow MRI[2] is a very useful method for assessing longitudinal changes in cardiovascular physiology in pediatric subjects and for monitoring common congenital disorders associated with complex alteration of cardiovascular physiology and flow. In this context, due to small vessel size, high heart rates and the limited capacity of children to perform breath-holding, flow MRI is challenging. Moreover, the method requires time-consuming and operator-dependent placement of multiple imaging sections in order to study multiple vessels. This can result in misalignment with respect to the flow direction and thus in underestimation of velocity. These issues in the evaluation of congenital diseases result in a long total examination time (60–90 min). In addition, pediatric flow MRI requires high spatial and temporal resolution, short imaging times, and full coverage of complex cardiovascular malformations. Generally, to benefit pediatric CMR and flow MRI, acceleration techniques using parallel imaging were developed to allow fast, high resolution, free-breathing, 3D and 4D acquisitions [15] (Fig. 2). Along with them, the recent introduction of Compressed Sensing acquisition and reconstruction techniques has made it possible to reduce acquisition times even further, thus allowing the optimal fusion of anatomic and flow data into a single 3D dataset as well as fast cine imaging[2]. However, we still do not have a standardized protocol for background correction in cardiovascular MR phase-contrast imaging. This indeed represents a challenge to be considered in pediatric CMR although various correction approaches have been investigated.

A new field emerging in pediatric CMR is fetal cardiovascular MRI[1]. Until now, cardiac MRI of the fetus was mostly based on anatomical imaging or, at best, on low spatial and low temporal resolution functional imaging, typically employing untriggered cine real-time balanced steady-state free-precession sequences. After some attempts at obtaining a fetal ECG signal with devices such as MR-compatible electrodes and cardiotocographs, the new frontier in fetal cardiovascular MRI currently involves self-gating approaches, the most common being Metric Optimized Gating (MOG). MOG is a method that can be applied to both cine and phase-contrast flow imaging. Data are retrospectively acquired with an artificial

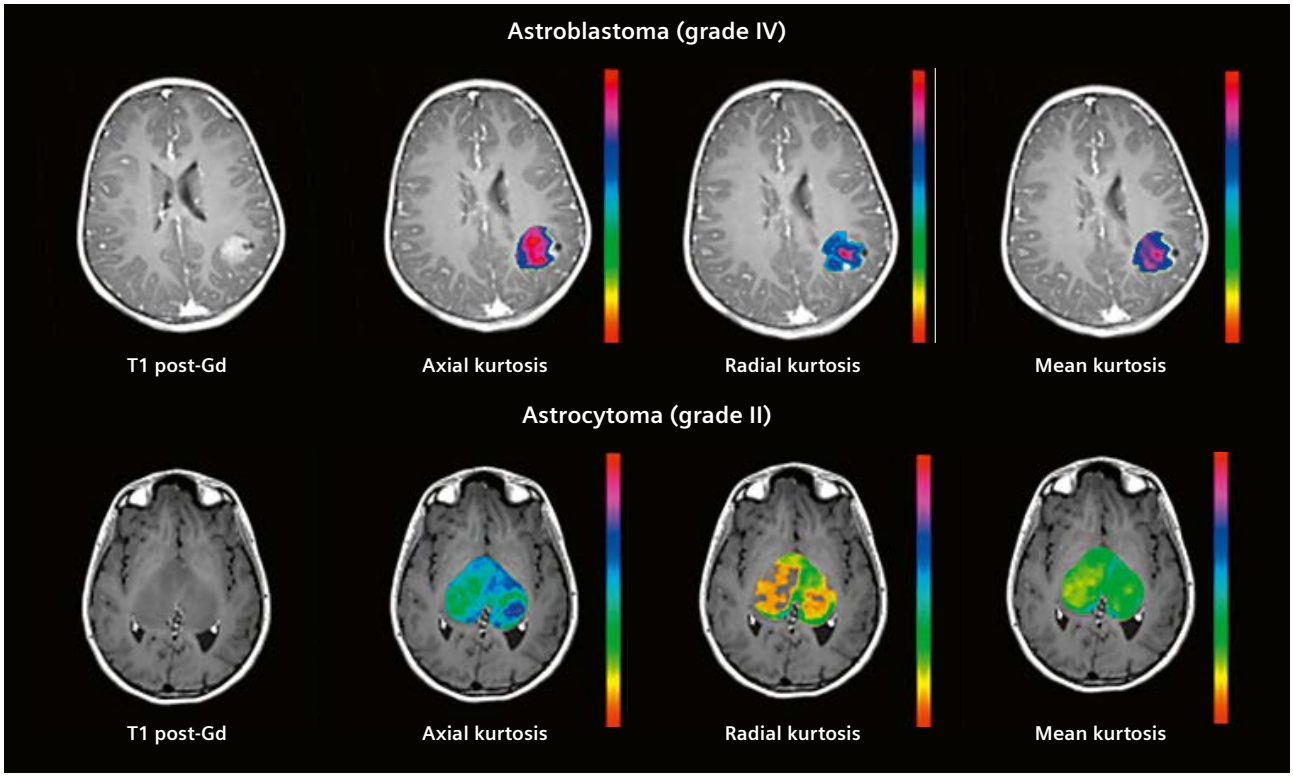

1 Example of diffusion kurtosis maps on two different pediatric brain tumors.

ECG-trigger and then subjected to iterative reconstruction, which performs an exhaustive search of all possible combinations of different heart rhythms until it finds the one yielding the minimum entropy due to the lack of ghosting-reconstruction artifacts. This identifies the real heart rate of the fetus [16]. Different self-gating techniques first reconstruct real-time images of limited image quality but high temporal resolution, subsequently analyzed to extract a self-gating signal that characterizes the periodic contraction of the fetal heart, which in turn is used to retrospectively sort all readouts into their corresponding cardiac phase [17]. The high-quality images that result can be used for a detailed functional assessment of the fetal heart. Another technique that is gaining favor in fetal imaging is MR oximetry, which aims to quantify oxygen saturation of the blood within the larger fetal vessels by applying mapping techniques. T2-mapping exploits the paramagnetic properties of hemoglobin, with deoxyhemoglobin shortening the T2 relaxation time, resulting in higher T2 values with higher oxygen content. However, to account for the fact that T2 measurements are also influenced by hemoglobin concentration (hematocrit), T1-mapping is additionally applied because of its strong correlation with this parameter, with lower T1 values for higher hematocrit percentages [18]. The combination of phase-contrast flow imaging and mapping oxygen measurements (Fig. 3) can be used to calculate fetal oxygen delivery, consumption, and extraction fraction, providing the only currently available noninvasive insight into advanced fetal hemodynamics.

Recent advances and future developments in artificial intelligence and machine learning, including neural networks and deep learning, have a promising role in medical imaging [19–21]. These techniques offer numerous applications and may potentially facilitate countless aspects of radiology workflow, namely scheduling and triage, clinical decision and examination support, image acquisition, detection and interpretation of findings, postprocessing, reporting, image management and archiving, dose estimation, quality control, and integration with other medical record data [22]. In MRI, machine learning could reduce imaging time and improve characterization, for example by recognizing lesions and suggesting appropriate protocol or sequence modifications. It could also improve image reconstruction by exploiting prior information extracted from existing image datasets to compensate for missing data in *k*-space undersampling. In pediatrics, bone age assessment algorithms based on hand radiographs could soon become a clinical reality [23], and many more applications are being investigated. Machine learning can even be used to identify, predict, or categorize subtle patterns beyond the threshold of the human eye, potentially

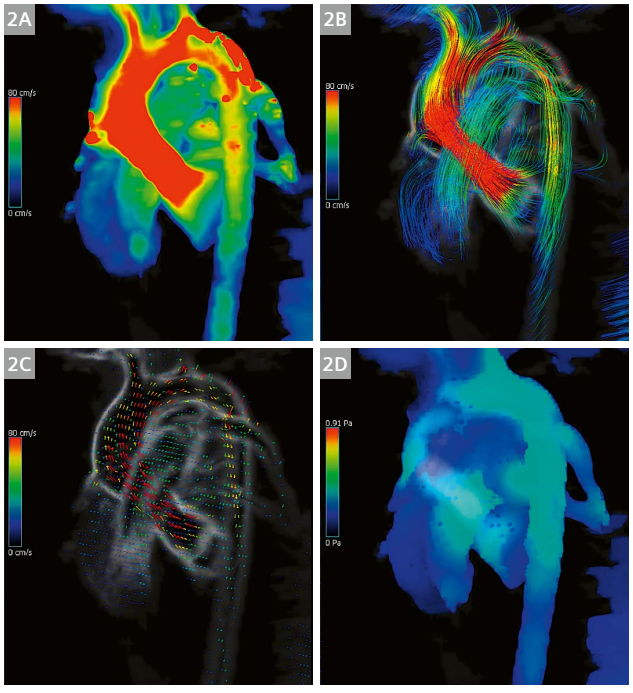

2 4D Flow. Velocity **(2A)**, vector **(2B)**, streamline **(2C)**, and wall-shear-stress **(2D)** systolic images of the aorta in a 15-year-old boy with bicuspid valve and aortic stenosis treated using the Ozaki procedure.

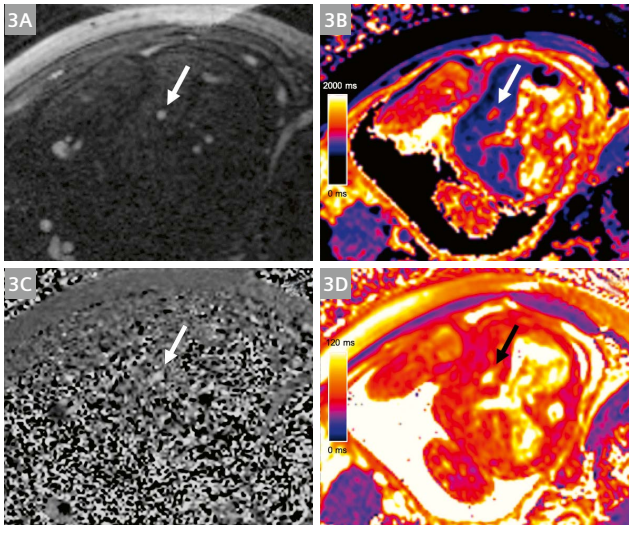

3 Fetal Cardiovascular MRI[1]. Flow magnitude **(3A)** and phase **(3B)**, T1-mapping **(3C)**, and T2-mapping **(3D)** images of the umbilical vein in a 32-week-old fetus affected by transposition of the great arteries with intact interventricular septum.

extracting new valuable information. Radiomics is one such development, where a large number of quantitative features are extracted from medical images using data-characterization algorithms, with the aim of revealing disease characteristics that cannot be detected by the human eye but may prove useful for predicting prognosis and treatment response. In children, this technique has mainly been applied in (neuro-)oncology [24]. MRI remains the most common imaging modality used to evaluate central nervous system tumors. The diagnosis, prognosis, and treatment of pediatric brain tumors are now becoming more reliant on the genetic profile and histopathologic features of the tumor rather than on the histopathologic features alone, which previously were the reference standard. Grasping the principles and advances in tumor genomics is crucial to radiologists who interpret neuro-oncology imaging studies. In this scenario, quantitative radiomic data can be extracted and analyzed together with clinical and genomic data, in a process that is known as radiogenomics. This information can be used to better predict the diagnosis and outcome for children with brain tumors. Artificial intelligence may further enhance the potentialities of radiomics and radiogenomics, allowing the conversion of radiologic images into highly mineable data. For example, machine-learning algorithms trained on radiomic features have shown promising results in predicting medulloblastoma molecular subgroups [25]. The potential of these techniques lies in their ability to inform subsequent clinical and surgical decision-making, which greatly impacts patient survival and quality of life. All this is paving the way to personalized medicine, in which variables gathered from different fields of medicine and life can be used for tailored prevention, diagnosis, and treatment approaches. Nevertheless, more work is needed to integrate novel technologies into existing systems before they can fully enter the clinical scenario. Also, these technologies are prone to bias and could potentially produce significant ethical and medico-legal issues. They are not expected to replace radiologists in the foreseeable future but rather to aid them, improving their accuracy and productivity, and enhancing their value in patient care and satisfaction. Besides, radiologists need to understand both the strengths and the pitfalls of these new tools and become actively involved in their research and development, performing critical assessment through evidence-based medicine.

In conclusion, more so than in adults, pediatric MRI challenges require the most advanced methods, hardware, and clinical staff, and I believe that pediatric MRI is now a pivotal area on which technology and new ideas must focus to improve diagnosis and care.

Many thanks to Giovanna Stefania Colafati, Davide Curione, Antonio Napolitano, and Aurelio Secinaro.

Paolo Tomà

References

1 M. J. Barkovich, Y. Li, R. S. Desikan, A. J. Barkovich, D. Xu. Challenges in pediatric. NeuroImage 185,793–801. 2019.
2 L. Bonnemainsa, F. Raimondie, F. Odille. Specifics of cardiac magnetic resonance imaging in children. Archives of Cardiovascular Disease,109, 143—149. 2016.
3 C. Dagia, M. Ditchfield. Corrigendum to "3T MRI in paediatrics: Challenges and clinical applications". Eur. J. Radiol. 68,2,309-319. 2008.
4 T. V. Phan, D. Smeets, J. B. Talcottc, M. Vandermostena. Processing of structural neuroimaging data in young children: Bridging the gap between current practice and state-of-the-art methods. Developmental Cognitive Neuroscience 33, 206–223. 2018.
5 R. Ahmad, H. H. Hu, R. Krishnamurthy, R. Krishnamurthy. Reducing sedation for pediatric body MRI using accelerated and abbreviated imaging protocols. Pediatr Radiol, 48:37–49. 2018.
6 C. Jaimes, J. Kirsch, M. S. Gee. Fast, free-breathing and motion-minimized techniques for pediatric body magnetic resonance imaging. Pediatr Radiol 48(9). 2018.
7 B. Bilgic, B. A. Gagoski, S. F. Cauley, A. P. Fan, J. R. Polimeni, P. E. Grant, L. L. Wald, and K. Setsompop. Wave-CAIPI for highly accelerated 3D imaging. Magn. Reson. Med. 2015;73(6):2152–2162.
8 S. Alibek, M. Vogel, W. Sun, D. Winkler, C. A. Baker, M. Burke, and H. Gloger. Acoustic noise reduction in MRI using Silent Scan: an initial experience. Diagn Interv Radiol 20(4):360-362. 2014.
9 E. T. Tan, C. J. Hardy, Y. S. M.H. In, A. Guidon, J. Huston III, M. A. Bernstein, T. K.F. Foo. Reduced acoustic noise in diffusion tensor imaging on a compact MRI system. Magnetic Resonance in Medicine 79:2902-2911. 2018.
10 M. Bastiani, J. L.R. Andersson, L. Cordero Grande, M. Murgasova, J. Hutter, A. N. Price, A. Makropoulos, S. P. Fitzgibbon, E. Hughes, D. Rueckert, S. Victor, M. Rutherford, A. D. Edwards, S. M. Smith, J. D. Tournier, J. V. Hajnal, S. Jbabdi, S. N. Sotiropoulos. Automated processing pipeline for neonatal diffusion MRI in the developing Human Connectome Project. NeuroImage 2019 Jan 15;185:750-763. doi: 10.1016/j.neuroimage.2018.05.064. Epub 2018 May 28.

11 C. K. Tamnesa, D. R. Roalfb, A. L. Goddingsc, C. Lebeld. Diffusion MRI of white matter microstructure development in childhood and adolescence: Methods, challenges and progress. Developmental Cognitive Neuroscience 33, 161–175. 2018.

12 M.J. Taylor, M.M. Vandewouw, J.M. Young, D. Card, J.G. Sled, M.M. Shroff, C. Raybaud. Magnetic resonance spectroscopy in very preterm-born children at 4 years of age: developmental course from birth and outcomes. Neuroradiology 60(10):1063–1073. 2018.

13 Falk Delgado A, Nilsson M, van Westen D, Falk Delgado A. Glioma Grade Discrimination with MR Diffusion Kurtosis Imaging: A Meta-Analysis of Diagnostic Accuracy. Radiology. 2018 Apr;287(1):119-127.

14 J. R. Dillman, S. D. Serai, A. T. Trout, R. Singh, J. A. Tkach, A. E. Taylor, B. C. Blaxall, L. Fei, A. G. Miethke. Diagnostic performance of quantitative magnetic resonance imaging biomarkers for predicting portal hypertension in children and young adults with autoimmune liver disease. Pediatr Radiol. 2019.

15 P. Banka, T. Geva. Advances in pediatric cardiac MRI. Curr Opin Pediatr, 28(5):575-83. 2016. neuroimaging.

16 Seed M. Fetal Cardiovascular MRI. In Kline-Fath B, Bahado-Singh R, Bulas D, Diagnostic Imaging of Fetal Anomalies: Ultrasound and MRI. Philadelphia, PA: Lippincott Williams and Wilkins; 2015:228-34.

17 Chaptinel J, Yerly J, Mivelaz Y, Prsa M, Alamo L, Vial Y, et al. Fetal cardiac cine magnetic resonance imaging in utero. Sci Rep. 2017;7(1):15540.

18 Portnoy S, Seed M, Sled JG, Macgowan CK. Non-invasive evaluation of blood oxygen saturation and hematocrit from T1 and T2 relaxation times: In-vitro validation in fetal blood. Magn Reson Med. 2017; 78(6):2352-2359.

19 J. M. B Bonnemainsa, M. Eder, W. C. Flood, D. S. Dhami, S. Natarajan, C. T. Whitlow. Machine Learning Applications to Resting-State Functional MR Imaging Analysis. Neuroimaging Clinics of North America 27(4):609-620. 2017.

20 P. Kokol, J. Zavrsnik, H. B. Vosner. Artificial intelligence and pediatrics: A synthetic mini review. Pediatr Dimension 2(4):1-5. 2017S. Eminian, S. D. Hajdu, R. A. Meuli, P. Maeder, P. Hagmann. Rapid high resolution T1 mapping as a marker of brain development: Normative ranges in key regions of interest. PLoS ONE 13(6). 2018.

21 W. Zhang, R.Li, H. Deng, L. Wang, W. Lind, S. Ji, D. Shen. Deep convolutional neural networks for multi-modality isointense infant brain image segmentation. Neuroimage 108, 214-224. 2015.

22 Choy G, Khalilzadeh O, Michalski M, Do S, Samir AE, Pianykh OS, et al. Current Applications and Future Impact of Machine Learning in Radiology. Radiology. 2018;288(2):318-328).

23 Lee H, Tajmir S, Lee J, et al. Fully automated deep learning system for bone age assessment. J Digit Imaging 2017;30(4):427–441.

24 Fetit AE, Novak J, Rodriguez D, Auer DP, Clark CA, Grundy RG, et al. Radiomics in paediatric neuro-oncology: A multicentre study on MRI texture analysis. NMR Biomed. 2018;31(1).

25 Iv M, Zhou M, Shpanskaya K, Perreault S, Wang Z, Tranvinh E, et al. MR Imaging-Based Radiomic Signatures of Distinct Molecular Subgroups of Medulloblastoma. AJNR Am J Neuroradiol. 2019 Jan;40(1):154-161.

We appreciate your comments.
Please contact us at magnetomworld.team@siemens-healthineers.com

Editorial Board

Review Board

Robust, Efficient, and Comprehensive Pediatric Imaging with BioMatrix Technology and High-End Applications

Johan Dehem, M.D.

VZW Jan Yperman, Ypres, Belgium

In the world of social media, the relationship between pediatrics[1] and MRI would be: "It's complicated." On the one hand, MRI is a completely radiation-free technique, which makes it an excellent *primum non nocere* tool. MRI is also a tool that, more than transfontanellar ultrasound or CT, excels in providing comprehensive diagnostic information. On the other hand, MRI can suffer from some "childish behavior". Keeping a toddler busy with toys in the waiting room is one thing, but having the same toddler immobilized completely for some time can be challenging with CT, let alone with MRI.

Many pediatric procedures therefore happen with a little help from our friends in the anesthesia department. Scheduling tasks and logistics becomes more complex, since you need anesthesia on site, but having the young patient securely ventilated and monitored throughout the exam is reassuring and only right. Parents trust their children to us, and we must live up to that duty and responsibility. For very young children[1] with a smaller head size, we use the dedicated pediatric head coil, which results in a high signal-to-noise ratio, even in these small children. It comes with a cradle into which patient is put immediately after anesthesia. The colleagues just love to transport the little one to the magnet in the cradle, which is then slid into the head coil.

It is a great relief to have the baby safe in the cradle instead of limp (anesthetized) in your arms. This picture shows our very first patient in the cradle. My colleague Leen did the anesthesia and she was delighted with the ease of use of this slide-cradle. A keen observer might see

1 **(1A)** The cradle allows safe, swift and easy transportation from the preparation room to the MRI room. **(1B)** Anesthetized, ventilated child (larynx mask) in the cradle, waiting in the preparation room of the MRI suite for transport to the MRI room. Notice the yellow earplug in the left ear.

[1] *MR scanning has not been established as safe for imaging fetuses and infants less than two years of age. The responsible physician must evaluate the benefits of the MR examination compared to those of other imaging procedures. Note: This disclaimer does not represent the opinion of the authors.*

the (fluorescent) earplug in the left ear. In keeping with the principle of *primum non nocere*, we do everything we can to protect our patients' hearing – including running quiet sequences. It is no coincidence that the dedicated pediatric coil is a head coil, since most indications in pediatric MRI are brain exams. However, the cradle is also ideal for combining with the Ultra Flex coil (small or large), which can be wrapped around the baby in the cradle to examine the abdomen, for instance.

Let's now have a look at some cases: In this four-year-old boy investigated for encopresis and enuresis, an altered Babinski was noted on clinical exam. A brain MRI was ordered to exclude brain lesion, and a spine MRI was ordered to exclude tethered cord and Chiari malformation. Brain (Fig. 2) and spine (Fig. 3) exams were acquired in one session. The patient was safely in the cradle, and the dedicated head coil was combined with the BioMatrix 32-channel spine coil embedded in the patient table.

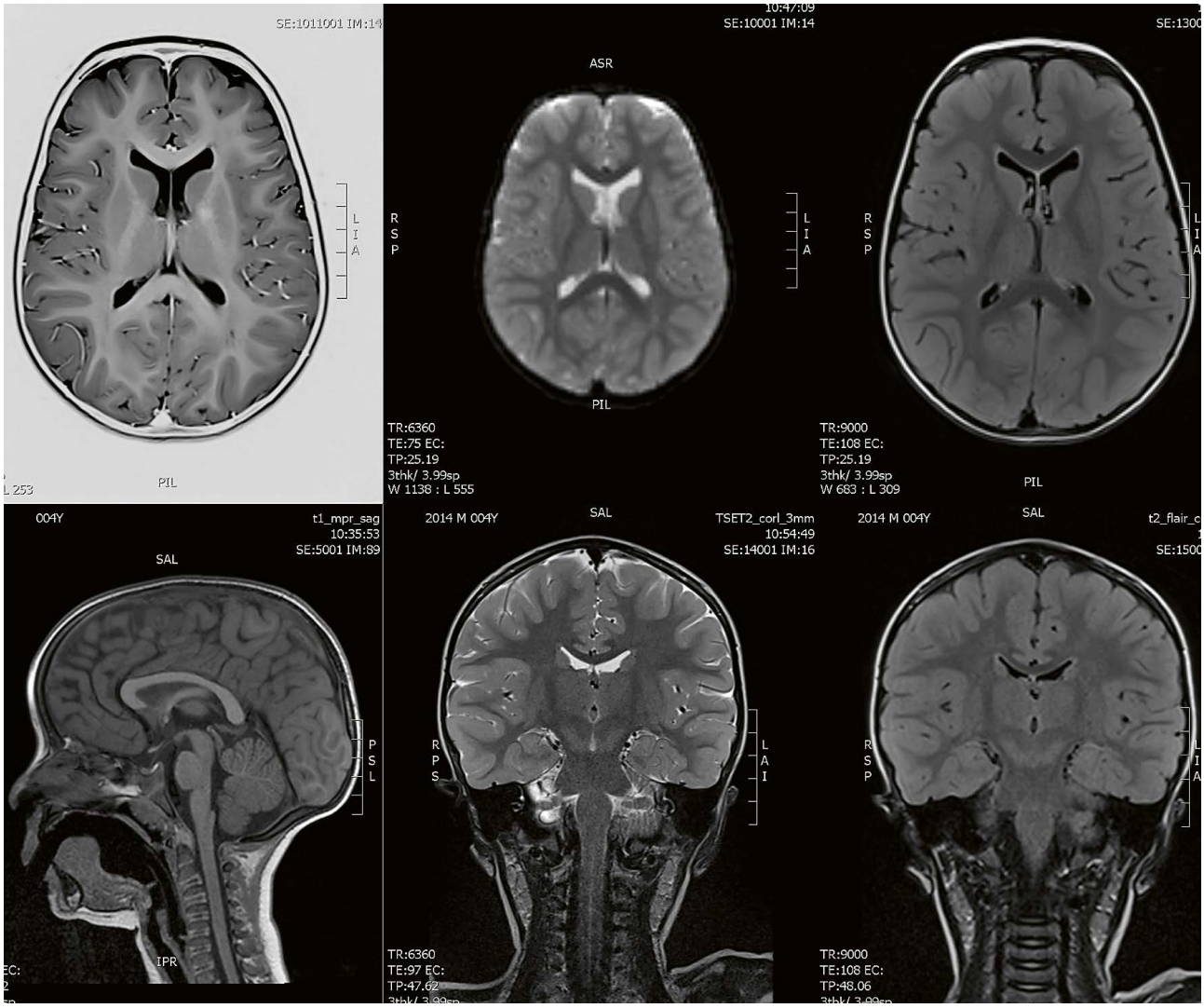

2 3 mm slice thickness T1 inversion recovery, quiet diffusion b_0 image and axial FLAIR (top row), 3D MPRAGE sagittal, and 3 mm coronal T2 and T2 FLAIR (bottom row); high signal from the dedicated pediatric coil that even fits this four-year-old.

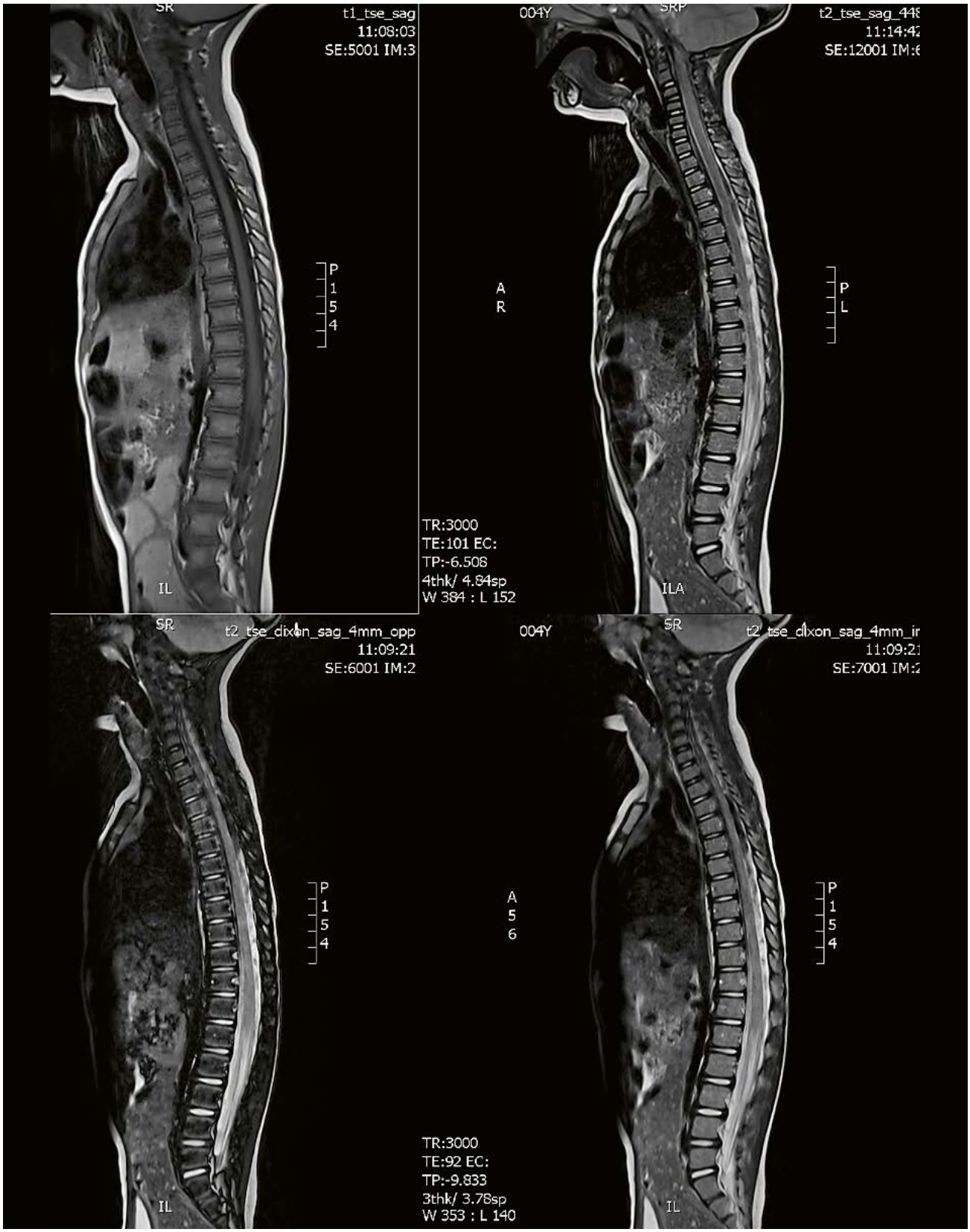

3 Same patient as in Figure 2, examined in the same session using the 32-channel spine coil in the 1.5T MAGNETOM Sola; 3 mm slice thickness (sagittal T1 and T2 TSE, FOV 30 cm; top row) and T2 TSE Dixon technique, FOV 30 cm, 3 mm slice thickness in phase and opposed phase (bottom row) effectively ruling out cord anomalies.

This one-week-old baby[1] has a sacral dimple and rather large skin tag. This raises the suspicion of closed spinal dysraphism, which is confirmed on MRI (Figs. 4–6) with associated myelolipoma and cord tethering. Since motor innervation of lower limbs is clinically normal, the neurosurgeon decided to postpone intervention. Intervention will become necessary when the cord tethering causes motor dysfunction, later on during growth of the spinal canal. Meanwhile, the baby is under close surveillance by the pediatrician. No associated brain lesions (Fig. 7) were demonstrated, and there was no Chiari II malformation.

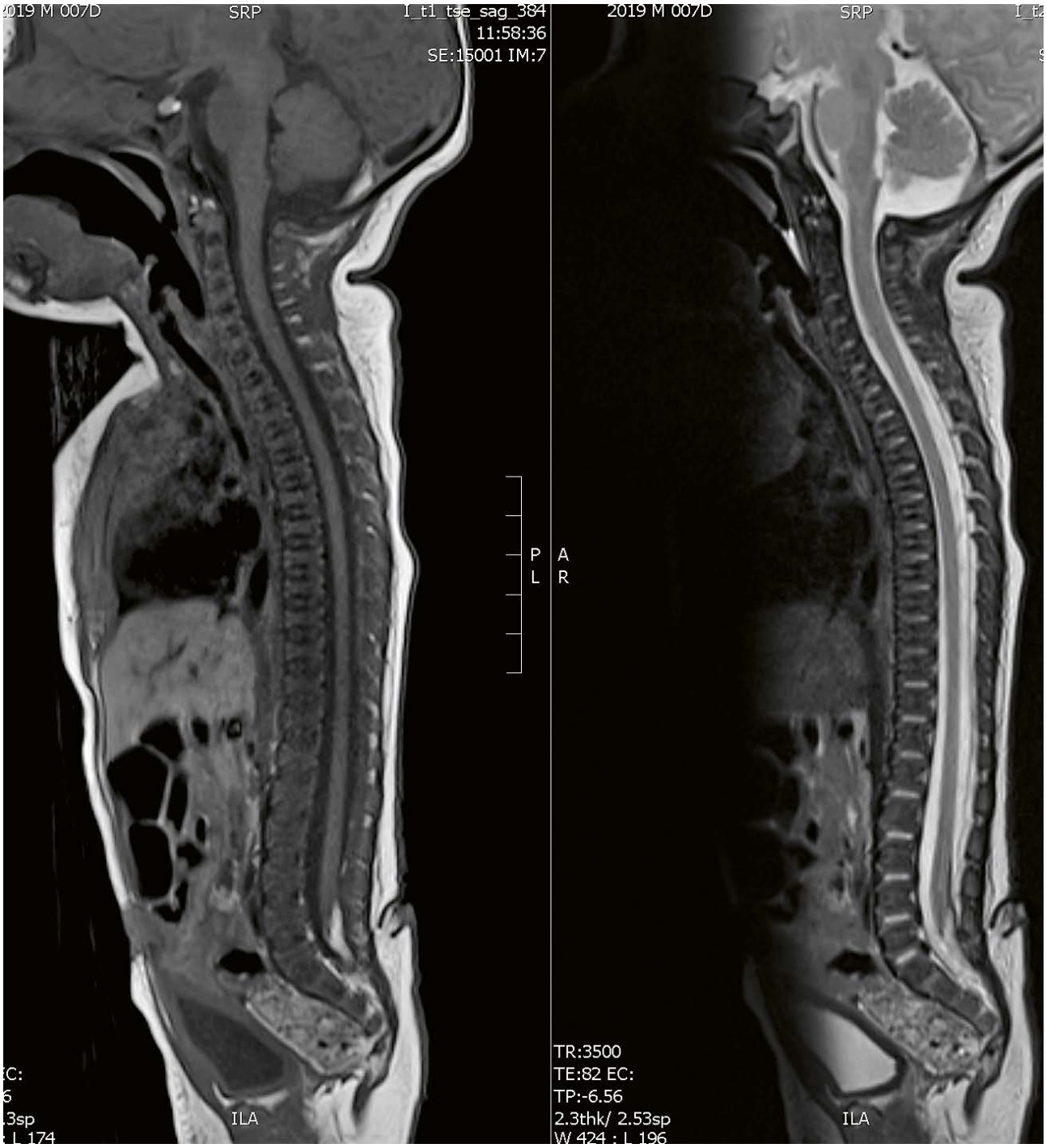

4 Sagittal T1 and T2 TSE 2.3 mm whole-spine images demonstrating the dimple, skin tag, and tethered cord with associated myelolipoma.

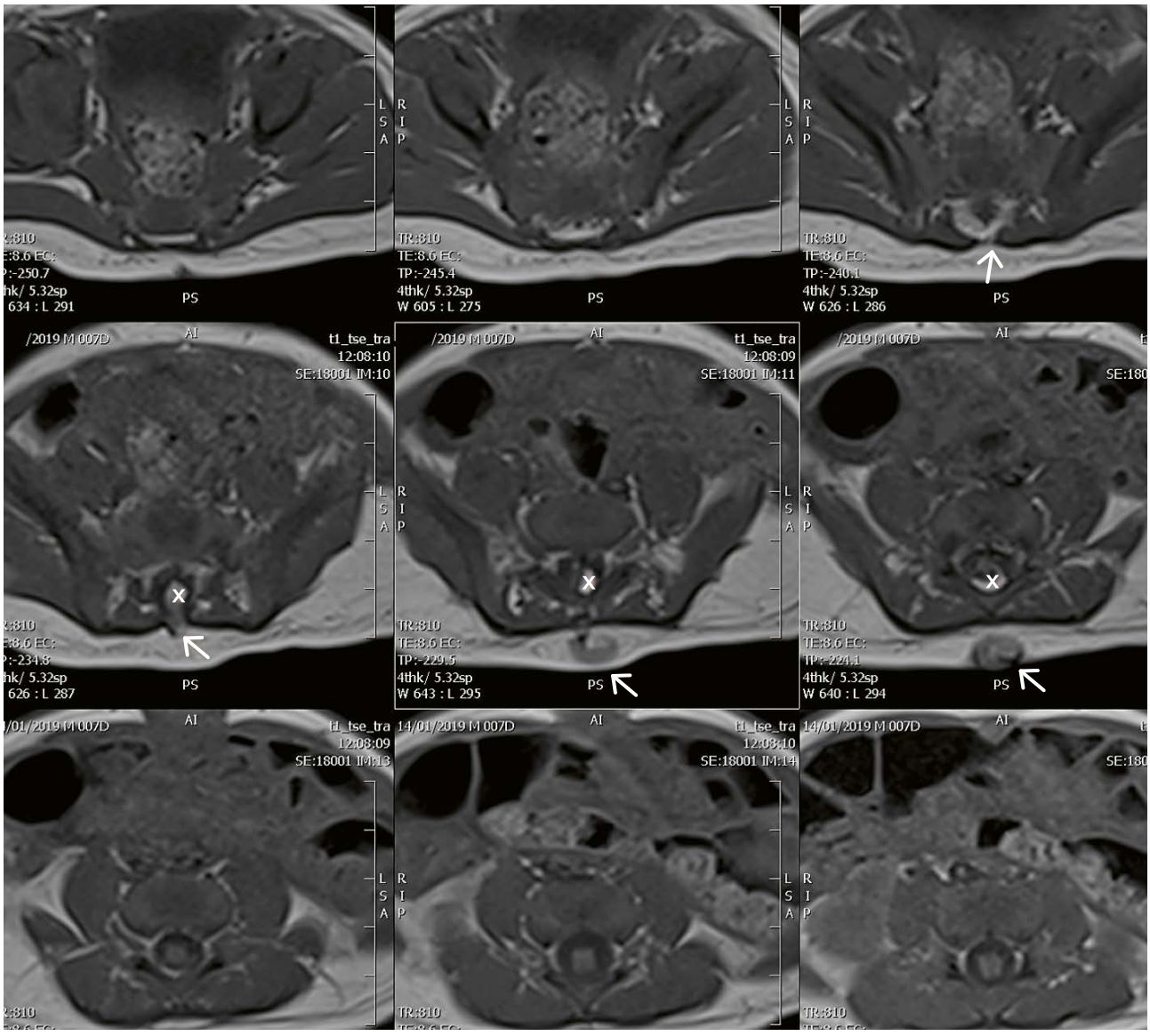

5 Axial T1 demonstrating dysraphism, dimple, and skin tag (arrow); white cross indicates myelolipoma.

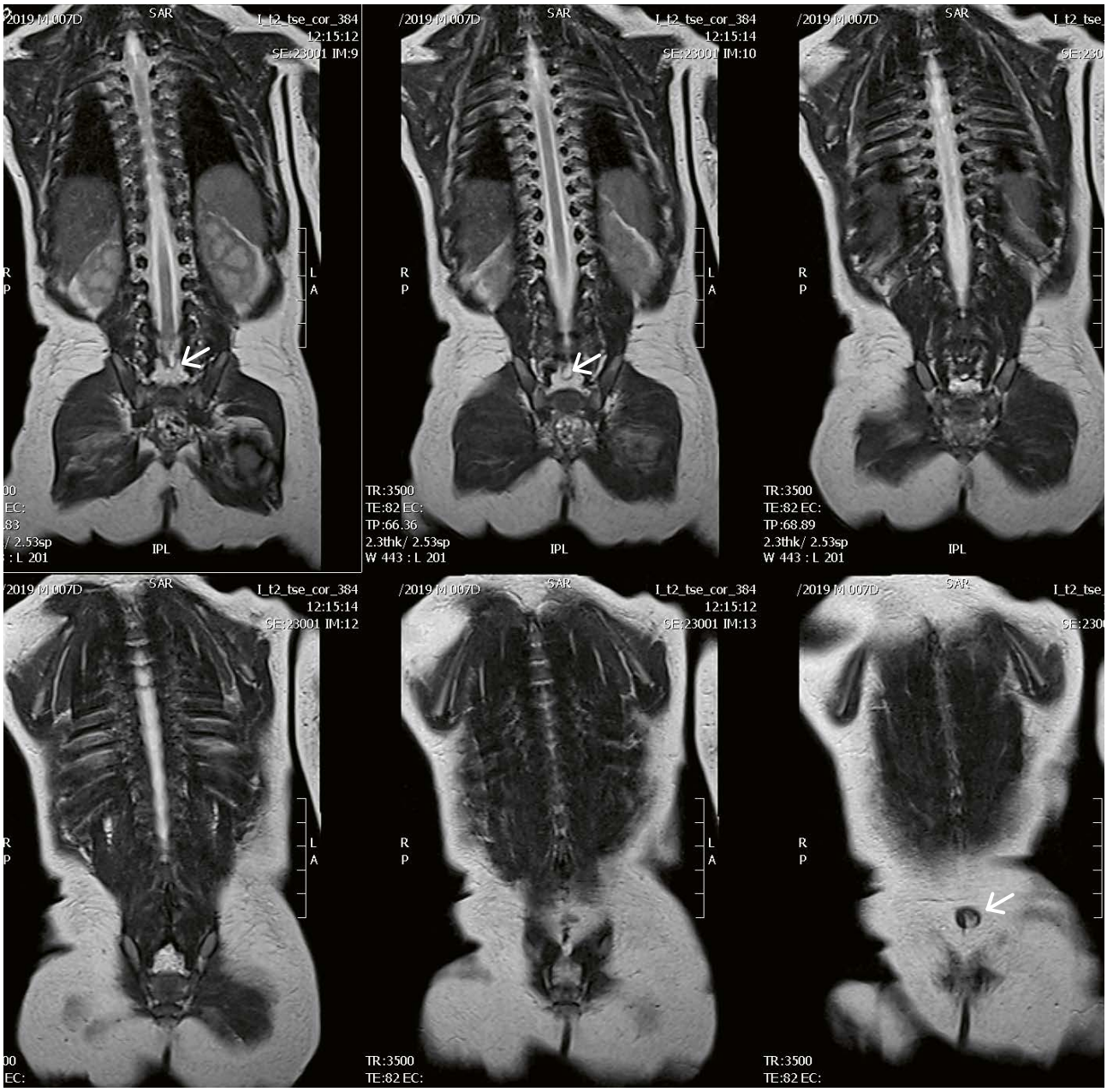

6 Coronal T2 TSE demonstrating dimple and skin tag (arrow), and myelolipoma (arrow).

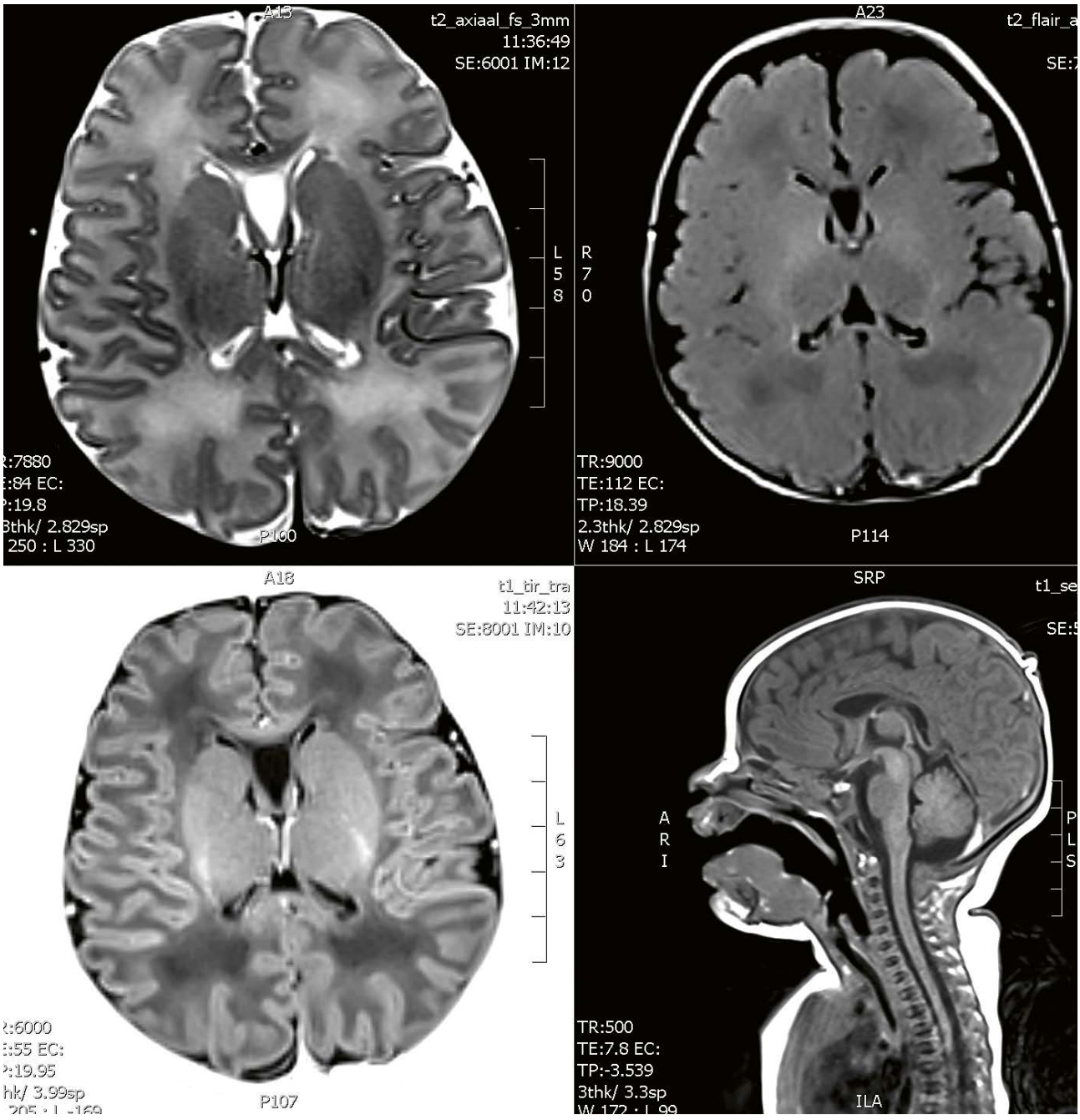

7 T2 axial fatsat and axial FLAIR with 3 mm slice thickness (top row); T1 inversion recovery axial 3 mm, T1 TSE sagittal 3 mm (bottom row); no associated brain lesions, no Chiari malformation.

Delayed neurological development in this 13-month-old baby[1] with genodermatosis (duplication proximal chromosome 6 (+/- 20 MB) (6q13q15 regio)) prompted a request for a brain MRI to exclude brain anomalies.

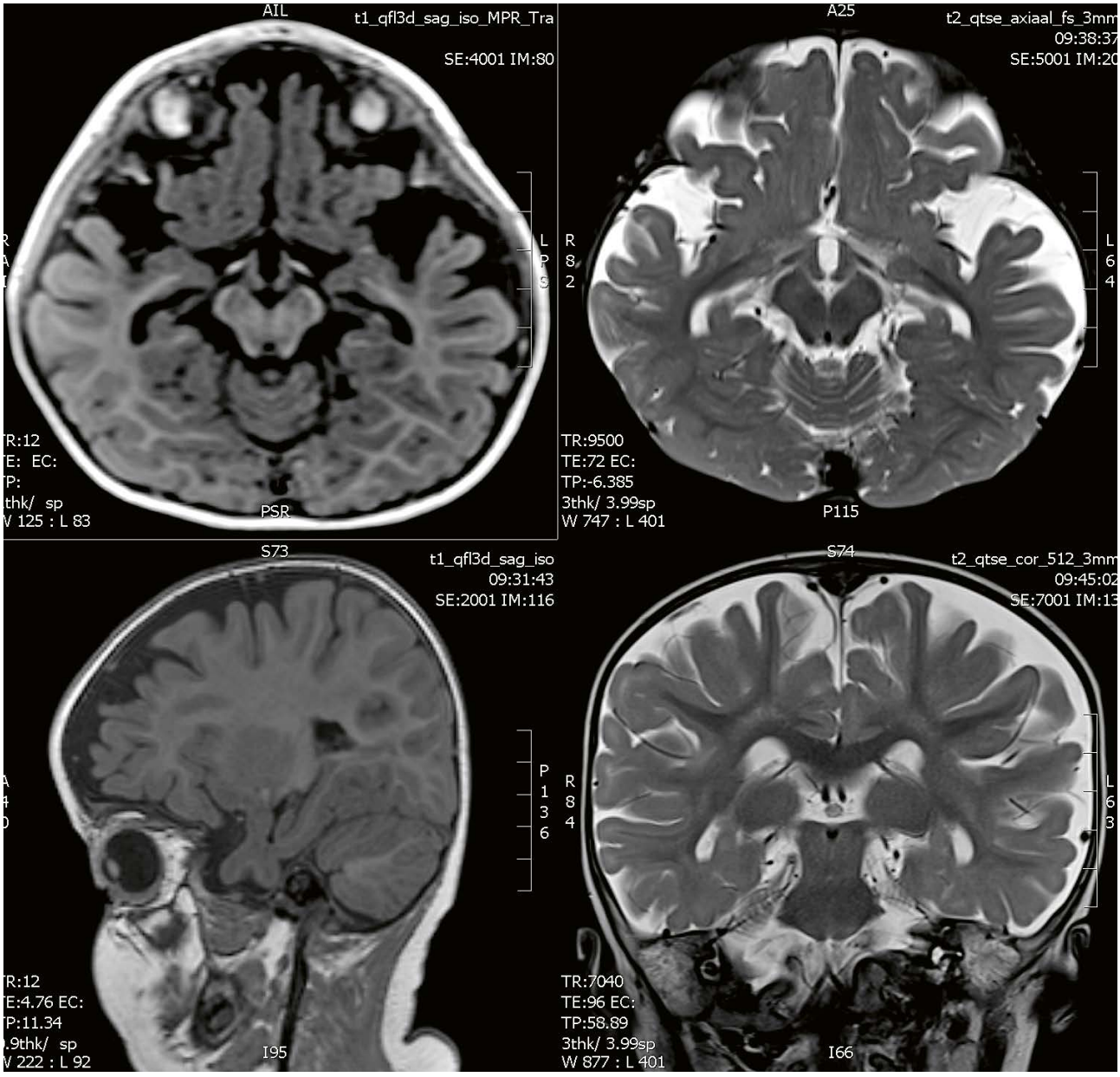

8 Quiet T2 TSE coronal and axial (right column) acquisition and quiet T1 FLASH 3D (left column) with sagittal acquisition and coronal reconstruction; besides benign enlargement of the subarachnoid spaces in infancy, a clear brachycephalic appearance is notable; age-correlated normal myelination; notice the high signal in 2D TSE images with 3 mm slice thickness and in the 0.9 isotropic T1 images in the dedicated pediatric head coil.

This four-year-old toddler experienced a witnessed seizure. Since clinical examination, EEG, and MRI were normal, no medication was started.

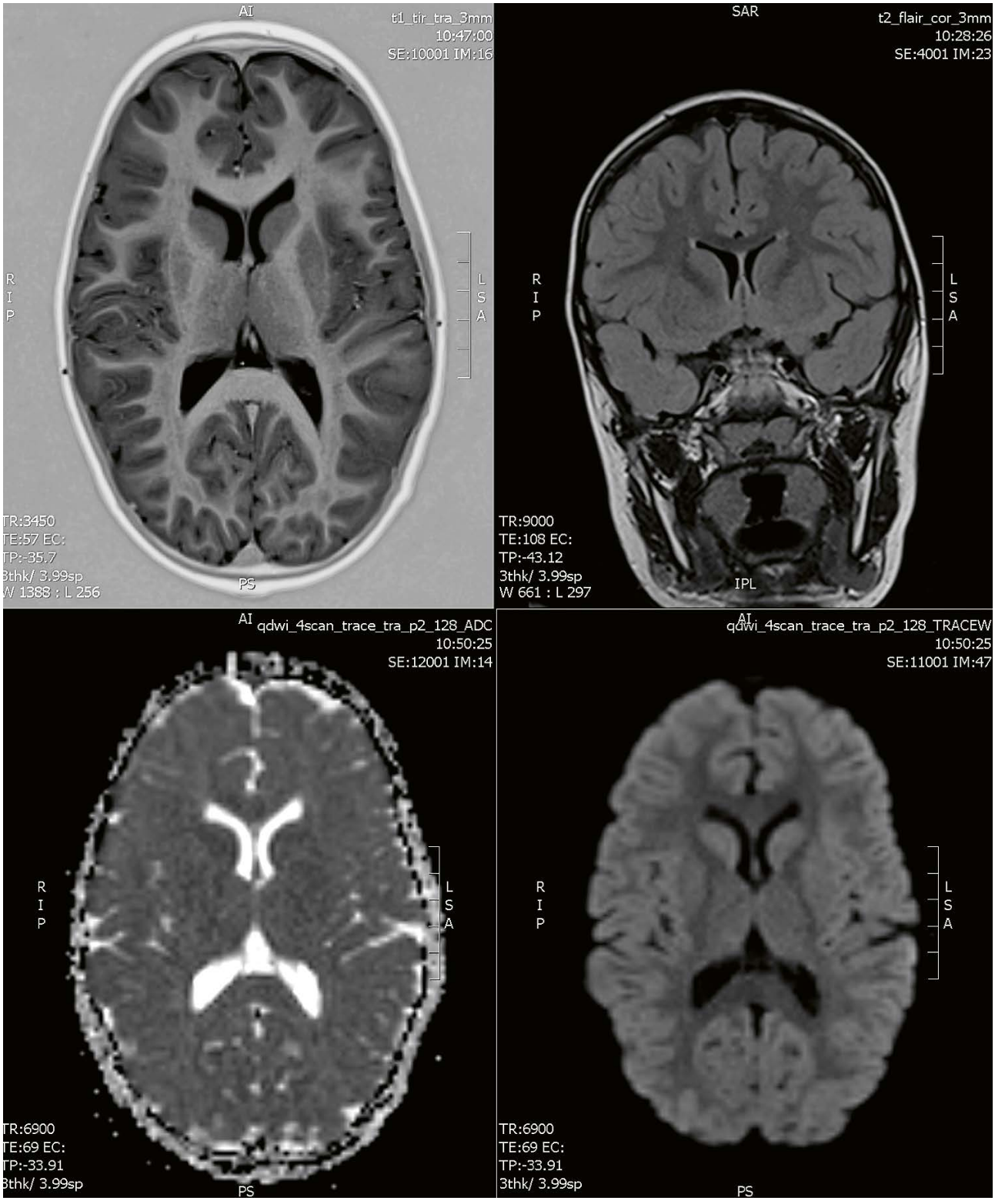

9 3 mm slices, axial T1 inversion recovery and coronal T2 FLAIR (top row), and axial quiet diffusion and ADC map (bottom row).

Repeated feverish convulsions were seen in this three-year-old. EEG was normal, but the last episode was atypical with lateralization.

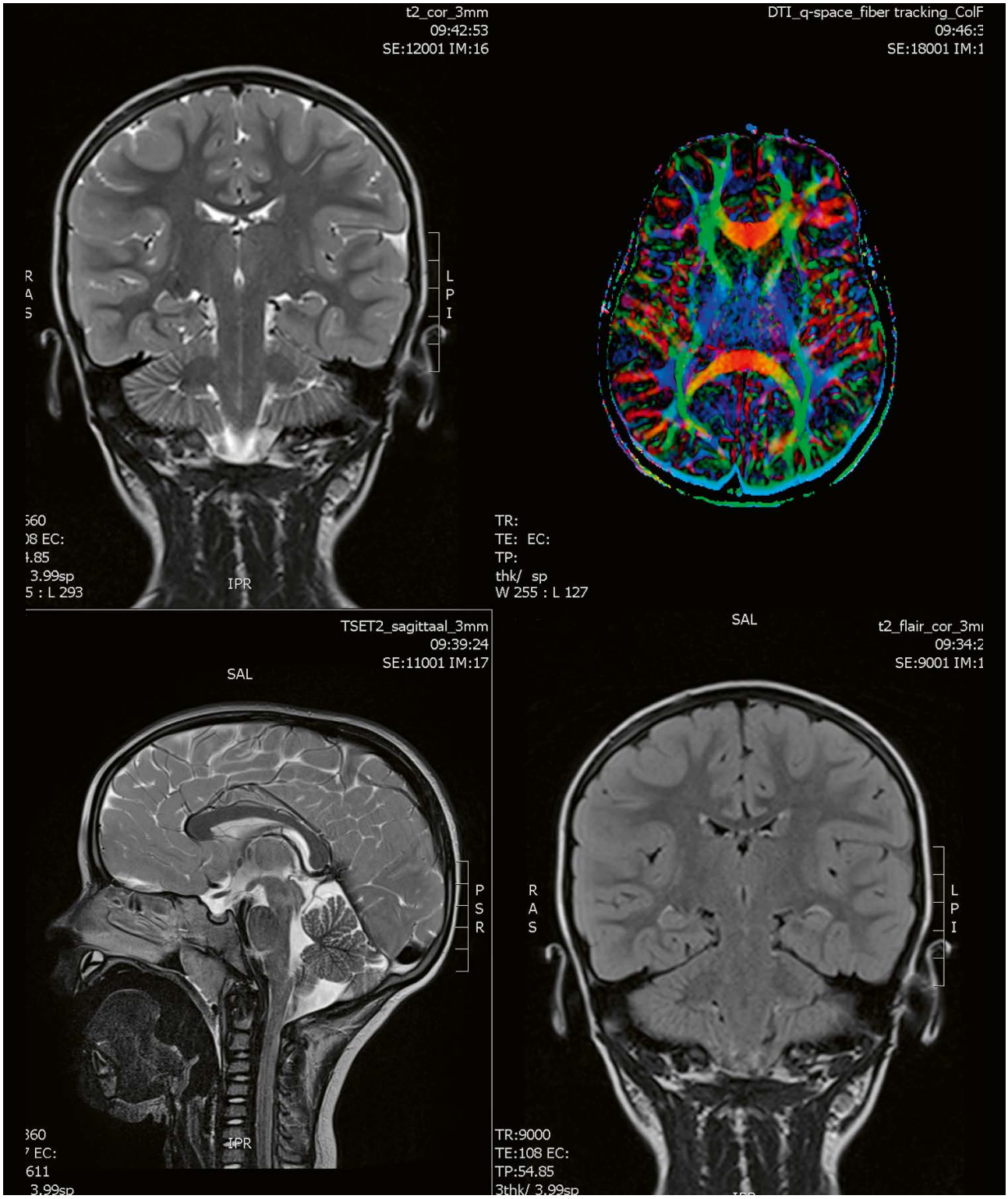

10 Coronal 3 mm quiet T2 TSE, and DTI q-space fiber tracking (top row); 3 mm quiet T2 sagittal and 3 mm coronal FLAIR (bottom row); no underlying anomaly.

This four-year-old suffered from excessive headaches and vomiting.

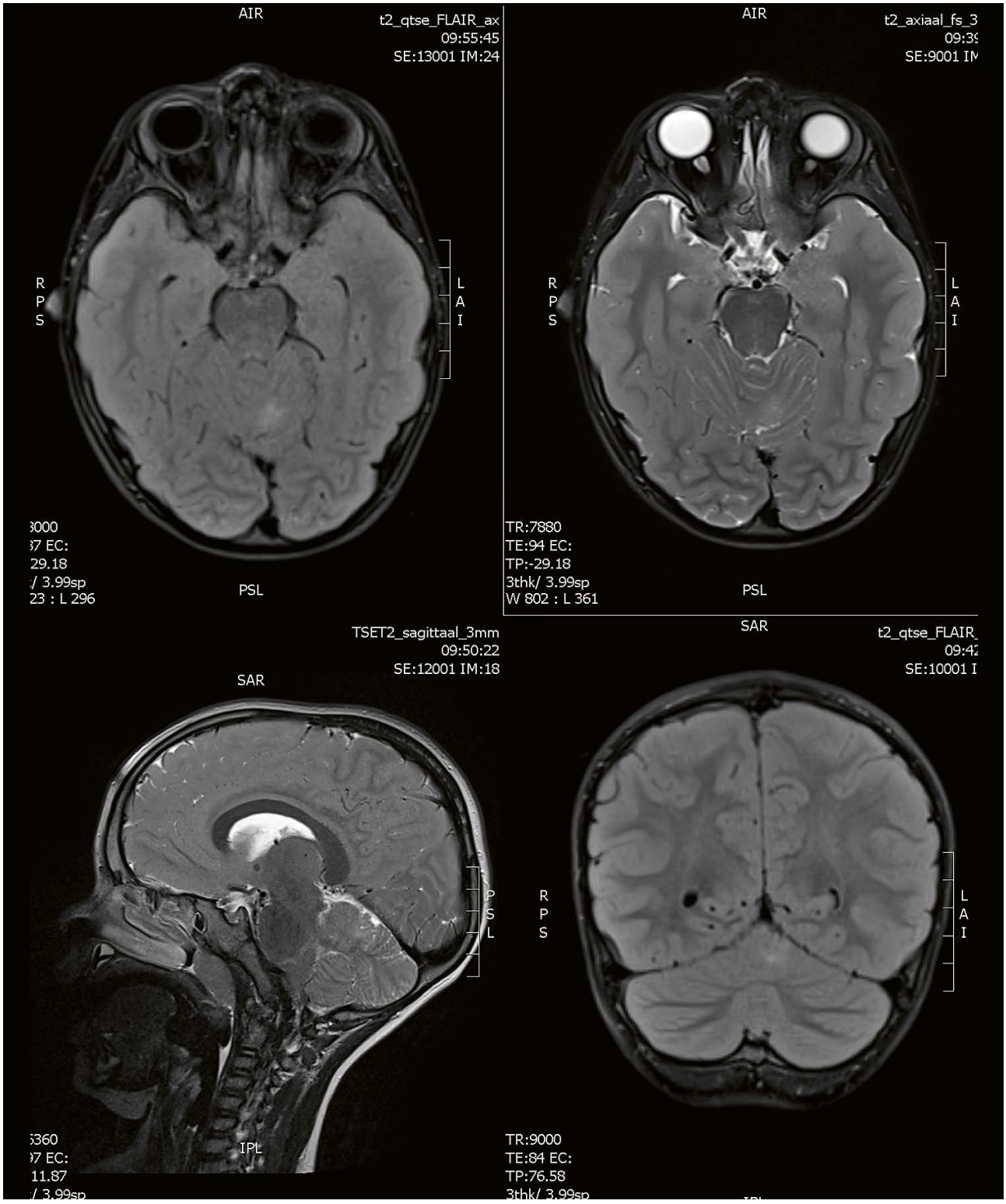

11 3 mm axial FLAIR and T2 TSE quiet sequence, 3 mm (top row) and sagittal T2 TSE and coronal FLAIR 3 mm quiet sequence (bottom row) demonstrate small T2 and FLAIR hyperintense cerebellar mass-like cortical and subcortical deformation in the vermis, suggestive of focal microgyria.

This three-year-old, ex-premature (32 weeks, chorioamnionitis) patient had Grade I bilateral germinal matrix bleeding (GMH) and delayed development.

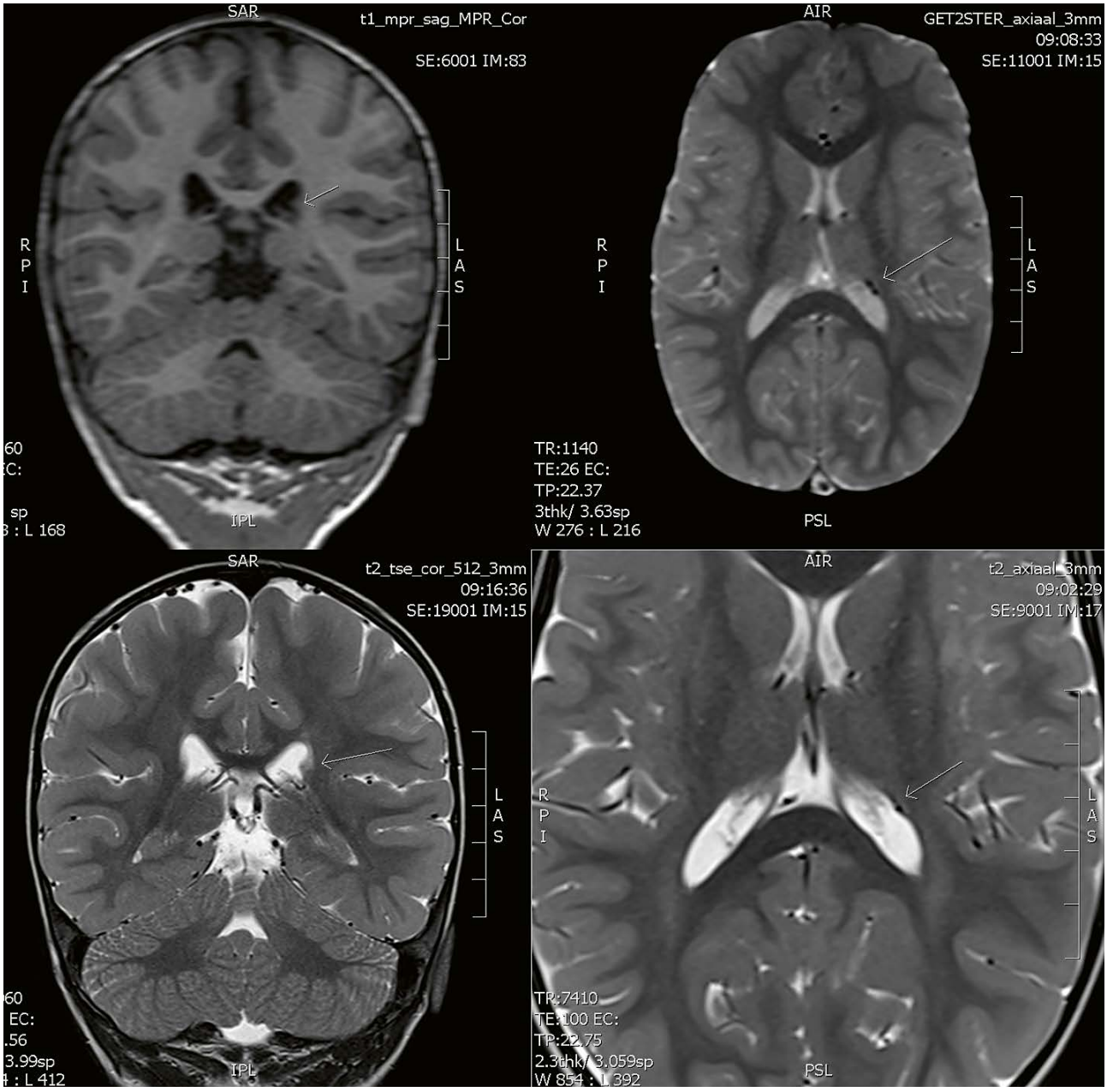

12 3D MPRAGE coronal reformat, 3 mm axial T2*(top row) and coronal T2 TSE quiet sequence, 3 mm (bottom row), and zoomed-in 3 mm axial T2 TSE sequences (bottom row) demonstrate small T2 and more obvious T2* hypointense spots that reflect the known Grade 1 GMH.

This 19-month-old baby[1] with cryptorchidism underwent orchiopexy on the left side and laparoscopic procedure/ search for suspected (previous ultrasound) intra-abdominal right testis below the kidney. Laparoscopy failed to prove suspected intra-abdominal testis. MRI was ordered to search for intra-abdominal testis.

Since the breath-holding technique is not an option for this patient, we used the StarVIBE sequence, running pre- and post-contrast images covering kidneys to groin. Inplane resolution was 1 mm and slice thickness was 1.1 mm. Acquisition time was 3 minutes and 45 seconds, and it was a free-breathing acquisition.

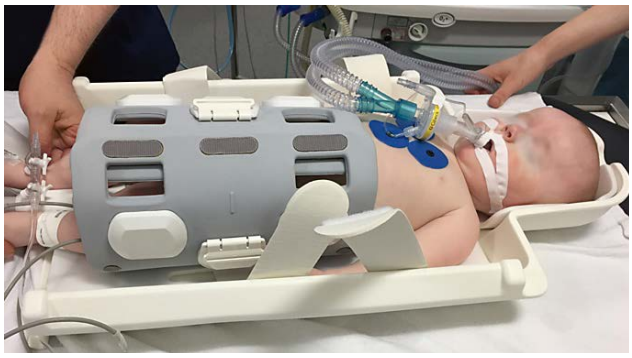

13 As a technical note: In the cradle one can easily wrap and fix the ultraflex coil for abdominal or pelvic examinations.

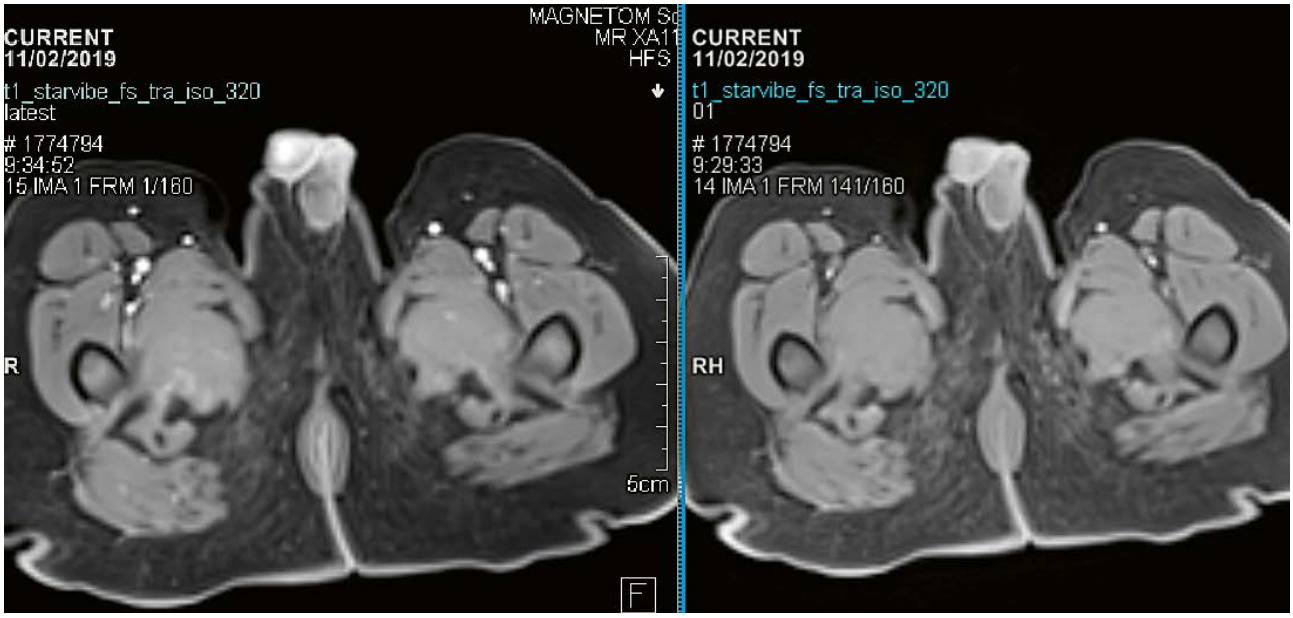

14 Axial StarVIBE with and without contrast, 1.2 mm slices; left testis *in situ* after orchiopexy.

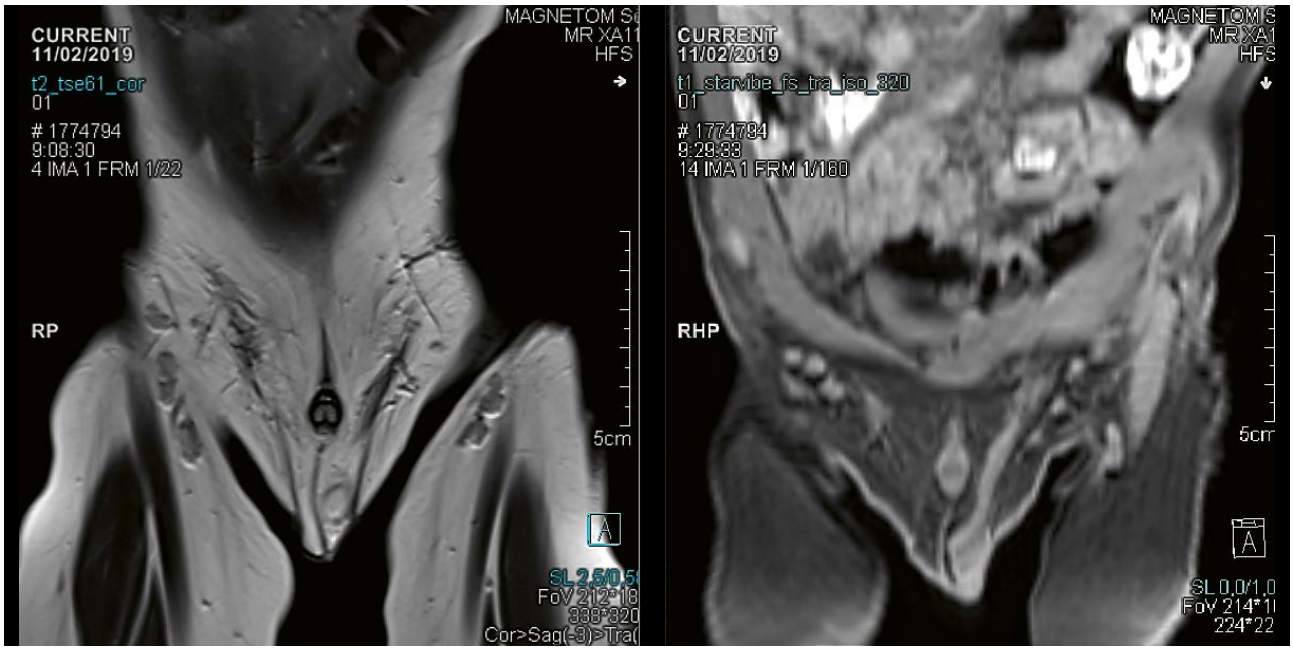

15 Coronal T2 TSE, inplane resolution 0.6 mm, slice thickness 2.5 mm, and coronal reconstructed T1 StarVIBE acquisition demonstrate scarring and fibrosis from laparoscopic access ports, and presence of testis and spermatic cord on the left side, with an empty scrotal sac and inguinal canal on the right side.

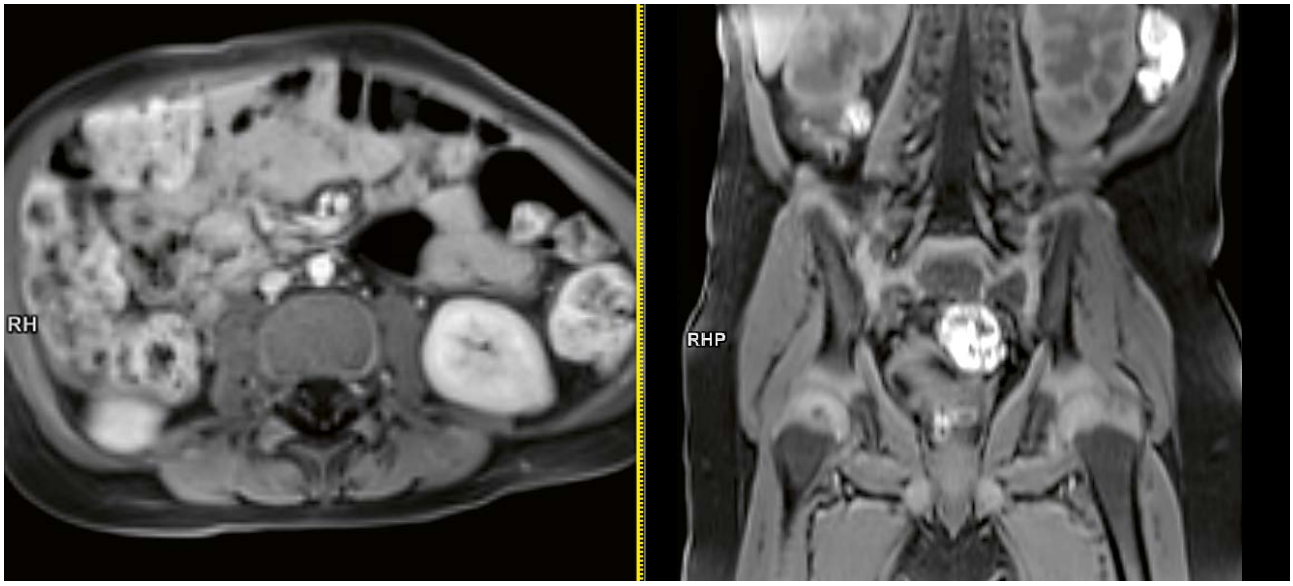

16 Axial T1 StarVIBE 1 mm slice and coronal reconstructed T1 StarVIBE: no intra-abdominal testis just below the right kidney, as was initially suggested on the first ultrasound.

In conclusion, MAGNETOM Sola and the pediatric coil team up very well to provide pediatric patients with the care they are entitled to.

Contact

Johan Dehem, M.D.
Jan Yperman Ziekenhuis
Briekestraat 12
8900 Ypres
Belgium
Phone: +32 57 35 74 00
johan.dehem@yperman.net

GOBrain 5-Minute MRI in Children: Shown to Reduce the Need for Sedation

Nadja Kadom, M.D.[1,2]; Anna Trofimova[1], M.D.

[1] Emory University School of Medicine, Department of Radiology and Imaging Sciences, Atlanta, GA, USA
[2] Children's of Atlanta (CHOA-Egleston), Department of Radiology, Atlanta, GA, USA

Abstract

Shorter MR imaging protocols can be very valuable in pediatrics[1], specifically when they reduce the need for sedation. In a pilot assessment of children under the age 8 years undergoing a 5-minute brain MR for primary headache, we found that the need for sedation was reduced by 70%. A current barrier to wide adoption of this imaging protocol is the lack of data directly comparing diagnostic quality between a 5-minute brain MRI protocol and a conventional MRI brain protocol.

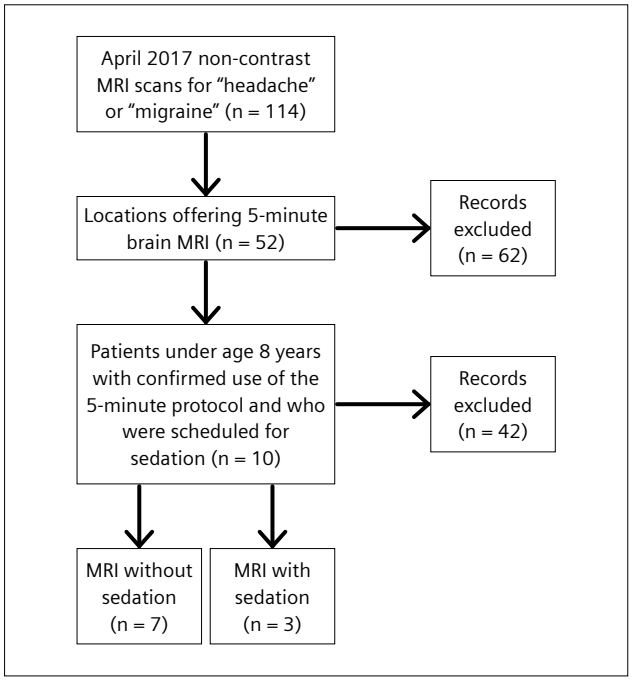

1 Study setup.

Background

The number of MRI studies requiring sedation in children increases at a rate of 8.5% annually, slightly exceeding the growth rate of CT and MRI imaging studies (8.1%) [1]. While sedation of children for imaging studies has been shown to be extremely safe, there has been some concern regarding potential neurotoxicity of certain anesthetics [2]. Sedation also adds cost to an MRI study, driving up health care expenses for individuals and for society [2]. From the patient and family perspective, use of sedation signifi-cantly increases the amount of time spent at the imaging facility and children may experience side effects post-sedation, such as motor imbalance, gastrointestinal symptoms, agitation, and restlessness [3].

Several strategies have been proposed to decrease the use of sedation in children. Child-life specialists can coach patients through MRI exams without sedation, but this may require training on 'mock' scanners, which are expen-sive and not widely available. Child-life coaching may lead to frequent interruptions during the scan, which could disrupt the MRI schedule. Video and audio technologies have been successful in serving this purpose and resulted in up to 45% decrease in sedation utilization [4]. In infants, feeding and bundling can be used to reduce motion artifacts, although this could result in overheating and respiratory compromise [5].

Here, we collected pilot data on using a 5-minute brain MRI protocol and its effect on the need for sedation in children with presumed primary headaches under the age of 8 years.

[1] *MR scanning has not been established as safe for imaging fetuses and infants less than two years of age. The responsible physician must evaluate the benefits of the MR examination compared to those of other imaging procedures. Note: This disclaimer does not represent the opinion of the authors.*

Material and methods

The pilot assessment was performed at a freestanding pediatric hospital that serves as a level I trauma center. We used a software application (Montage Health Solutions Inc, Philadelphia, PA, USA) to search radiology reports for any patients with an imaging indication containing the words "headache" or "migraine" and who underwent a non-contrast brain MRI. The study period was April 1–30, 2017. We excluded any patients 9 years or older assuming that they would be able to undergo MRI brain imaging without sedation. We also excluded two locations within our health care system that do not offer the 5-minute brain MRI protocol. We included only patients in whom we could confirm that the 5-minute brain MRI protocol had been used. For patients meeting inclusion criteria, we checked the medical records to determine whether they were scheduled as a sedated MRI and whether they were completed as a sedated or a non-sedated MRI.

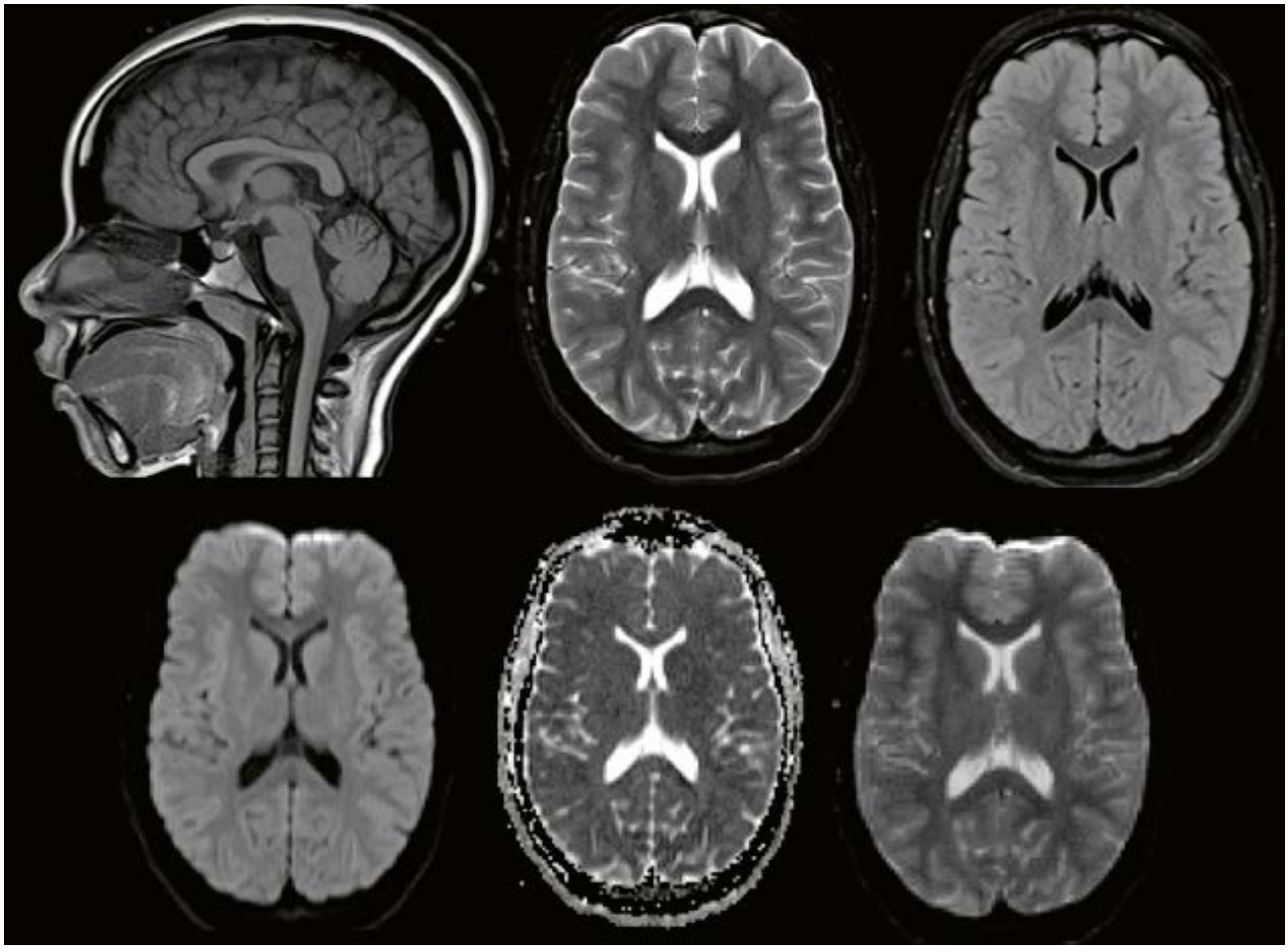

2 GOBrain 5-minute protocol.

Results

In the study period April 1–30, 2017 we found 114 non-contrast brain MRI studies done for indications containing the words "headache" or "migraine", 52 were done at locations that offer the 5-minute brain MRI protocol, and, of these, there were 10 patients under the age of 8 years in whom we confirmed that the 5-min brain protocol was used and who were scheduled to undergo the MRI with sedation. Of these, 7 were able to complete the MRI without sedation and 3 patients were imaged with sedation (Fig. 1). The percentage of patients converted to a non-sedated exam was 70% (7/10), which equals 6% of the entire cohort (7/114).

Discussion

By using the GOBrain 5-minute protocol we were able to reduce the number of sedated MRI's in the target cohort by 70%. This effect is stronger than the 45% reduction that can be achieved through use of audio-visual distraction. There is potential for increasing the cohort that can benefit from the GOBrain 5-minute protocol by > 50% if this protocol was offered at other locations within our network. While the focus of this pilot data assessment was to observe the impact of a 5-minute brain MRI protocol on sedation requirements, we observed other benefits: given that the MRI slots are still 30 minutes long, the conversion of a full brain MRI to a 5-minute protocol opened up time on the MRI schedule that could be used for inpatient imaging or catching up on schedule delays.

The image quality of the 5-minute protocol was good (Fig. 2), but may not meet diagnostic quality standards for certain imaging findings. For example, small parenchymal lesions or small blood products may not be as readily visible given the constraints of the image acquisition in order to achieve short scan times. For this reason, we are limiting the use of this MRI protocol to a patient cohort with "headache" or "migraine" as the sole indication, where most patients are presumed to be screened in the setting of a primary headache with low probability of underlying structural pathology of the brain. Future studies will be needed to compare the diagnostic perfor-mance of short MRI protocols in direct comparison to MRI protocols with conventional exam length.

Contact

Nadja Kadom, M.D.
Director of Pediatric Neuroradiology, Children's Healthcare of Atlanta (Egleston)
Associate Professor, Emory University School of Medicine
Department of Radiology and Imaging Sciences
1405 Clifton Rd NE
Atlanta, GA 30322
USA
Cell/text: +1 703 585 6554
nkadom@emory.edu

Nadja Kadom

Dr Anna Trofimova

Acknowledgement

We would like to thank the MRI technologists at CHOA-Egleston and CHOA-Towncenter for their help with data collection and for their enthusiasm and engagement towards the goal of minimizing sedation for children, without compromising the quality of care: Nicole Chin, Melissa Weisel, Jennifer Bagley, and Shane Stewart.

References:

1 Wachtel RE, Dexter F, Dow AJ (2009) Growth rates in pediatric diagnostic imaging and sedation. Anesth Analg 108:1616–1621.
2 Barton K, Nickerson JP, Higgins T, Williams RK. Pediatric anesthesia and neurotoxicity: what the radiologist needs to know. Pediatr Radiol. 2017 May 3.doi: 10.1007/s00247-017-3871-4. [Epub ahead of print] Review. PubMed PMID: 28470388.
3 Malviya S, Voepel-Lewis T, Prochaska G, Tait AR. Prolonged recovery and delayed side effects of sedation for diagnostic imaging studies in children. Pediatrics. 2000 Mar;105(3):E42. PubMed PMID: 10699144.
4 Khan JJ, Donnelly LF, Koch BL et al (2007). A program to decrease the need for pediatric sedation for CT and MRI. Appl Radiol 36:30–33.
5 Antonov NK, Ruzal-Shapiro CB, Morel KD, Millar WS, Kashyap S, Lauren CT, Garzon MC. Feed and Wrap MRI Technique in Infants. Clin Pediatr (Phila). 2016 Nov 20. pii: 0009922816677806. [Epub ahead of print] PubMed PMID: 27872353.

The results by the Siemens' customer described herein are based on results that were achieved in the customer's unique setting. Since there is no "typical" hospital and many variables exist (e.g., hospital size, case mix, level of IT adoption) there can be no guarantee that other customers will achieve the same results.

Perfusion Imaging in Pediatric Brain Tumors: Pseudo-continuous Arterial Spin Labeling at Work

Giovanna Stefania Colafati[1]; Chiara Carducci[1]; Ioan Paul Voicu[1,2]; Antonio Napolitano[3]

[1]Department of Imaging, Neuroradiology Unit, Bambino Gesù Children's Hospital, Rome, Italy
[2]Department of Hematology/Oncology and Stem Cell Transplantation, Bambino Gesù Children's Hospital, IRCCS, Rome, Italy
[3]Medical Physics Unit, Risk Management Enterprise, Bambino Gesù Children's Hospital, Rome, Italy

Patient history

A 2-year-old male patient[1] with a history of gait and balance problems, associated with nausea, was admitted to our Emergency Department. A brain CT scan revealed a posterior fossa mass.

Patient underwent brain and spine MRI with MAGNETOM Skyra 3T (Siemens Healthcare, Erlangen, Germany) to characterize the lesion. The protocol in use in our institution includes conventional 2D and 3D sequences as well as advanced sequences acquired before and after endovenous injection of contrast medium, including the Pseudo-Continuous Arterial Spin Labeling (PCASL) sequence[2] (Fig. 1).

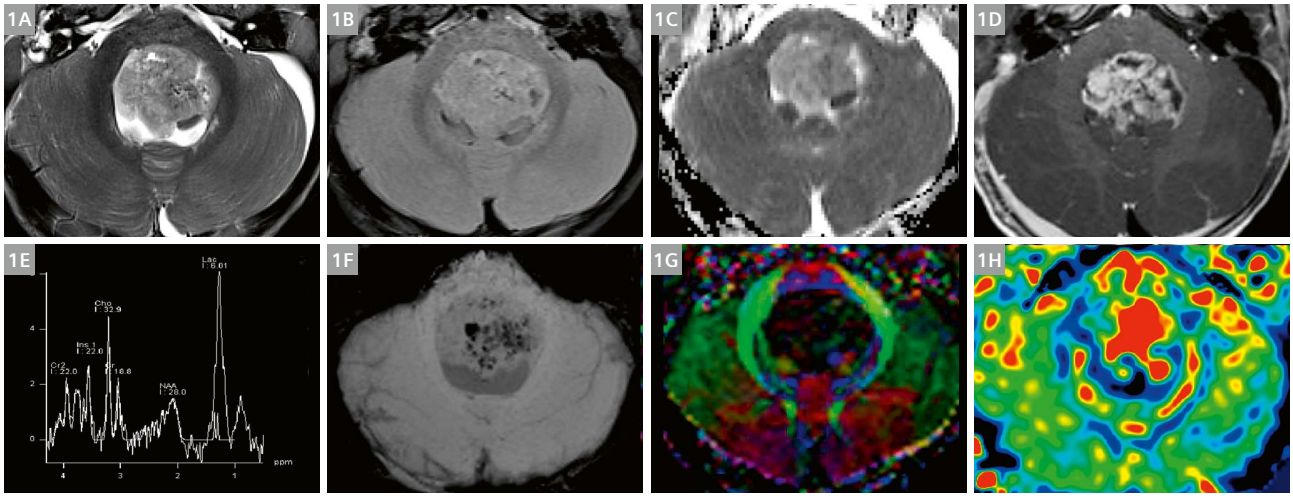

1 Multiparametric MR imaging of the lesion (**1A** axial T2-weighted; **1B** axial FLAIR; **1C** ADC map; **1D** axial high-resolution 3D T1-weighted Gradient Echo Sequence (MPRAGE) reconstruction; **1E** Spectroscopy; **1F** axial Susceptibility-Weighted Imaging (SWI); **1G** Fractional Anisotropy color map from Diffusion Tensor Imaging (DTI); **1H** Pseudo-continuous Arterial Spin Labeling (PCASL)[2] with a 3D background-suppressed Gradient and Spin-Echo (GRASE)). An intraventricular posterior fossa mass is seen (1A–D, 1F–H). The lesion presents a heterogeneous appearance due to solid-enhancing components (1A, B, D), necrotic portions (1D), regions with restricted diffusivity (1C) and low-signal foci consistent with calcifications (1F). Spectroscopy reveals increase of Choline, decrease in N-acetylaspartate, and a peak of lactate and lipids (1E). Low FA values are seen within the lesion (1G). PCASL cerebral blood flow (CBF) color maps (1H) show high CBF values within the lesion.

[1]MR scanning has not been established as safe for imaging fetuses and infants less than two years of age. The responsible physician must evaluate the benefits of the MR examination compared to those of other imaging procedures. Note: This disclaimer does not represent the opinion of the authors.
[2]WIP, the product is currently under development and is not for sale in the US and in other countries. Its future availability cannot be ensured.

PCASL sequence details

Pseudo-continuous labeling was performed with a prototype sequence[2] using a labeling period of 1500 ms, followed by a 1500-ms post-label delay (inversion time 3000 ms). Whole-brain images were obtained with a 3D background-suppressed Gradient and Spin-Echo (GRASE) sequence, with a TR of 4.6 s, turbo factor = 14 and EPI factor = 21. The sequence required a 6-minute acquisition time, including M0 used for Cerebral Blood Flow (CBF) quantification. Other ASL parameters were TE 15.6 ms; FOV 192 x 192 mm; matrix 64 x 64; measurements 6, and segments 6. For CBF quantification T1 blood and T1 tissue of 1650 ms and 1330 ms respectively was used. Circular 2D regions of interest (ROIs) with a mean area of 50 mm^2 were manually positioned in the most perfused area of the lesion. In addition to CBF, an rCBF was computed normalizing it with the mean value within another ROI in the normal-appearing gray matter of a cerebellar hemisphere.

Quantitative analysis revealed CBF and rCBF values of 58 mL/min/100 g and 1.9 respectively. The child underwent surgical resection of the lesion. Histology revealed an ependymoma grade 2, according to the 2016 World Health Organization classification.

Conclusion

MRI has a key role in examining pediatric brain tumors noninvasively. Both conventional and advanced sequences allow to obtain useful information at diagnosis for surgical planning, after surgery, for monitoring treatment response, and at further follow-up. In the pediatric population, among Perfusion-Weighted Imaging (PWI) techniques, a growing interest is currently emerging in arterial spin labeling (ASL) [1–3], a completely noninvasive and repeatable perfusion technique, that generates an image by magnetically "labeling" water molecules in arterial blood as an endogenous tracer. ASL can be generated using three main techniques of proton labeling: continuous labeling (CASL), pulsed labeling (PASL) and pseudo-continuous labeling (PCASL) [4]. A consensus paper from the ISMRM Perfusion Study Group and the European Consortium for ASL in Dementia recommends pseudo-continuous labeling, background suppression, a segmented three-dimensional readout without vascular crushing gradients, and calculation and presentation of both label/control difference images and cerebral blood flow in absolute units using a simplified model [5].

The evaluation of brain tumor perfusion with ASL may have a different impact in children compared to the adult population, due to their distinct clinical characteristics. Specifically, because of the advantage of higher CBF signal with a better signal-to-noise ratio in children compared to adults, it is possible to obtain robust quantitative perfusion data in this population without endovenous gadolinium administration. This could potentially avoid recently emerging concerns regarding gadolinium tissue accumulation [3]. Another potential advantage of ASL is that the sequence can be repeated in cases of failed sedation or patient motion [1].

Quantitative ASL-derived CBF and rCBF values have been proven useful in pediatric tumor evaluation and grading and quantitative CBF values have shown similar diagnostic accuracy to the most commonly used contrast-based cerebral blood volume, in differentiating between tumoral subtypes [3]. It has also been reported that ASL CBF values correlate significantly with micro-vascular density [1]. The quantitative CBF values we obtained in our patient are in line with literature.

ASL imaging is proving to be a useful tool from diagnosis to follow-up. It should be considered for implementation in the routine workup of pediatric patients with brain tumors.

Contact

Dr. Giovanna Stefania Colafati
Bambino Gesù Children's Hospital
Department of Imaging
Neuroradiology Unit
Largo S. Onofrio 4
Rome, Italy (00165)
gstefania.colafati@opbg.net

References

1 Yeom KW, Mitchell LA, Lober RM et al. Arterial spin-labeled perfusion of pediatric brain tumors. AJNR Am J Neuroradiol 2014;35(2):395-401. doi: 10.3174/ajnr.A3670.
2 Dangouloff-Ros V, Deroulers C, Foissac F, et al. Arterial Spin Labeling to predict brain tumor grading in children: correlations between histopathologic vascular density and perfusion MR imaging. Radiology.2016 Nov;281(2):553-566. Epub 2016 Jun 3.
3 Morana G, Tortora D, Staglianò S et al. Pediatric astrocytic tumor grading: comparison between arterial spin labeling and dynamic susceptibility contrast MRI perfusion. Neuroradiology. 2018 Apr;60(4):437-446. doi: 10.1007/s00234-018-1992-6. Epub 2018 Feb 16.J.-C.
4 Ferré, E. Bannier, H. Raoult et al. Arterial spin labeling (ASL) perfusion: techniques and clinical use. Diagn Interv Imaging. 2013 Dec;94(12):1211-23. doi: 10.1016/j.diii.2013.06.010. Epub 2013 Jul 11.
5 Alsop DC, Detre JA, Golay X et al. Recommended implementation of arterial spin-labeled perfusion MRI for clinical applications: A consensus of the ISMRM perfusion study group and the European consortium for ASL in dementia. MagnReson Med. 2015 Jan;73(1):102-16. doi: 10.1002/mrm.25197. Epub 2014 Apr 8.

Clinical Benefits of Multiple Post-Labeling Delay Pseudo-Continuous Arterial Spin Labeling (Multi-PLD PCASL) in Pediatric Patients with Moyamoya Disease

Aya Tominaga[1]; Masaomi Sasaki[1]; Reizo Shirane[2]

[1] Department of Radiology, Miyagi Children's Hospital, Sendai, Japan
[2] Department of Neurosurgery, Miyagi Children's Hospital, Sendai, Japan

Introduction

Moyamoya disease, which frequently occurs in Asian countries including Japan, causes stenosis or obstruction in the circle of Willis and results in a number of new small blood vessels forming around the stenotic or obstructed arteries. The incidence peaks in two age groups: childhood and adulthood. It is roughly classified into either stenotic type or hemorrhagic type, depending on the onset condition. It is known that revascularization is effective in ischemic moyamoya disease, which is common in young patients, and that receiving treatment before the condition becomes serious leads to a better prognosis. The disease received the name "moyamoya" at Tohoku University in 1969 [1, 2]. The word, which means "puff of cigarette smoke" in Japanese, was chosen because this is what the newly generated cerebral blood vessels look like on cerebral angiography. This name is currently used worldwide. Our hospital conducts research on moyamoya disease as a related institute of Tohoku University, and is one of the representative facilities for studying pediatric moyamoya disease in Japan. We are working on safer and more effective treatments using a perioperative management method such as postoperative cerebral blood flow evaluation [3–5].

In the treatment of pediatric patients[1] with moyamoya disease, examining cerebral blood flow dynamics plays an important role in determining the treatment strategy. Although several methods exist, measurement by ^{15}O-H_2O PET is said to be the most reliable. However, in actual clinical practice, dual-table autoradiography (DT-ARG) by single photon emission computed tomography (SPECT) is popular and widely used because it is a simple and reliable method that requires less capital investment [6]. In our hospital, although we use DT-ARG for long-term follow-up, we do not apply it to younger patients because it requires arterial blood sampling during the examination, which is rather invasive. In recent years, 3T MRI has become widespread and noninvasive quantification of cerebral blood flow is routinely available with arterial spin labeling (ASL), which provides regional cerebral blood flow (rCBF). However, it has been reported that cerebral blood flow measured by ASL changes significantly depending on age and sex [8]. Buxton proposed a more robust ASL methodology to assess blood flow differences in individuals. The rCBF map is calculated from PCASL data obtained with multiple post-labeling delays (PLDs) in a process called multiple-PLD pseudo-continuous ASL (multi-PLD PCASL) [9]. Furthermore, by observing perfusion-weighted imaging (PWI) with different PLDs performed with this method, it is also possible to see pseudo hemodynamics. The method is highly advantageous, especially for children: It is noninvasive and can be repeatedly performed because it involves no radiation exposure or contrast media. We used a Siemens Healthineers prototype multi-PLD PCASL sequence[2] following the ASL study group recommendations [10], in

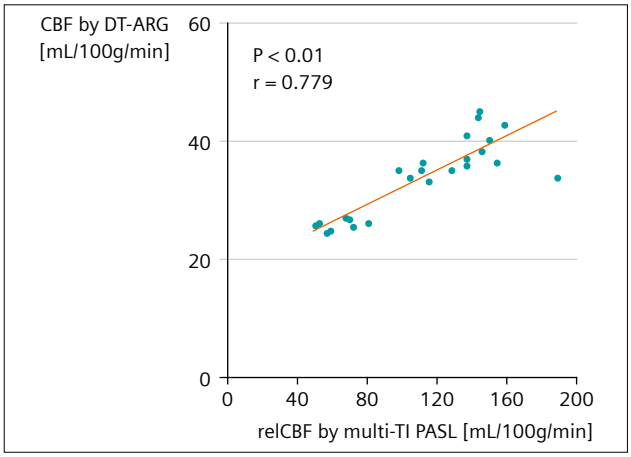

1 **Comparison of multi-TI PASL and DT-ARG**
ROIs were taken from four regions in each hemisphere of three moyamoya patients (24 ROIs).

[1] *MR scanning has not been established as safe for imaging fetuses and infants less than two years of age. The responsible physician must evaluate the benefits of the MR examination compared to those of other imaging procedures. Note: This disclaimer does not represent the opinion of the authors.*
[2] *Work in progress: Multi-PLD PCASL is currently under development and is not for sale in the US and in other countries. Its future availability cannot be ensured.*

which a Buxton model fit was also implemented. 3T MR is generally advantageous for ASL, which requires a higher signal-to-noise ratio (SNR). Therefore, prior to clinical application, we optimized the protocol for our 1.5T MAGNETOM Aera. We also tried to reduce the scan time to make it suitable for pediatric examinations. In this paper, we present two clinical cases for which multi-PLD ASL was useful, and a case which requires attention.

Materials and methods

The local institutional review board approved all study protocols, and written informed consent was obtained from healthy volunteers and from the parents of patients with moyamoya disease. We optimized the protocol with five healthy volunteers (aged between 25 and 43 years).

Protocol optimization and validation

A MAGNETOM Aera 1.5T and a 20-channel head/neck coil were used for this study. As the ASL signal from blood flow is acquired during T1 relaxation of magnetization labeled by inversion pulse, it is strongly influenced by the T1 value of blood and the PLD, which is the time between the labeling inversion pulse and data acquisition. In order to determine an acceptable PLD range at 1.5T, the rCBF of healthy volunteers was evaluated with single-PLD PCASL by changing the PLD from 1600 to 3200 ms with a step of 200 ms (labeling duration 1500 ms). The rCBF obtained with each PLD was compared in each brain region, and the upper PLD limit at 1.5T was decided. A small PLD step was set for the accuracy of rCBF estimation regarding the upper limit of the PLD. In terms of TGSE segments, which form the data-acquisition part of ASL, we investigated three, two, and one segment(s) in order to reduce scan time.

Concerning the accuracy of rCBF by ASL, we found a good correlation between DT-ARG and multi-TI PASL, which was used on the same moyamoya patients (n = 3) in our previous study (Fig. 1). In this study, due to the difficulty of collecting DT-ARG and ASL data from the same patient, we evaluated rCBF correlations between the previous multi-TI PASL and the new multi-PLD PCASL protocol on healthy volunteers.

Results

Protocol optimization

Figure 2 shows that the obtained rCBF was almost equivalent up to a PLD of 2800 ms, but decreased markedly at 2800 ms and above. As a result, we recognized that the upper limit of PLD was 2800 ms at 1.5T.

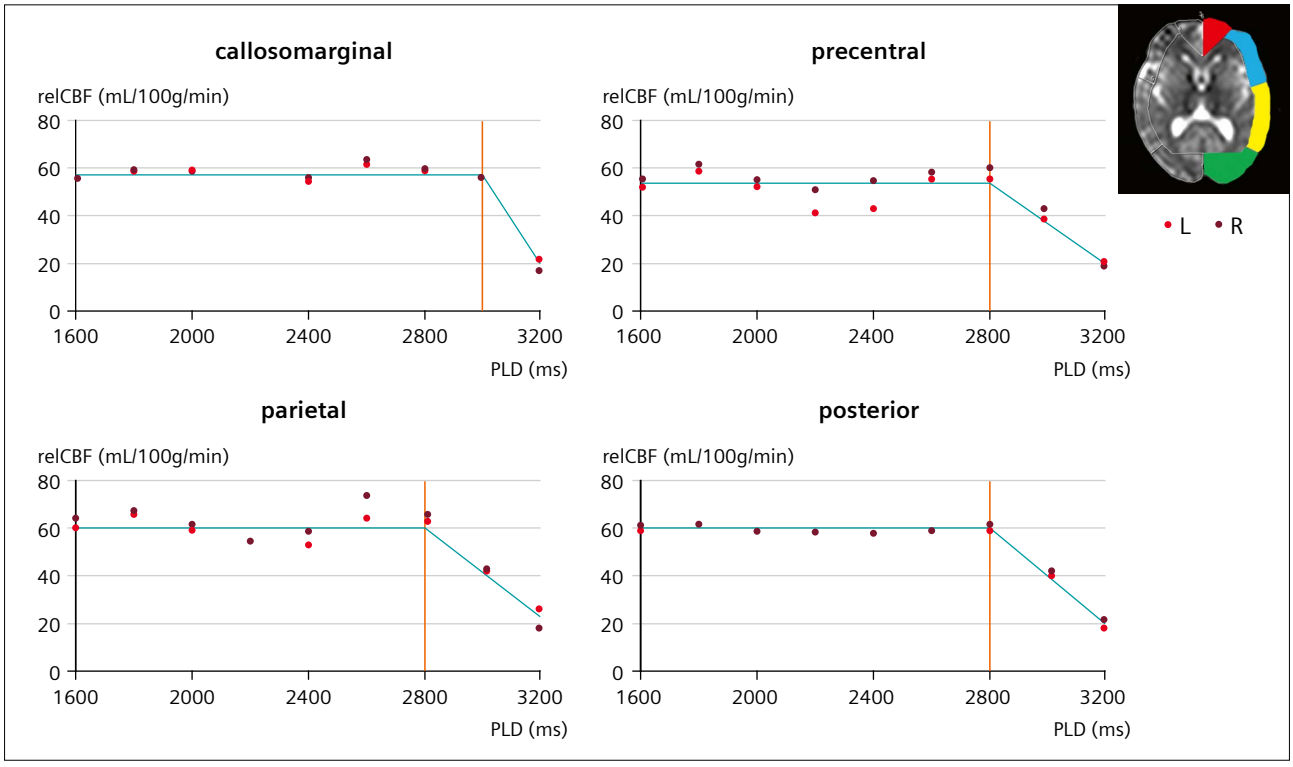

2 **relCBF depending on PLD by single-PLD PCASL (healthy adult volunteer)**
SNR of perfusion-weighed imaging decreased markedly (not shown in Figure) at a PLD of > 2800 ms (PLD) and affected relCBF. The reliable relCBF will be provided with a PLD of less than 2800 ms.

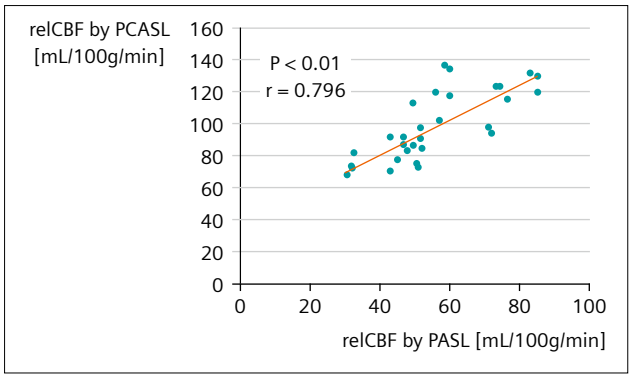

3 **Comparison of PASL (3 segments; 8 min) and PCASL (3 segments; 8 min)**
ROIs were taken from four regions in each hemisphere of four healthy volunteers (32 ROIs).

Strong correlation was found between multi-TI PASL and multi-PLD PCASL (Fig. 3). In addition, strong correlation in rCBF was found between the TGSE segments numbering one to three (Fig. 4A). Although a higher number of segments should theoretically provide a higher spatial resolution due to less T2 blurring, we could not see any major differences in one, two, or three segments (Fig. 4B). Since pediatric examinations need minimal scan times in order to avoid the possibility of patient motion during the examination, we chose to use one segment, which provided a scan time of 2 min 52 sec. Table 1 shows the detailed parameters, which are within the recommendation of the white paper [9] (TE x turbo factor < 300 ms, ESP x EPI factor < 15 ms). We were also able to observe pseudo cerebral hemodynamics by continuously showing PWI with multi-PLD.

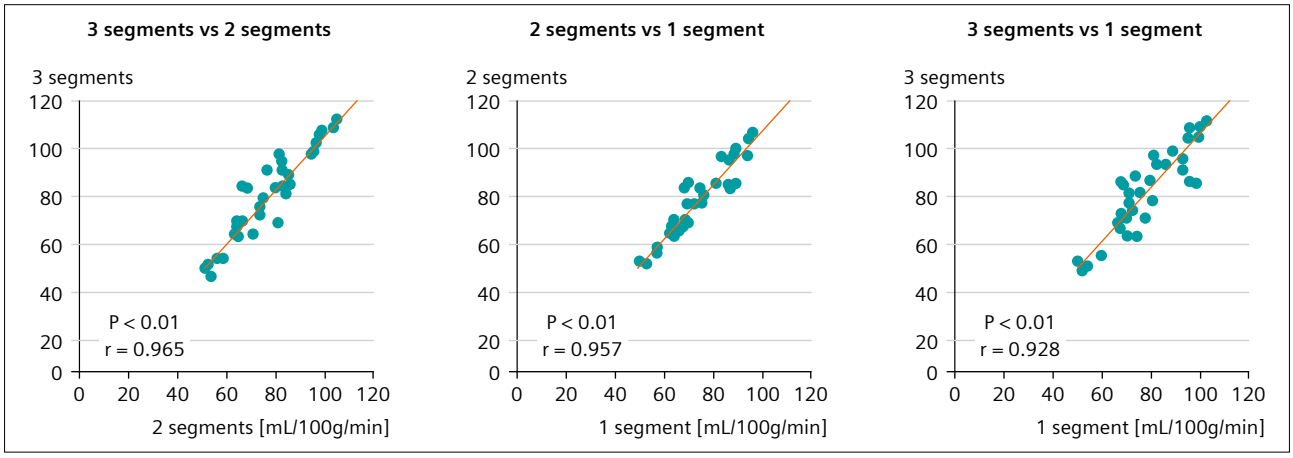

4A **Comparison of PCASL (3 segments), PCASL (2 segments), and PCASL (1 segment)**
ROIs were taken from four regions in each hemisphere of five healthy volunteers (40 ROIs).

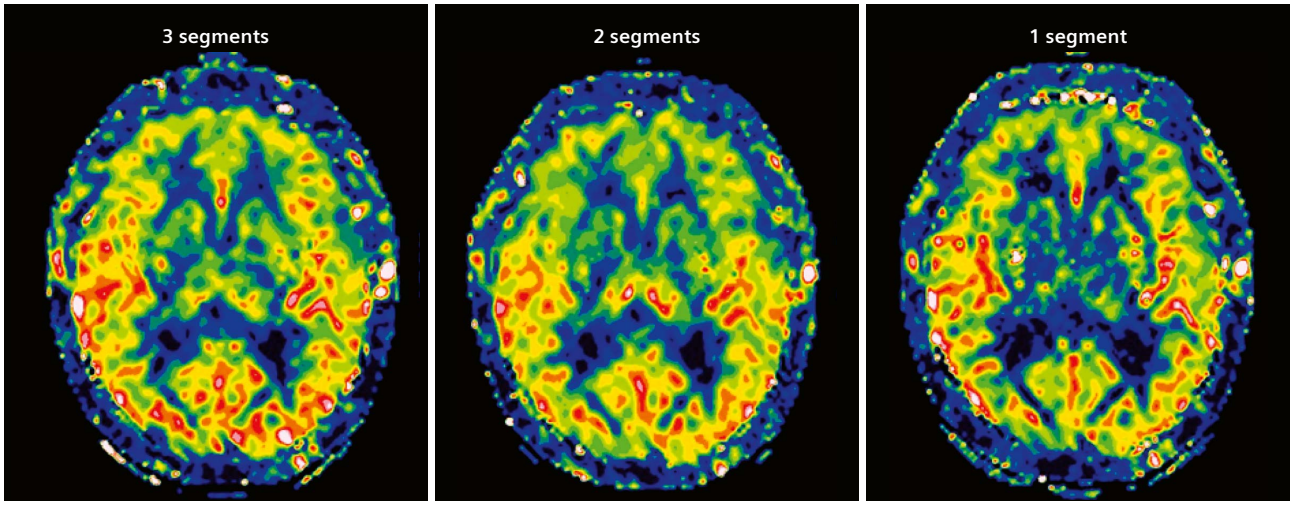

4B Comparison of PCASL 3, 2, and 1 segment(s).

All moyamoya patients in our hospital are examined with this optimized protocol. Below, we present three clinical cases.

Case 1

This is a postoperative follow-up case of a 10-year-old boy who underwent left direct and indirect revascularization in April 2016. As shown in the PWI, it was confirmed that the left reconstructed vessel was depicted later than the contralateral side (Figs. 5A, B). MRA performed on the same day showed narrowing at the left internal carotid artery from the end to the left A1-M1 and also at the right A1 (Fig. 5C). This result was consistent with the result observed in PWI. On the other hand, single-PLD ASL with a PLD of 1800 ms showed an erroneous result that suggested the CBF was high (Fig. 5D).

TR	TE	FOV	Slice thickness
5000 ms	11.1 ms	250 mm	5 mm
Matrix	**PAT mode**	**Bandwidth**	**Multi TI**
120 x 128	GRAPPA 3	2440 Hz/px	600~3600 ms

Table 1: Multi-TI PCASL parameters, TA 2 min 52 sec.

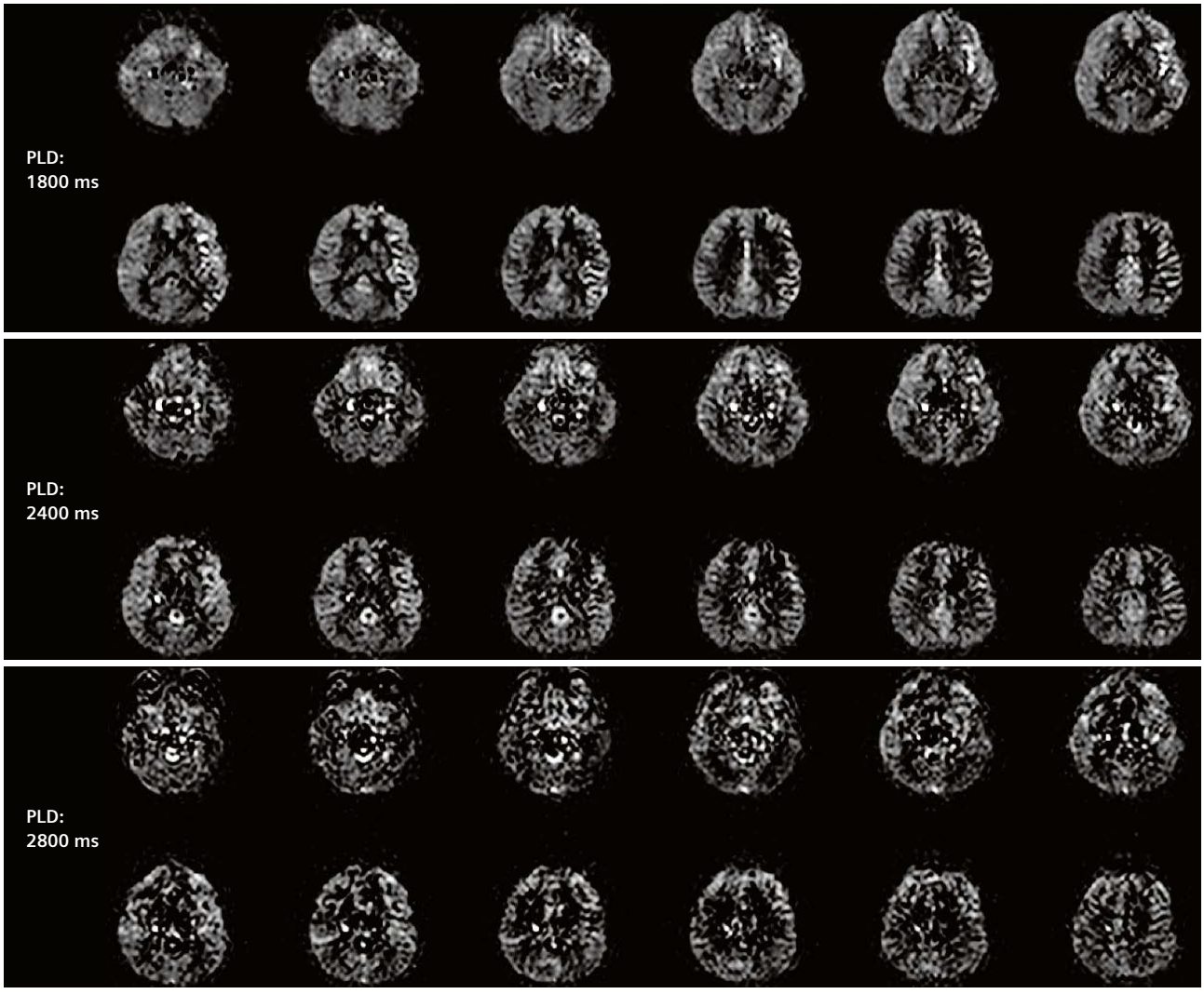

5A Moyamoya disease in a 10-year-old boy
Revascularization by left STC, single-PCASL PWI.

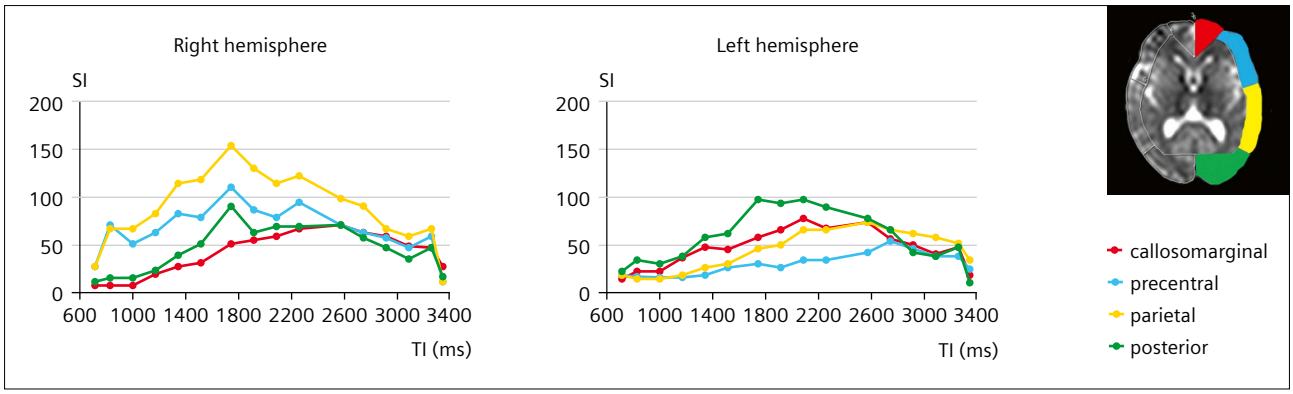

5B **PWI signal intensity (SI) by multi-TI PCASL**
The BAT in the left hemisphere extended. This result was consistent with the MRA showing narrowing at Lt. carotids ~A1, M1, and Rt. A1.

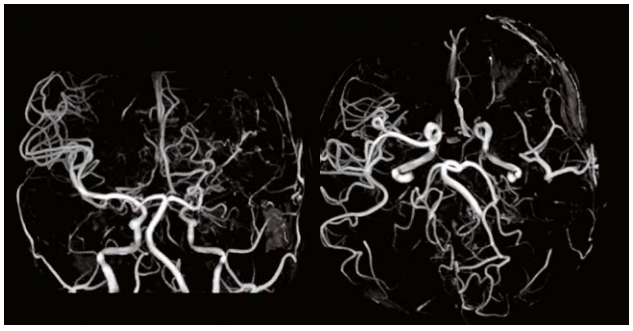

5C **Moyamoya disease in a 10-year-old boy**
Revascularization by left STC, MRA-MIP.

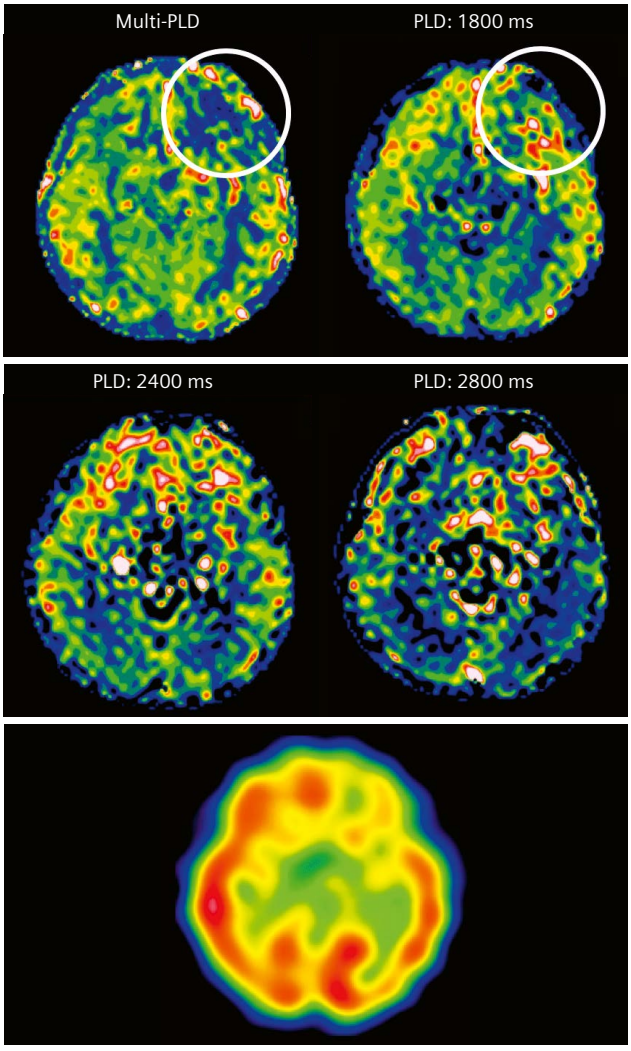

5D Comparison of SPECT and ASL.

Case 2

This is the case of a two-year-old boy who was too young for perfusion quantification by SPECT. He was diagnosed with moyamoya disease due to the onset of cerebral infarction at 10 months. Revascularization on the right side, opposite to the infarction, was quickly performed and postoperative follow-up was initiated (Fig. 6A). In April 2018, MRA and an rCBF map suggested a decrease in blood flow in the left hemisphere. However, no change was observed in the qualitative SPECT and follow-up observation was continued. A re-examination using MR after two months showed further progression at the same lesion in MRA and on the rCBF map from ASL. The qualitative SPECT again failed to detect the decrease in blood flow (Figs. 6B–D). Based on these results, a neurosurgeon decided to perform left vascular reconstruction. Although the postoperative course was good and the child was discharged, he was hospitalized again for examination in August 2018 because right upper and lower limb cataplexy was observed several times when he cried at home. Even then, no changes were found in qualitative SPECT. MRA showed stenosis at both sides of the PCA and the left reconstructed vessel. An rCBF map revealed a perfusion defect caused by the stenosis (Figs. 6E–G).

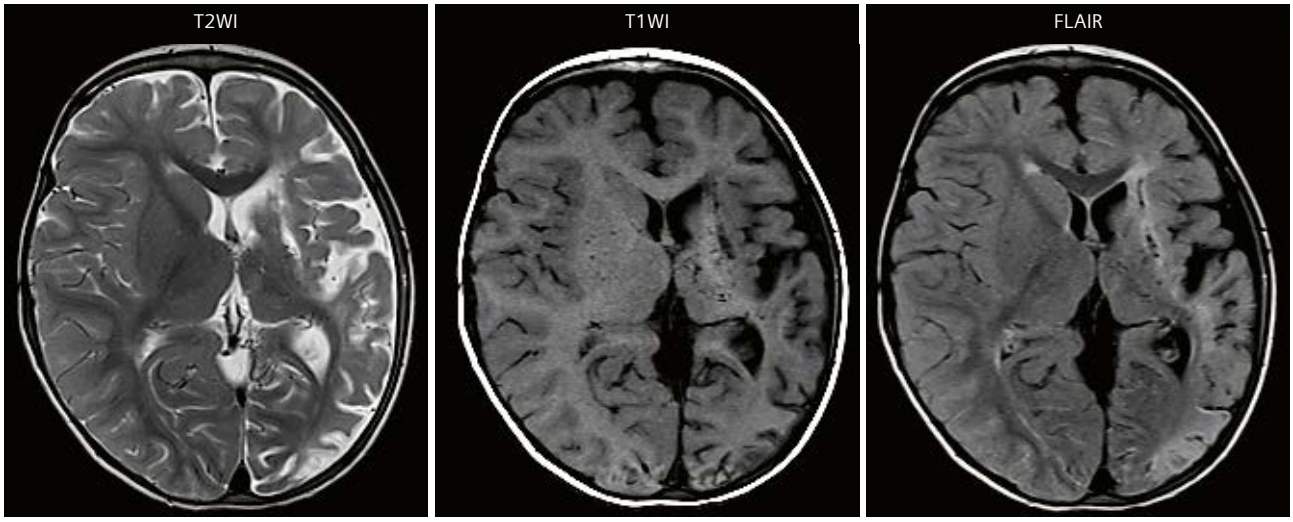

6A **Moyamoya disease in a two-year-old boy**
Revascularization by both STC, MR.

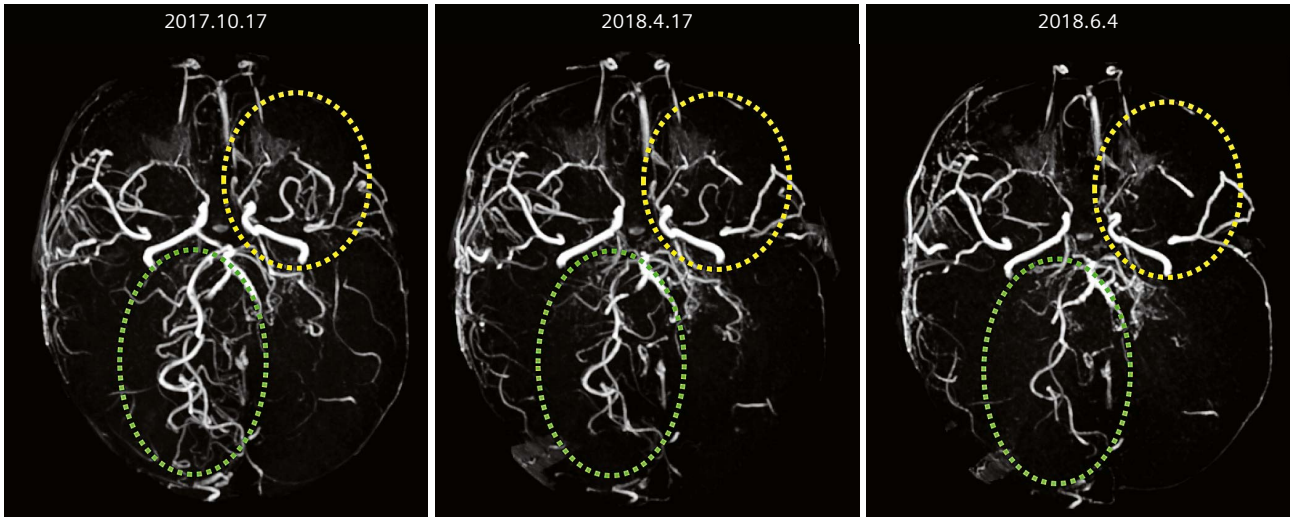

6B **Moyamoya disease in a two-year-old boy**
Revascularization by both STC, MRA-MIP.

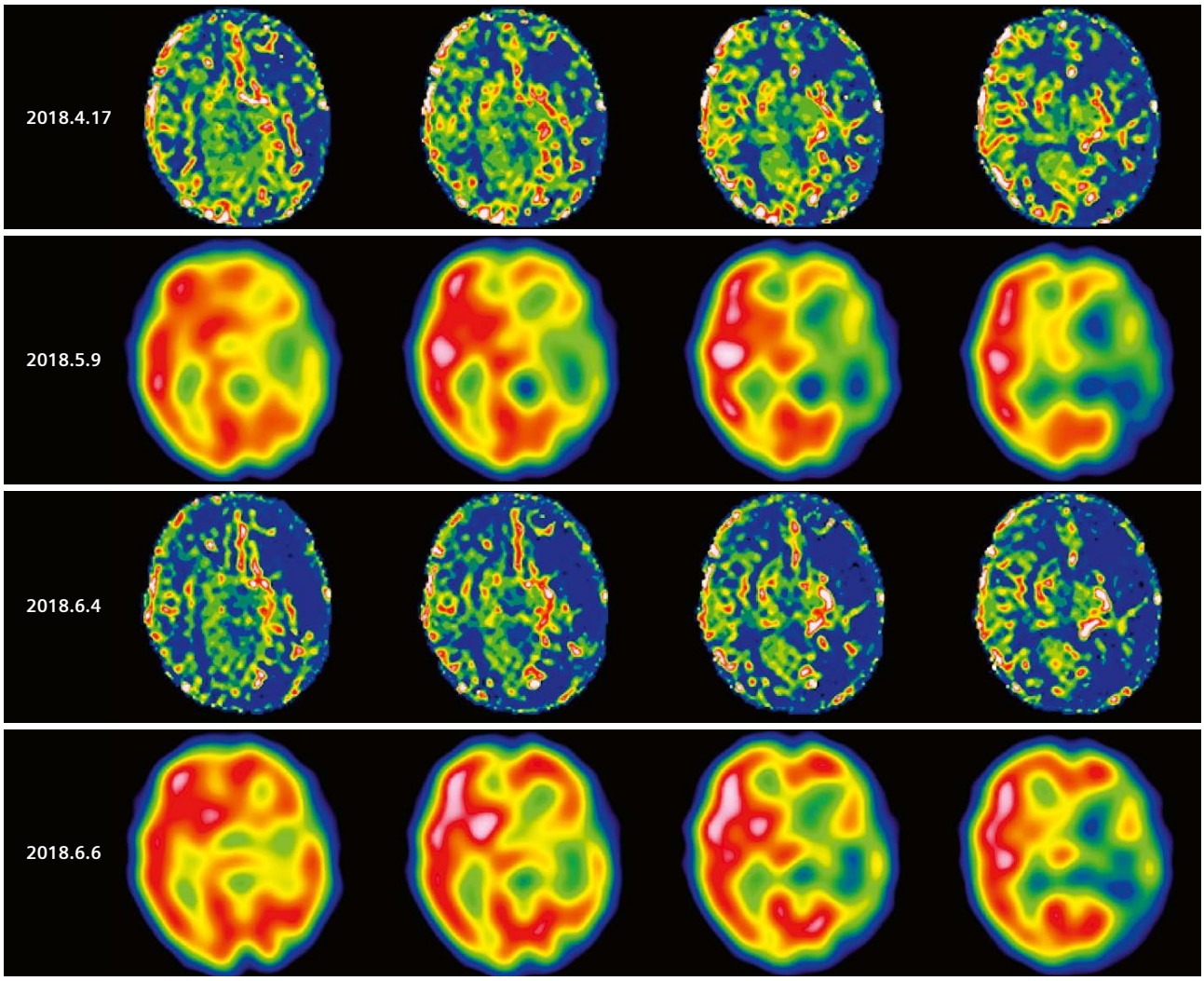

6C Comparison of SPECT and ASL.

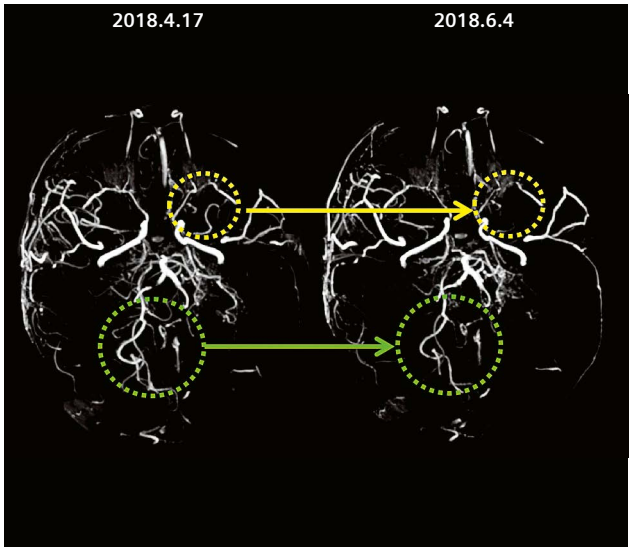

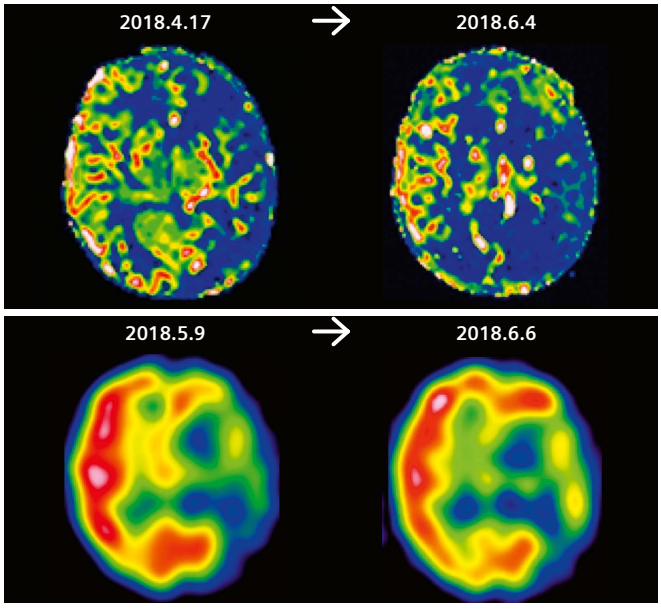

6D Comparison of SPECT and ASL.

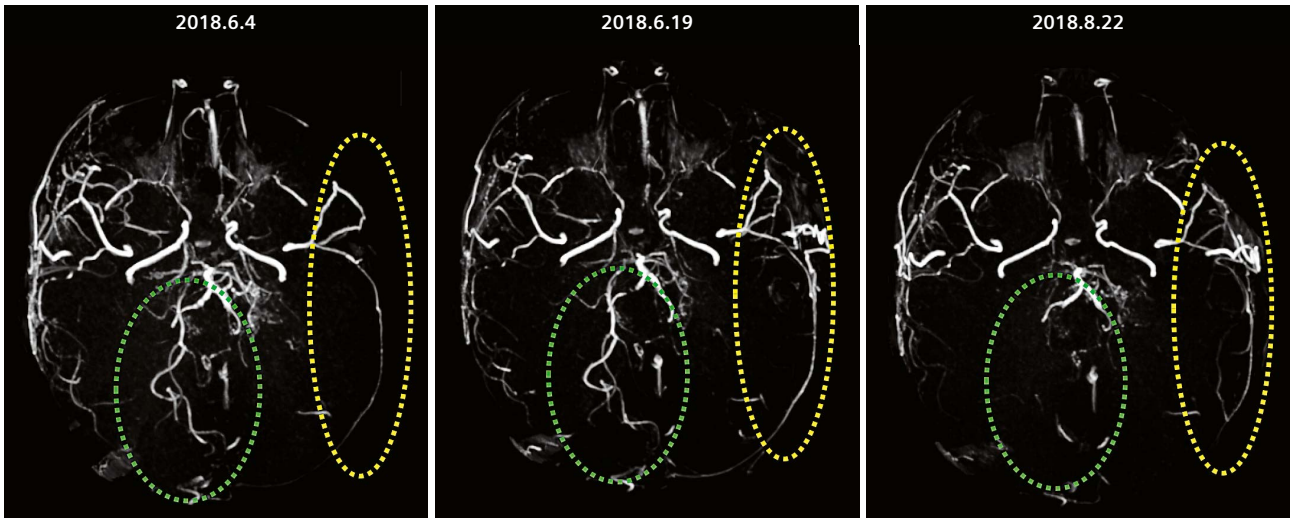

6E **Moyamoya disease in a two-year-old boy**
Revascularization by both STC, MRA-MIP.

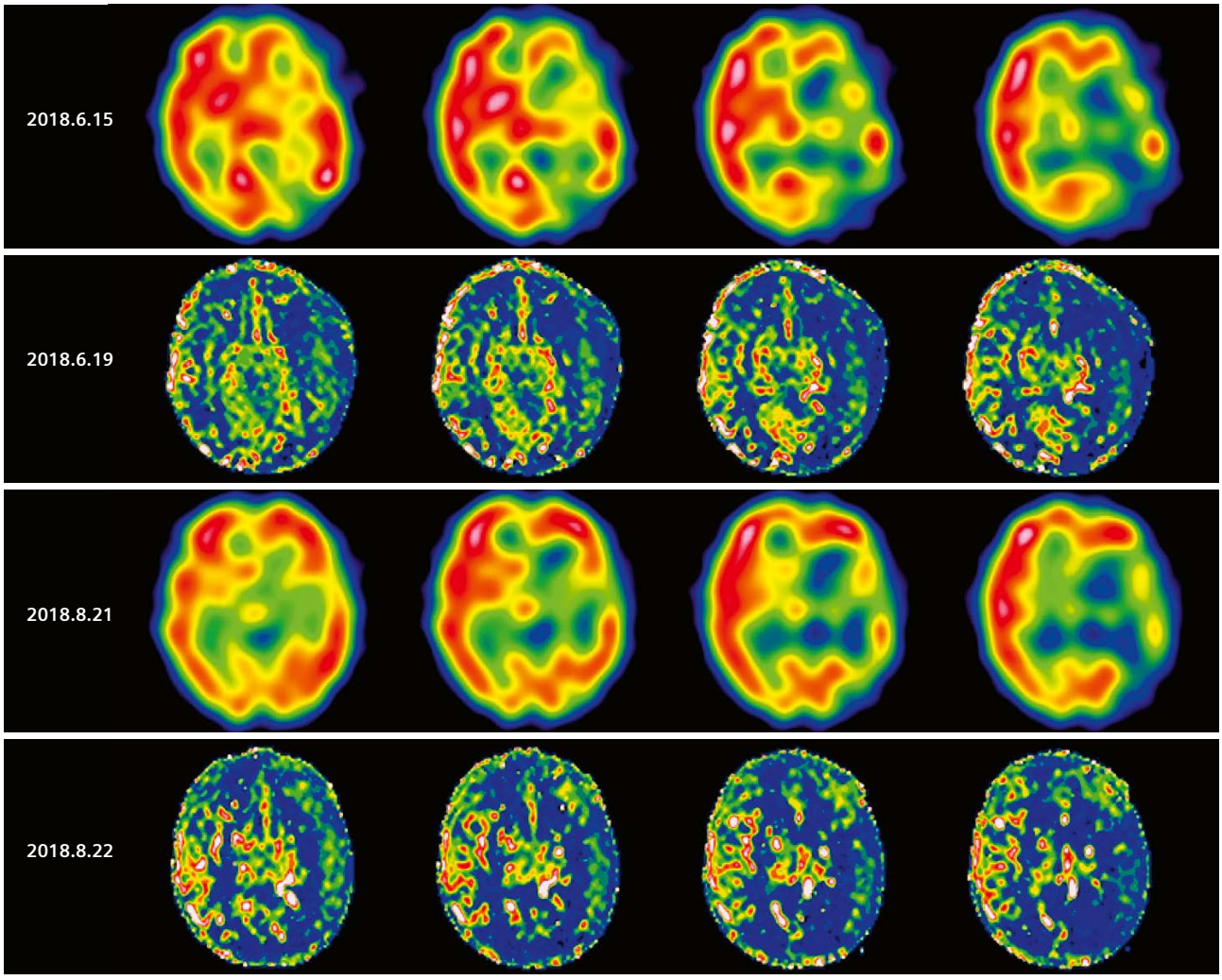

6F Comparison of SPECT and ASL.

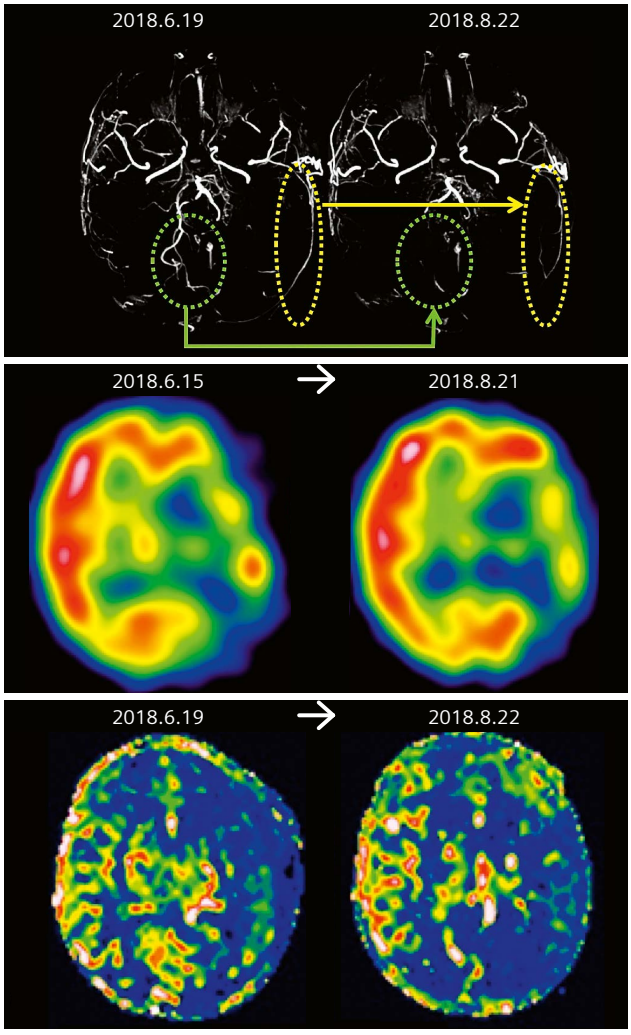

6G Comparison of SPECT and ASL.

Case 3

This is a postoperative follow-up case of a 16-year-old female who underwent left-direct and indirect revascularization in March 2016. The perfusion delay was clearly visible in the PLD vs. PWI signal curve (Figs. 7A–C) at the left hemisphere where revascularization was done. On the other hand, in the left MCA and PCA dominant region, the PWI signal in the vessel was high for a long period of PLD, from 1600 to 3000 ms (Fig. 7D), resulting in high rCBF even with Buxton model analysis. As a result, the rCBF map differed a great deal between quantitative SPECT (Fig. 7E) and the multi-PCASL method (Fig. 7F).

Discussion

The upper limit of PLD obtained in this study at 1.5T was 2800 ms. It is thought that at a PLD of 2800 ms or longer, rCBF estimation might fail (Fig. 2) because the T1 value at 1.5T is shorter than at 3T and the difference between the tagged signal and the control signal becomes smaller. We reduced the scan time to less than three minutes, as desired for pediatric examinations. The rCBF also showed strong correlation with the conventional protocol, so it can be considered a sufficiently useful condition for clinical practice.

Case 1 clearly showed the decrease in PWI signal and the prolongation of bolus arrival time in the dominant region of narrowing vessels, which was also recognized in MRA. The progression of vascular lesions in moyamoya disease does not occur symmetrically. In addition, every revascularization procedure results in the hemodynamics of the brain becoming more complicated. Therefore, PWI over time allows us to easily obtain valuable information on current hemodynamics. In this case, rCBF by single-PLD PCASL showed incorrect results that suggested the CBF was high in the left hemisphere (Fig. 5D). This was caused by the stagnated blood flow in the revascularized vessels. On the other hand, since multi-PLD PCASL takes bolus arrival time into account (Fig. 5D), it showed the same result as SPECT, even in a patient with very slow blood flow. This indicates the usefulness of this method.

In Case 2, there was no change in qualitative SPECT, and ASL showed lesion progression. In fact, based on the ASL results, we canceled a scheduled SPECT study with pharmacologic challenge, and a neurosurgeon decided on revascularization. In infancy[1], the immature brain is actively developing and needs a relatively high blood flow, so moyamoya disease onset in infancy carries a high risk [10]. Unlike SPECT, which requires a radioactive tracer, ASL can be easily carried out whenever necessary. It is very convenient and its application is clinically valuable.

Case 3, on the other hand, showed a mismatch in the results between SPECT and ASL. In patients with slow blood flow maintaining signals in vessels at PLD above the upper limit of field strength, we have to be careful because there is a possibility that multi-PLD ASL will produce incorrect results. Generally, in patients with moyamoya disease, bolus arrival time is slower than in healthy subjects. Therefore, in order to make an accurate diagnosis, it is very important to not only investigate the rCBF map but also the PWI time series in terms of bolus arrival time.

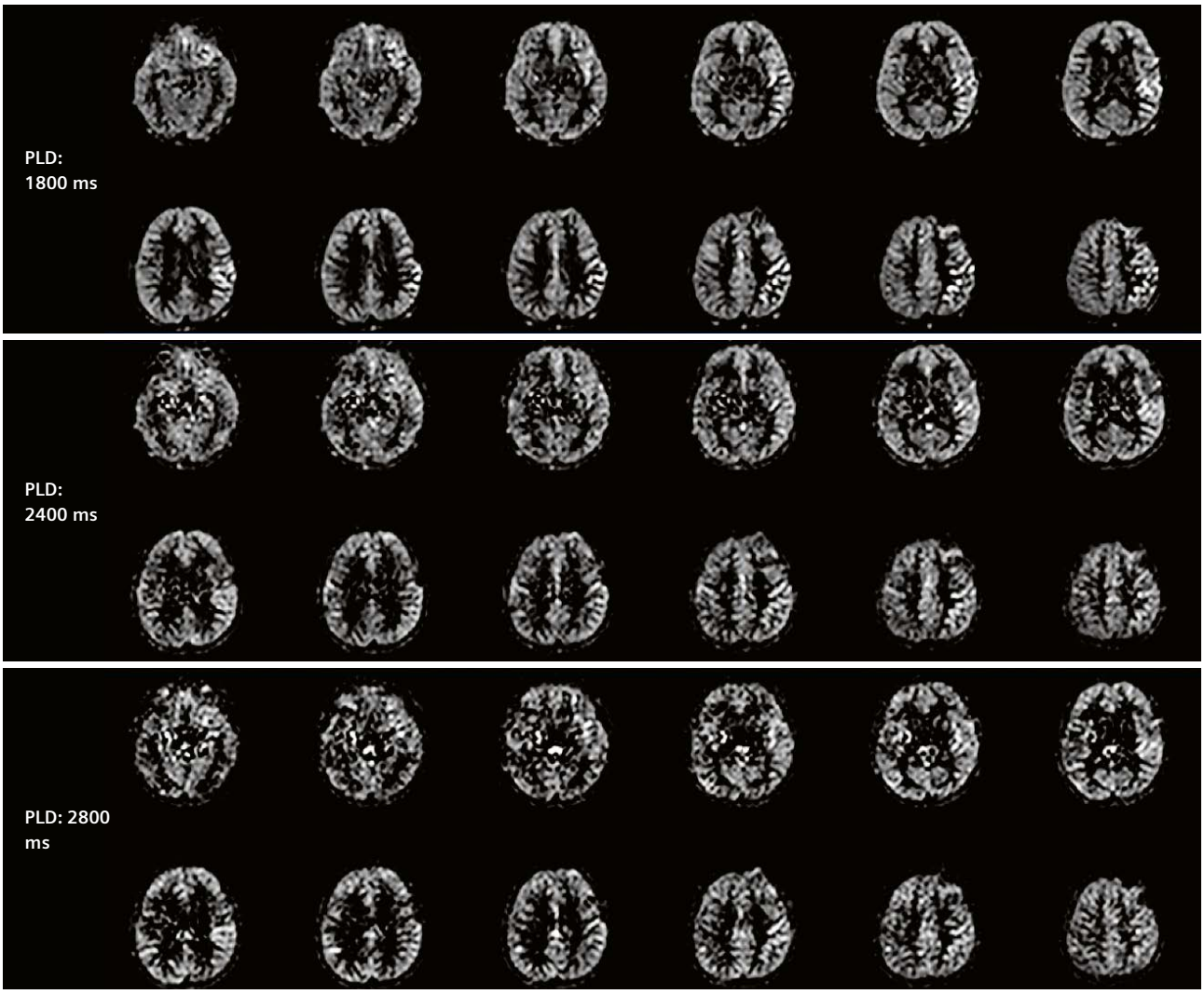

7A **Moyamoya disease in a 16-year-old female**
Revascularization by left STC, single-PCASL PWI.

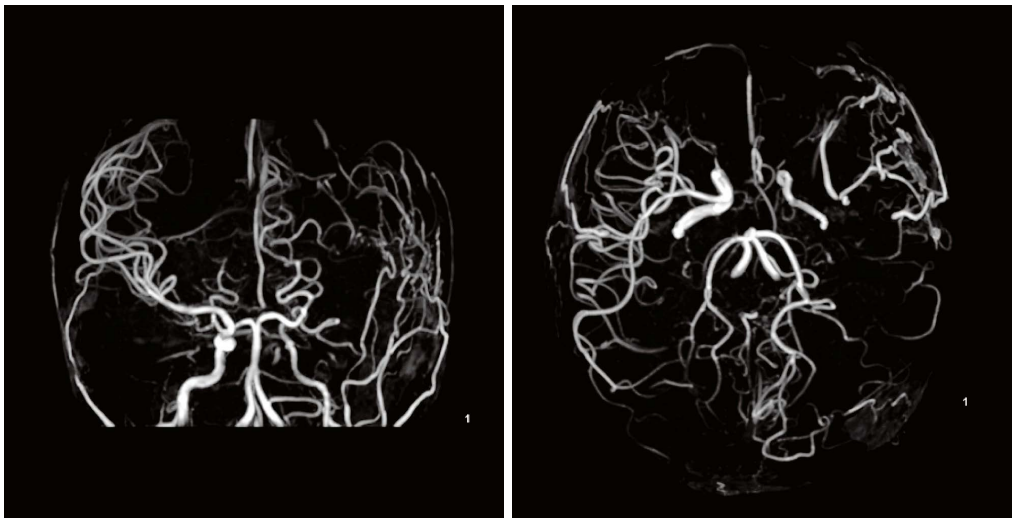

7B **Moyamoya disease in a 16-year-old female**
Revascularization by left STC, MRA-MIP.

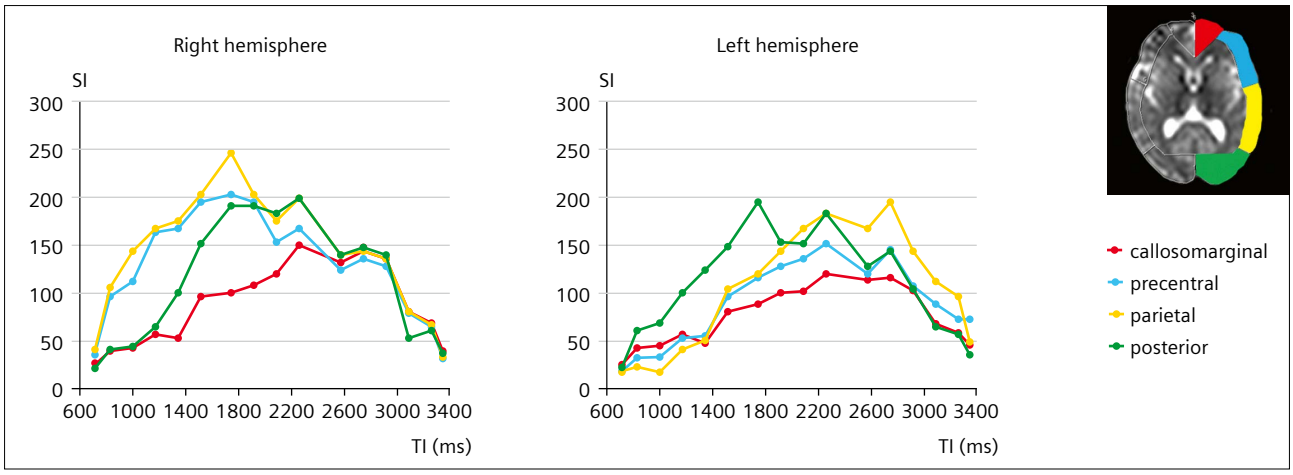

7C PWI signal intensity (SI) by multi-TI PCASL.

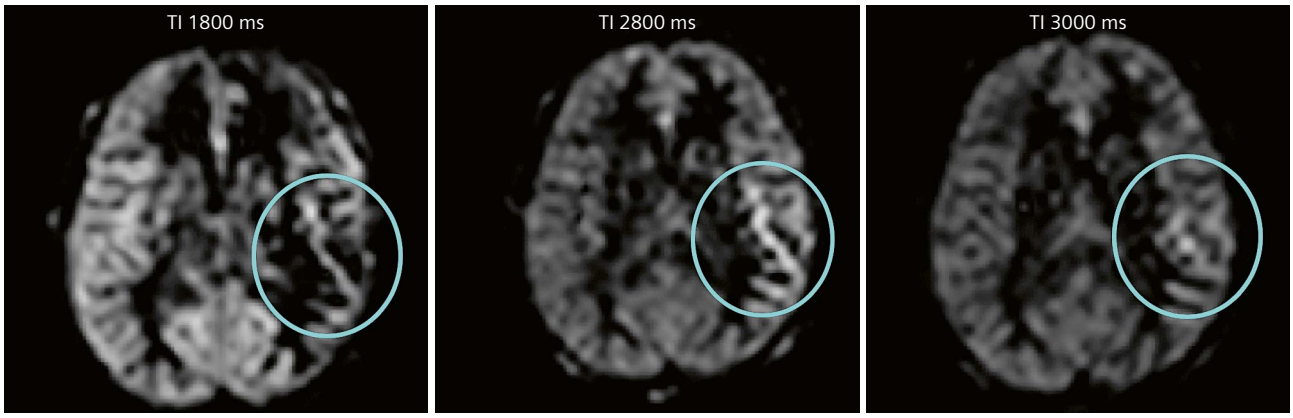

7D Multi-PLD PCASL PWI

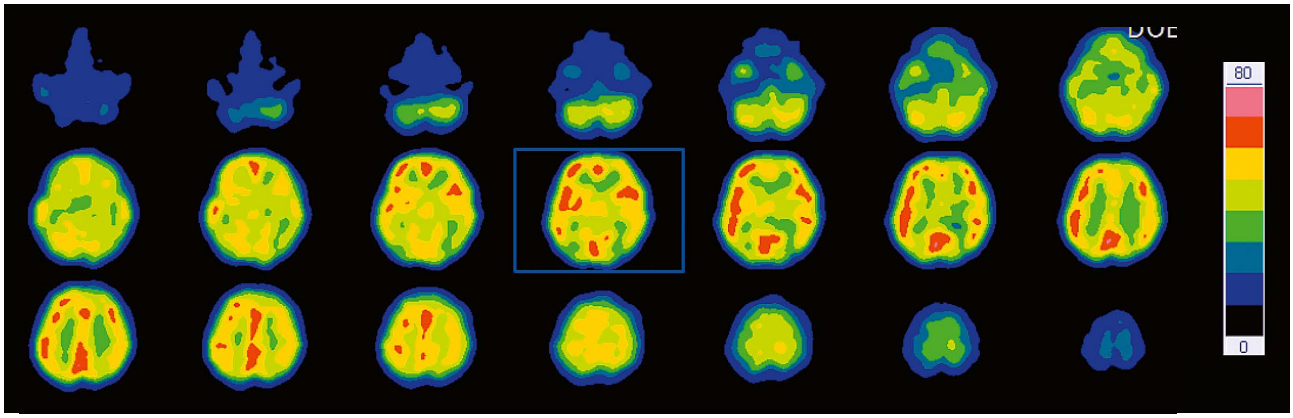

7E DT-ARG

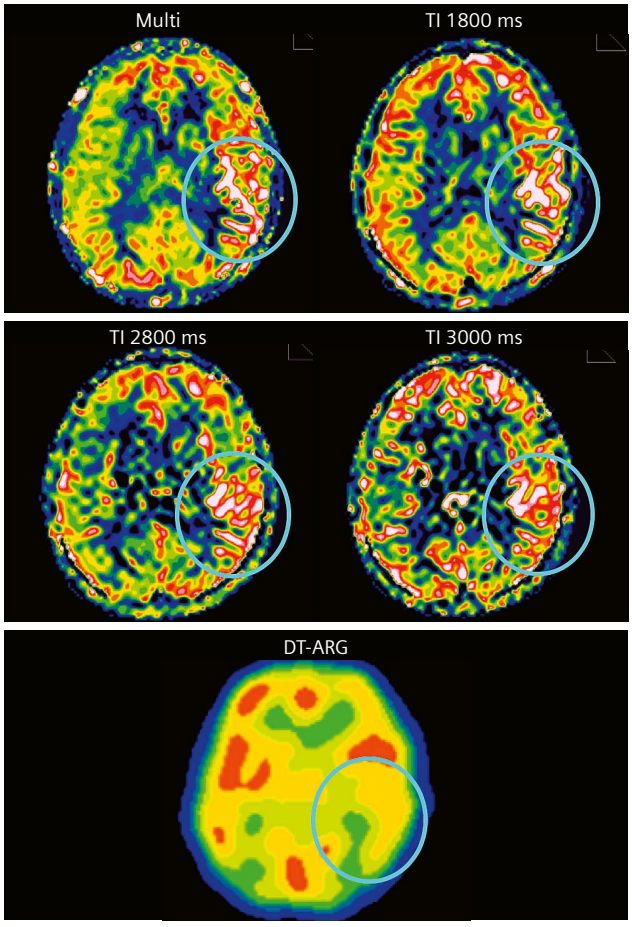

7F **Comparison of SPECT and ASL**
Long-stagnating blood flow cannot be evaluated correctly.

Conclusion

Moyamoya disease requires follow-up for a long period of time, and ASL can be a suitable examination for this disease. The multi-PLD PCASL is significant as a screening tool because it provides information on whole-brain perfusion distribution in a 3D rCBF map as well as information on pseudo hemodynamics by PWI time series and bolus arrival time, respectively. Brain perfusion examination by MRI is especially significant for pediatric patients because it can be performed easily, is repeatable and noninvasive with no need for arterial blood sampling, and enables us to quickly decide on a procedure. In this paper, we presented clinical cases in which perfusion evaluation by multi-PCASL was useful for pediatric patients with moyamoya disease who had unusual blood flow caused by stenosis or revascularization. We also presented a case that showed incorrect results caused by very slow blood flow compared with the upper limit of PLD.

Therefore, when viewing the results of multi-PLD PCASL, it is necessary to consider them carefully and in conjunction with clinical symptoms and findings from PWI and other modalities. We aim to continue our work on finding the best way to provide information that will improve diagnosis and clinical decisions for pediatric patients.

Contact

Aya Tominaga
Radiological Technologist
Miyagi Children's Hospital
Dept. of Radiology
4 3-17 Ochiai, Aoba-ku, Sendai
Miyagi Prefecture 989-3126
Japan
Tel: +81 22-391-5111
ayatominaga5559@gmail.com

Acknowledgments

The authors wish to thank Dr. Josef Pfeuffer, Siemens Healthcare, Erlangen, for providing the 3D ASL prototype sequence.

References

1 Tominaga T, Suzuki N, Miyamoto S, et al. Recommendations for the Management of Moyamoya Disease: A Statement from Research Committee on Spontaneous Occlusion of the Circle of Willis (Moyamoya Disease) [2nd Edition]. Surgery for Cerebral Stroke. 2018;46(1):1–24.
2 Kamada F, Aoki Y, Narisawa A, et al. A genome-wide association study identifies RNF213 as the first Moyamoya disease gene. J Hum Genet. 2011;56(1):34-40.
3 Hayashi T, Shirane R, Tominaga T. Additional surgery for postoperative ischemic symptoms in patients with moyamoya disease: the effectiveness of occipital artery-posterior cerebral artery bypass with an indirect procedure: technical case report. Neurosurgery. 2009;64(1):E195–6.
4 Hayashi T, Shirane R, Fujimura M, et al. Postoperative neurological deterioration in pediatric Moyamoya disease: watershed shift and Hyperperfusion. J Neurosurg Pediatr. 2010;6(1):73–81.
5 Yokozawa M, Hayashi T, Shirane R, et al. Efficacy of superficial temporal artery-middle cerebral artery double anastomoses in a patient with rapidly progressive moyamoya disease: case report. Neurol Med Chir (Tokyo). 2014;54(10):836–40.
6 Shirane R, Nishimura S TT. Functional Diagnosis with PET and SPECT. In: Moyamoya Disease. Rolling Meadows: AANS Press; 2001:95–106.
7 Noguchi T, Kawashima M, Irie H, et al. Arterial spin-labeling MR imaging in moyamoya disease compared with SPECT imaging. Eur J Radiol. 2011;80(3):e557–62.
8 Buxton RB, Frank LR, Wong EC, et al. A general kinetic model for quantitative perfusion imaging with arterial spin labeling. Magn Reson Med. 1998;40(3):383–96.
9 Alsop DC, Detre JA, Golay X, et al. Recommended implementation of arterial spin-labeled perfusion MRI for clinical applications: A consensus of the ISMRM perfusion study group and the European consortium for ASL in dementia. Magn Reson Med. 2015;73(1):102–16.
10 Liu W, Lou X, Ma L. Use of 3D pseudo-continuous arterial spin labeling to characterize sex and age differences in cerebral blood flow. Neuroradiology. 2016;58(9):943–8.

"Puff of Smoke": An MR/PET Case of Moyamoya (もやもや) Disease

Valentina Bodanza[1]; Mariagiulia Anglani[2]; Pietro Zucchetta[1]; Francesco Causin[2]; Franco Bui[1]; Stefano Sartori[3]; Renzo Manara[2]; Diego Cecchin[1,4]

[1]Nuclear Medicine Unit, Department of Medicine – DIMED, University Hospital of Padova, Italy
[2]Neuroradiology Unit, University Hospital of Padova, Italy
[3]Paediatric Neurology and Neurophysiology Unit, Department of Women's and Children's Health, University Hospital of Padova, Italy
[4]Padova Neuroscience Center, University of Padova, Italy

Background

In cases of arteriovenous shunts and malformations, it can be difficult to assess the real status of brain blood flow and metabolism using MR alone. This can result in underestimation of the brain areas affected by the pathology. A combined multimodal approach using MR/PET can provide a much better explanation of the clinical symptoms and can help to plan neurosurgery based on the real extent of the impaired areas. We present a pediatric case of moyamoya disease in which MR/PET drastically changed the surgical approach.

Case report

A previously healthy 7-year-old girl presented with irritability, right arm pain, and transient non-fluent aphasia. The following day, the persistence of pain and the occurrence of right arm weakness led to her being admitted to the emergency department at the University Hospital of Padova. Her parents reported previous mild and transient episodes of limb weakness.

The neurological evaluation showed right hemiparesis and central facial palsy. A brain MRI performed the same day (Fig. 1) revealed a large left frontal cortical-subcortical acute ischemic lesion in the territory of the middle cerebral artery (MCA). Another acute ischemic lesion involved the left head of the caudate / anterior limb of the internal capsule in the territory of the recurrent artery of Heubner.

MR angiography demonstrated a moyamoya [1, 2] pattern (Fig. 2) with occlusion of both internal carotid arteries (ICAs), with poor representation of the distal branches of the left MCA (probably because of severe blood perfusion impairment), with severe steno-ectasia at the origin of the posterior cerebral arteries and posterior communicating arteries, and with compensatory dilatation of the perforant arteries of the posterior circulation. Minimal lumen irregularities of the vertebral arteries were noted, while the basilar artery was unremarkable.

The girl was transferred to the emergency pediatric ward and therapy was initiated with heparin (15 units/kg/h) followed by ASA (25 mg/die). Three days later, digital subtraction angiography (Fig. 3) was performed and confirmed a moyamoya pattern with bilateral ICA occlusion (probably acute on the left side and chronic on the right side) and severe stenosis of the proximal left middle and anterior cerebral arteries. The vertebrobasilar arteries were compensatory.

The neurological picture appeared slightly improved two days later. Extensive investigations ruled out common and rare underlying acquired and genetic conditions, and therefore allowed a definite diagnosis of moyamoya disease. To assess the brain metabolic activity before surgery, an ^{18}F-FDG MR/PET (Biograph mMR; Siemens Healthcare, Erlangen, Germany; co-funded by the Fondazione Cassa di Risparmio di Padova e Rovigo and by the Hospital of Padova) was performed ten days later (Fig. 4).

The fast (awake pediatric patient) MR/PET protocol (Table 1) included 3D T1 (MPRAGE, 1 mm isotropic), 3D T2-FLAIR (1 mm isotropic), and 2D T2 (slice thickness: 4 mm) sequences, as well as MR angiography (time-of-flight, TOF, sequence).

Sequence name	T1-weighted 3D MPRAGE	T2 TSE (t2_tse_tra)	T2-weighted 3D FLAIR (t2_spc_da-fl_iso)	TOF 3D multislab
TR/TE/TI; FA	2400/3.24/1000 ms; 8°	5000/105 ms; 150°	5000/394 ms	24/4.16 ms; 18°
Voxel size	1 x 1 x 1 mm	0.5 x 0.5 x 4 mm	1 x 1 x 1 mm	0.4 x 0.4 x 1 mm
BW	210 Hz/pix	223 Hz/pix	781 Hz/pix	184 Hz/pix

Table 1: MR protocol (Biograph mMR)

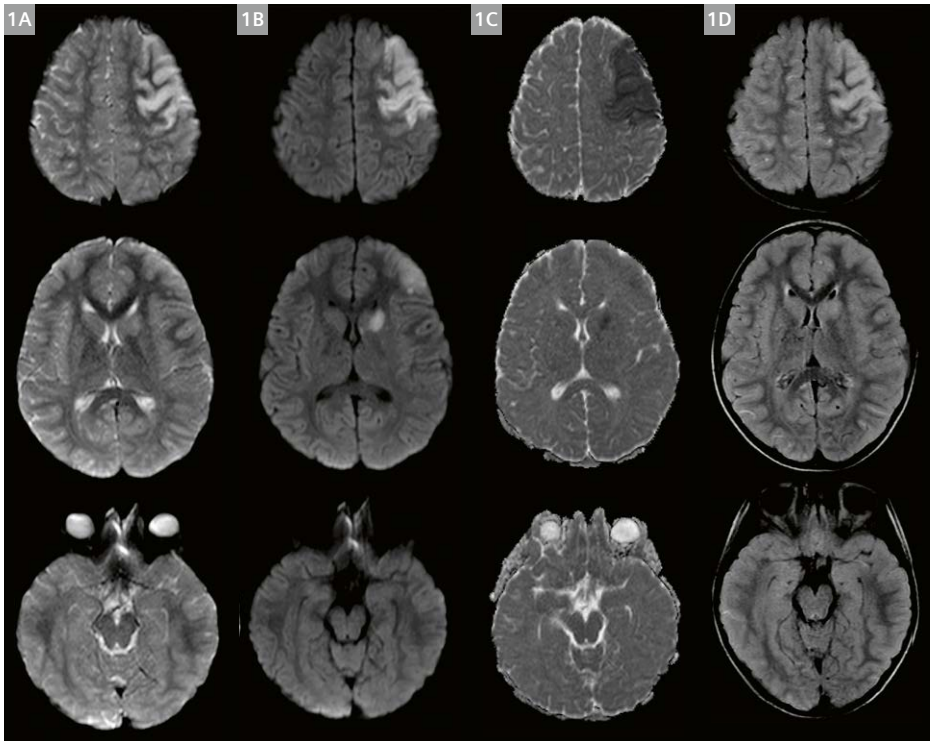

1 MR at hospital admission showing a large and acute ischemic area in the territory of the left middle cerebral artery (first row), and areas with similar characteristics (second row) in the nucleo-capsular region (head of caudate and anterior branch of the internal capsule). The temporal cortex showed no significant lesions. **(1A)** DWI b50; **(1B)** DWI b1000; **(1C)** apparent diffusion coefficient (ADC); **(1D)** T2-FLAIR (1 mm isotropic).

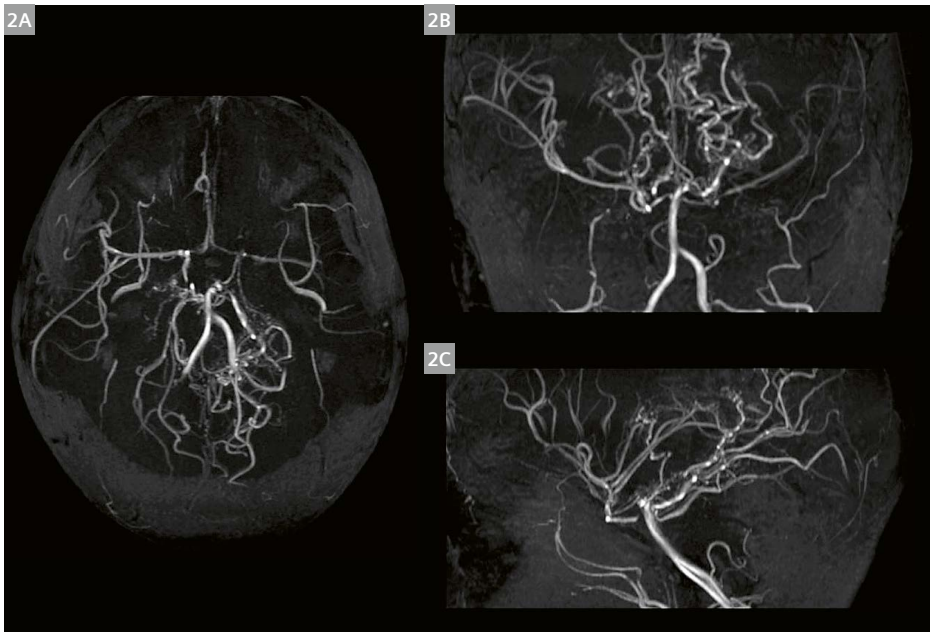

2 TOF MR (**2A**: transaxial MIP; **2B**: coronal MIP; **2C**: lateral MIP) showing occlusion at the origin of both internal carotid arteries, a steno-occlusion of the initial portion of the posterior cerebral arteries and posterior communicating arteries with compensatory dilatation of the perforant arteries of the posterior circle, and ectasis of the distal portion of the posterior cerebral arteries. Severe stenosis of the left MCA with scarce distal ramifications was also reported.

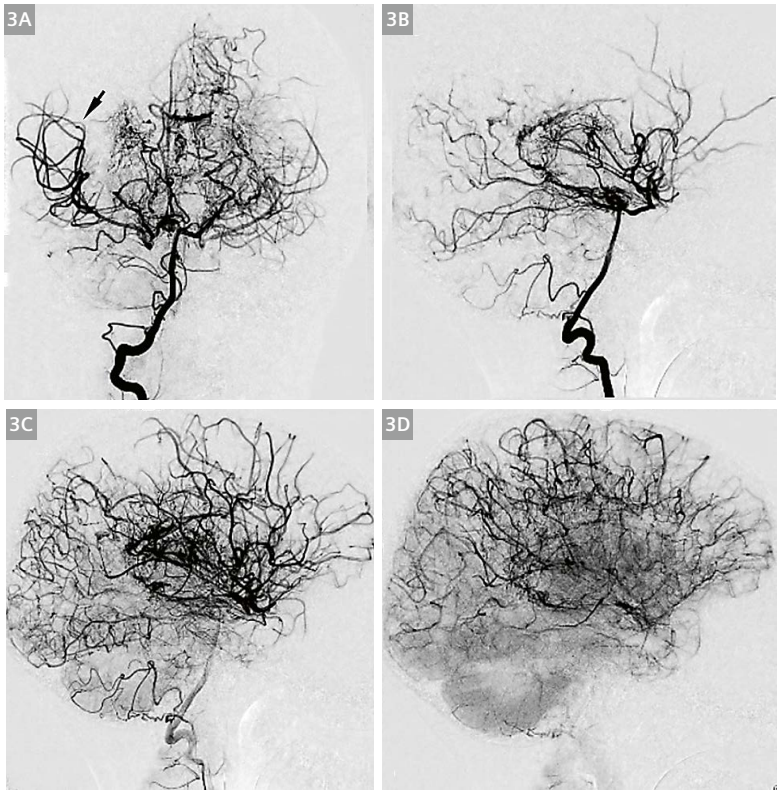

3 Digital subtraction angiography: Following selective catheterism of the right vertebral artery, a moyamoya pattern is evident. The anterior-posterior view **(3A)** shows the MCA branches, especially on the right side (arrow) due to collateral circulation. The lateral views **(3B–D)** show the progressive whole-brain blood supply through the rich collateral network.

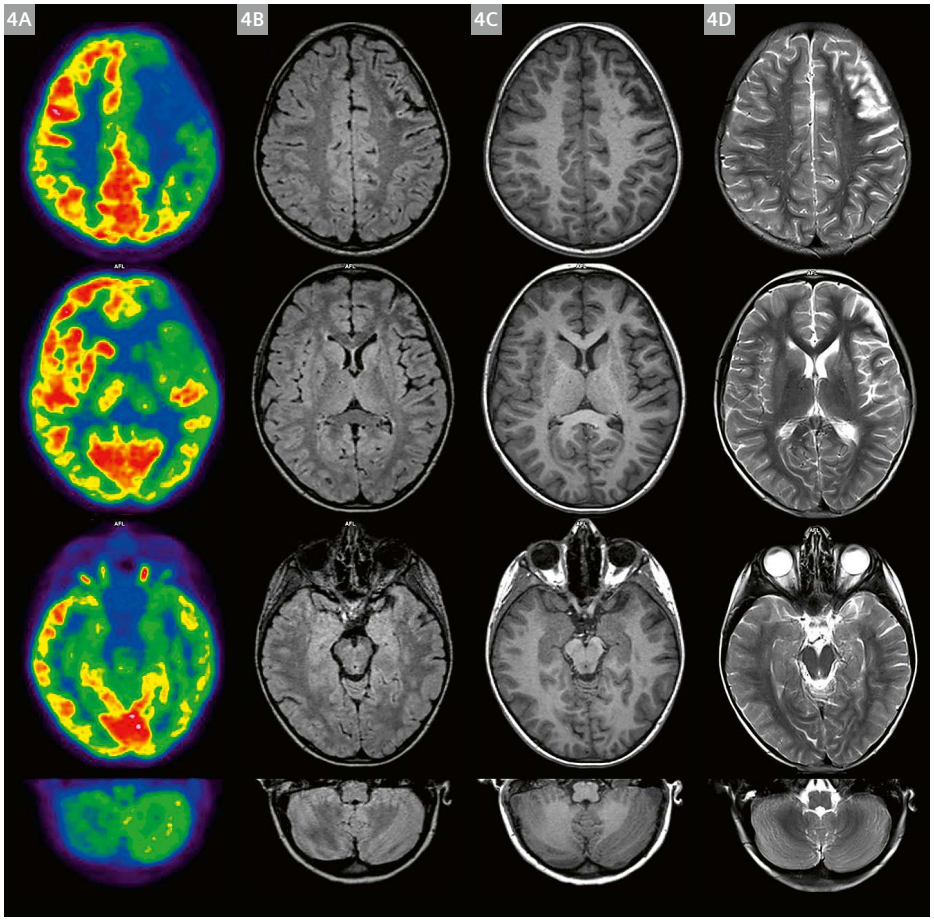

4 MR/PET: In the first column **(4A)**, ^{18}F-FDG PET demonstrates severe hypometabolism in the left frontal and fronto-parietal cortex (first and second row), in the left basal ganglia, and in the left part of the thalamus and pons (second row). Moderate hypometabolism was observed in the left parietal and parie-to-temporal cortex, and mild hypometabolism was seen in the left temporal cortex (third row). The scan also demonstrated a crossed cerebellar diaschisis (last row). **(4B)** T2-FLAIR; **(4C)** isotropic (1 mm) T1-MPRAGE; **(4D)** T2-TSE (4 mm). Atrophy is visible at MR in the frontal cortex.

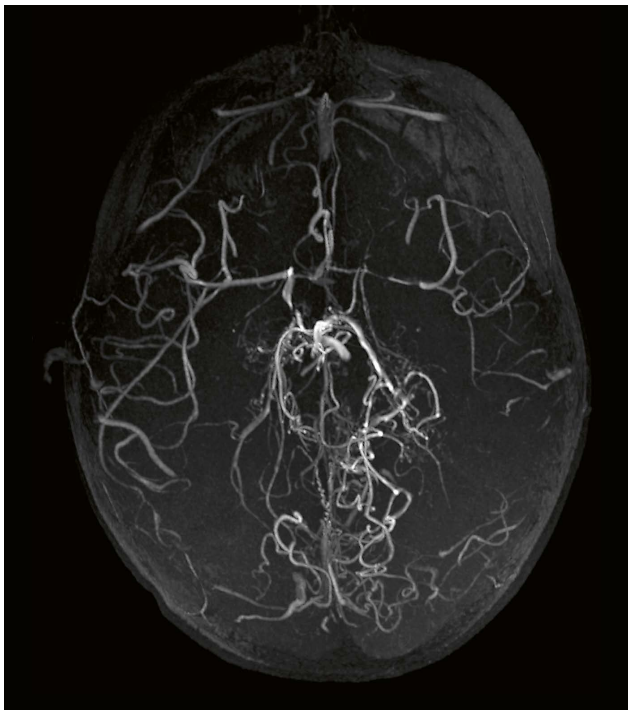

5 A TOF sequence acquired during an MR/PET scan confirmed previous findings and showed a weak progression of the occlusion in the left MCA (initial tract) and in the right anterior cerebral artery.

MR/PET imaging showed severe hypometabolism in the left frontal and fronto-parietal cortex, in the left basal ganglia and thalamus, and in the left part of the pons. Moderate hypometabolism was observed in the left parietal and parieto-temporal cortex, and mild hypometabolism was seen in the left temporal cortex. The scan also demonstrated a crossed cerebellar diaschisis. Interestingly, hypometabolism was much more widespread than expected on the basis of MR alone – possibly because a chronic ischemia could induce diffuse brain microstructural damage [3]. Furthermore, hypometabolism could also be explained by a loss of connectivity. The MR angiography confirmed previous extra-intracranial artery findings (Fig. 5) and showed weak progression of the occlusion in the left MCA (initial tract) and in the right anterior cerebral artery. The worsening of the vascular stenosis coupled with the widespread hypometabolism visible with MR/PET reinforced the indication for a prompt extracranial-intracranial bypass. MR/PET could be useful for assessing both brain metabolism and vascular status in moyamoya angiopathy, where it can be difficult to carefully assess brain blood-flow impairment. The technique can provide additional data for planning neurosurgery and evaluating outcomes.

Acknowledgments

We would like to thank Domenico Zacà and Nashiely S. Pineda Alonso from Siemens Healthcare for their assistance in preparing this manuscript.

Contact

Professor Diego Cecchin
University Hospital of Padova
Nuclear Medicine Unit
Department of Medicine – DIMED
Via Giustiniani 2
35128 Padova
Italy
diego.cecchin@unipd.it

Diego Cecchin

Valentina Bodanza

References

1 Huang S, Guo ZN, Shi M, Yang Y, Rao M. Etiology and pathogenesis of Moyamoya Disease: An update on disease prevalence. Int J Stroke. 2017 Apr;12(3):246–253
2 Fujimura M, Bang OY, Kim JS. Moyamoya Disease. Front Neurol Neurosci. 2016;40:204–220.
3 Hara S, Hori M, Ueda R, Hayashi S, Inaji M, Tanaka Y, Maehara T, Ishii K, Aoki S, Nariai T. Unraveling Specific Brain Microstructural Damage in Moyamoya Disease Using Diffusion Magnetic Resonance Imaging and Positron Emission Tomography. J Stroke Cerebrovasc Dis. 2019; Jan 21; doi: 10.1016/j.jstrokecerebrovasdis.2018.12.038. [Epub ahead of print].

HIGHLIGHTS OF PRESCRIBING INFORMATION

These highlights do not include all the information needed to use Fludeoxyglucose F 18 Injection safely and effectively. See full prescribing information for Fludeoxyglucose F 18 Injection. Fludeoxyglucose F 18 Injection, USP For intravenous use Initial U.S. Approval: 2005

RECENT MAJOR CHANGES

Warnings and Precautions	
(5.1, 5.2)	7/2010
Adverse Reactions (6)	7/2010

INDICATIONS AND USAGE

Fludeoxyglucose F18 Injection is indicated for positron emission tomography (PET) imaging in the following settings:

- Oncology: For assessment of abnormal glucose metabolism to assist in the evaluation of malignancy in patients with known or suspected abnormalities found by other testing modalities, or in patients with an existing diagnosis of cancer.
- Cardiology: For the identification of left ventricular myocardium with residual glucose metabolism and reversible loss of systolic function in patients with coronary artery disease and left ventricular dysfunction, when used together with myocardial perfusion imaging.
- Neurology: For the identification of regions of abnormal glucose metabolism associated with foci of epileptic seizures (1).

DOSAGE AND ADMINISTRATION

Fludeoxyglucose F 18 Injection emits radiation. Use procedures to minimize radiation exposure. Screen for blood glucose abnormalities.

- In the oncology and neurology settings, instruct patients to fast for 4 to 6 hours prior to the drug's injection. Consider medical therapy and laboratory testing to assure at least two days of normoglycemia prior to the drug's administration (5.2).
- In the cardiology setting, administration of glucose-containing food or liquids (e.g., 50 to 75 grams) prior to the drug's injection facilitates localization of cardiac ischemia (2.3).

Aseptically withdraw Fludeoxyglucose F 18 Injection from its container and administer by intravenous injection (2).

The recommended dose:

- for adults is 5 to 10 mCi (185 to 370 MBq), in all indicated clinical settings (2.1).
- for pediatric patients is 2.6 mCi in the neurology setting (2.2).

Initiate imaging within 40 minutes following drug injection; acquire static emission images 30 to 100 minutes from time of injection (2).

DOSAGE FORMS AND STRENGTHS

Multi-dose 30mL and 50mL glass vial containing 0.74 to 7.40 GBq/mL (20 to 200 mCi/mL) Fludeoxyglucose F 18 Injection and 4.5mg of sodium chloride with 0.1 to 0.5% w/w ethanol as a stabilizer (approximately 15 to 50 mL volume) for intravenous administration (3).

CONTRAINDICATIONS

None

WARNINGS AND PRECAUTIONS

- Radiation risks: use smallest dose necessary for imaging (5.1).
- Blood glucose adnormalities: may cause suboptimal imaging (5.2).

ADVERSE REACTIONS

Hypersensitivity reactions have occurred; have emergency resuscitation equipment and personnel immediately available (6).

To report SUSPECTED ADVERSE REACTIONS, contact PETNET Solutions, Inc. at 877-473-8638 or FDA at 1-800-FDA-1088 or www.fda.gov/medwatch.

USE IN SPECIFIC POPULATIONS

Pregnancy Category C: No human or animal data. Consider alternative diagnostics; use only if clearly needed (8.1).

- Nursing mothers: Use alternatives to breast feeding (e.g., stored breast milk or infant formula) for at least 10 half-lives of radioactive decay, if Fludeoxyglucose F 18 Injection is administered to a woman who is breast-feeding (8.3).
- Pediatric Use: Safety and effectiveness in pediatric patients have not been established in the oncology and cardiology settings (8.4).

See 17 for PATIENT COUNSELING INFORMATION

Revised: 1/2011

FULL PRESCRIBING INFORMATION: CONTENTS*

*Sections or subsections omitted from the full prescribing information are not listed.

FULL PRESCRIBING INFORMATION

1 INDICATIONS AND USAGE

Fludeoxyglucose F 18 Injection is indicated for positron emission tomography (PET) imaging in the following settings:

1.1 Oncology

For assessment of abnormal glucose metabolism to assist in the evaluation of malignancy in patients with known or suspected abnormalities found by other testing modalities, or in patients with an existing diagnosis of cancer.

1.2 Cardiology

For the identification of left ventricular myocardium with residual glucose metabolism and reversible loss of systolic function in patients with coronary artery disease and left ventricular dysfunction, when used together with myocardial perfusion imaging.

1.3 Neurology

For the identification of regions of abnormal glucose metabolism associated with foci of epileptic seizures.

2 DOSAGE AND ADMINISTRATION

Fludeoxyglucose F 18 Injection emits radiation. Use procedures to minimize radiation exposure. Calculate the final dose from the end of synthesis (EOS) time using proper radioactive decay factors. Assay the final dose in a properly calibrated dose calibrator before administration to the patient [see Description (11.2)].

2.1 Recommended Dose for Adults

Within the oncology, cardiology and neurology settings, the recommended dose for adults is 5 to 10 mCi (185 to 370 MBq) as an intravenous injection.

2.2 Recommended Dose for Pediatric Patients

Within the neurology setting, the recommended dose for pediatric patients is 2.6 mCi, as an intravenous injection. The optimal dose adjustment on the basis of body size or weight has not been determined [see Use in Special Populations (8.4)].

2.3 Patient Preparation

- To minimize the radiation absorbed dose to the bladder, encourage adequate hydration. Encourage the patient to drink water or other fluids (as tolerated) in the 4 hours before their PET study.
- Encourage the patient to void as soon as the imaging study is completed and as often as possible thereafter for at least one hour.
- Screen patients for clinically significant blood glucose abnormalities by obtaining a history and/or laboratory tests [see Warnings and Precautions (5.2)]. Prior to Fludeoxyglucose F 18 PET imaging in the oncology and neurology settings, instruct patient to fast for 4 to 6 hours prior to the drug's injection.
- In the cardiology setting, administration of glucose-containing food or liquids (e.g., 50 to 75 grams) prior to Fludeoxyglucose F18 Injection facilitates localization of cardiac ischemia

2.4 Radiation Dosimetry

The estimated human absorbed radiation doses (rem/mCi) to a newborn (3.4 kg), 1-year-old (9.8 kg), 5-year-old (19 kg), 10-year-old (32 kg), 15-year-old (57 kg), and adult (70 kg) from intravenous administration of Fludeoxyglucose F 18 Injection are shown in Table 1. These estimates were calculated based on human[2] data and using the data published by the International Commission on Radiological Protection[4] for Fludeoxyglucose ^{18}F. The dosimetry data show that there are slight variations in absorbed radiation dose for various organs in each of the age groups. These dissimilarities in absorbed radiation dose are due to developmental age variations (e.g., organ size, location, and overall metabolic rate for each age group). The identified critical organs (in descending order) across all age groups evaluated are the urinary bladder, heart, pancreas, spleen, and lungs.

Table 1. Estimated Absorbed Radiation Doses (rem/mCi) After Intravenous Administration of Fludeoxyglucose F-18 Injection[a]

Organ	Newborn (3.4 kg)	1-year-old (9.8 kg)	5-year-old (19 kg)	10-year-old (32 kg)	15-year-old (57 kg)	Adult (70 kg)
Bladder wall[b]	4.3	1.7	0.93	0.60	0.40	0.32
Heart wall	2.4	1.2	0.70	0.44	0.29	0.22
Pancreas	2.2	0.68	0.33	0.25	0.13	0.096
Spleen	2.2	0.84	0.46	0.29	0.19	0.14
Lungs	0.96	0.38	0.20	0.13	0.092	0.064
Kidneys	0.81	0.34	0.19	0.13	0.089	0.074
Ovaries	0.80	0.8	0.19	0.11	0.058	0.053
Uterus	0.79	0.35	0.19	0.12	0.076	0.062
LLI wall *	0.69	0.28	0.15	0.097	0.060	0.051
Liver	0.69	0.31	0.17	0.11	0.076	0.058
Gallbladder wall	0.69	0.26	0.14	0.093	0.059	0.049
Small intestine	0.68	0.29	0.15	0.096	0.060	0.047
ULI wall **	0.67	0.27	0.15	0.090	0.057	0.046
Stomach wall	0.65	0.27	0.14	0.089	0.057	0.047
Adrenals	0.65	0.28	0.15	0.095	0.061	0.048
Testes	0.64	0.27	0.14	0.085	0.052	0.041
Red marrow	0.62	0.26	0.14	0.089	0.057	0.047
Thymus	0.61	0.26	0.14	0.086	0.056	0.044
Thyroid	0.61	0.26	0.13	0.080	0.049	0.039
Muscle	0.58	0.25	0.13	0.078	0.049	0.039
Bone surface	0.57	0.24	0.12	0.079	0.052	0.041
Breast	0.54	0.22	0.11	0.068	0.043	0.034
Skin	0.49	0.20	0.10	0.060	0.037	0.030
Brain	0.29	0.13	0.09	0.078	0.072	0.070
Other tissues	0.59	0.25	0.13	0.083	0.052	0.042

[a] MIRDOSE 2 software was used to calculate the radiation absorbed dose. Assumptions on the biodistribution based on data from Gallagher et al.1 and Jones et al.[2]

[b] The dynamic bladder model with a uniform voiding frequency of 1.5 hours was used.

*LLI = lower large intestine; **ULI = upper large intestine

2.5 Radiation Safety – Drug Handling

- Use waterproof gloves, effective radiation shielding, and appropriate safety measures when handling Fludeoxyglucose F 18 Injection to avoid unnecessary radiation exposure to the patient, occupational workers, clinical personnel and other persons.
- Radiopharmaceuticals should be used by or under the control of physicians who are qualified by specific training and experience in the safe use and handling of radionuclides, and whose experience and training have been approved by the appropriate governmental agency authorized to license the use of radionuclides.
- Calculate the final dose from the end of synthesis (EOS) time using proper radioactive decay factors. Assay the final dose in a properly calibrated dose calibrator before administration to the patient [see Description (11.2)].
- The dose of Fludeoxyglucose F 18 used in a given patient should be minimized consistent with the objectives of the procedure, and the nature of the radiation detection devices employed.

2.6 Drug Preparation and Administration

- Calculate the necessary volume to administer based on calibration time and dose.
- Aseptically withdraw Fludeoxyglucose F 18 Injection from its container.
- Inspect Fludeoxyglucose F 18 Injection visually for particulate matter and discoloration before administration, whenever solution and container permit.
- Do not administer the drug if it contains particulate matter or discoloration; dispose of these unacceptable or unused preparations in a safe manner, in compliance with applicable regulations. Use Fludeoxyglucose F 18 Injection within 12 hours from the EOS.

2.7 Imaging Guidelines

- Initiate imaging within 40 minutes following Fludeoxyglucose F 18 Injection administration.
- Acquire static emission images 30 to 100 minutes from the time of injection.

3 DOSAGE FORMS AND STRENGTHS

Multiple-dose 30 mL and 50 mL glass vial containing 0.74 to 7.40 GBq/mL (20 to 200 mCi/mL) of Fludeoxyglucose F 18 Injection and 4.5 mg of sodium chloride with 0.1 to 0.5% w/w ethanol as a stabilizer (approximately 15 to 50 mL volume) for intravenous administration.

4 CONTRAINDICATIONS

None

5 WARNINGS AND PRECAUTIONS

5.1 Radiation Risks

Radiation-emitting products, including Fludeoxyglucose F 18 Injection, may increase the risk for cancer, especially in pediatric patients. Use the smallest dose necessary for imaging and ensure safe handling to protect the patient and health care worker [see Dosage and Administration (2.5)].

5.2 Blood Glucose Abnormalities

In the oncology and neurology setting, suboptimal imaging may occur in patients with inadequately regulated blood glucose levels. In these patients, consider medical therapy and laboratory testing to assure at least two days of normoglycemia prior to Fludeoxyglucose F 18 Injection administration.

6 ADVERSE REACTIONS

Hypersensitivity reactions with pruritus, edema and rash have been reported in the post-marketing setting. Have emergency resuscitation equipment and personnel immediately available.

7 DRUG INTERACTIONS

The possibility of interactions of Fludeoxyglucose F 18 Injection with other drugs taken by patients undergoing PET imaging has not been studied.

8 USE IN SPECIFIC POPULATIONS

8.1 Pregnancy

Pregnancy Category C

Animal reproduction studies have not been conducted with Fludeoxyglucose F 18 Injection. It is also not known whether Fludeoxyglucose F 18 Injection can cause fetal harm when administered to a pregnant woman or can affect reproduction capacity. Consider alternative diagnostic tests in a pregnant woman; administer Fludeoxyglucose F 18 Injection only if clearly needed.

8.3 Nursing Mothers

It is not known whether Fludeoxyglucose F 18 Injection is excreted in human milk. Consider alternative diagnostic tests in women who are breast-feeding. Use alternatives to breast feeding (e.g., stored breast milk or infant formula) for at least 10 half-lives of radioactive decay, if Fludeoxyglucose F 18 Injection is administered to a woman who is breast-feeding.

8.4 Pediatric Use

The safety and effectiveness of Fludeoxyglucose F 18 Injection in pediatric patients with epilepsy is established on the basis of studies in adult and pediatric patients. In pediatric patients with epilepsy, the recommended dose is 2.6 mCi. The optimal dose adjustment on the basis of body size or weight has not been determined. In the oncology or cardiology settings, the safety and effectiveness of Fludeoxyglucose F 18 Injection have not been established in pediatric patients.

11 DESCRIPTION

11.1 Chemical Characteristics

Fludeoxyglucose F 18 Injection is a positron emitting radiopharmaceutical that is used for diagnostic purposes in conjunction with positron emission tomography (PET) imaging. The active ingredient 2-deoxy-2-[^{18}F]fluoro-D-glucose has the molecular formula of $C_6H_{11}{}^{18}FO_5$ with a molecular weight of 181.26, and has the following chemical structure:

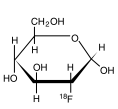

Fludeoxyglucose F 18 Injection is provided as a ready to use sterile, pyrogen free, clear, colorless solution. Each mL contains between 0.740 to 7.40GBq (20.0 to 200 mCi) of 2-deoxy-2-[^{18}F]fluoro-D-glucose at the EOS, 4.5 mg of sodium chloride and 0.1 to 0.5% w/w ethanol as a stabilizer. The pH of the solution is between 4.5 and 7.5. The solution is packaged in a multiple-dose glass vial and does not contain any preservative.

11.2 Physical Characteristics

Fluorine F 18 decays by emitting positron to Oxygen O 16 (stable) and has a physical half-life of 109.7 minutes. The principal photons useful for imaging are the dual 511 keV gamma photons, that are produced and emitted simultaneously in opposite direction when the positron interacts with an electron (Table 2).

Table 2. Pricipal Radiation Emission Data for Fluorine F18		
Radiation/Emission	% Per Disintegration	Mean Energy
Positron (b+)	96.73	249.8 keV
Gamma (±)*	193.46	511.0 keV

*Produced by positron annihilation

From: Kocher, D.C. Radioactive Decay Tables DOE/TIC-I 1026, 89 (1981)

The specific gamma ray constant (point source air kerma coefficient) for fluorine F 18 is 5.7 R/hr/mCi (1.35 x 10-6 Gy/hr/kBq) at 1 cm. The half-value layer (HVL) for the 511 keV photons is 4 mm lead (Pb). The range of attenuation coefficients for this radionuclide as a function of lead shield thickness is shown in Table 3. For example, the interposition of an 8 mm thickness of Pb, with a coefficient of attenuation of 0.25, will decrease the external radiation by 75%.

Table 3. Radiation Attenuation of 511 keV Photons by lead (Pb) shielding	
Shield thickness (Pb) mm	Coefficient of attenuation
0	0.00
4	0.50
8	0.25
13	0.10
26	0.01
39	0.001
52	0.0001

For use in correcting for physical decay of this radionuclide, the fractions remaining at selected intervals after calibration are shown in Table 4.

Table 4. Physical Decay Chart for Fluorine F18	
Minutes	Fraction Remaining
0*	1.000
15	0.909
30	0.826
60	0.683
110	0.500
220	0.250

*calibration time

12 CLINICAL PHARMACOLOGY

12.1 Mechanism of Action

Fludeoxyglucose F 18 is a glucose analog that concentrates in cells that rely upon glucose as an energy source, or in cells whose dependence on glucose increases under pathophysiological conditions. Fludeoxyglucose F 18 is transported through the cell membrane by facilitative glucose transporter proteins and is phosphorylated within the cell to [^{18}F] FDG-6-phosphate by the enzyme hexokinase. Once phosphorylated it cannot exit until it is dephosphorylated by glucose-6-phosphatase. Therefore, within a given tissue or pathophysiological process, the retention and clearance of Fludeoxyglucose F 18 reflect a balance involving glucose transporter, hexokinase and glucose-6-phosphatase activities. When allowance is made for the kinetic differences between glucose and Fludeoxyglucose F 18 transport and phosphorylation (expressed as the ‚lumped constant" ratio), Fludeoxyglucose F 18 is used to assess glucose metabolism. In comparison to background activity of the specific organ or tissue type, regions of decreased or absent uptake of Fludeoxyglucose F 18 reflect the decrease or absence of glucose metabolism. Regions of increased uptake of Fludeoxyglucose F 18 reflect greater than normal rates of glucose metabolism.

12.2 Pharmacodynamics

Fludeoxyglucose F 18 Injection is rapidly distributed to all organs of the body after intravenous administration. After background clearance of Fludeoxyglucose F 18 Injection, optimal PET imaging is generally achieved between 30 to 40 minutes after administration.

In cancer, the cells are generally characterized by enhanced glucose metabolism partially due to (1) an increase in activity of glucose transporters, (2) an increased rate of phosphorylation activity, (3) a reduction of phosphatase activity or, (4) a dynamic alteration in the balance among all these processes. However, glucose metabolism of cancer as reflected by Fludeoxyglucose F 18 accumulation shows considerable variability. Depending on tumor type, stage, and location, Fludeoxyglucose F 18 accumulation may be increased, normal, or decreased. Also, inflammatory cells can have the same variability of uptake of Fludeoxyglucose F 18.

In the heart, under normal aerobic conditions, the myocardium meets the bulk of its energy requirements by oxidizing free fatty acids. Most of the exogenous glucose taken up by the myocyte is converted into glycogen. However, under ischemic conditions, the oxidation of free fatty acids decreases, exogenous glucose becomes the preferred myocardial sub strate, glycolysis is stimulated, and glucose taken up by the myocyte is metabolized immediately instead of being converted into glycogen. Under these conditions, phosphorylated Fludeoxyglucose F 18 accumulates in the myocyte and can be detected with PET imaging.

In the brain, cells normally rely on aerobic metabolism. In epilepsy, the glucose metabolism varies. Generally, during a seizure, glucose metabolism increases. Interictally, the seizure focus tends to be hypometabolic.

12.3 Pharmacokinetics

Distribution: In four healthy male volunteers, receiving an intravenous administration of 30 seconds in duration, the arterial blood level profile for Fludeoxyglucose F 18 decayed triexponentially. The effective half-life ranges of the three phases were 0.2 to 0.3 minutes, 10 to 13 minutes with a mean and standard deviation (STD) of 11.6 (±) 1.1 min, and 80 to 95 minutes with a mean and STD of 88 (±) 4 min. Plasma protein binding of Fludeoxyglucose F 18 has not been studied.

Metabolism: Fludeoxyglucose F 18 is transported into cells and phosphorylated to [^{18}F]-FDG-6-phosphate at a rate proportional to the rate of glucose utilization within that tissue. [F18]-FDG-6-phosphate presumably is metabolized to 2-deoxy-2-[F18]fluoro-6-phospho-D-mannose([F 18]FDM-6-phosphate).

Fludeoxyglucose F 18 Injection may contain several impurities (e.g., 2-deoxy-2-chloro-D-glucose (ClDG)). Biodistribution and metabolism of ClDG are presumed to be similar to Fludeoxyglucose F 18 and would be expected to result in intracellular formation of 2-deoxy-2-chloro-6-phospho-D-glucose (ClDG-6-phosphate) and 2-deoxy-2-chloro-6-phospho-D-mannose (ClDM-6-phosphate). The phosphorylated deoxyglucose compounds are dephosphorylated and the resulting compounds (FDG, FDM, ClDG, and ClDM) presumably leave cells by passive diffusion. Fludeoxyglucose F 18 and related compounds are cleared from non-cardiac tissues within 3 to 24 hours after administration. Clearance from the cardiac tissue may require more than 96 hours. Fludeoxyglucose F 18 that is not involved in glucose metabolism in any tissue is then excreted in the urine.

Elimination: Fludeoxyglucose F 18 is cleared from most tissues within 24 hours and can be eliminated from the body unchanged in the urine. Three elimination phases have been identified in the reviewed literature. Within 33 minutes, a mean of 3.9% of the administrated radioactive dose was measured in the urine. The amount of radiation exposure of the urinary bladder at two hours post-administration suggests that 20.6% (mean) of the radioactive dose was present in the bladder.

Special Populations: The pharmacokinetics of Fludeoxyglucose F 18 Injection have not been studied in renally-impaired, hepatically impaired or pediatric patients. Fludeoxyglucose F 18 is eliminated through the renal system. Avoid excessive radiation exposure to this organ system and adjacent tissues. The effects of fasting, varying blood sugar levels, conditions of glucose intolerance, and diabetes mellitus on Fludeoxyglucose F 18 distribution in humans have not been ascertained [see Warnings and Precautions (5.2)].

13 NONCLINICAL TOXICOLOGY

13.1 Carcinogenesis, Mutagenesis, Impairment of Fertility

Animal studies have not been performed to evaluate the Fludeoxyglucose F 18 Injection carcinogenic potential, mutagenic potential or effects on fertility.

14 CLINICAL STUDIES

14.1 Oncology

The efficacy of Fludeoxyglucose F 18 Injection in positron emission tomography cancer imaging was demonstrated in 16 independent studies. These studies prospectively evaluated the use of Fludeoxyglucose F 18 in patients with suspected or known malignancies, including non-small cell lung cancer, colo-rectal, pancreatic, breast, thyroid, melanoma, Hodgkin's and non-Hodgkin's lymphoma, and various types of metastatic cancers to lung, liver, bone, and axillary nodes. All these studies had at least 50 patients and used pathology as a standard of truth. The Fludeoxyglucose F 18 Injection doses in the studies ranged from 200 MBq to 740 MBq with a median and mean dose of 370 MBq. In the studies, the diagnostic performance of Fludeoxyglucose F 18 Injection varied with the type of cancer, size of cancer, and other clinical conditions. False negative and false positive scans were observed. Negative Fludeoxyglucose F 18 Injection PET scans do not exclude the diagnosis of cancer. Positive Fludeoxyglucose F 18 Injection PET scans can not replace pathology to establish a diagnosis of cancer. Non-malignant conditions such as fungal infections, inflammatory processes and benign tumors have patterns of increased glucose metabolism that may give rise to false-positive scans. The efficacy of Fludeoxyglucose F 18 Injection PET imaging in cancer screening was not studied.

14.2 Cardiology

The efficacy of Fludeoxyglucose F 18 Injection for cardiac use was demonstrated in ten independent, prospective studies of patients with coronary artery disease and chronic left ventricular systolic dysfunction who were scheduled to undergo coronary revascularization. Before revascularization, patients underwent PET imaging with Fludeoxyglucose F 18 Injection (74 to 370 MBq, 2 to 10 mCi) and perfusion imaging with other diagnostic radiopharmaceuticals. Doses of Fludeoxyglucose F 18 Injection ranged from 74 to 370 MBq (2 to 10 mCi). Segmental, left ventricular, wall-motion assessments of asynergic areas made before revascularization were compared in a blinded manner to assessments made after successful revascularization to identify myocardial segments with functional recovery. Left ventricular myocardial segments were predicted to have reversible loss of systolic function if they showed Fludeoxyglucose F 18 accumulation and reduced perfusion (i.e., flow-metabolism mismatch). Conversely, myocardial segments were predicted to have irreversible loss of systolic function if they showed reductions in both Fludeoxyglucose F 18 accumulation and perfusion (i.e., matched defects). Findings of flow-metabolism mismatch in a myocardial segment may suggest that successful revascularization will restore myocardial function in that segment. However, false-positive tests occur regularly, and the decision to have a patient undergo revascularization should not be based on PET findings alone. Similarly, findings of a matched defect in a myocardial segment may suggest that myocardial function will not recover in that segment, even if it is successfully revascularized. However, false-negative tests occur regularly, and the decision to recommend against coronary revascularization, or to recommend a cardiac transplant, should not be based on PET findings alone. The reversibility of segmental dysfunction as predicted with Fludeoxyglucose F 18 PET imaging depends on successful coronary revascularization. Therefore, in patients with a low likelihood of successful revascularization, the diagnostic usefulness of PET imaging with Fludeoxyglucose F 18 Injection is more limited.

14.3 Neurology

In a prospective, open label trial, Fludeoxyglucose F 18 Injection was evaluated in 86 patients with epilepsy. Each patient received a dose of Fludeoxyglucose F 18 Injection in the range of 185 to 370 MBq (5 to 10 mCi). The mean age was 16.4 years (range: 4 months to 58 years; of these, 42 patients were less than 12 years and 16 patients were less than 2 years old). Patients had a known diagnosis of complex partial epilepsy and were under evaluation for surgical treatment of their seizure disorder. Seizure foci had been previously identified on ictal EEGs and sphenoidal EEGs. Fludeoxyglucose F 18 Injection PET imaging confirmed previous diagnostic findings in 16% (14/87) of the patients; in 34% (30/87) of the patients, Fludeoxyglucose F 18 Injection PET images provided new findings. In 32% (27/87), imaging with Fludeoxyglucose F 18 Injection was inconclusive. The impact of these imaging findings on clinical outcomes is not known. Several other studies comparing imaging with Fludeoxyglucose F 18 Injection results to subsphenoidal EEG, MRI and/or surgical findings supported the concept that the degree of hypometabolism corresponds to areas of confirmed epileptogenic foci. The safety and effectiveness of Fludeoxyglucose F 18 Injection to distinguish idiopathic epileptogenic foci from tumors or other brain lesions that may cause seizures have not been established.

15 REFERENCES

- 1. Gallagher B.M., Ansari A., Atkins H., Casella V., Christman D.R., Fowler J.S., Ido T., MacGregor R.R., Som P., Wan C.N., Wolf A.P., Kuhl D.E., and Reivich M. "Radiopharmaceuticals XXVII. ^{18}F-labeled 2-deoxy-2-fluoro-d-glucose as a radiopharmaceutical for measuring regional myocardial glucose metabolism in vivo: tissue distribution and imaging studies in animals," J Nucl Med, 1977; 18, 990-6.
- 2. Jones S.C., Alavi, A., Christman D., Montanez, I., Wolf, A.P., and Reivich M. "The radiation dosimetry of 2 [F-18] fluoro-2-deoxy-D-glucose in man," J Nucl Med, 1982; 23, 613-617.
- 3. Kocher, D.C. "Radioactive Decay Tables: A handbook of decay data for application to radiation dosimetry and radiological assessments," 1981, DOE/TIC-I 1026, 89.
- 4. ICRP Publication 53, Volume 18, No. I-4,1987, pages 75-76.

16 HOW SUPPLIED/STORAGE AND DRUG HANDLING

Fludeoxyglucose F 18 Injection is supplied in a multi-dose, capped 30 mL and 50 mL glass vial containing between 0.740 to 7.40 GBq/mL (20 to 200 mCi/mL), of no carrier added 2-deoxy-2-[F 18] fluoro-D-glucose, at end of synthesis, in approximately 15 to 50 mL.
The contents of each vial are sterile, pyrogen-free and preservative-free.
NDC 40028-511-30; 40028-511-50
Receipt, transfer, handling, possession, or use of this product is subject to the radioactive material regulations and licensing requirements of the U.S. Nuclear Regulatory Commission, Agreement States or Licensing States as appropriate.
Store the Fludeoxyglucose F 18 Injection vial upright in a lead shielded container at 25°C (77°F); excursions permitted to 15-30°C (59-86°F).
Store and dispose of Fludeoxyglucose F 18 Injection in accordance with the regulations and a general license, or its equivalent, of an Agreement State or a Licensing State.
The expiration date and time are provided on the container label. Use Fludeoxyglucose F 18 Injection within 12 hours from the EOS time.

17 PATIENT COUNSELING INFORMATION

Instruct patients in procedures that increase renal clearance of radioactivity.
Encourage patients to:
- drink water or other fluids (as tolerated) in the 4 hours before their PET study.
- void as soon as the imaging study is completed and as often as possible thereafter for at least one hour.

Manufactured by: PETNET Solutions Inc. 810 Innovation Drive Knoxville, TN 37932
Distributed by: PETNET Solutions Inc.^ 810 Innovation Drive Knoxville, TN 37932^
PETNET Solutions
PN0002262 Rev. A
Marcg 1, 2011

Indications

Fludeoxyglucose F18 Injection is indicated for positron emission tomography (PET) imaging in the following settings:

Oncology: For assessment of abnormal glucose metabolism to assist in the evaluation of malignancy in patients with known or suspected abnormalities found by other testing modalities, or in patients with an existing diagnosis of cancer.

Cardiology: For the identification of left ventricular myocardium with residual glucose metabolism and reversible loss of systolic function in patients with coronary artery disease and left ventricular dysfunction, when used together with myocardial perfusion imaging.

Neurology: For the identification of regions of abnormal glucose metabolism associated with foci of epileptic seizures.

Important Safety Information

Radiation Risks: Radiationemitting products, including Fludeoxyglucose F18 Injection, may increase the risk for cancer, especially in pediatric patients. Use the smallest dose necessary for imaging and ensure safe handling to protect the patient and healthcare worker.

Blood Glucose Abnormalities: In the oncology and neurology setting, suboptimal imaging may occur in patients with inadequately regulated blood glucose levels. In these patients, consider medical therapy and laboratory testing to assure at least two days of normoglycemia prior to Fludeoxyglucose F18 Injection administration.

Adverse Reactions: Hypersensitivity reactions with pruritus, edema and rash have been reported; have emergency resuscitation equipment and personnel immediately available.

Dosage Forms and Strengths: Multiple-dose 30 mL and 50 mL glass vial containing 0.74 to 7.40 GBq/mL (20 to 200 mCi/mL) of Fludeoxyglucose F^{18} injection and 4.5 mg of sodium chloride with 0.1 to 0.5% w/w ethanolas a stabilizer (approximately 15 to 50 mL volume) for intravenous administration. Fludeoxyglucose F^{18} injection is manufactured by Siemens' PETNET Solutions, 810 Innovation Drive, Knoxville, TN 39732, USA.

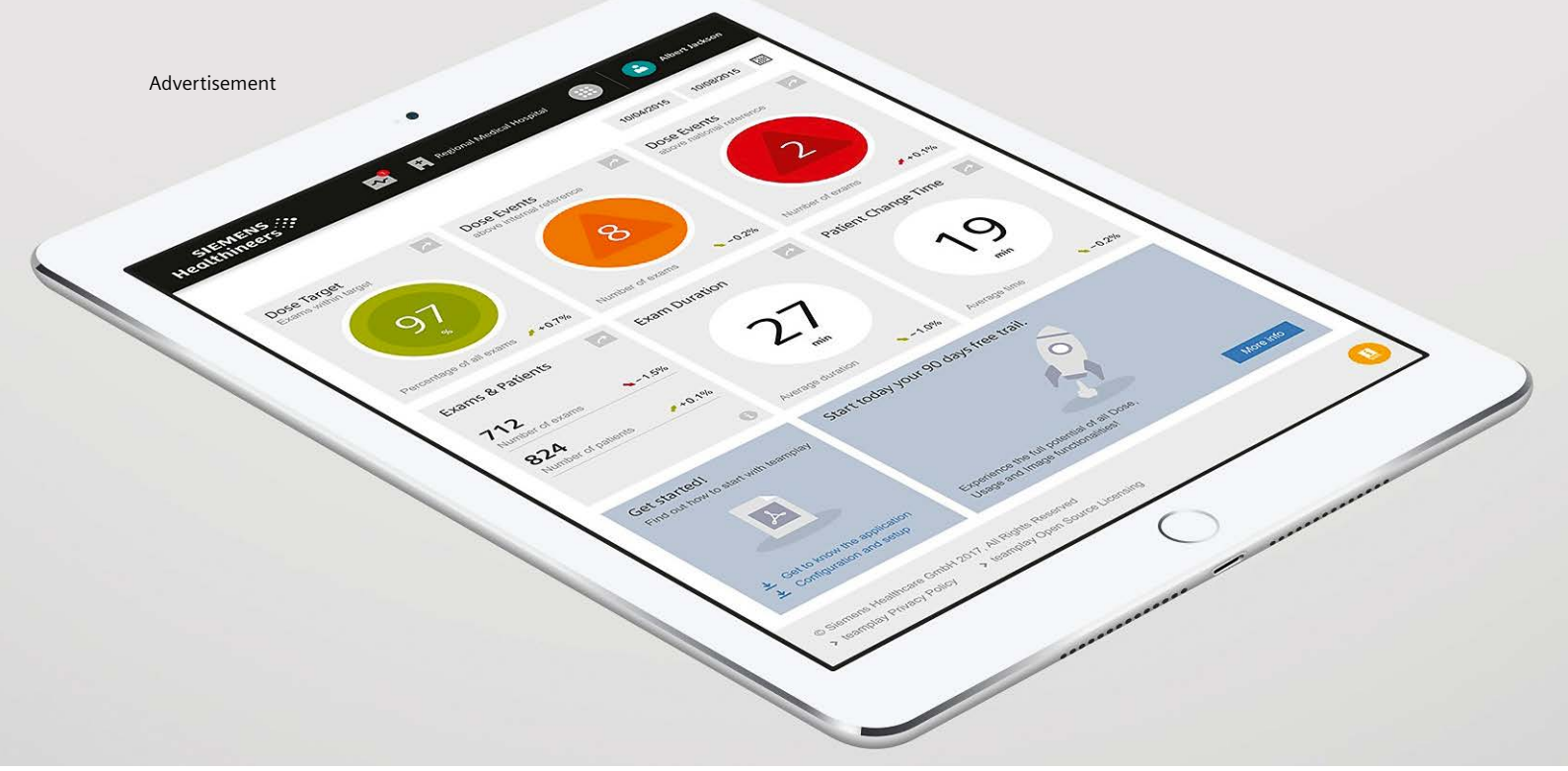

teamplay – Get the most out of your data in radiology and cardiology

healthcare.siemens.de/healthineers-digital-ecosystem/teamplay

To advance digitalization in healthcare, teamplay[1] is a departmental performance management solution that brings together healthcare professionals in a team effort. By connecting medical institutions and their imaging devices, teamplay apps aspire to create the biggest radiology and cardiology team in the world and provide its members with tools to tackle big data and the challenges of increasing cost pressure.

The cloud-based solution teamplay with its apps will help you make prompt and well-informed decisions by offering an intelligible overview of your performance data.

It monitors quantities such as imaging throughput or dose levels, utilization of staff, rooms and resources of your whole department down to every device and procedure, simplifying your reporting and showing you where workflows need adjustments. It links you to other users of teamplay and their data to offer comparable benchmarks[2] and an effortless exchange of images and reports with other healthcare providers.

[1] *Please check if teamplay is available in your country.*
[2] *Availability of Benchmarking option depends on a minimum number of considered subscribers to guarantee customer anonymity and data protection.*

SIEMENS Healthineers

Advanced Neuroimaging and Pediatric Epilepsy Surgery

Sarah Barton[1,2,3]; Michael Kean[1,2,3]; Simon Harvey[1,2,3]; Joseph Yang[1,2]

[1] Murdoch Children's Research Institute, Parkville, VIC, Australia
[2] Royal Children's Hospital, Melbourne, VIC, Australia
[3] Department of Paediatrics, University of Melbourne, VIC, Australia

Neuroimaging in epilepsy surgery

Epilepsy, a common chronic brain disorder characterized by recurrent unprovoked seizures, usually has onset during childhood. Worldwide, epilepsy affects 10.5 million children and represents about a quarter of the global epilepsy population [1]. At least 50% of epilepsy during childhood is of focal onset, and up to 30% of children with focal epilepsy have seizures that are incompletely controlled on medications [2]. Epilepsy surgery offers some of these children the opportunity for seizure freedom, improvements in development and overall better quality of life for them and their family [3].

Advanced multi-modal magnetic resonance imaging (MRI) techniques are pivotal to comprehensive presurgical evaluation in children[1] with drug-resistant focal epilepsy [4]. These advanced imaging techniques contribute to lesion identification; localization of the seizure focus, with concordant clinical and electrophysiological information; lateralisation of the language dominant cerebral hemisphere [5]; and localization of functional cortical and subcortical brain regions subserving movement, memory, language and visual function. Advanced multi-modal MRI has the potential to simplify the patient's presurgical workup, obviate the need for intracranial EEG monitoring and electrical stimulation, improve postoperative seizure outcome, and avoid or minimize postoperative neurological deficits.

[1] *MR scanning has not been established as safe for imaging fetuses and infants less than two years of age. The responsible physician must evaluate the benefits of the MR examination compared to those of other imaging procedures. Note: This disclaimer does not represent the opinion of the authors.*

TR	TE	FOV	Matrix	Slice	Grappa	SMS	B_0 Shim	Ref Scan	RF Mode Gradient	ESP	BW
Multi-Shell DWI MAGNETOM Prisma *syngo* MR E11C 32-channel Head Coil											
4000	78 ms	244	122 100%	2 mm	2	2	Adv	Gre/Sep	Normal Performnace	0.58 ms	2276 Hz/Px
fMRI Language Task MAGNETOM Prisma MB Acquisition *syngo* MR E11C 32-channel Head Coil											
1500	30 ms	255	104 100%	2.5 mm	2	3	Adv	FLEET	Normal Performnace	0.5 ms	2404 Hz/Px
Resting State MAGNETOM Prisma MB Acquisition *syngo* MR E11C 32-channel Head Coil											
1500	30 ms	255	104 100%	2.5 mm	2	3	Adv	FLEET	Normal Performnace	0.5 ms	2404 Hz/Px

Table 1: MR acquisition parameters for DWI, fMRI, and fMRI sequences.

Diffusion MRI tractography – limitations of Diffusion Tensor Imaging (DTI)

Diffusion MRI tractography is a post-processing imaging technique that generates virtual reconstructions of the anatomy of brain nerve fibre tracts, also known as white matter tracts (WMTs) [6, 7]. Accuracy of the tractography reconstruction is paramount in neurosurgery because surgical injury to the WMTs or their blood supply can lead to permanent neurological deficits [8–10]. MRI data can be coregistered and overlaid on a live view of the patient's brain during surgery, using image-guided navigation software. Preoperative tractography combined with the intraoperative live view of the patient, provide important information to the neurosurgeon to plan the optimal surgical approach to minimize injury to surrounding healthy brain structures.

The tractography techniques adopted in neurosurgery traditionally involve diffusion tensor imaging (DTI) data acquisition and a deterministic tractography algorithm, but this approach is unable to accurately model diffusion over crossing fibre regions [11, 12], present in up to 90% of the cerebral white matter (WM) [13]. State-of-the-art methods are available that improve WMT modelling, with advances in diffusion MRI data acquisition, improved tracking algorithms, and better methods for image-based tract reconstructions. Modern tractography techniques incorporate high angular resolution diffusion imaging (HARDI) data acquisition and probabilistic fibre tracking [14] based on the constrained spherical deconvolution (CSD) crossing fibre models [15, 16], improving tractography results in ways that have a significant impact on surgical planning and intraoperative image-guidance.

More recent advances in tractography include multi-shell and multi-band diffusion acquisitions. Multi-shell diffusion imaging acquires low, intermediate and high b-value diffusion data in one sitting, producing diffusion propagation maps that are more specific to the WM tissue domain [17]. This is termed the multi-shell multi-tissue-CSD (MSMT-CSD) technique. MSMT-CSD improves the accuracy of fibre-orientation distribution (FOD) estimation in WM regions over the grey-white matter tissue interface and removes noisy isotropic voxels that belong to the cerebrospinal fluid space, thereby improving further the anatomical accuracy of the tractography reconstruction (Fig. 1). Multi-band or simultaneous multi-slice acquisition schemes reduce the time needed to acquire multi-shell diffusion data within a clinically acceptable timeframe [18, 19].

Diffusion MRI tractography at the Royal Children's Hospital, Melbourne

Since 2012, advanced tractography reconstructions using HARDI data acquisition and based on CSD crossing-fibre modelling and probabilistic tracking have been used for preoperative planning for epilepsy surgery at the Royal Children's Hospital, Melbourne, Australia. The introduction of multi-band, multi-shell DWI acquisition in 2016 further improved the anatomical accuracy of our tractography reconstructions. Combined with clinical expertise and other imaging and electrophysiological modalities, we believe our clinical tractography program has contributed to improved seizure and functional outcomes in children undergoing epilepsy surgery. In this article we present the neuroimaging data for three children in whom tractography played a role in pre-surgical planning for their epilepsy surgery.

MR protocol at the Royal Children's Hospital, Melbourne

Our early implementation of multi-band diffusion sequences and SMS TSE into our comprehensive epilepsy protocol utilized MAGNETOM Trio / MAGNETOM Verio *syngo* MR B17 software and resulted in a significant improvement in our diagnostic imaging protocols (spatial resolution, reduction in scan times and integration of advanced image analysis). Prior to implementing these sequences into clinical practice we undertook comprehensive comparative studies in volunteers using conventional and multi-band acquisitions plus analysis pipeline verification. The comparative studies looked at the optimization of protocols for 3T [20–22], variations in tSNR that could affect analysis of resting state data [23], interslice artefacts [24, 25], effects of patient movement during the ACS acquisition [26, 27] and how far we could push the multi-band factor on our systems [28–30]. Our initial protocols (DWI, fMRI and rfMRI) have been transitioned through to our current systems (MAGNETOM Prisma *syngo* MR E11C and Biograph mMR *syngo* MR E11P) with modifications to the imaging parameters, notably multi-band factors and spatial resolution (Table 1). Multi-shell acquisitions are acquired using 3 separate scans (Monopolar diffusion scheme; b = 3000 s/mm^2, 69 dir including 5 b = 0, b = 2000 s/mm^2, 50 dir including 5 b = 0 and b = 1000 s/mm^2, 30 dir including 5 b = 0) using a custom vector file.

WIP, the product is currently under development and is not for sale in the US and in other countries. Its future availability cannot be ensured.

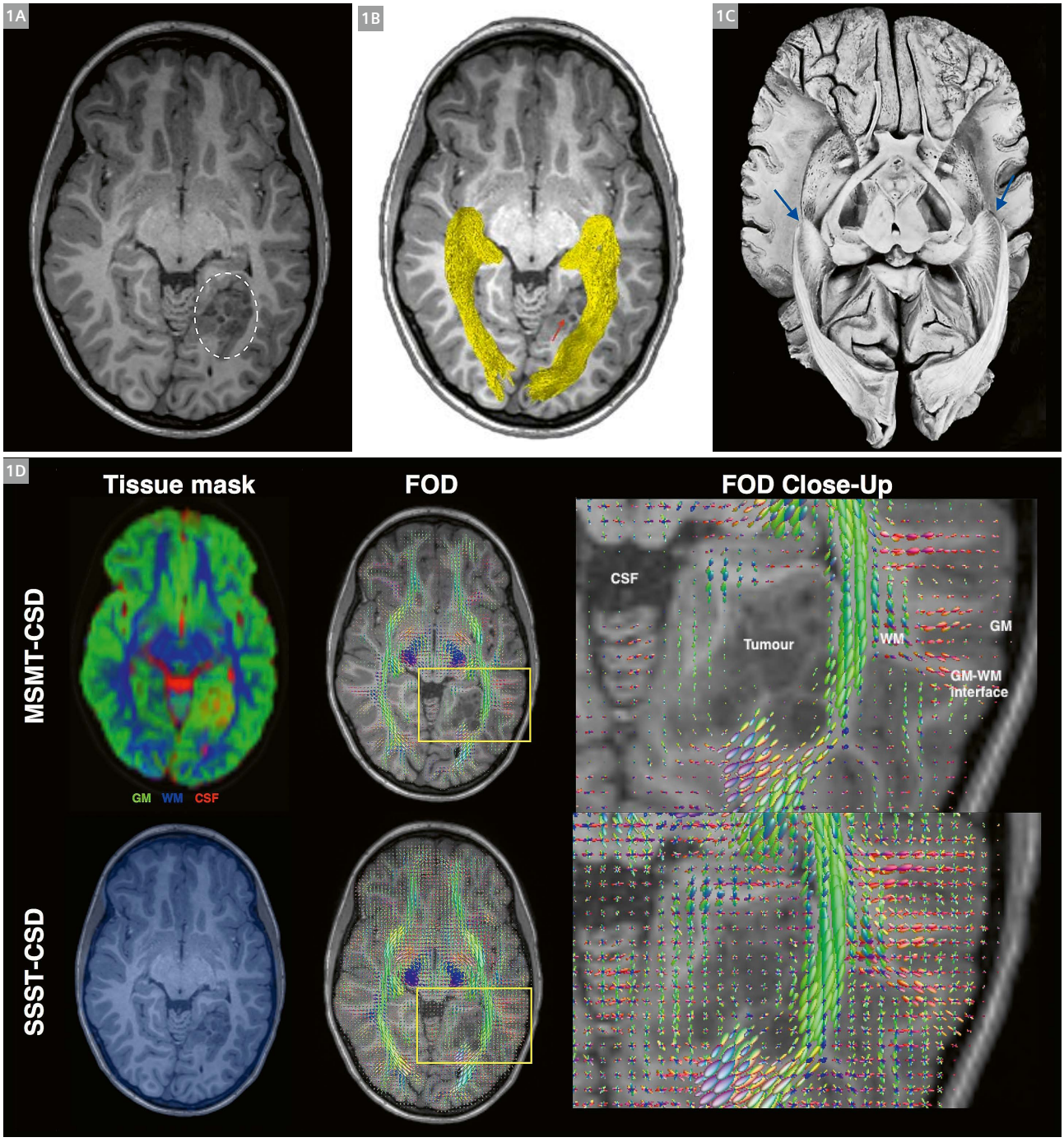

1 **(1A–C)** Advanced diffusion MRI white matter modelling and tractography reconstruction in a patient with focal drug refractory epilepsy referable to a developmental brain tumor located in the left fusiform gyrus (white dashed circle, **(1A)** T1-weighted image). Multi-band, multi-shell diffusion data acquired using a 3T MAGNETOM Prisma Siemens scanner, was used to reconstruct the optic radiation tractography (yellow color in **1B**) closely abutting the tumor. The reconstructed tractography closely resemble cadaveric fibre dissection (blue arrows in **1C**); *taken from Ludwig & Klinger's atlas, 1956.*

(1D) shows the multi-shell multi-tissue-constrain spherical deconvolution (MSMT-CSD) framework improves tissue specificity of the diffusion mask, and the accuracy of corresponding fibre orientation distribution (FOD) estimations, than the traditional approach of using single-shell single-tissue-CSD (SSST-CSD). Combinations of these features improved anatomical accuracy of the tractography output.
CSF = cerebrospinal fluid; GM = gray matter; WM = white matter.

Case 1

In this case, we present neuroimaging data from an adolescent with temporal lobe epilepsy. Seizure onset was at two years of age, with seizures from wake and sleep characterized by staring, confusion, speech difficulties and sometimes convulsing. The seizures were refractory to numerous antiepileptic medications. MRI showed a long bottom-of-sulcus focal cortical dysplasia in the left superior temporal sulcus, which merged into the sylvian fissure at the lateral convexity. The dysplasia was characterized by cortical thickening and grey-white blurring on T1-weighted MPR images, subcortical signal hyperintensity on FLAIR and T2-weighted images, and hypometabolism on FDG-PET images. Also associated with the dysplasia was an unusual transmantle band leading to a periventricular nodule in the left trigone.

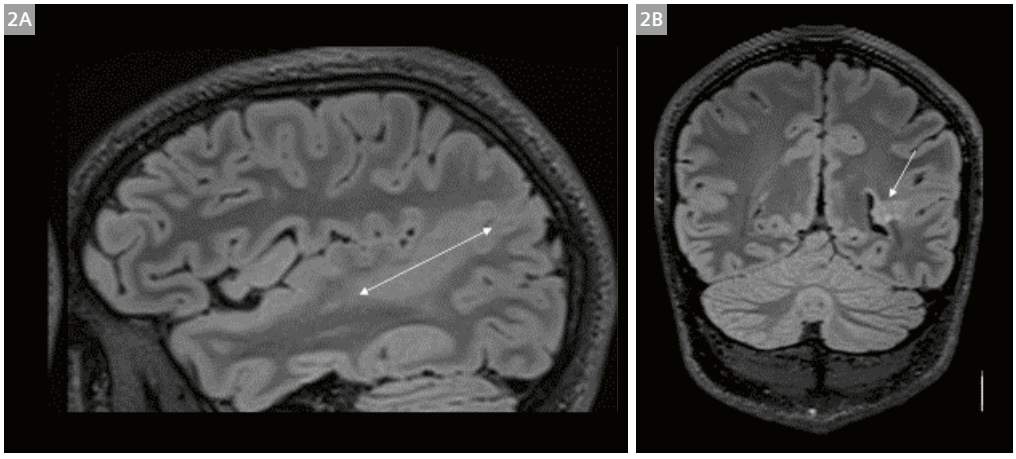

2 FLAIR image showing an extensive focal cortical dysplasia in the left superior temporal sulcus **(2A)** with a transmantle band and periventricular nodule at the trigone **(2B)**.

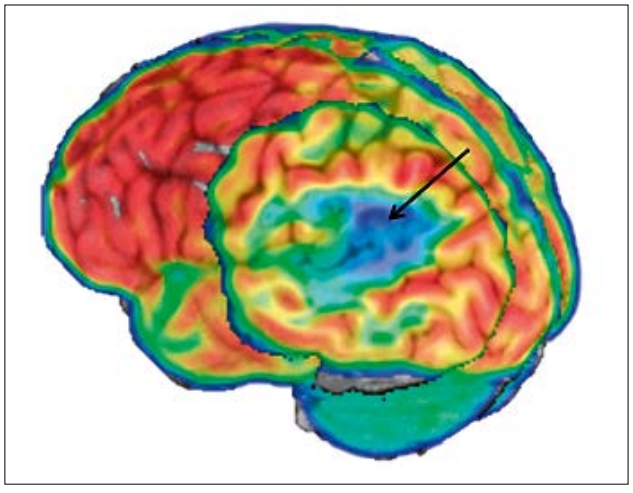

3 3D surface-rendered, co-registered T1-weighted MRI and FDG-PET with oblique slice showing focal hypometabolism in the depth of the cortical dysplasia which involved the left superior temporal sulcus at the depth and the sylvian fissure at the lateral convexity superior temporal sulcus.

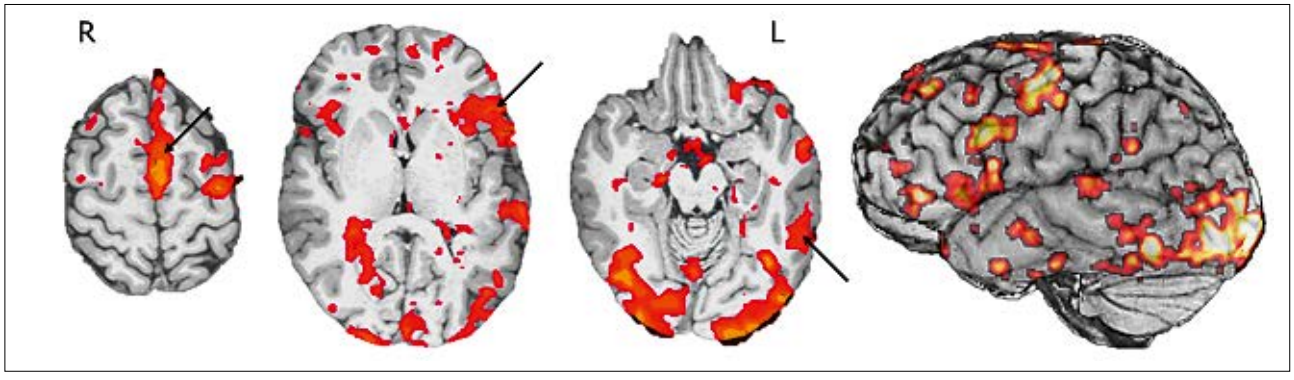

4 Axial slices from language fMRI with a verb generation task showing left medial frontal, inferior frontal and inferior temporal BOLD activation. The surface-rendered 3D image shows the atypical localization of temporal activation in the inferior temporal gyrus.

Functional MRI with a visually-presented verb generation paradigm [31] showed left lateralization of language activation. Typical distribution of frontal activation was observed in the posterior-medial frontal region and frontal operculum; however, temporal activation was somewhat atypical, with the greatest activation in the inferior (as opposed to superior) temporal gyrus. No BOLD activation was seen in the dysplasia.

Probabilistic tractography was performed on HARDI data [15, 16, 32] to localize the superior longitudinal fasciculus (SLF) and the optic radiations (OR), in particular their relationship to the deeper components of the dysplasia. The temporal projections of the left SLF travelled immediately medial to the depth of the dysplastic superior temporal sulcus. The majority of the cortical terminations of the left SLF were in the inferior temporal gyrus, which corresponded with location of the temporal BOLD activation. The left OR travelled through and around the transmantle band in the WM between the depth of the dysplasia and the periventricular nodule.

The functional and structural imaging therefore showed the extent of the dysplasia, the likely absence of function in the dysplasia, the proximity of language cortex and WM pathways to the superficial and deeper components of the dysplasia, and the passage of the transmantle component of the dysplasia through the visual pathways. The epilepsy surgery team could conceivably proceed with knowledge of the operative risks and without need for additional electrical stimulation mapping.

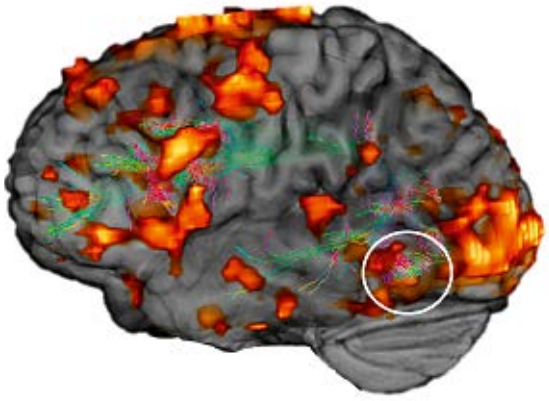

5 3D projection of the left SLF showing the correspondence with language BOLD activation in the inferior temporal gyrus.

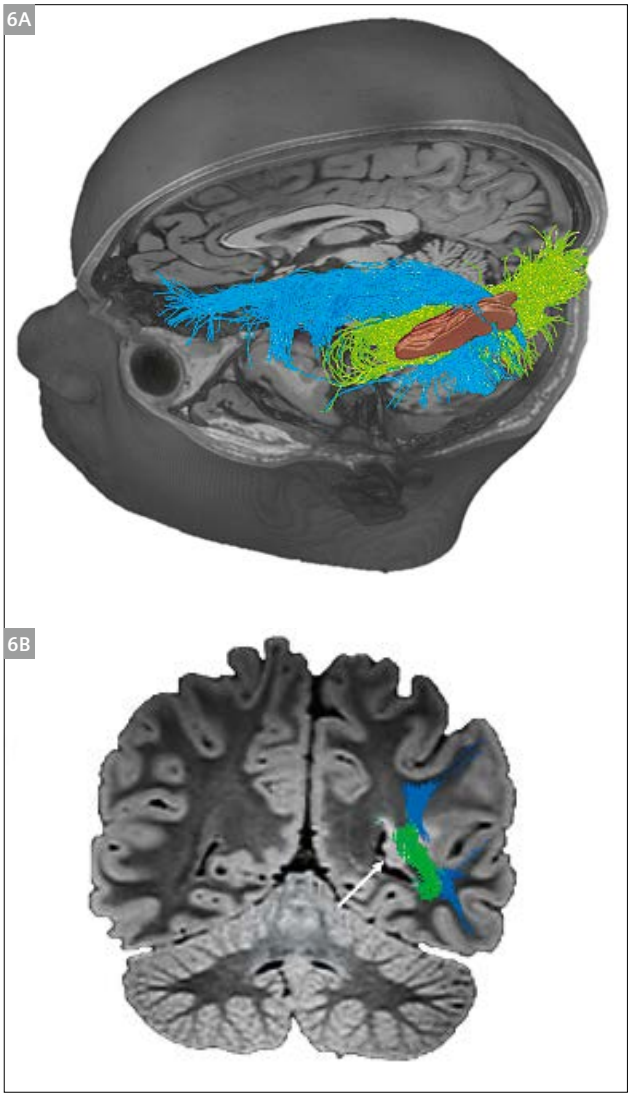

6 Location of the SLF (blue) and OR (green) in relation to the dysplastic superior temporal sulcus (brown) in 3D **(6A)** and relative to periventricular nodule on axial FLAIR **(6B)**.

Case 2

This patient was a primary school aged child with a brief history of focal seizures with prominent confusion and aphasia. They occurred at weekly frequency, despite several antiepileptic medications being trialled. MRI revealed a lesion in the left temporal lobe laterally and posteriorly, involving grey and white matter and filling a gyrus. The lesion was believed to be a low-grade glioma, rather than a focal cortical dysplasia or developmental tumor. Minor growth was seen on serial imaging over six months.

On functional MRI using a visually-presented verb generation task [31], language was left lateralized. There was language activation in cortex medial to and surrounding the lesion. Probabilistic tractography was performed on HARDI data [15, 16, 32] to localize the superior longitudinal fasciculus (SLF). The terminations of the SLF tracts were in the cortex and WM abutting the lesion, where BOLD activation was seen on fMRI. Optic radiation (OR) tractography showed visual pathways travelled deeper to the SLF. The functional imaging indicated that surgery would need to be a conservative lesionectomy, sparing superficial and deep language cortex and pathways.

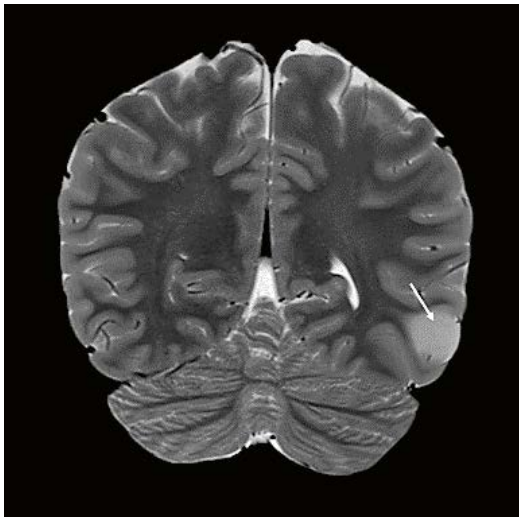

7 Appearance of left temporal lesion on T2-weighted coronal image.

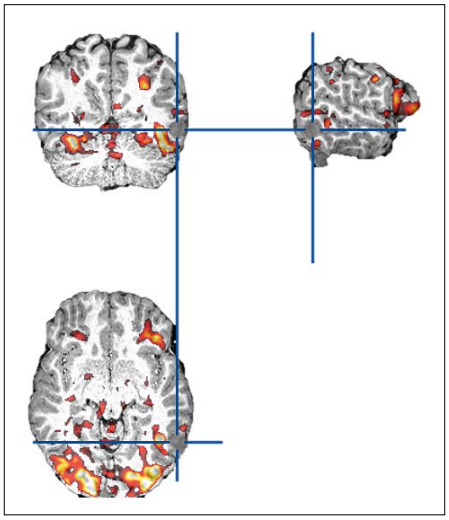

8 Language BOLD activation in left hemisphere relative to temporal lesion (crosshair).

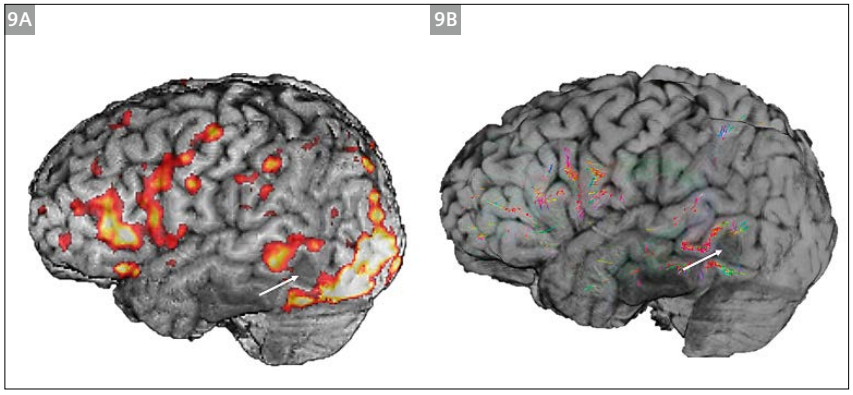

9 3D renders of the left hemisphere showing language BOLD activation **(9A)** and SLF terminations **(9B)** relative to the temporal lesion.

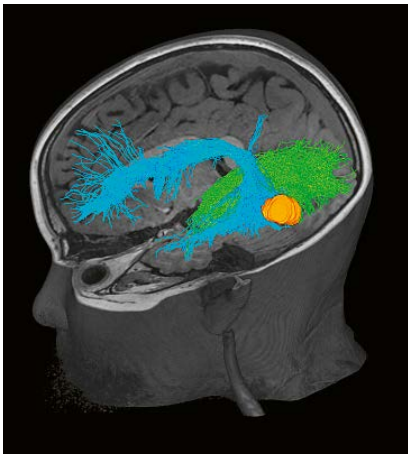

10 3D tractography showing the location of the SLF (blue) and OR (green) in relation to the lesion (yellow).

Case 3

Here we present neuroimaging data from a child with recent-onset of seizures secondary to a left medial temporal-occipital tumour. Seizures were characterized by behavioural arrest, head and eye deviation and repetitive hand movements, followed by brief nonsensical speech. MRI showed a multi-cystic, cortically-based and contrast-enhancing tumor in the left fusiform gyrus, abutting the parahippocampal gyrus and calcarine fissure. The tumor had mixed MRI features of a DNET and PCA and showed slight change in enhancement and size on serial imaging. Left language dominance was established with functional MRI utilizing verb generation and verbal fluency paradigms [31]. Additionally, it revealed prominent BOLD activation in the posterior-basal temporal lobe, just lateral to the tumor.

Probabilistic tractography was performed on HARDI data [15, 16, 32] to localize the SLF and OR pathways. It revealed that the tumor was encircled by visual and language pathways, indicating significant risk of deficits in cognition, language, verbal memory and peripheral vision with attempted resection. However, with the aid of neuronavigation, preoperative simulated surgery using the detailed tractography data, and intraoperative MRI (IMRIS), surgery was performed with the impression of complete resection and no neurological deficits. Post-operative imaging and assessments are pending.

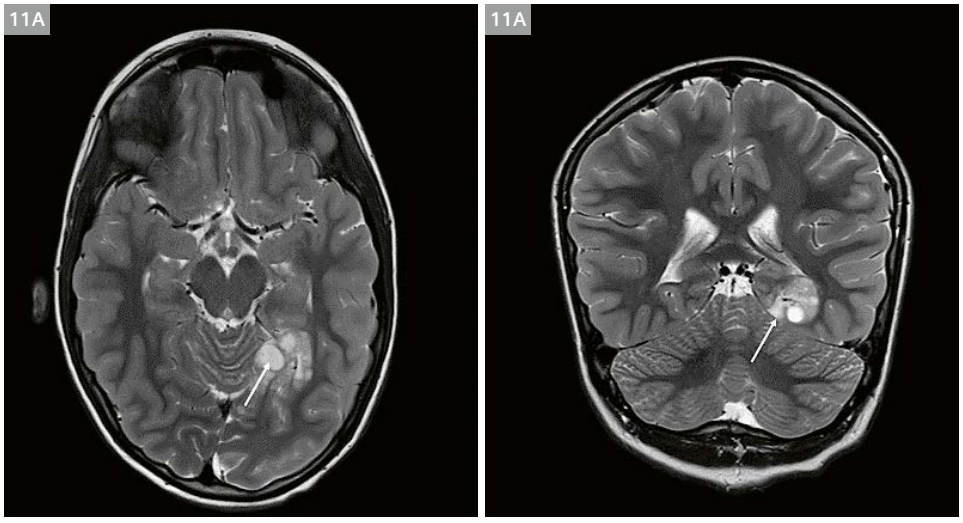

11 Appearance of left medial temporal-occipital tumour on T2-weighted axial **(11A)** and coronal **(11B)** image.

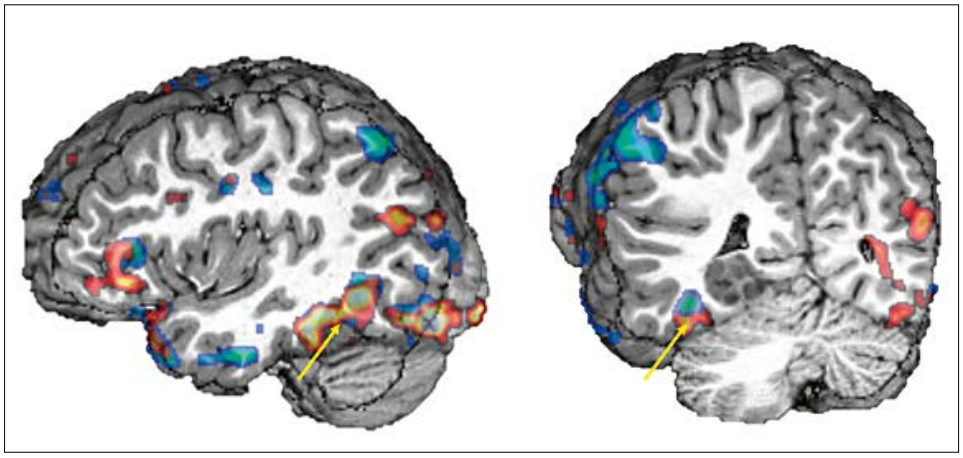

12 Lateral and oblique cut-aways showing the basal temporal language BOLD (noun verb = orange; verbal fluency = blue) overlying the tumor.

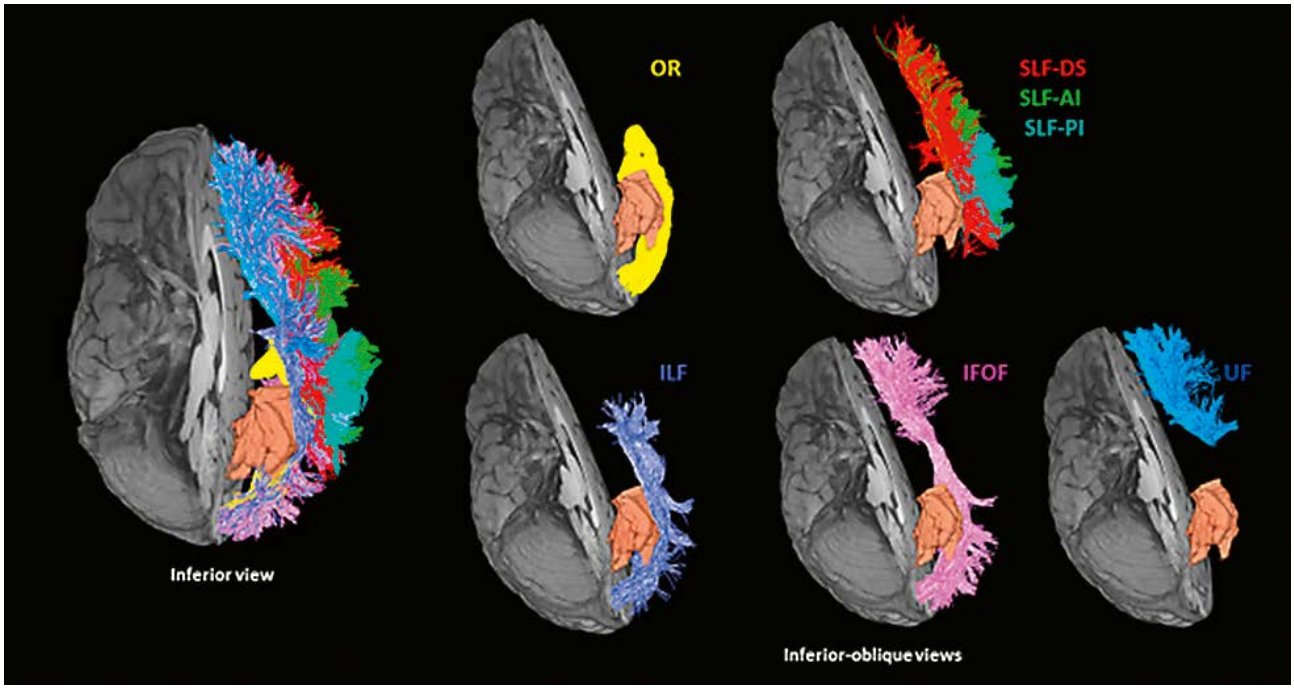

13 Tractography in relation to the tumor (brown). OR = optic radiation, SLF-AI = anterior indirect segment of superior longitudinal fasciculus, SLF-DS = direct segment of superior longitudinal fasciculus, SLF-PI = posterior indirect segment of superior longitudinal fasciculus, ILF = inferior longitudinal fasciculus, IFOF = inferior fronto-occipital fasciculus; UF = uncinate fasciculus.

Acknowledgments

This work was conducted within the Department of Neurology and Neurosurgery, Royal Children's Hospital, and the Developmental Imaging and Neuroscience Research groups, Murdoch Children's Research Institute at the Melbourne Children's MRI and PET centre, Melbourne, Victoria, Australia. It was supported by the Royal Children's Hospital Foundation, Murdoch Children's Research Institute, The University of Melbourne Department of Paediatrics, and the Victorian Government's Operational Infrastructure Support Program.

The authors acknowledge the assistance of Siemens Healthineers for ongoing support with works in progress sequences (WIPs) plus scientific support and the Centre for Magnetic Resonance Research Minnesota for access to multiband sequences through a C2P agreement. The authors also acknowledge the staff of the Melbourne Children's MRI and PET centre for their efforts in scanning our patients.

The authors and author's institutions did not receive any incentive or inducement, financial or otherwise, from Siemens Healthineers for the preparation of this article. The data in this article was generated by the authors on institutional infrastructure and was not edited by Siemens Healthineers.

References

1 Guerrini, R. Epilepsy in children. Lancet 367, 499-524, doi:10.1016/S0140-6736(06)68182-8 (2006).
2 Berg, A. T. et al. How long does it take for epilepsy to become intractable? A prospective investigation. Ann Neurol 60, 73-79, doi:10.1002/ana.20852 (2006).
3 Snead, O. C., 3rd. Surgical treatment of medically refractory epilepsy in childhood. Brain Dev 23, 199-207 (2001).
4 Rastogi, S., Lee, C. & Salamon, N. Neuroimaging in pediatric epilepsy: a multimodality approach. Radiographics 28, 1079-1095, doi:10.1148/rg.284075114 (2008).
5 Binder, J. R. Functional MRI is a valid noninvasive alternative to Wada testing. Epilepsy & behavior 20, 214-222 (2011).
6 Basser, P. J., Mattiello, J. & LeBihan, D. Estimation of the effective self-diffusion tensor from the NMR spin echo. J Magn Reson B 103, 247-254 (1994).
7 Basser, P. J., Pajevic, S., Pierpaoli, C., Duda, J. & Aldroubi, A. In vivo fiber tractography using DT-MRI data. Magnetic resonance in medicine : official journal of the Society of Magnetic Resonance in Medicine / Society of Magnetic Resonance in Medicine 44, 625-632 (2000).
8 Duffau, H. The dangers of magnetic resonance imaging diffusion tensor tractography in brain surgery. World Neurosurg 81, 56-58, doi:10.1016/j.wneu.2013.01.116 (2014).
9 Farquharson, S. et al. White matter fiber tractography: why we need to move beyond DTI. Journal of neurosurgery 118, 1367-1377, doi:10.3171/2013.2.JNS121294 (2013).
10 Kinoshita, M. et al. Fiber-tracking does not accurately estimate size of fiber bundle in pathological condition: initial neurosurgical experience using neuronavigation and subcortical white matter stimulation. Neuroimage 25, 424-429, doi:10.1016/j.neuroimage.2004.07.076 (2005).

11 Tournier, J. D., Calamante, F. & Connelly, A. MRtrix: diffusion tractography in crossing fiber regions. International Journal of Imaging Systems and Technology 22, 53-66, doi:10.1002/ima.22005 (2012).

12 Tournier, J. D., Mori, S. & Leemans, A. Diffusion tensor imaging and beyond. Magnetic resonance in medicine : official journal of the Society of Magnetic Resonance in Medicine / Society of Magnetic Resonance in Medicine 65, 1532-1556, doi:10.1002/mrm.22924 (2011).

13 Jeurissen, B., Leemans, A., Tournier, J. D., Jones, D. K. & Sijbers, J. Investigating the prevalence of complex fiber configurations in white matter tissue with diffusion magnetic resonance imaging. Hum Brain Mapp 34, 2747-2766, doi:10.1002/hbm.22099 (2013).

14 Tuch, D. S. Q-ball imaging. Magnetic resonance in medicine : official journal of the Society of Magnetic Resonance in Medicine / Society of Magnetic Resonance in Medicine 52, 1358-1372, doi:10.1002/mrm.20279 (2004).

15 Tournier, J. D., Calamante, F. & Connelly, A. Robust determination of the fibre orientation distribution in diffusion MRI: non-negativity constrained super-resolved spherical deconvolution. Neuroimage 35, 1459-1472, doi:S1053-8119(07)00124-3 [pii] 10.1016/j.neuroimage.2007.02.016 (2007).

16 Tournier, J. D., Calamante, F., Gadian, D. G. & Connelly, A. Direct estimation of the fiber orientation density function from diffusion-weighted MRI data using spherical deconvolution. Neuroimage 23, 1176-1185, doi:S1053-8119(04)00410-0 [pii] 10.1016/j.neuroimage.2004.07.037 (2004).

17 Jeurissen, B., Tournier, J. D., Dhollander, T., Connelly, A. & Sijbers, J. Multi-tissue constrained spherical deconvolution for improved analysis of multi-shell diffusion MRI data. Neuroimage 103, 411-426, doi:10.1016/j.neuroimage.2014.07.061 (2014).

18 Feinberg, D. A. & Setsompop, K. Ultra-fast MRI of the human brain with simultaneous multi-slice imaging. J Magn Reson 229, 90-100, doi:10.1016/j.jmr.2013.02.002 (2013).

19 Moeller, S. et al. Multiband multislice GE-EPI at 7 tesla, with 16-fold acceleration using partial parallel imaging with application to high spatial and temporal whole-brain fMRI. Magnetic resonance in medicine : official journal of the Society of Magnetic Resonance in Medicine / Society of Magnetic Resonance in Medicine 63, 1144-1153, doi:10.1002/mrm.22361 (2010).

20 Barth, M., Breuer, F., Koopmans, P.J., Norris, D.G. and Poser, B.A., 2016. Simultaneous multislice (SMS) imaging techniques. Magnetic resonance in medicine, 75(1), pp.63-81.

21 Todd, N., Moeller, S., Auerbach, E.J., Yacoub, E., Flandin, G. and Weiskopf, N., 2016. Evaluation of 2D multiband EPI imaging for high-resolution, whole-brain, task-based fMRI studies at 3T: sensitivity and slice leakage artifacts. Neuroimage, 124, pp.32-42.

22 Xu, J., Moeller, S., Auerbach, E.J., Strupp, J., Smith, S.M., Feinberg, D.A., Yacoub, E. and Uğurbil, K., 2013. Evaluation of slice accelerations using multiband echo planar imaging at 3 T. Neuroimage, 83, pp.991-1001.

23 Preibisch, C., Bührer, M. and Riedl, V., 2015. Evaluation of multiband EPI acquisitions for resting state fMRI. PloS one, 10(9), p.e0136961.

24 Cauley, S.F., Setsompop, K., Polimeni, J.R. and Wald, L.L., 2012. Inter-slice artifact reduction for slice-GRAPPA reconstruction of simultaneous multi-slice (SMS) acquisitions. In Proceedings of the 20th Annual Meeting of ISMRM, Melbourne, Australia (p. 2543).

25 Cauley, S.F., Polimeni, J.R., Bhat, H., Wald, L.L. and Setsompop, K., 2014. Interslice leakage artifact reduction technique for simultaneous multislice acquisitions. Magnetic resonance in medicine, 72(1), pp.93-102.

26 Bhat,H., Polimeni, J.R., Cauley, S.J., Setsompop, K, Wald, L., Heberlein,K., 2014. Motion Insensitive ACS Acquisition Method for in-plane Simultaneous Multi-Slice Accelerated EPI. In Proceedings of the ISMRM, Abstract(Vol. 0644)

27 Kelly, M.E., Duff, E.P., Bijsterbosch, J.D., Voets, N.L., Filippini, N., Moeller, S., Xu, J., Yacoub, E.S., Auerbach, E.J., Ugurbil, K. and Smith, S.M., 2013. An assessment of motion artefacts in multi band EPI for high spatial and temporal resolution resting state fMRI. In Proceedings of the ISMRM, Abstract(Vol. 3275)

28 Golestani, A. M., Faraji-Dana, Z., Kayvanrad, M., Setsompop, K., Graham, S. J., & Chen, J. J. (2018). Simultaneous Multislice Resting-State Functional Magnetic Resonance Imaging at 3 Tesla: Slice-Acceleration-Related Biases in Physiological Effects. Brain connectivity, 8(2), 82-93.

29 Demetriou, L., Kowalczyk, O.S., Tyson, G., Bello, T., Newbould, R.D. and Wall, M.B., 2018. A comprehensive evaluation of increasing temporal resolution with multiband-accelerated protocols and effects on statistical outcome measures in fMRI. NeuroImage.

30 Setsompop, K., Cohen-Adad, J., McNab, J., Gagoski, B.A., Wedeen, V.J. and Wald, L.L., 2010. Improving SNR per unit time in diffusion imaging using a blipped-CAIPIRINHA simultaneous multi-slice EPI acquisition. In Proceedings of the 18th Annual Meeting of ISMRM (p. 187).

31 Wood, A. G. et al. Language cortex activation in normal children. Neurology 63, 1035-1044 (2004).

32 Yang, J. Y.-M. et al. A systematic evaluation of intraoperative white matter tract shift in pediatric epilepsy surgery using high-field MRI and probabilistic high angular resolution diffusion imaging tractography. Journal of Neurosurgery: Pediatrics 19, 592-605 (2017).

Contact

Michael Kean, FSMRT
Chief MR Technologist
Children's MRI and PET Centre
Department of Medical Imaging
Honorary Fellow, Developmental Imaging,
Murdoch Children's Research Institute
Honorary Senior Research Fellow,
Department of Paediatrics,
The University of Melbourne
Royal Children's Hospital,
Flemington Road
Parkville
Australia
Tel.: +61 411681198
Michael.Kean@rch.org.au

Advanced Multi-Parametric Neuroimaging in Pediatric Neurology

Arun Joseph[1]; Steffi Dreha-Kulaczewski[2,3]

[1]Biomedizinische NMR, Max-Planck-Institut für biophysikalische Chemie, Göttingen, Germany
[2]Department of Pediatrics and Adolescent Medicine, Division of Pediatric Neurology, University Medical Center Göttingen, Germany
[3]Department of Cognitive Neurology, MR-Research in Neurology and Psychiatry, University Medical Center Göttingen, Germany

Introduction

MR imaging and spectroscopy play important roles in the management of our neuropediatric patients. While structural assessments of the central nervous system by conventional MRI constitute an essential part of clinical routine, recent technical advances have facilitated insights not only into brain structures but also into function and metabolism as well as into the dynamics of cerebrospinal fluid (CSF) and aspects of myelination as an indicator of brain maturation. Many of these techniques contribute to faster diagnosis and, even more importantly, to evaluation of therapies, e.g., in neurometabolic disorders. Furthermore, novel methods like real-time phase-contrast (PC) flow MRI will be of great importance in unravelling the pathophysiological mechanisms in pediatric patients with disturbed CSF circulation like hydrocephalus, pseudotumor cerebri, as well as spinal cord disorders such as syringomyelia. Pertinent insights promise a basis for new approaches to therapeutic interventions.

^{1}H-MR spectroscopy for diagnostics and therapy monitoring

MRS characterizes brain cellular composition and metabolism and thus offers complementary information to structural MRI. For example, tissue-specific placements of volumes-of-interests may help to differentiate between gray-matter (GM) and white-matter (WM) diseases. The

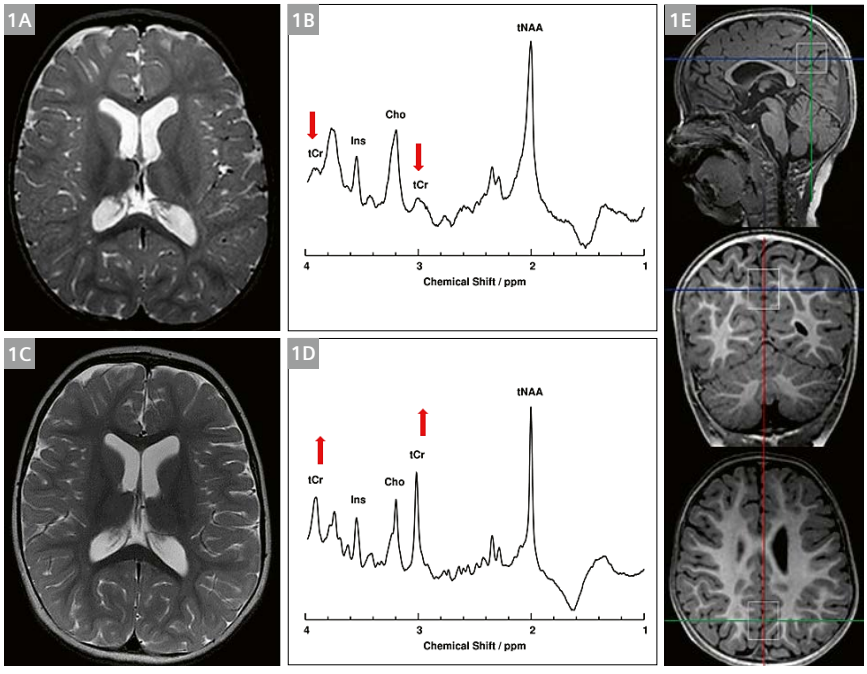

1 **^{1}H-MR spectroscopy in a girl with creatine deficiency syndrome** (caused by guanidinoacetate methyltransferase deficiency).

(1A, B) (Age 1.3 years[1]): (1A) axial T2-weighted image without abnormalities. Myelination is appropriate for the age. (1B) Gray matter (GM) spectrum reveals two significantly reduced tCr peaks indicating cerebral creatine deficiency.

(1C, D) After three months of creatine and ornithine supplementation (age 1.6 years): (1C) Axial T2-weighted image demonstrates physiological advancement of myelination. (1D) tCr peaks have increased, reflecting effective therapy. (1E) Voxel placement in posterior paramedian GM.

tNAA: *N*-acetylaspartate and *N*-acetylaspartylglutamate
tCr: creatine and phosphocreatine
Cho: choline-containing compounds
Ins: *myo*-inositol
ppm: parts per million

neuronal marker *N*-acetylaspartate (NAA) dominates a pediatric brain spectrum from about five months of age and is of significant clinical relevance. Other metabolites accessible by MRS are creatine (Cr), which reflects energy metabolism, choline-containing compounds (Cho) depicting membrane turnover, and *myo*-inositol (Ins) as an astrocytic marker [1]. Postnatal brain development and maturation processes (e.g., myelination) result in considerable biochemical changes and correspondingly altered metabolite patterns [2]. Such knowledge allows for the evaluation of normal and pathological brain development and is one essential feature in pediatric applications. Insights into the "*in vivo* biochemistry" of the brain by MRS may greatly facilitate the diagnostic work-up of patients with neurometabolic or WM diseases, neurodegeneration, or brain tumors. In general, only very few metabolite patterns in a MR spectrum unequivocally point toward a specific diagnosis and hence obviate the need for further diagnostic procedures except for appropriate genetic tests. Prominent examples are the appearance of succinate (2.4 ppm) in succinate dehydrogenase deficiency [3], of succinyladenosine (8.3 ppm) in adenylosuccinate lyase deficiency [4], or the absence of Cr in creatine deficiency syndromes (Fig. 1) [5, 6]. In cases where specific MRS results precede genetic or biochemical confirmation, decisions about therapies can be made earlier in the process. More commonly, MRS patterns reflect general pathophysiologic processes like neurodegeneration (decrease in NAA), astrocytosis (elevation of Ins), hypomyelination (decrease in Cho) or demyelination (increase in Cho). Detection of lactate (doublet at 1.3 ppm) facilitates the diagnosis of a mitochondriopathy and supports the clinical management of those patients (Fig. 2).

In our understanding, MRS techniques will be of increasing relevance for the evaluation and monitoring of future therapies. To date, the effective supplementation of creatine and ornithine in the treatment of a creatine deficiency is monitored by a rise in the intracerebral Cr concentration as measured by MRS (Fig. 1). Sufficient substitution of folinic acid normalizes perturbed brain metabolism in cerebral folate deficiency, which can also be monitored by MRS, as shown in Figure 3 [7].

^{1}H-MR spectroscopy protocol

Our routine MRS protocol is well established and easy to handle in order to allow for comparable and reliable follow-up studies. Currently, we use a 3T MAGNETOM Prisma^{fit} for our patient measurements and a 64-channel receive array. Sometimes we utilize the 20-channel head coil, depending on patient condition. Fully relaxed ^{1}H MR spectra (64 accumulations) are almost consistently acquired using a single-voxel STEAM (stimulated echo acquisition mode) localization sequence with TR/TE/TM = 6000/20/10 ms [8]. Short TE ensures access to a large number of metabolites. Voxel sizes range between 4.1 mL in WM and 12 mL in GM and are routinely placed within frontal or parieto-occipital WM, posterior paramedian GM, basal ganglia and thalamus, or cover a structural lesion. Usually, a manual shim further improves the homogeneity achieved by automated shimming. Absolute concentrations of *N*-acetylaspartate and *N*-acetylaspartylglutamate (tNAA) at 2.01 ppm, creatine and phosphocreatine (tCr) at 3.02 and 3.93 ppm, Cho at 3.22 ppm, Ins at 3.35 ppm, and lactate are determined by LCModel [9] and compared with age-matched controls from our own data base.

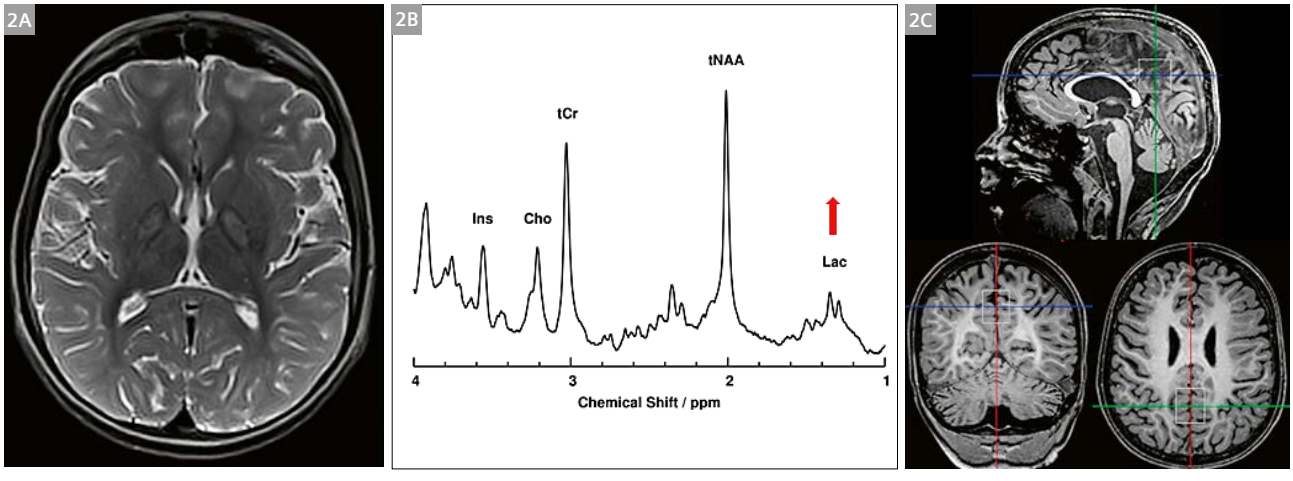

2 **^{1}H-MR spectroscopy in a boy (age 10.5 years) with a mitochondriopathy** (caused by Kearns-Sayre syndrome).
(2A) Axial T2-weighted image with high signal bilateral in the pallidum as well as subcortical occipital. **(2B)** Gray matter (GM) spectrum with lactate doublet at 1.3 ppm indicating increased brain lactate concentration. **(2C)** Voxel placement in posterior paramedian GM. Note the atrophy of the whole brain.

Lac: lactate; other parameters see Fig. 1.

Cerebrospinal fluid dynamics studied by real-time flow MRI

So far, almost all studies investigating CSF flow have employed ECG-synchronized cine PC MRI [10–12]. Thus, CSF dynamics have been thought to mainly follow cardiac-related oscillations as implicitly suggested by the experimental approach. Recent methodological advances toward real-time PC flow MRI now allow for the unique possibility of directly measuring CSF dynamics at high spatial and temporal resolution irrespective of the assumption of any periodicity. These studies have revealed the significant influence of respiration. In particular, forced inspiration has been identified as the dominant regulator of CSF dynamics in all its compartments (Fig. 4D and Fig. 5, left column) [13, 14]. The onset of every forced inspiration prompted an upward surge of CSF from the spinal canal into the head and further into the aqueduct toward the 3rd ventricle (Fig. 5). On the other hand, forced expiration led to a reversal of the flow direction and hence a downward movement, albeit to a variable extent (Fig. 4, column E and Fig. 5, left column). Figure 5 illustrates CSF flow and flow volumes during four cycles of forced respiration (see breathing protocol at the bottom). The occurrence of upward CSF flow into the head and brain in response to forced inspiration has been explained as a necessity to counterbalance the inspiratory-regulated venous flow out of the head/neck region [15]. CSF and venous blood flow appear tightly interconnected and balanced to ensure the Monro-Kellie doctrine of a constant intracranial volume. So far, CSF dynamics has mainly been investigated under normal physiological conditions, as illustrated in Figures 4 and 5 for a healthy eight-year-old boy. We are currently in the process of translating real-time PC flow MRI to clinical applications in pediatrics, which will be of eminent importance to reveal mechanisms of perturbed CSF circulation and open new approaches to therapeutic nterventions. For example, spinal cord malformations and many forms of pediatric hydrocephalus are still poorly understood and therapeutic options often controversially discussed.

Real-time PC flow MRI protocol[2]

Real-time PC flow MRI is based on highly undersampled radial gradient-echo acquisitions in combination with image reconstruction by regularized nonlinear inversion (NLINV). It offers access to high spatial and temporal resolutions [16–18]. Recently, real-time PC flow MRI was extended to a model-based reconstruction technique that jointly estimates an anatomical image, a set of coil sensitivities, and a PC velocity map directly from the flow-encoded raw data [19]. The model-based reconstruction, as seen in Figure 4 (column C, lower parts), provides velocity maps free of phase noise in regions without signal support (e.g., the lungs) thereby improving the spatial acuity of flow regions. A highly parallelized version of the reconstruction algorithm was used to reconstruct the real-time data online on a bypass computer (Sysgen, Bremen, Germany) consisting of two processors (SandyBridge E5-2650, Intel) and eight graphical processing units (GeForce GTX TITAN, Nvidia) [20]. The entire reconstruction process is fully integrated into the MRI system so that the reconstructed magnitude images and

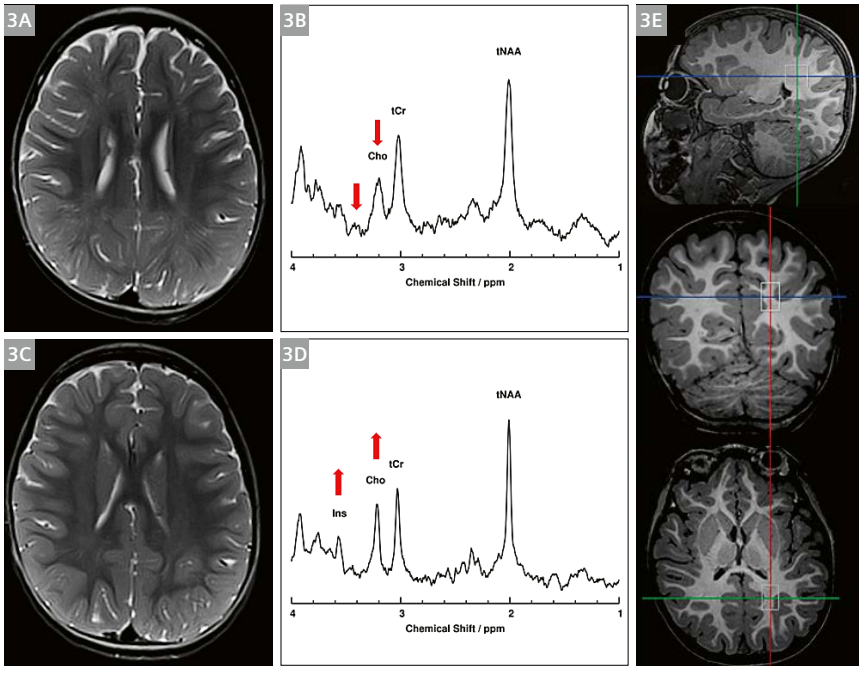

3 **^{1}H-MR spectroscopy in a girl with cerebral folate deficiency** (caused by cerebral folate transporter α deficiency).

(3A, B) (Age 5 years): (3A) Axial T2-weighted image depicts hypomyelination. (3B) White matter (WM) spectrum reveals absence of an Ins peak and a significantly reduced Cho peak.

(3C, D) After two years of folinic acid therapy (age 7 years): (3C) Axial T2-weighted image shows significant advancement of myelination now appropriate for the age. (3D) Ins and Cho peaks have increased, indicating normalization of brain metabolism under therapy.

(3E) Voxel placement in left parieto-occipital WM. Note mild cerebellar atrophy.

Parameters see Fig. 1.

velocity maps can be viewed on the scanner monitor during the measurement.

For CSF flow studies, the scan parameters were optimized to provide images with an in-plane resolution of 0.75 × 0.75 mm^2 and a temporal resolution of 125 ms. The other parameters are TR / TE = 5.68 / 4.61 ms, a flip angle of 10°, and slice thickness of 5 mm. The flow-encoded and flow-compensated acquisitions were each acquired with 11 radial spokes. Quantitative and qualitative analyses of real-time PC flow MRI measurements were performed using CaFur prototype software (Fraunhofer Mevis, Bremen, Germany) especially designed for automatic segmentation tasks using real-time image series [21].

Acknowledgments

We gratefully acknowledge the support and assistance of Prof. Jens Frahm Ph.D. and Jost Kollmeier Ms Sci from the Biomedizinische NMR at the Max-Planck-Institut für biophysikalische Chemie, Goettingen, as well as of Ilona Pfahlert, medical technician, and Dr. Peter Dechent Ph.D. from the MR-Research in Neurology and Psychiatry, University Medical Center, Goettingen.

continued on page 62

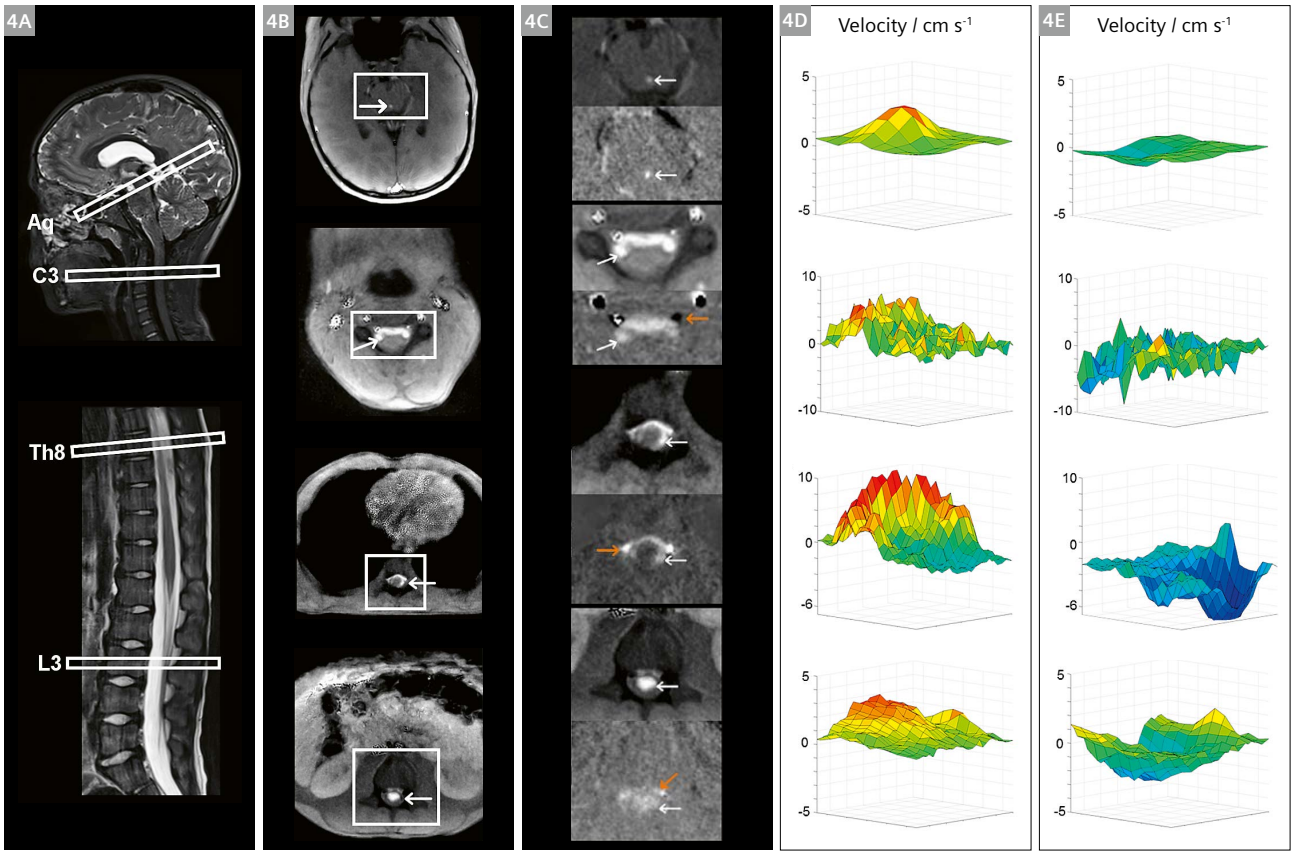

4 **Real-time PC flow MRI of CSF dynamics in spinal canal and aqueduct** (healthy control (age 8.2 years))

(4A) Lower image: Midline sagittal T2-weighted images of lumbar and lower thoracic spine; Upper image: cervical spine and brain. White rectangles indicate placement of ROIs.

(4B): Magnitude images of all ROIs during forced inspiration. Note bright flow signal in the CSF spaces at all levels (white arrows). White rectangles indicate magnified sections displayed in column (C).

(4C): Magnified sections of the magnitude images (upper part) and corresponding velocity maps (lower part) indicating upward fluid flow (bright signal; white arrows) in CSF spaces. Note the dark signal in spinal epidural veins at C3 (orange arrow) reflecting downward venous blood flow (note also phase wrap in right vein). Spinal epidural veins are also visible at Th8 and L3 (orange arrows) showing upward blood flow (bright signal).

(4D): Selected CSF flow velocity profiles during forced inspiration and

(4E): during forced expiration. Color code ranges from -10 to 10 cm/s; blue and red represent minimum and maximum velocities respectively.

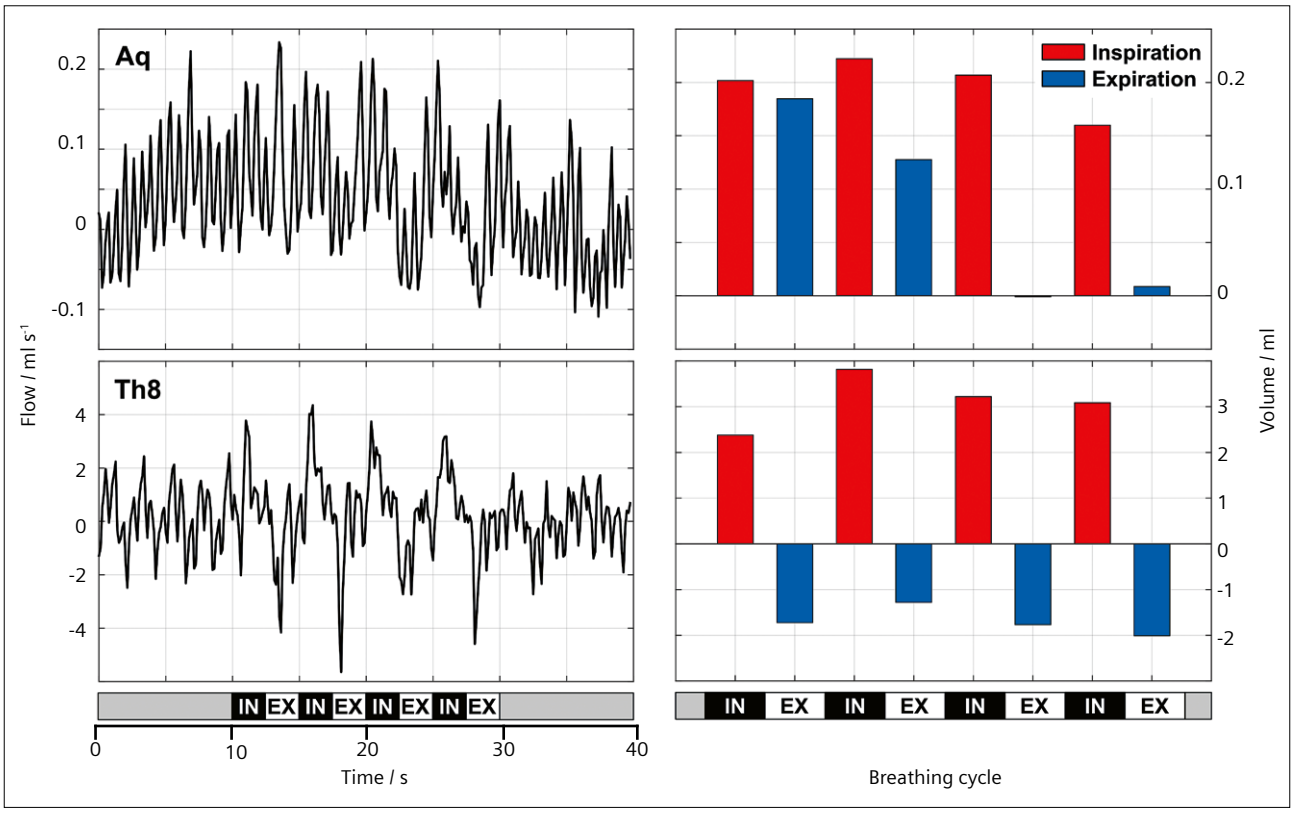

5 **CSF flow and flow volumes before, during, and after 20 sec of forced breathing** (healthy control (age 8.2 years))

Left column: CSF flow in aqueduct (Aq) (upper part) and at thoracic level 8 (Th8) (lower part) for a 40-s period comprising 20 s of forced breathing (see protocol at bottom). Onset of forced inspiration leads to distinct increase in upward CSF flow at both positions, which is reversed during expiration. Cardiac-related flow represents a continuous component of lower amplitude. Note the much smaller flow scale (mL s^{-1}) for the delicate Aq.

Right column: Corresponding CSF flow volumes for every forced inspiration (2.5 s) and expiration (2.5 s) (see breathing cycles at bottom). Inspiratory flow volumes (red) refer to upward motions (positive values) in the Aq (upper part) and at Th8 (lower part). Expiratory flow volumes (blue) were directed downward (negative values) at Th8. Of note are the small flow volumes in the Aq and the continuous positive values pointing to upward (towards the 3rd ventricle) fluid movement over the whole respiratory cycle.

Aq: aqueduct; Th8: thoracic level 8; IN: inspiration; EX: expiration.

[1]MR scanning has not been established as safe for imaging fetuses and infants less than two years of age. The responsible physician must evaluate the benefits of the MR examination compared to those of other imaging procedures. Note: This disclaimer does not represent the opinion of the authors.

[2]The information shown herein refers to products of 3rd party manufacturers and thus are in their regulatory responsibility. Please contact the 3rd party manufacturer for further information.

References

1 Dreha-Kulaczewski SF, Helms G, Dechent P, Hofer S, Gartner J, Frahm J. Serial proton MR spectroscopy and diffusion tensor imaging in infantile Balo's concentric sclerosis. Neuroradiology. 2009 Feb;51(2):113-21.

2 Kreis R, Ernst T, Ross BD. Development of the human brain: in vivo quantification of metabolite and water content with proton magnetic resonance spectroscopy. Magn Reson Med. 1993 Oct;30(4):424-37.

3 Brockmann K, Bjornstad A, Dechent P, Korenke CG, Smeitink J, Trijbels JM, et al. Succinate in dystrophic white matter: a proton magnetic resonance spectroscopy finding characteristic for complex II deficiency. Ann Neurol. 2002 Jul;52(1):38-46.

4 Henneke M, Dreha-Kulaczewski S, Brockmann K, van der Graaf M, Willemsen MA, Engelke U, et al. In vivo proton MR spectroscopy findings specific for adenylosuccinate lyase deficiency. NMR Biomed. 2010 Jun;23(5):441-5.

5 Dreha-Kulaczewski S, Kalscheuer V, Tzschach A, Hu H, Helms G, Brockmann K, et al. A Novel SLC6A8 Mutation in a Large Family with X-Linked Intellectual Disability: Clinical and Proton Magnetic Resonance Spectroscopy Data of Both Hemizygous Males and Heterozygous Females. JIMD Rep. 2014;13:91-9.

6 Almeida LS, Verhoeven NM, Roos B, Valongo C, Cardoso ML, Vilarinho L, et al. Creatine and guanidinoacetate: diagnostic markers for inborn errors in creatine biosynthesis and transport. Mol Genet Metab. 2004 Jul;82(3):214-9.

7 Steinfeld R, Grapp M, Kraetzner R, Dreha-Kulaczewski S, Helms G, Dechent P, et al. Folate receptor alpha defect causes cerebral folate transport deficiency: a treatable neurodegenerative disorder associated with disturbed myelin metabolism. Am J Hum Genet. 2009 Sep;85(3):354-63.
8 Frahm J, Michaelis T, Merboldt KD, Hanicke W, Gyngell ML, Chien D, et al. Localized NMR spectroscopy in vivo. Progress and problems. NMR Biomed. 1989 Dec;2(5-6):188-95.
9 Provencher SW. Estimation of metabolite concentrations from localized in vivo proton NMR spectra. Magn Reson Med. 1993 Dec;30(6):672-9.
10 Enzmann DR, Pelc NJ. Normal flow patterns of intracranial and spinal cerebrospinal fluid defined with phase-contrast cine MR imaging. Radiology. 1991 Feb;178(2):467-74.
11 Greitz D. Cerebrospinal fluid circulation and associated intracranial dynamics. A radiologic investigation using MR imaging and radionuclide cisternography. Acta Radiol Suppl. 1993;386:1-23.
12 Greitz D. Radiological assessment of hydrocephalus: new theories and implications for therapy. Neurosurg Rev. 2004 Jul;27(3):145-65; discussion 66-7.
13 Dreha-Kulaczewski S, Joseph AA, Merboldt KD, Ludwig HC, Gartner J, Frahm J. Inspiration is the major regulator of human CSF flow. J Neurosci. 2015 Feb 11;35(6):2485-91.
14 Chen L, Beckett A, Verma A, Feinberg DA. Dynamics of respiratory and cardiac CSF motion revealed with real-time simultaneous multi-slice EPI velocity phase contrast imaging. Neuroimage. 2015 Nov 15;122:281-7.
15 Dreha-Kulaczewski S, Joseph AA, Merboldt KD, Ludwig HC, Gartner J, Frahm J. Identification of the Upward Movement of Human CSF In Vivo and its Relation to the Brain Venous System. J Neurosci. 2017 Mar 1;37(9):2395-402.
16 Joseph A, Kowallick JT, Merboldt KD, Voit D, Schaetz S, Zhang S, et al. Real-time flow MRI of the aorta at a resolution of 40 msec. J Magn Reson Imaging. 2014 Jul;40(1):206-13.
17 Joseph AA, Merboldt KD, Voit D, Zhang S, Uecker M, Lotz J, et al. Real-time phase-contrast MRI of cardiovascular blood flow using undersampled radial fast low-angle shot and nonlinear inverse reconstruction. NMR Biomed. 2012 Jul;25(7):917-24.
18 Uecker M, Zhang S, Voit D, Karaus A, Merboldt KD, Frahm J. Real-time MRI at a resolution of 20 ms. NMR Biomed. 2010 Oct;23(8):986-94.
19 Tan Z, Roeloffs V, Voit D, Joseph AA, Untenberger M, Merboldt KD, et al. Model-based reconstruction for real-time phase-contrast flow MRI: Improved spatiotemporal accuracy. Magn Reson Med. 2017 Mar;77(3):1082-93.
20 Schaetz S, Voit D, Frahm J, Uecker M. Accelerated Computing in Magnetic Resonance Imaging: Real-Time Imaging Using Nonlinear Inverse Reconstruction. Comput Math Methods Med. 2017;2017:3527269.
21 Chitiboi T, Hennemuth A, Tautz L, Huellebrand M, Frahm J, Linsen L, Hahn H. Context-based segmentation and analysis of multi-cycle real-time cardiac MRI. IEEE Int Symp Biomed Imaging. 2014:943-6.

Contact

Steffi Dreha-Kulaczewski M.D.
Department of Pediatrics and Adolescent Medicine
Division of Pediatric Neurology
University Medical Center Göttingen
37075 Göttingen
Germany
Tel.: +49 551 39 22570
sdreha@gwdg.de

We are looking forward to hearing from you

Founded in 1993 the MAGNETOM Flash magazine has been around almost as long as MAGNETOM MRI scanners.

In times of online media and digitalization we would value your feedback to ensure that the magazine continues to fit your interests and professional needs.

Please take a moment to complete a brief reader survey at
www.siemens.com/magnetom-world

Case Series: Utilization of the Pediatric 16 Coil for 1.5T and 3T Systems

Bac Nguyen, RT (R) (MR)

Oslo University Hospital, Rikshospitalet, Oslo, Norway

Introduction

At our institution we have a high rate of pediatric cases which can be both difficult and challenging. As a University Hospital, we perform pediatric imaging[1] for a wide range of indications including the brain, spine, heart, abdomen, pelvis and whole-body and the imaging of children can involve either general anesthesia or the feed and wrap technique. In all cases, fast and robust workflows for high-resolution imaging are required. In this article, we would like to share our experiences with the Pediatric 16 coil on both 1.5T and 3T to demonstrate what it can help achieve. We had acquired the coils in December 2015 for our 1.5T MAGNETOM Aera and 3T MAGNETOM Skyra. This gives us the opportunity to easily setup our program either with anesthesia or as feed and wrap. It simplifies the setup of our busy daily program and helps us to avoid any dead- or delay time that may arise from these cases.

The Pediatric 16 is a 16-channel receive coil with 16 integrated preamplifiers for head and neck imaging of new-borns and infants up to 18 months of age[1]. There are 13 channels for head imaging and 3 channels for the neck, and these channels can be used independently. The coil is equipped with DirectConnect technology and it connects directly into the scanner table with no connecting cables. Other special features include a recess in the anterior coil for easy positioning of intubation tubes, and a 4 cm aperture at the top of the coil for better ventilation. As a Tim4G Matrix coil, the Pediatric 16 can be combined flexibly with other coils including the Spine, Body, Flex and Special Purpose coils for whole CNS and whole-body imaging and this opens many opportunities for the imaging of infants and small children[1].

While this coil is intended for infants from 0–18 months, we have experienced a few cases where children did not fit. For instance, a 1-year-old infant with hydrocephalus may not fit due to the size of the head. Conversely, a 20-month-old infant may fit perfectly. Obviously, infants vary in size and this needs to be checked in each case.

In our experience, compared to the Head/Neck 20 this dedicated pediatric coil provides much better performance at the same scan times due to the fact that the coil fits more closely to the heads of small infants. Cases 1–4 illustrate the fast and high-resolution imaging we can achieve with this coil across infants of varying ages.

Along with Pediatric 16 comes a cradle with two straps and cushions to help with fixation. This cradle was designed to enable the preparation of infants away from the scanner and to provide safe and efficient transport of the infant to the scanner. This cradle has proven itself to be a true workflow enhancer at our institution, especially for our feed and wrap examinations. Firstly, we can plan our exam in good time with other departments so the patient can come to us in a position ready for examination. We do not lose time preparing the baby at the scanner, and we find that most babies lie much more still when everything is ready. All we need to do at our department is a final check for safety aspects (puls oximetry, ECG etc.). For children requiring only brain or brain and spine scans, the cradle can be slid easily into the Pediatric 16 coil (without the need to remove the anterior part) and the patient can be put into the scanner without further coil management. If the baby requires whole-body imaging, the Body coil can be easily placed on the child. This cradle has high edges, which means that coils can be put directly on these edges for stabilization, rather than laying them directly on top of the child. There are also cases where smaller coils would be needed, such as the small Flex coil. We can position this inside the edges along with cushions. This is much easier compared to the situation where the patient is lying directly on the table with positioning sandbags along the sides. Our use of the cradle has enabled faster, robust and more comfortable examinations for the child so much so that we use the cradle even for patients requiring only body or cardiac imaging.

Cases 5 and 6 are illustrations of our patients who have undergone liver and cardiac examinations where the cradle has helped with the workflow.

[1] *MR scanning has not been established as safe for imaging fetuses and infants less than two years of age. The responsible physician must evaluate the benefits of the MR examination compared to those of other imaging procedures. Note: This disclaimer does not represent the opinion of the authors.*

Case 1

10-day-old infant[1] with left-sided seizure and suspicion of cerebral infarct. The patient weight was approximately 3 kg. Imaging was performed on a 3T MAGNETOM Skyra with the Pediatric 16 coil, as a feed and wrap procedure. There were no findings.

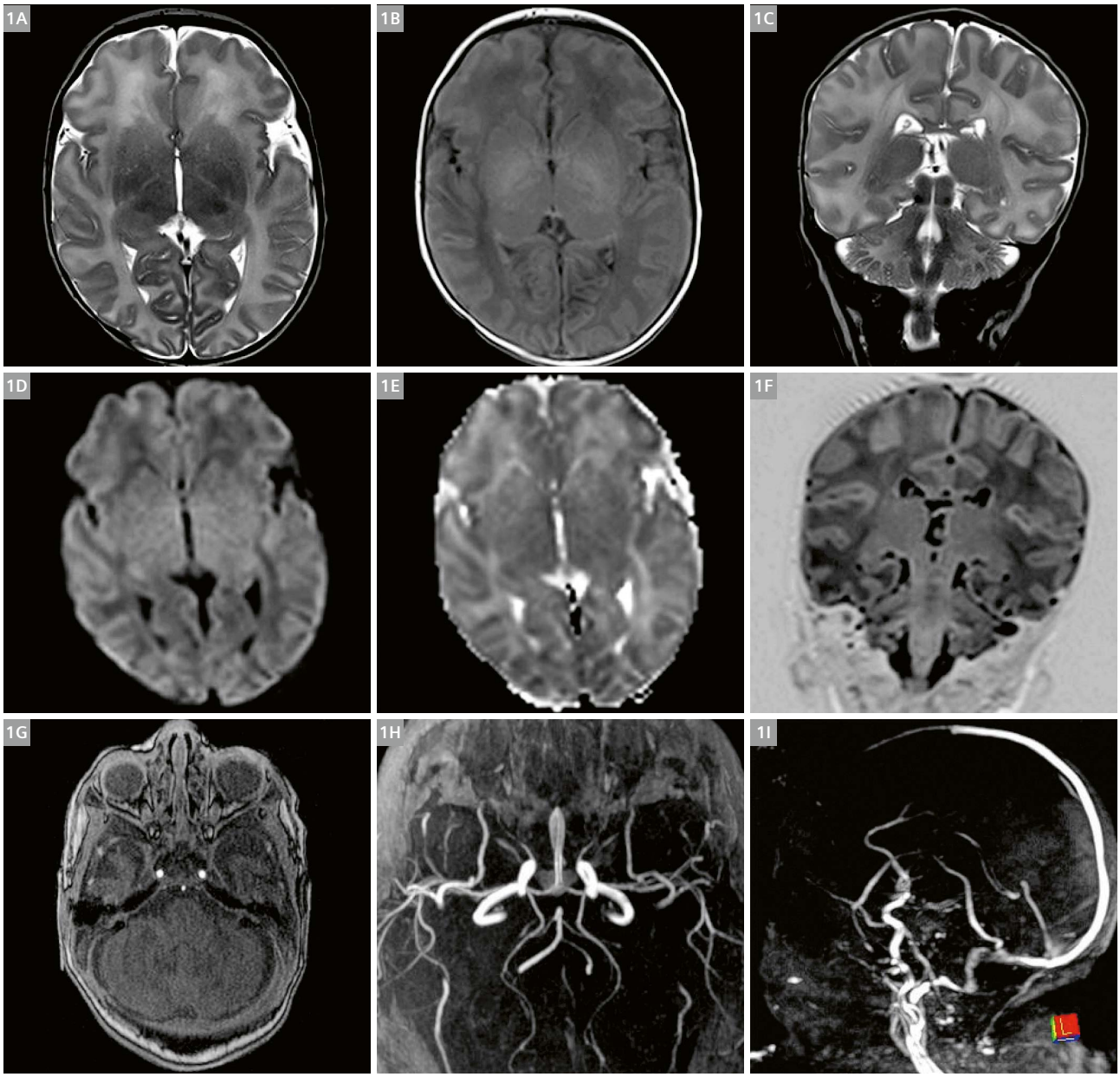

1 **(1A)** T2w TSE transversal, voxel 0.49 x 0.49 x 3 mm, TA: 2 min 12 sec.
(1B) T1w TSE transversal, voxel 0.74 x 0.74 x 3 mm, TA: 2 min 32 sec.
(1C) T2w TSE coronal, voxel 0.49 x 0.49 x 3 mm, TA: 2 min 12 sec.
(1D) Diffusion-weighted imaging (DWI) RESOLVE, b-value 1000 (acquired b0, b500 and b1000), voxel 1.5 x 1.5 x 4 mm, TA: 2 min 30 sec.
(1E) DWI apparent diffusion coefficient (ADC) map.
(1F) T1w SPACE IR coronal, voxel 1.17 x 1.17 x 0.9 mm, TA: 2 min 16 sec.
(1G) Time-of-flight (TOF) transversal, voxel 0.5 x 0.5 x 0.5 mm, TA: 3 min 42 sec.
(1H) TOF maximum intensity projection (MIP).
(1I) Phase contrast (PC) MIP sagittal, voxel 1.3 x 1 x 1 mm, TA: 4 min 37 sec.

Case 2

1-year-old male infant[1] with increasing frequency of epileptic seizures, hemiparesis, fever and a cold. The patient's weight is approximately 10 kg. Imaging was performed on a 3T MAGNETOM Skyra with the Pediatric 16 in combination with the Spine 32. The exam was performed under general anesthesia. The report for this patient indicated slight hypomyelination with a possible small syrinx in the distal medulla.

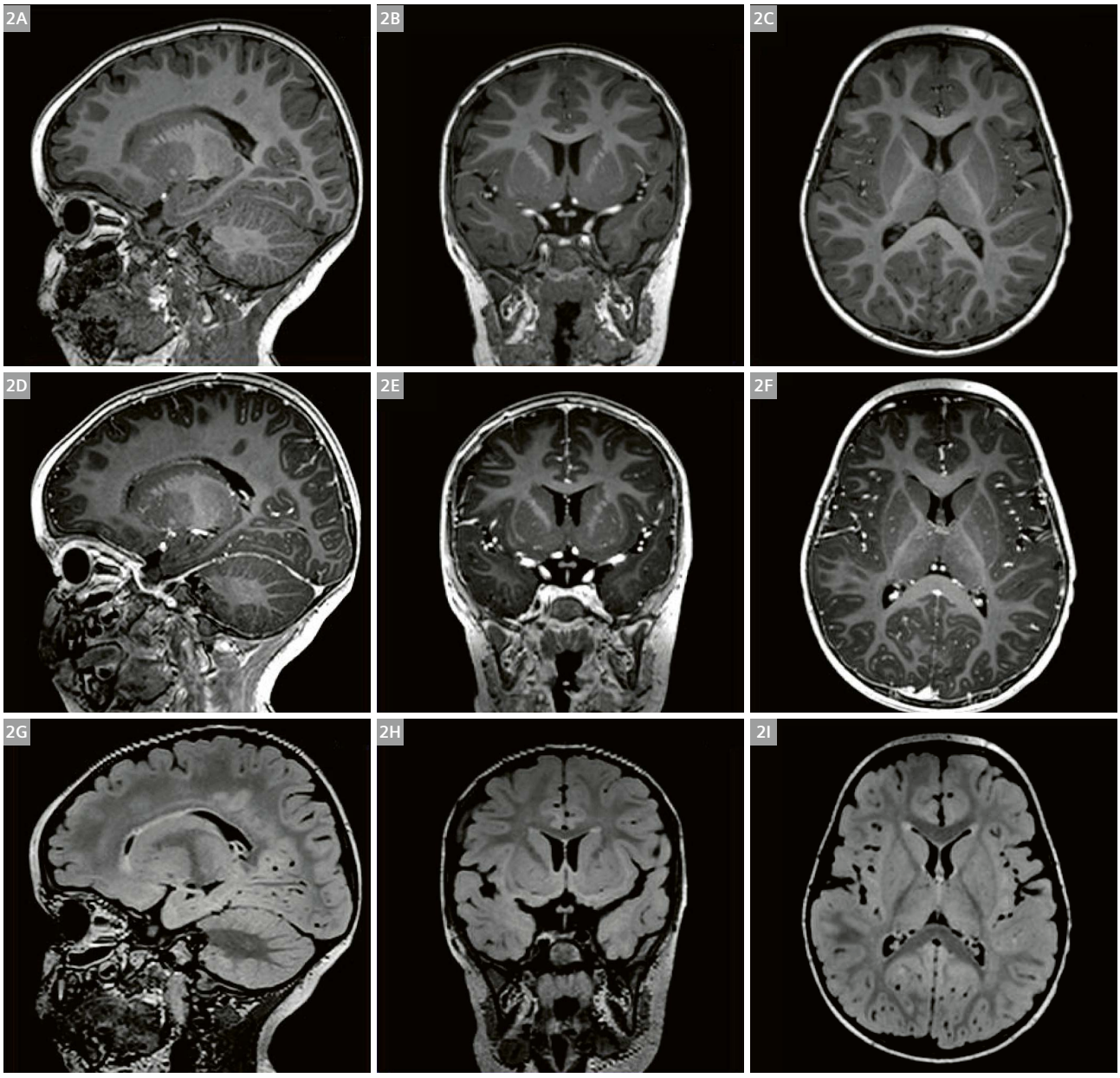

2 **(2A)** T1w 3D MPRAGE acquired in sagittal plane without contrast medium, voxel 1 x 1 x 1 mm, TA: 5 min 5 sec.
(2B) T1w 3D MPRAGE 1 mm coronal multi-planar reconstruction (MPR) without contrast.
(2C) T1w 3D MPRAGE 1 mm transversal MPR without contrast.
(2D) T1w 3D MPRAGE 1 mm acquired in sagittal plane with contrast medium, voxel 1 x 1 x 1 mm, TA: 5 min 5 sec.
(2E) T1w 3D MPRAGE 1 mm coronal MPR with contrast medium.
(2F) T1w 3D MPRAGE 1 mm transversal MPR with contrast medium.
(2G) T2w 3D SPACE FLAIR acquired in sagittal plane, voxel 1 x 1 x 1 mm, TA: 5 min 24 sec.
(2H) T2w 3D SPACE FLAIR 1 mm coronal MPR.
(2I) T2w 3D SPACE FLAIR 1 mm transversal MPR.

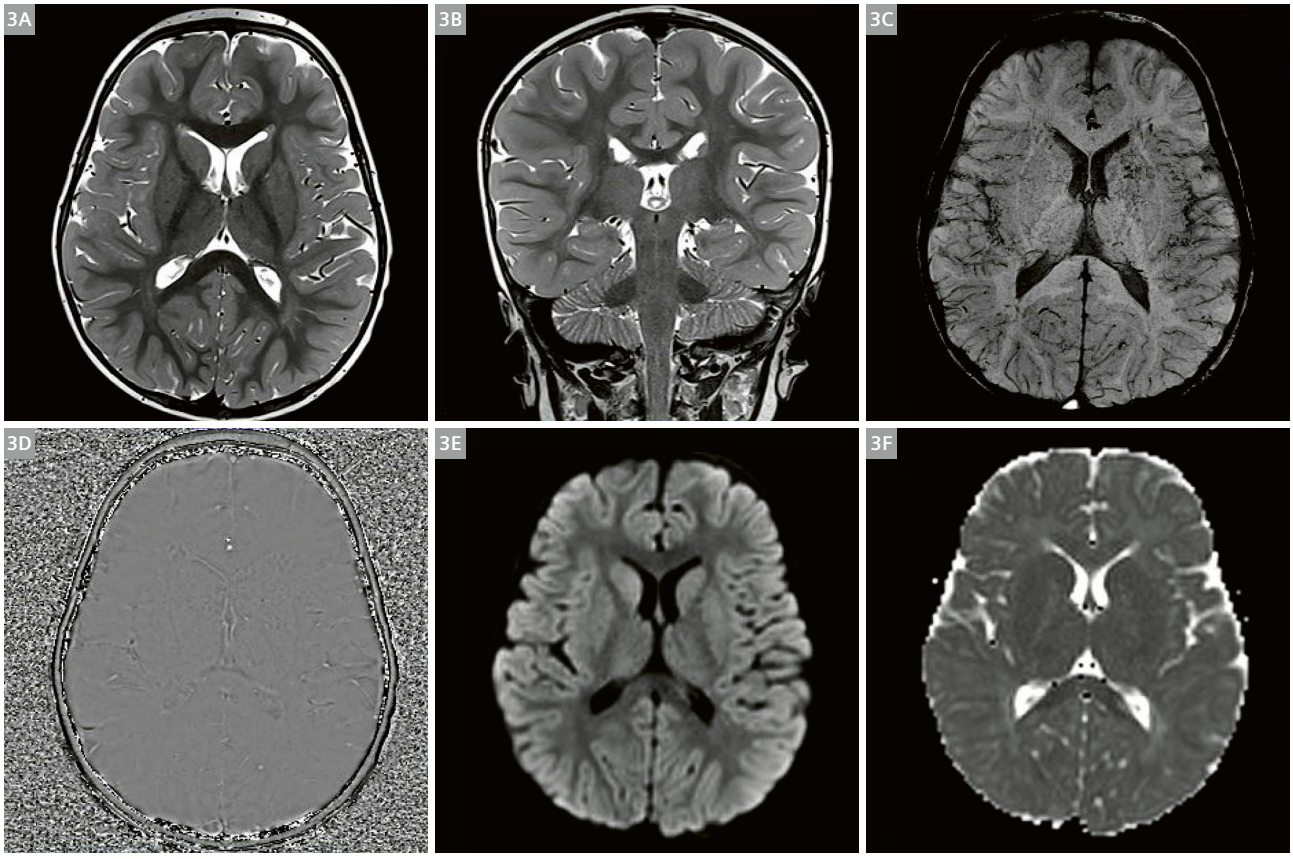

3 **(3A)** T2w TSE transversal, voxel 0.2 x 0.2 x 2 mm, TA: 4 min 32 sec.
(3B) T2w TSE coronal, voxel 0.2 x 0.2 x 2 mm, TA: 4 min 32 sec.
(3C) Susceptibility-weighted imaging (SWI) transversal minIP image, voxel 0.6 x 0.5 x 1.4 mm, TA: 5 min.
(3D) SWI Phase image.
(3E) DWI RESOLVE, b-value 1000 (acquired b0, b500 and b1000), voxel 1.5 x 1.5 x 4 mm, TA: 4 min 21 sec.
(3F) DWI ADC map.

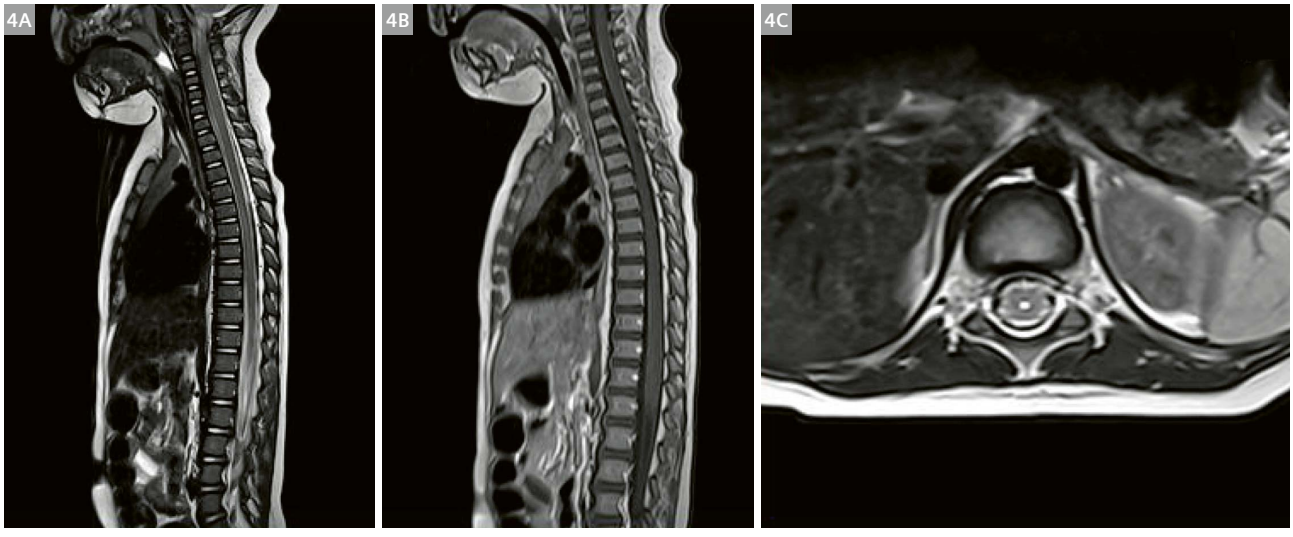

4 **(4A)** T2w TSE sagittal, voxel 0.9 x 0.8 x 2 mm, TA: 2 min 58 sec.
(4B) T1w TSE sagittal, voxel 1 x 0.9 x 2 mm, TA: 3 min 42 sec.
(4C) T2w TSE transversal, voxel 0.8 x 0.6 x 3 mm, TA: 3 min 10 sec.

Case 3

A 2-week-old infant[1] with increased head circumference with suspicion of hydrocephalus. The patient's weight is approximately 4.8 kg. Imaging was performed on the 1.5T MAGNETOM Aera with the Pediatric 16, as a feed and wrap procedure. The report indicated that this infant might have BESS (benign enlargement of the subarachnoid spaces in infancy).

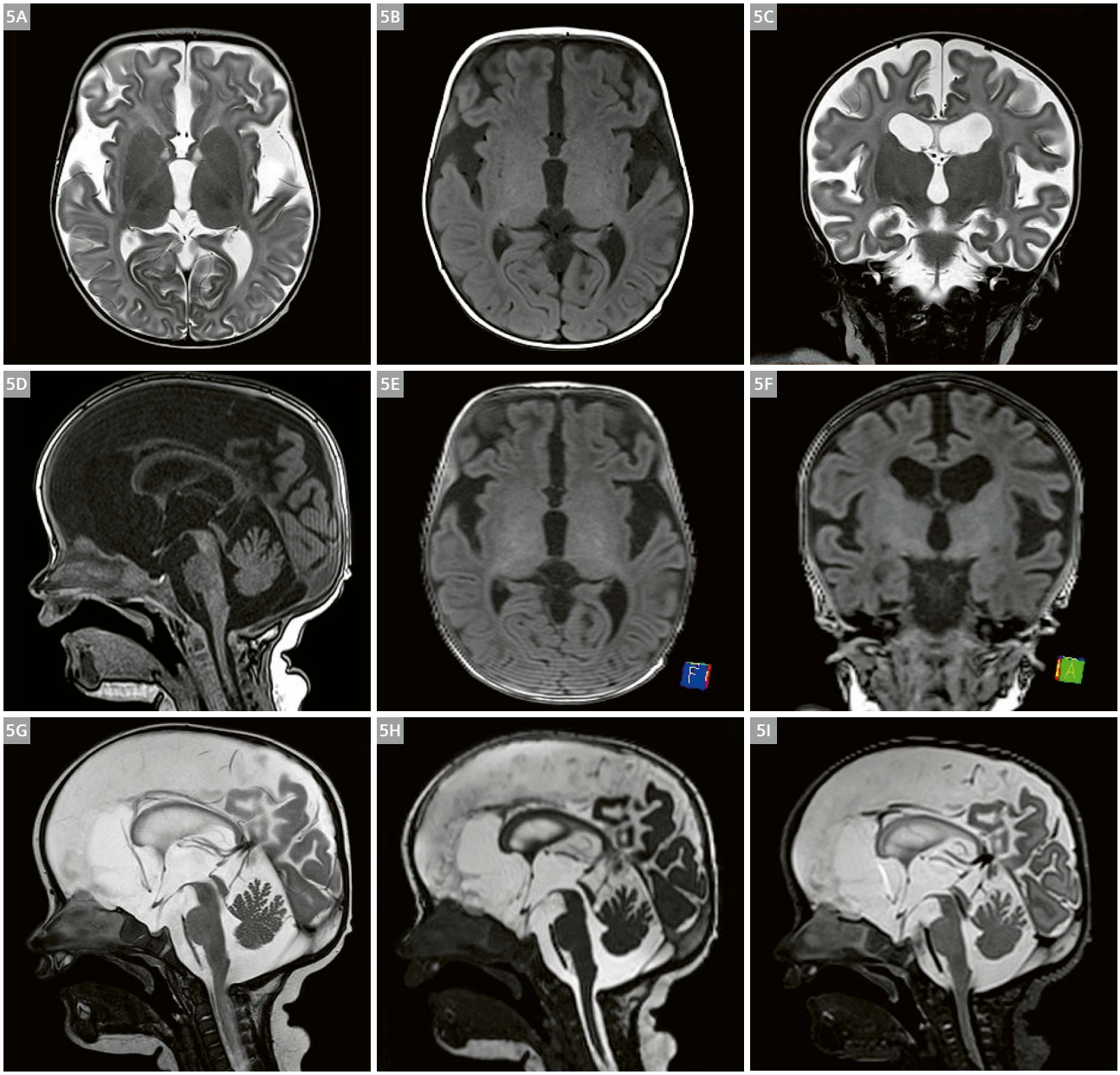

5 **(5A)** T2w TSE transversal, voxel 0.4 x 0.4 x 4 mm, TA: 4 min 32 sec.
(5B) T1w TSE transversal, voxel 0.7 x 0.7 x 4 mm, TA: 3 min 48 sec.
(5C) T2w TSE coronal, voxel 0.4 x 0.4 x 4 mm, TA: 4 min 32 sec.
(5D) T1w 3D MPRAGE, voxel 1 x 1 x 1 mm, TA: 4 min 23 sec.
(5E) T1w 3D MPRAGE 1 mm transversal MPR.
(5F) T1w 3D MPRAGE 1 mm coronal MPR.
(5G) T2w TSE sagittal, voxel 0.5 x 0.4 x 3 mm, TA: 4 min 19 sec.
(5H) CISS sagittal, voxel 0.9 x 0.9 x 0.7 mm, TA: 4 min 8 sec.
(5I) T2w 3D SPACE, voxel 1 x 1 x 1 mm, TA: 4 min 3 sec.

Case 4

2-year-old-child[1] with neuroblastoma of the neck. The patient has been imaged previously with both ultrasound and MR, but has not yet been treated. The patient's weight was approximately 6.8 kg. Imaging was performed on a 3T MAGNETOM Skyra with the Pediatric 16 in combination with Spine 32. The examination was performed under general anesthesia. The report indicated that central parts of the tumor show less contrast-enhancement compared to an earlier MRI exam, and tumor measurements remain the same.

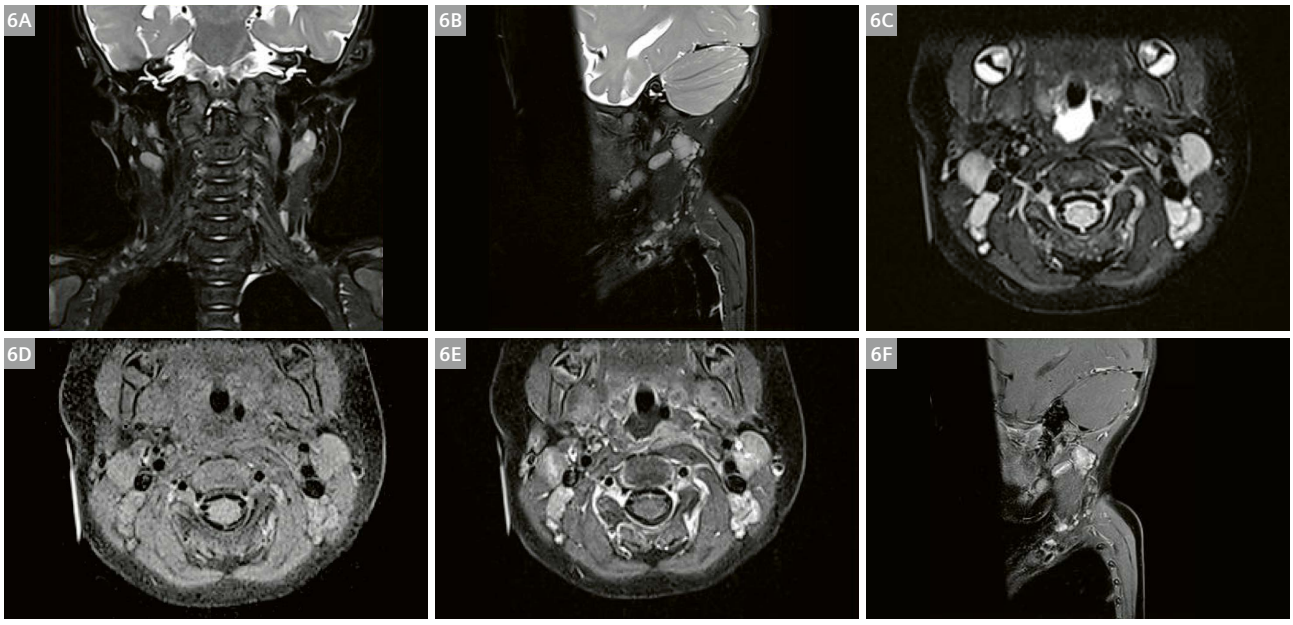

6 **(6A)** T2w TSE Dixon water only, voxel 0.7 x 0.7 x 2.5 mm, TA: 3 min 6 sec.
(6B) T2w TSE Dixon water only, voxel 0.7 x 0.7 x 2.5 mm, TA: 3 min 9 sec.
(6C) T2w TSE Dixon water only, voxel 0.7 x 0.7 x 2.5 mm, TA: 3 min 9 sec.
(6D) T1w TSE Dixon water only, voxel 0.5 x 0.5 x 2.5 mm, TA: 4 min 40 sec precontrast.
(6E) T1w TSE Dixon water only, voxel 0.5 x 0.5 x 2.5 mm, TA: 4 min 40 sec postcontrast.
(6F) T1w TSE Dixon water only, voxel 0.5 x 0.5 x 2.5 mm, TA: 4 min 23 sec postcontrast.

Case 5

A 3-week-old infant[1] with Trisomy 21 with a focal lesion seen on the left liver lobe with ultrasound and suspicion of malignancy. The patient's weight was approximately 5 kg. The examination was performed on a 1.5T MAGNETOM Aera with the Spine 32 in combination with the Flex 4 Small. The cradle of the Pediatric 16 coil was used for the preparation, transport and positioning of the patient for imaging. The examination was performed as a feed and wrap procedure. The report indicated the presence of a hypervascular tumor in the left liver lobe that could be a hemangioma.

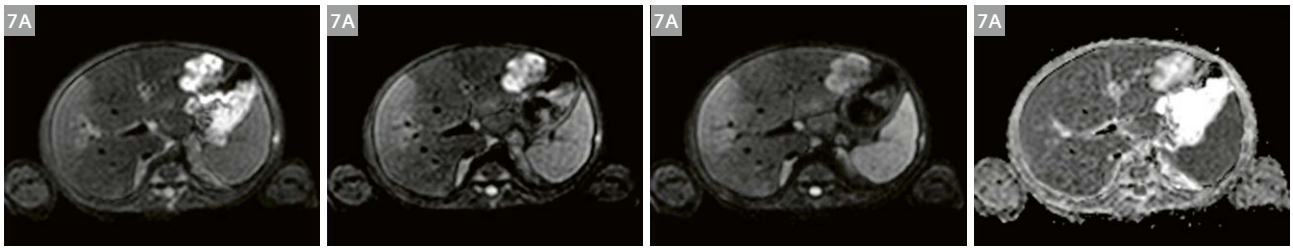

7 DWI free-breathing
(7A) b50, **(7B)** b400, **(7C)** b800, **(7D)** ADC map
voxel 2 x 2 x 3 mm, TA: 3 min.

Case continued on page 70.

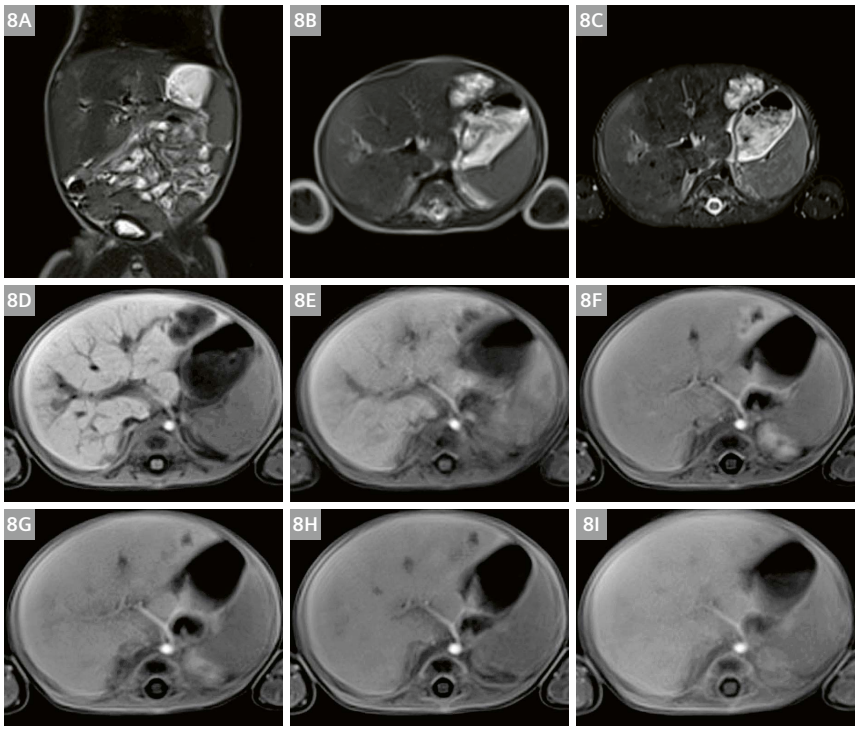

8 **(8A)** T2w HASTE coronal respiratory triggering, voxel 1.3 x 1.3 x 3.5 mm, TA: 44 sec.
(8B) T2w HASTE transversal respiratory triggering, voxel 1.3 x 1.3 x 3.5 mm, TA: 58 sec.
(8C) T2w 3D SPACE with SPAIR fatsat and respiratory triggering, voxel 1 x 1 x 1 mm, TA: approx. 5 min 20 sec.
(8D) T1w StarVIBE precontrast, voxel 1 x 1 x 3 mm, TA: 2 min 20 sec.
(8E–I) Multiple T1w StarVIBE images captured continuously after injection of contrast medium.

Case 6

A 2-year-old child[1] with congenital heart disease. The patient has DORV (double outlet right ventricle) and TGA (transposition of the great arteries). The patient was referred with the question of possible hypertrophy and for pre-operative imaging. The patient's weight was approximately 10 kg. The examination was performed on a 1.5T MAGNETOM Aera with the Spine 32 in combination with the Flex 4 Small. The cradle of the Pediatric 16 coil was used for the preparation, transport and positioning of the patient for imaging. The examination was performed under general anesthesia. The report confirmed the known clinical conditions with no change to anatomy. No hypertrophy was found.

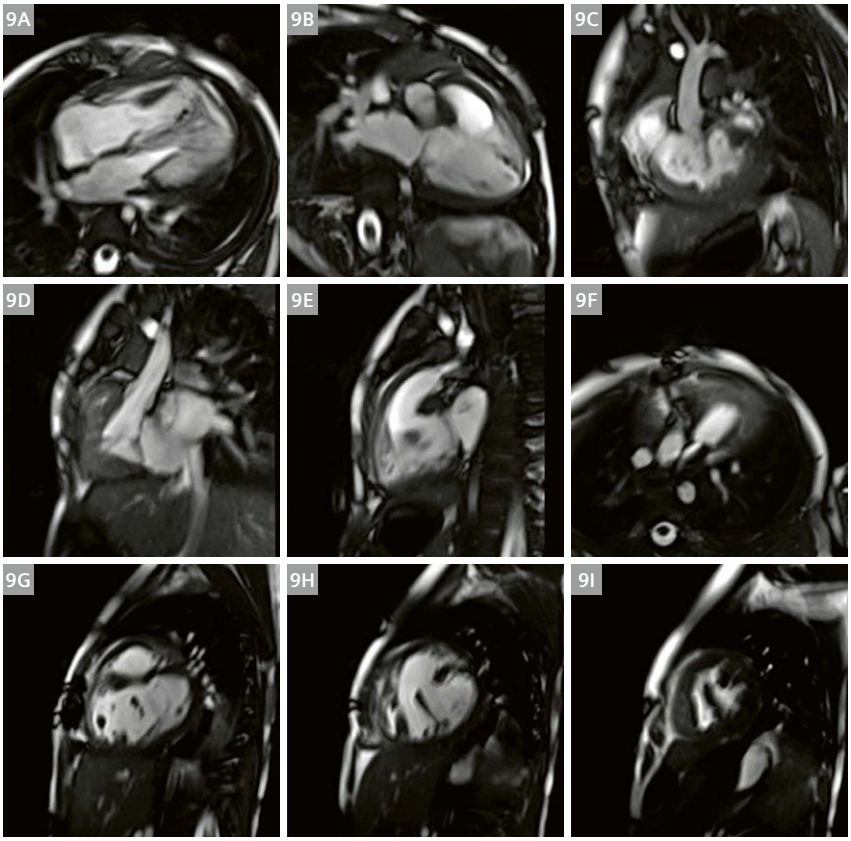

9 All images are CINE TrueFISP done as free-breathing, voxel 1.2 x 1 x 5 mm, TA: 30 sec.

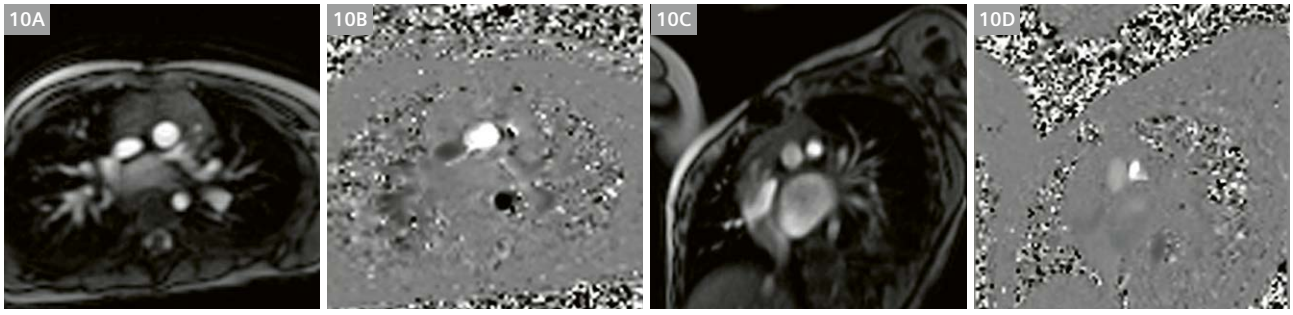

10 **(10A, B)** Flow aorta free-breathing (magnitude and phase images) VENC 120 cm/sec, voxel 1.7 x 1.5 x 5 mm, TA: 40 sec.
(10C, D) Flow pulmonary free-breathing (magnitude and phase images) VENC 400 cm/sec, voxel 1.7 x 1.5 x 5 mm, TA: 40 sec.

Conclusion

If your site does many pediatric cases, I can definitely recommend this coil. For the head imaging of neonates and small children, the size of the coil provides higher signal-to-noise ratio (SNR) which allows us to achieve better imaging in short scan times. After we started using this coil, we had many more successful feed and wrap exams thanks to the cradle itself. Given the complexity and sensitivity of an MR examination for small infants and children, it makes clinical sense to use a coil that is dedicated to their care. With the significant number of such exams that we perform at our site, the workflow benefits are, for us, innumerous.

Acknowledgments

I would like to thank my good friend and MR mentor Rolf Svendsmark. My fellow colleagues at work, and my friend Lisa Chuah.

References

1 Siemens Healthineers: https://www.healthcare.siemens.com/magnetic-resonance-imaging/options-and-upgrades/coils/pediatric-16
2 Chavhan, G., et al. Diffusion-weighted Imaging in Pediatric Body Imaging: Principles, Technique, and Emerging Applications. Radiographics 2014; 34:E73-E88.
3 Verschuuren, S., et al. Susceptibility-Weighted Imaging of the Pediatric Brain. AJR 2012;198:W440-W449.
4 Mitchell, C., et al. An Approach to Pediatric Liver MRI. AJR 2011; 196:W519-W526.
5 Panigrahy, A., et al. Basic Principles and Concepts Underlaying Recent Advances In MRI of the Developing Brain. Semin Perinatol. 2010 Feb;32(1):3-19.
6 Tong, K.A., et al. Susceptibility- Weighted MR Imaging: A Review of Clinical Applications in Children. AJR 2008.

Contact

Bac Nguyen, RT (R) (MR)
Senior MR Radiographer
Oslo University Hospital,Rikshospitalet
Sognsvannsveien 20
0372 Oslo, Norway
Phone: +47 97702111
og_23@hotmail.com

MR Total Tumor Load – First Clinical Experience in Pediatric Oncology Patients

Ilias Tsiflikas, M.D.[1]; Robert Grimm, Ph.D.[2]; Jürgen F. Schäfer, M.D.[1]

[1]Pediatric Radiology, Department of Diagnostic and Interventional Radiology, University Hospital of Tübingen, Tübingen, Germany
[2]Siemens Healthineers, Erlangen, Germany

Abstract

The *syngo*.via Frontier MR Total Tumor Load application[1] comes with benefits in pediatric oncology evaluation not only in cases of metastatic bone disease but also in solid tumors, and could further help to establish DWI as a prognostic factor in the assessment of tumor therapy.

Introduction

In recent years, advancements in MR techniques have shortened examination times. This has led to whole-body (WB) MRI becoming essential in staging and managing pediatric oncology patients, where a curative approach is much more common [1]. As a result, an S1 guideline entitled "Whole-body MRI in children" was recently published in Germany [2]. Besides the benefits of radiation-free examinations and excellent tissue characterization, MRI offers the possibility of combining anatomical and functional imaging using techniques such as diffusion-weighted imaging (DWI) for local staging and precise assessments of metastatic spread and total tumor burden at diagnosis as an important factor in planning treatment and predicting outcomes. Several recent studies have compared the diagnostic accuracy of whole-body DWI (WB-DWI) in pediatric lymphomas with conventional methods such as computed tomography (CT), scintigraphic methods, and positron emission tomography (PET). The results are promising [3, 4]. In neuroblastic tumors, DWI has also proved valuable for differentiating malignant and benign tumors based on differences in the apparent diffusion coefficient (ADC), finding higher ADC values in benign tumors like ganglioneuroma than in malignant neuroblastoma [5–7]. Two recent papers further evaluated the role of, respectively, DWI and ADC values as a complementary prognostic marker in neuroblastoma. The findings showed that, under therapy, increasing ADC values were an indicator of good response and prognosis [8, 9]. A limitation of quantitative ADC measurement is the lack of tools to perform efficient evaluation for multifocal disease. The recently introduced *syngo*.via Frontier MR Total Tumor Load prototype application[1] provides a solution that uses threshold-based segmentation on diffusion-weighted images to identify regions of disease and to analyze the overall tumor volume and histogram metrics of the corresponding ADC maps [10]. A pilot study demonstrated excellent inter- and intra-observer agreement using this application in metastatic bone disease [11].

In this report, we will show the diagnostic options for the *syngo*.via Frontier MR Total Tumor Load application in pediatric oncology based on three case studies on Hodgkin lymphoma and stage 4 neuroblastoma respectively.

Case study 1

A 14-year-old girl presented with a supraclavicular swelling first noticed a week previously. Sonography revealed pathological lymph node enlargement suspicious for lymphoma. Biopsy of the lymph node established the diagnosis of classical Hodgkin lymphoma. A WB-PET-MRI using a standardized protocol including WB-DWI on a 3T PET/MR imaging system (Biograph mMR; Siemens Healthcare, Erlangen, Germany) [12] was performed for initial staging and early response after two months.

In the initial staging, cervical, mediastinal, and left axillary lymph node involvement without extranodal manifestations was demonstrated, resulting in a stage 2 classification. The early response study after two cycles of chemotherapy shows a complete metabolic response with only a small residual morphological tumor on the left supraclavicular region (Fig. 1).

The diffusion-weighted images of both examinations were analyzed using a *syngo*.via Frontier MR Total Tumor Load threshold-based segmentation. The pretreatment ADC histogram shows an unimodal distribution of ADC values with high excess kurtosis (Fig. 2). The follow-up study after two months shows significant reduction in volume and a greater spread in the lower ADC range, which is related to partial response.

[1]*syngo.via Frontier is for research only, not a medical device. syngo.via Frontier MR Total Tumor Load is a released research prototype.*

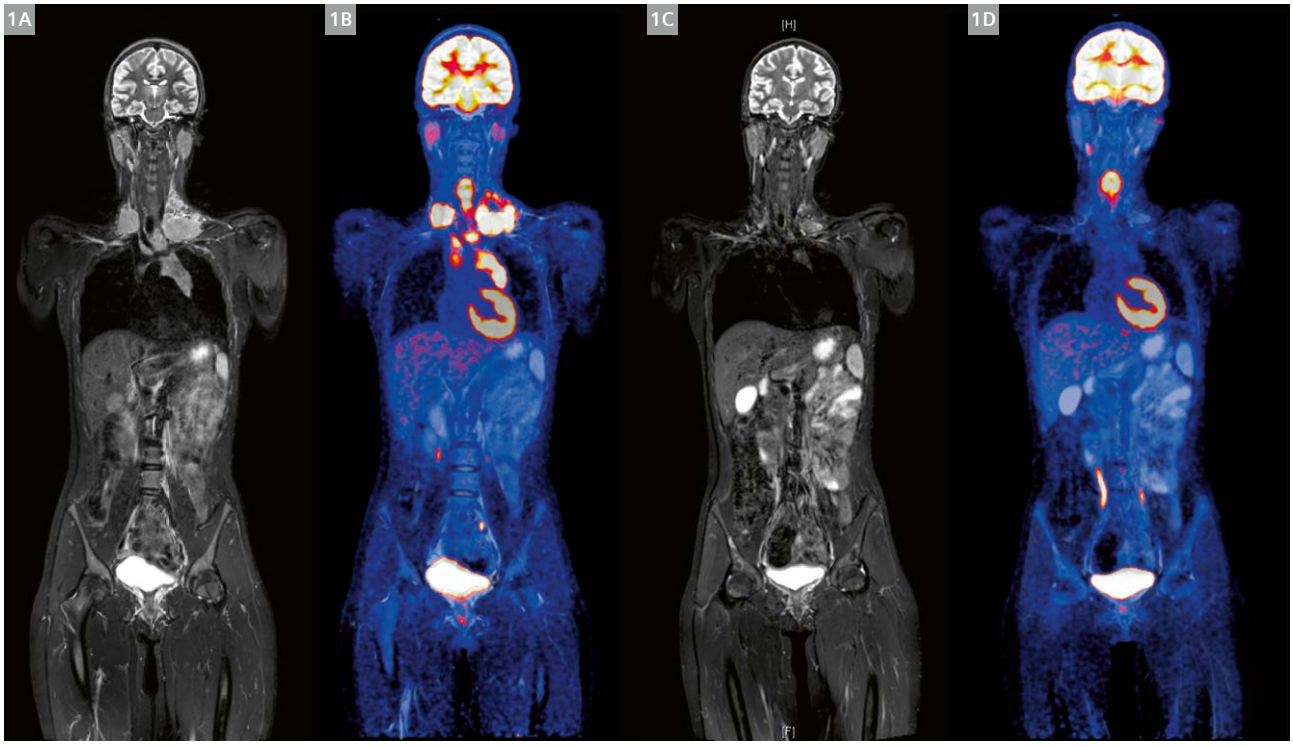

1 **Morphological and functional images of baseline and follow-up PET/MRI**
Baseline examination **(1A, 1B)** shows cervical and mediastinal lymph node involvement in a coronal short tau inversion recovery whole-body sequence (1A) and fused ^{18}F FDG-PET and short tau inversion recovery sequence. In the follow-up examination **(1C, 1D)**, only morphological residuals in the left supraclavicular regions remain.

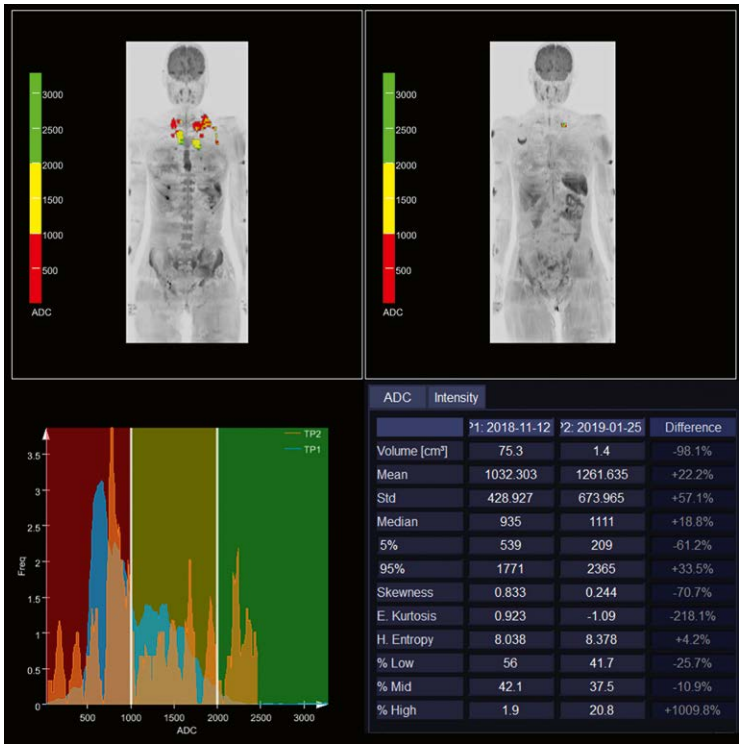

2 **ADC histogram changes over time**
WB tumor load segmentations were undertaken using the *syngo*.via Frontier MR Total Tumor Load software[1]. Besides the reduction in tumor volume, a shift in ADC value distribution between baseline and follow-up examination indicate a partial response.

Case study 2

A 10-month-old[2] boy presented with ptosis that had been noted for four weeks. In addition, a palpable abdominal mass was detected. WB-MRI was performed using our institution's standard protocol as previously published [13] on a 1.5T MR imaging system (MAGNETOM Avanto; Siemens Healthcare, Erlangen, Germany). The examination demonstrated a suprarenal mass on the right side with suspicious mesenteric nodes and hepatic metastases as well as osseous lesions in the left orbit, both proximal humerus and femora, the lumbar vertebra, and the pelvis. Chemotherapy was initiated. In the follow-up study after three months, the osseous lesions show almost complete regression and the suprarenal mass also shows a significant reduction (Fig. 3). Evaluation with *syngo*.via Frontier MR Total Tumor Load shows an unimodal distribution of ADC values with high excess kurtosis (Fig. 4) in both examinations without significant change in the mean ADC value. After surgical resection, the histopathological evaluation of the suprarenal mass revealed that it still contained 90% vital tumor cells.

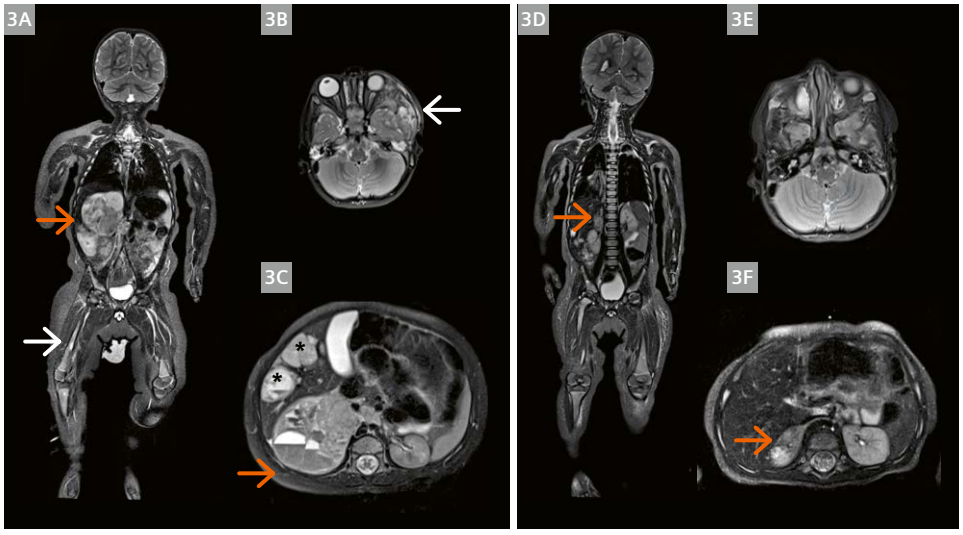

3 Morphological images of baseline and follow-up WB-MRI
The baseline examination **(3A–C)** shows a suprarenal mass in a coronal short tau inversion recovery whole-body sequence **(3A)** and a transversal T2-weighted fat-suppressed sequence (**3C**, orange arrow) with signs of tumor bleeding and necrosis. Osseous metastases are also visible in the right femur (**3A**, white arrow) and left orbit (**3B**, white arrow). The follow-up examination **(3D–F)** shows only residual suprarenal tumor on the right side (**3F**, right-hand arrow).

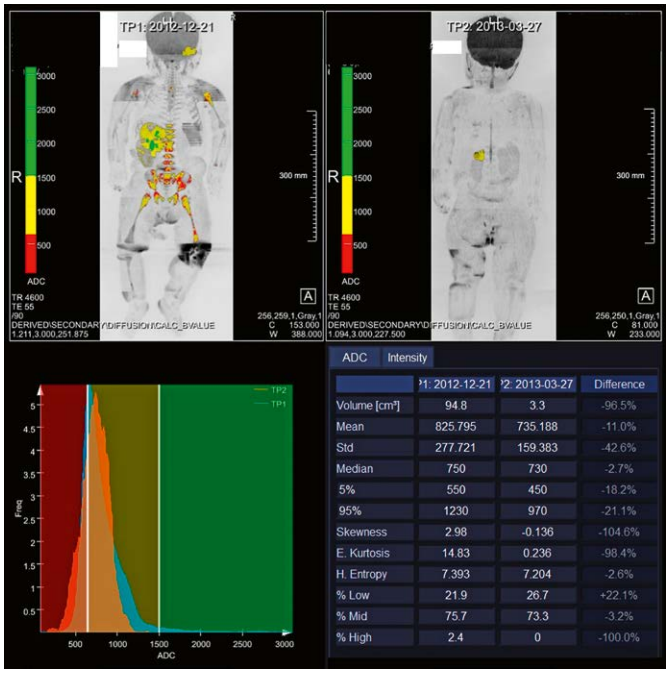

4 ADC histogram changes over time
WB tumor load segmentations indicate a clear reduction in tumor volume is visible, but the distribution of ADC values of tumor mass has not changed significantly between baseline and follow-up examination. This is interpreted as a sign of tumor vitality.

[2] *MR scanning has not been established as safe for imaging fetuses and infants less than two years of age. The responsible physician must evaluate the benefits of the MR examination compared to those of other imaging procedures. Note: This disclaimer does not represent the opinion of the authors.*

Case study 3

A 10-year-old girl presented with a histopathologically proven ganglioneuroma after surgical biopsy at a different hospital. The MRI shows a heterogenous suprarenal tumor on the left side with heterogenous ADC values suspicious for a mixed tumor in the form of a ganglioneuroblastoma (Fig. 5A). Evaluation with *syngo*.via Frontier MR Total Tumor Load shows the heterogeneity of the tumor with a three-modal distribution of ADC values that were measured in the complete tumor (Fig. 5B).

Discussion

The *syngo*.via Frontier MR Total Tumor Load application has been developed for ADC histogram analysis. The main advantage is the possibility to analyze the ADC histogram of the complete tumor volume, rather than just a region of interest (ROI) or volume of interest (VOI). Several case reports show the opportunities for using the application in cases of metastatic bone disease in particular [14–16]. Further, a pilot study demonstrated that the application achieved excellent inter- and intra-observer agreement in metastatic bone disease [11].

MRI plays an important role in pediatric radiology, and this is not only due to its ability to perform radiation-free examinations. A variety of pediatric oncologic diseases have a better prognosis than oncologic diseases in adults, but precise staging and follow-up are crucial for the outcome. In addition to providing morphological information, MRI offers the opportunity to combine functional imaging using DWI. So far, DWI has been analyzed visually or by measuring the ADC values in an ROI. The possibility of evaluating ADC histograms of the total tumor volume opens up new approaches for assessing treatment response or even generating a complementary prognostic factor.

In the first case study, we demonstrated that, as well as a reduction in tumor volume, a shift in the distribution of ADC values is observed with a good therapy response in Hodgkin lymphoma.

The second case study shows that, in neuroblastoma, a lack of change in ADC value distribution under therapy is a sign of persistent tumor vitality despite a significant reduction in tumor volume.

In the third case study, we saw that *syngo*.via Frontier MR Total Tumor Load can visualize tumor heterogeneity in neuroblastic tumors using ADC color projections, histograms, and descriptive histogram statistics.

We have demonstrated that the *syngo*.via Frontier MR Total Tumor Load application has benefits for evaluating pediatric oncology in both metastatic bone disease and solid tumors, and could further help to establish DWI as a prognostic factor in assessments of tumor therapy. However, proving this hypothesis will require large-scale, multicenter studies.

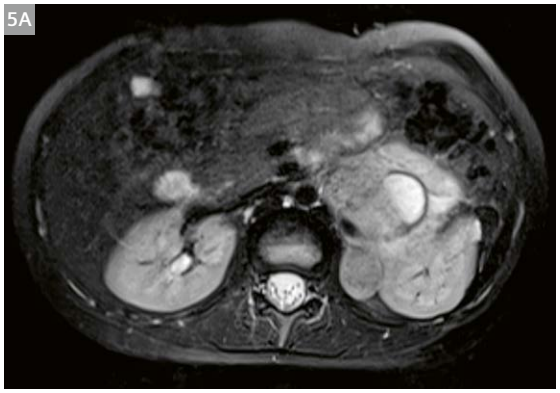

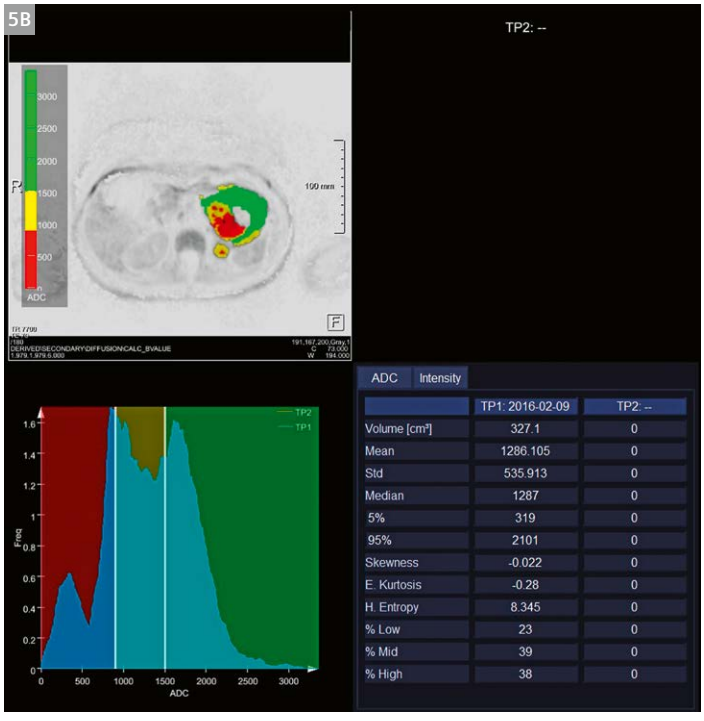

5 **Morphological images and ADC histogram**
In the transversal T2-weighted fat-suppressed sequence **(5A)** the heterogeneous suprarenal tumor of the left side is well demonstrated. Correlating the ADC histogram **(5B)** in the MR Total Tumor Load software[1] shows the heterogeneity in the color projection and also in the three-modal distribution of the ADC values. The lowest ADC peak corresponds to active tumor core and is visualized in red, the second peak at an ADC of approximately 900–1300 µm²/s represents surrounding tissue with increased cellularity and is overlaid in yellow. ADC values of 1500 µm²/s and above are considered fluid components and are back-mapped in green.

References

1 Atkin KL, Ditchfield MR. The role of whole-body MRI in pediatric oncology. J Pediatr Hematol Oncol. 2014;36(5):342-52.
2 Mentzel H-J, Schäfer JF, et al. Whole-Body MRI in Children [Ganzkörpermagnetresonanztomografie im Kindes- und Jugendalter]. 2018; AWMF Registernummer: 064/018. Klasse: S1. Available from: https://www.awmf.org/leitlinien/detail/ll/064-018.html.
3 Baranska D, Matera K, Podgorski M, et al. Feasibility of diffusion-weighted imaging with DWIBS in staging Hodgkin lymphoma in pediatric patients: comparison with PET/CT. MAGMA. 2018; doi: 10.1007/s10334-018-0726-4. [Epub ahead of print].
4 Regacini R, Puchnick A, Luisi FAV, et al. Can diffusion-weighted whole-body MRI replace contrast-enhanced CT for initial staging of Hodgkin lymphoma in children and adolescents? Pediatr Radiol. 2018;48(5):638-47.
5. Gahr N, Darge K, Hahn G, et al. Diffusion-weighted MRI for differentiation of neuroblastoma and ganglioneuroblastoma/ganglioneuroma. Eur J Radiol. 2011;79(3):443-6.
6 Neubauer H, Li M, Muller VR, et al. Diagnostic Value of Diffusion-Weighted MRI for Tumor Characterization, Differentiation and Monitoring in Pediatric Patients with Neuroblastic Tumors. Fortschr Röntgenstr. 2017;189(7):640-50.
7 Uhl M, Altehoefer C, Kontny U, et al. MRI-diffusion imaging of neuroblastomas: first results and correlation to histology. Eur Radiol. 2002;12(9):2335-8.
8 Demir S, Altinkaya N, Kocer NE, et al. Variations in apparent diffusion coefficient values following chemotherapy in pediatric neuroblastoma. Diagn Interv Radiol. 2015;21(2):184-8.
9 Peschmann AL, Beer M, Ammann B, et al. Quantitative DWI predicts event-free survival in children with neuroblastic tumours: preliminary findings from a retrospective cohort study. Eur Radiol Exp. 2019;3(1):6.
10 Grimm R, Padhani AR. Whole-body Diffusion-weighted MR Image Analysis with *syngo*.via Frontier MR Total Tumor Load. MAGNETOM Flash. 2017;68(2):73-5.
11 Blackledge MD, Tunariu N, Orton MR, et al. Inter- and Intra-Observer Repeatability of Quantitative Whole-Body, Diffusion-Weighted Imaging (WBDWI) in Metastatic Bone Disease. PLoS One. 2016;11(4):e0153840.
12 Schafer JF, Gatidis S, Schmidt H, et al. Simultaneous whole-body PET/MR imaging in comparison to PET/CT in pediatric oncology: initial results. Radiology. 2014;273(1):220-31.
13 Schaefer JF, Tsiflikas I. Whole body MRI in children [Ganzkörper-MRT bei Kindern]. Radiologie up2date. 2014;14(3):259-78.
14 Dalili D, Padhani AR, Grimm R. Quantitative WB-MRI with ADC Histogram Analysis for Response Assessment in Diffuse Bone Disease. Magnetom Flash. 2017;69(3):32-7.
15 Dalili D, Padhani AR, Grimm R. Quantitative WB-MRI with ADC Histogram Analysis for Complex Response of Bone Marrow Metastatic Disease. MAGNETOM Flash. 2017;69(3):38-42.
16 Dalili D, Joshi PV, Padhani AR, Grimm R. Evolution of the Malignant Bone Marrow with Successful Therapy – Quantitative Analysis with Whole-body Diffusion-weighted MRI. MAGNETOM Flash. 2017;69(3):43-8.

Contact

Ilias Tsiflikas, M.D.
Pediatric Radiology
Department of Diagnostic and Interventional Radiology
University Hospital of Tübingen
Hoppe-Seyler-Str. 3
72072 Tübingen
Germany
ilias.tsiflikas@med.uni-tuebingen.de


Ilias Tsiflikas


Jürgen Schäfer

Musculoskeletal and Body MRI in Children

Sarah D. Bixby, M.D.; Reid C. Nichols, RT (R) MR; Ali Gholipour, Ph.D.

Department of Radiology, Boston Children's Hospital, Boston, MA, USA

MRI imaging in pediatric patients is as much about the process as it is about the result. While high-quality images are the ultimate goal, for children an imaging study is a success if diagnostic images are obtained while minimizing the risk to the patient, which includes reducing the risk of anesthesia [1–2]. There are many ways to improve spatial resolution and gain signal-to-noise ratio (SNR) in MRI, though most strategies cost time. In clinical practice there are limitations on patient cooperation and magnet utilization that require a practical approach to imaging. While working with children is enormously satisfying, there are also challenges that come with pediatric imaging which require minimizing exam times, eliminating labor-intensive breath-holding instructions, and imaging through motion (respiratory and gross motion). Motion is a major obstacle when it comes to imaging young children. In many instances, the difference between a non-diagnostic exam and a successful exam may simply require reducing sequence time by half. While this used to require unacceptable compromise in image quality, this is no longer true. With increased field strength magnets (i.e. 3T), appropriate selection of multichannel phased array coils, and parallel imaging techniques, scan times have decreased considerably from where they started. With a few additional strategies it is not only possible, but more than likely that a complete exam can be performed in a young child[1] without sedation.

Advanced protocol planning, sequence prioritization, real-time exam monitoring, and skilled patient handling are also critical elements of a successful MRI examination in a young child.

A fundamental principle in imaging pediatric patients is to limit sequences to only those that are necessary, acquiring the most high yield sequences first. Patient cooperation is limited and young patients often have tolerance for two or three sequences. Radiologists should assume the most critical diagnostic information must be obtained in the first ten minutes of an exam. If those first sequences are diagnostic, the patient will be spared a follow-up exam under anesthesia. MRI is increasingly being used to screen patients with certain symptoms for presence or absence of disease, such as fracture detection in limping toddlers, evaluation for infection in children with fever of unknown origin, or appendicitis screening in patients with right lower quadrant pain. MRI may be the best means of detecting fractures in certain locations when the bones have not yet ossified (Fig. 1), and for localizing disease when patients are unable to verbalize symptoms.

[1] *MR scanning has not been established as safe for imaging fetuses and infants less than two years of age. The responsible physician must evaluate the benefits of the MR examination compared to those of other imaging procedures. Note: This disclaimer does not represent the opinion of the authors.*

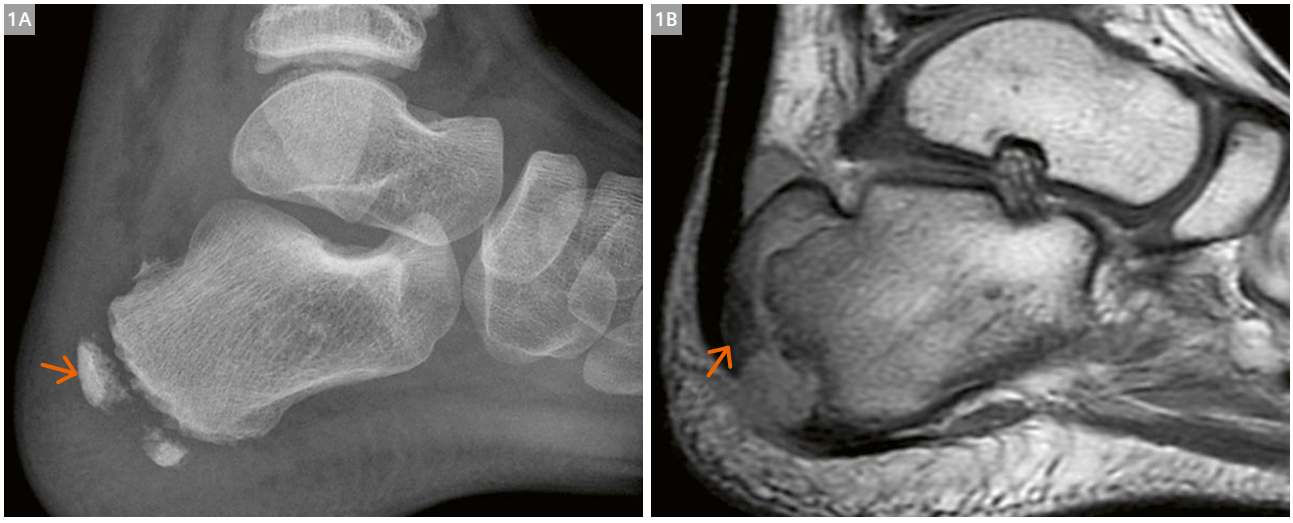

1 6-year-old female with calcaneal apophyseal fracture **(1A)** Lateral radiograph of the ankle reveals a normal-appearing apophysis (orange arrow). **(1B)** Sagittal PD-weighted TSE sequence reveals avulsion of the calcaneal apophysis, not appreciated on radiographs secondary to the lack of ossification.

It is more important to acquire images quickly to allow actionable diagnosis, rather than spending additional time enhancing imaging quality at the expense of patient cooperation.

Monitoring MRI examinations in real-time allows for adjustment of imaging parameters as the study unfolds [3]. As toddlers are often unable to articulate the location and nature of their symptoms, imaging requires looking far and wide initially and focusing down on an abnormality once identified. Setting up an MRI in a toddler with an unexplained limp, for example, often requires using one or more body matrix coils (depending on the child) to perform initial sequences with a large field of view (FOV) from the pelvis to the feet (Fig. 2). These sequences can be performed quickly, with need for additional sequences determined by the presence or absence of abnormal findings. Without real-time radiologist supervision, these protocol modifications would not be possible and the examination may need to be repeated.

While vigilant exam monitoring, careful protocoling, and adept patient handling are critical to successful imaging of children, these efforts may still fall short of the goal without additional sequence advancements. Accelerated acquisitions and motion robust sequences are, therefore, particularly valuable in pediatric imaging. Acceleration techniques allow for substantial reductions in imaging times so that they may be tolerated by young patients; in our experience this generally means shorter than two minutes per sequence. In pediatric musculoskeletal imaging, MRI protocols rely heavily on turbo spin-echo (TSE) sequences which include proton density (PD), intermediate weighted (IW), and T2-weighted images. Accelerated TSE acquisitions can be obtained through *k*-space undersampling in parallel imaging [4]; however a reduction or acceleration factor of R comes with a reduction of $1/\sqrt{R}$ in (SNR). In addition, SNR is also reduced by the noise amplification factor, or the *g*-factor (geometry factor) penalty that varies by the location in an image depending on the number of aliased replicates per voxel based on coil sensitivities [5]. The *g*-factor penalty depends on the receive coil design and coverage, and the geometry of imaging and can vary between 1 and 2 across the image. Simultaneous multi-slice (SMS) is another technique to accelerate imaging that excites multiple spatially distributed slices simultaneously by using a multi-band radiofrequency pulse and techniques to control aliasing and reduce the *g*-factor penalty [5–11]. Data obtained from receive coils from simultaneously excited slices are separated to reconstruct images. When parallel imaging and SMS are both applied, imaging times can be reduced 4- to 8-fold over traditional methods. In our routine knee MRI protocol we compared an accelerated T2-weighted TSE sequence using a parallel imaging iPAT factor of 2 with an SMS factor of 2 to achieve 4-fold acceleration against our traditional sequence without the SMS acceleration (Figs. 3, 4). We found both the SMS TSE and the TSE were equivalent in identifying pertinent imaging findings [12]. Compared to the traditional sequence, the SMS accelerated sequence is nearly twice as fast (Table 1). Further reduction in imaging time can be gained by increasing the SMS factor, with incremental cost to SNR. In our patient population we found that 4-fold acceleration is sufficient for most patients, and additional acceleration can be reserved for patients who are extremely nervous or fidgety, given the modest reduction in SNR.

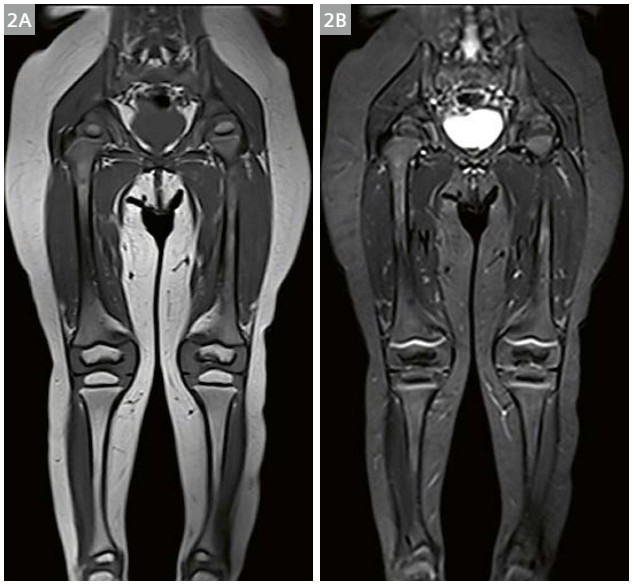

2 2-year-old female with limp. Coronal T1 **(2A)** and STIR **(2B)** sequences through the entire pelvis and lower extremities were performed using a body matrix coil as an initial screen to identify areas of pathology. No abnormality was identified.

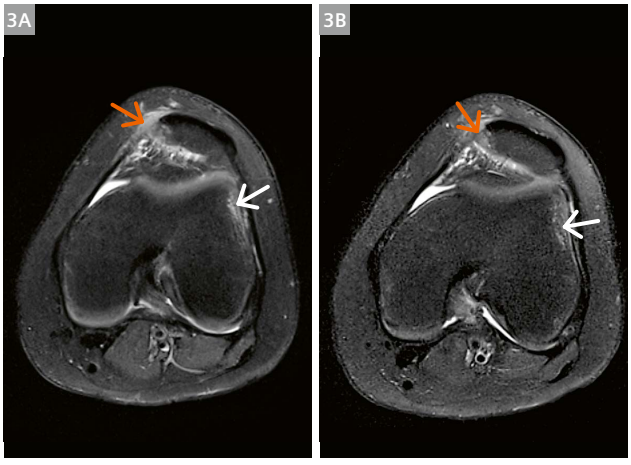

3 11-year-old female with patellar dislocation. **(3A)** Axial T2-weighted TSE image with fat suppression and **(3B)** corresponding axial T2-weighted SMS TSE image demonstrates a tear of the medial retinaculum (orange arrow) and a bone contusion at the lateral femoral condyle (white arrow).

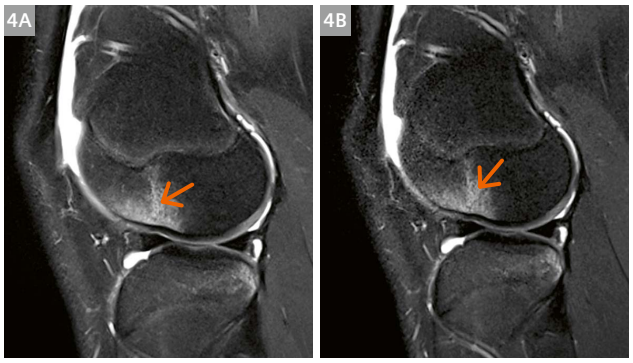

4 14-year-old boy with lateral femoral contusion (orange arrow) undergoing MRI. **(4A)** Sagittal T2-weighted TSE sequence and **(4B)** corresponding sagittal T2-weighted SMS TSE sequence for comparison.

The 3D TSE volumetric SPACE (Sampling Perfection with Application optimized Contrasts using different flip angle Evolution) acquisition is integral for imaging of large joints (knee and ankle) in children [13–18]. The three-dimensional, high-spatial resolution, isotropic images can be reconstructed into any imaging plane from a single volumetric data set, making it helpful for identifying subtle cartilage defects or ligamentous injuries. The imaging time, however, is relatively long which makes it particularly vulnerable to motion. The standard PD-weighted SPACE sequence in the knee protocol at our institution is 7 minutes and 40 seconds. Parallel imaging techniques can be applied to the acquisition but may cause aliasing artifacts and increase noise. CAIPIRINHA "Controlled Aliasing in Parallel Imaging Results in Higher Acceleration" [19] is a parallel imaging strategy that uses *k*-space sampling patterns designed to reduce aliasing and overlap on reconstructed images. While aliasing artifacts are still present, they are shifted to the corners of the image space.

Parameters	T2-weighted TSE	T2-weighted SMS TSE
Plane	Sagittal	Sagittal
Acquistion time (min:sec)	2:45	1:50
TR (ms)	4500	3000
TE (ms)	53	53
Echo train length	34	33
Matrix	384	384
Parallel imaging acceleration factor and reconstruction	2 (GRAPPA)	2 (GRAPPA)
FOV (mm)	140	140
Voxel dimension (mm)	0.4 x 0.4 x 3.0	0.4 x 0.4 x 3.0

Table 1: MRI parameters for T2-weighted TSE sequence versus T2-weighted SMS TSE sequence in the knee.

Parameters	PD-weighted 3D SPACE	PD-weighted 3D CAIPIRINHA SPACE
Plane	Sagittal	Sagittal
Acquistion time (min:sec)	7:40	4.00
TR (ms)	1000	1000
TE (ms)	49	49
Echo train length	41	41
Flip angle (°)	120	120 (variable)
Matrix	320 x 320 x 240	320 x 320 x 240t
Parallel imaging acceleration factor and reconstruction	2 (GRAPPA)	2 (GRAPPA)
FOV (mm)	162 x 249	162 x 249
Voxel dimension (mm)	0.54 x 0.54 x 1	0.54 x 0.54 x 1

Table 2: MRI parameters for Proton Density (PD)-weighted 3D SPACE sequence versus PD-weighted 3D CAIPIRINHA SPACE sequence in the knee.

Combined CAIPIRINHA and SPACE allows for 4-fold acceleration through undersampling in both the phase and partition encoding directions [14]. We compared the standard PD-weighted SPACE sequence in the knee with the CAIPIRINHA PD-weighed SPACE sequence (Table 2). Applying CAIPIRINHA to SPACE reduced our scan time from 7:40 minutes to 4:00 minutes without compromise in image quality (Figs. 5, 6). We reserve this sequence for slightly older patients (above the age of 8) who are able to cooperate for the 4 minute long acquisitions. In the younger patients, 2D sequences are still generally preferred. Anticipated pathologies in our youngest patients do not typically require such fine spatial resolution, and these patients reap greatest benefit from short acquisitions that require periodic opportunities for breaks.

Motion robust imaging alternatives are highly valuable in pediatric patients, particularly for abdominal and pelvic imaging [20]. Examinations that require breath-held sequences often require the child to be anesthetized and intubated to allow for periods of suspended respiration. With the aim of reducing need for anesthesia and/or the depth of anesthesia, free-breathing imaging capabilities are imperative. In the abdomen, 3D volumetric interpolated breath-hold examination (VIBE) imaging offers the most robust approach to acquiring T1-weighted imaging. VIBE allows for high spatial resolution with relatively fast imaging acquisitions of the entire abdomen [21, 22]. Depending on parameter selection, it is possible to acquire images through the entire field of view in approximately 20 seconds in a cooperative patient. Even adult patients may have difficulty breath-holding for a 20 second sequence [23], and children are even less likely to manage this. Cartesian VIBE obtained during free-breathing produces motion artifact within the image (Fig. 7) which limits the diagnostic quality of the sequence [24, 25]. T1-weighted images can be acquired with respiratory navigation, though this is less developed than navigated T2-weighted sequences, and image quality is inferior to the conventional breath-hold sequences [26–28]. Additionally, navigated T1-weighted imaging is not possible with fat suppression, which limits its utility for post-contrast imaging. A modified version of the VIBE sequence is a radial VIBE sequence that uses rectilinear sampling in the *z*-direction and radial sampling in the *xy* plane [24]. This sequence can be performed during free-breathing, and the radial sampling of *k*-space mitigates the effect of respiratory motion such that image quality is superior to the traditional breath-hold Cartesian VIBE [24]. The product version of this sequence is called StarVIBE, which is our standard for T1-weighted imaging in pediatric patients. Although the acquisition time is longer than a traditional VIBE sequence, the respiratory motion is distributed throughout the image such that there is little perception of the motion within the image. This technique is especially helpful for post-gadolinium enhanced imaging in the liver, kidneys, and bowel (Fig. 8). The ability to obtain high spatial-resolution, motionless imaging in patients who are freely breathing has dramatically altered our approach to sedating patients. We utilize the StarVIBE sequence in any child undergoing abdominopelvic imaging, for both pre and post-contrast fat-suppressed imaging.

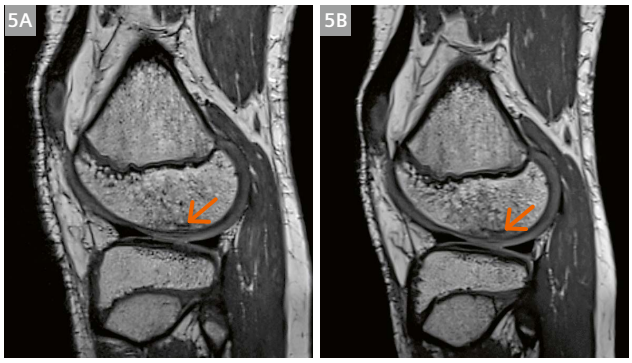

5 11-year-old female with lateral femoral condylar impaction fracture (orange arrow) seen on both **(5A)** sagittal PD-weighted SPACE sequence, and **(5B)** corresponding sagittal PD-weighted CAIPIRINHA SPACE sequence for comparison.

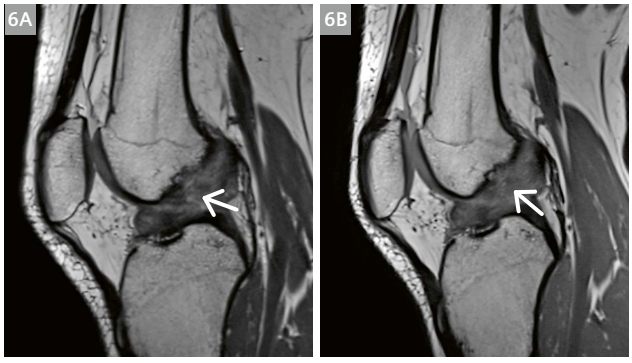

6 15-year-old female with ACL tear (white arrow). **(6A)** Sagittal PD-weighted SPACE sequence and **(6B)** corresponding sagittal PD-weighted CAIPIRINHA SPACE sequence through the ruptured ACL for comparison.

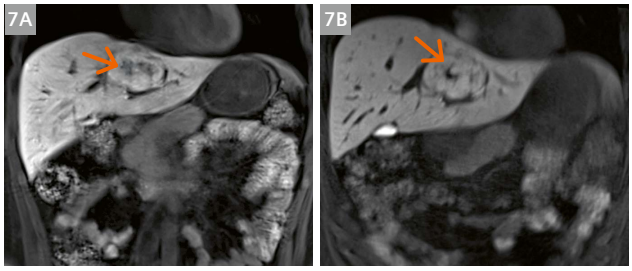

7 20-year-old female with FNH-like liver lesion. **(7A)** Coronal T1 VIBE with breath-holding after administration of Eovist contrast media reveals delayed uptake in a liver lesion (orange arrows), though images are degraded by motion. **(7B)** Sequence repeated with StarVIBE sequence with free-breathing demonstrates reduced motion artifact with better depiction of the lesion.

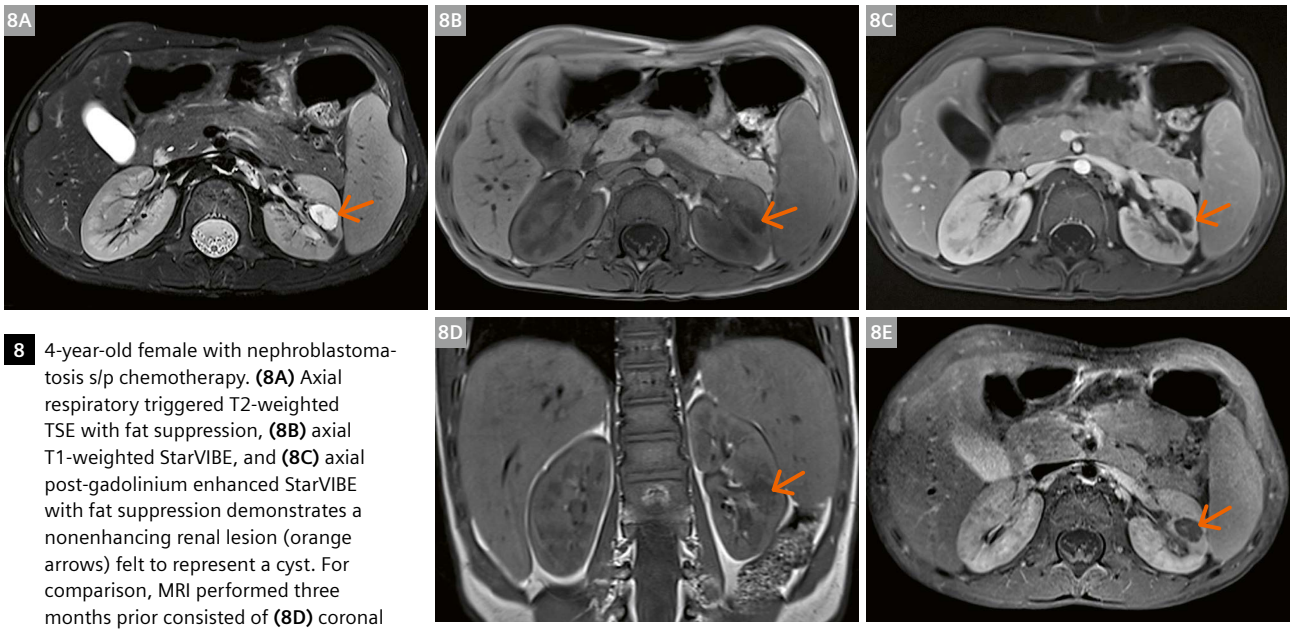

8 4-year-old female with nephroblastomatosis s/p chemotherapy. **(8A)** Axial respiratory triggered T2-weighted TSE with fat suppression, **(8B)** axial T1-weighted StarVIBE, and **(8C)** axial post-gadolinium enhanced StarVIBE with fat suppression demonstrates a nonenhancing renal lesion (orange arrows) felt to represent a cyst. For comparison, MRI performed three months prior consisted of **(8D)** coronal respiratory triggered T1-weighted TSE, **(8E)** axial post-gadolinium enhanced T1 TSE with fat suppression. Motion artifact is noted in the image from respiration.

The lack of breath-holding as a requirement for imaging obviates the requirement for endotracheal intubation, unless there are other reasons for which it would be required. A dynamic StarVIBE sequence is also available which allows for both high temporal resolution in addition to high spatial resolution images during dynamic contrast injection [29, 30], using compressed sensing techniques as a means to vastly undersample the data and reduce imaging times [20]. We are currently investigating this technique in the pediatric population, particularly with regard to renal, hepatic and bowel wall imaging.

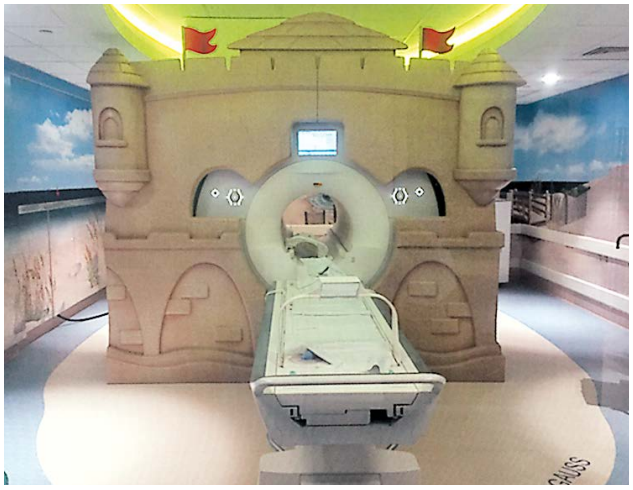

9 3T MAGNETOM Prisma MR scanner embedded in a sandcastle design. The room is decorated with decals in the theme of an ocean scene.

MR imaging in pediatric patients requires a team approach and collective efforts toward reducing our dependency upon sedation as a mechanism to acquire diagnostic, motion-free images. These include tailored protocoling, real-time monitoring, and utilization of accelerated or motion robust sequences. With the use of SMS TSE and CAIPIRINHA SPACE, MSK imaging examinations in children can be dramatically shortened without compromising image quality. StarVIBE imaging in the abdomen allows for high-resolution, free-breathing, T1-weighted imaging thereby eliminating requirement for endotracheal intubation for abdominal MRI in sedated patients. Reducing the anxiety and apprehension around the scanner and the scan room is also important in achieving patient cooperation. This can be achieved through embedding the scanner in a structure, such as a sandcastle, train, or boat (Fig. 9), decorating the room with colorful designs, distracting the patient with a movie during the scan, or preparing prior to the scan at a mock scanner or simulating the experience with virtual reality headsets. All of these strategies are currently employed at our hospital, oftentimes in combination. Further developments in prospective motion correction using motion cameras embedded in the magnet and sensors on the patient are currently being developed through collaborations with KinetiCor (Honolulu, HI, USA), with broad applications in the pediatric population. Our hope is that through these collective efforts we will drastically reduce the number of children requiring sedation for MRI, and improve the patient experience by reducing exam lengths and delays.

References

1 Callahan MJ, MacDougall RD, Bixby SD, Voss SD , Robertson RL, Cravero JP. Ionizing radiation from computed tomography versus anesthesia for magnetic resonance imaging in infants and children: patient safety considerations. Pediatr Radiol 2018; 48(1):21-30.
2 Paterson N, Waterhouse P. Risk in pediatric anesthesia. Paediatr Anaesth 2011; 21:848-857.
3 Robertson RL, Silk S, Ecklund K, Bixby SD, Voss SD, Robson CD. Imaging optimization in children. J Am Coll Radiol 2018; 15(3 Pt A):440-443.
4 Griswold MA, Jakob PM, Heidemann RM, Nittka M, Jellus V, Wang J, Kiefer B, Haase A. Generalized autocalibrating partially parallel acquisitions (GRAPPA). Magn Reson Medicine 2002 Jun; 47(6):1202-1210.
5 Breuer FA, Kannengiesser SA, Blaimer M, Seiberlich N, Jakob PM, Griswold MA. General formulation for quantitative G-factor calculation in GRAPPA reconstructions. Magn Reson Med 2009 Sep; 62(3):739-746.
6 Setsompop K, Gagoski BA, Polimeni JR, Witzel T, Wedeen VJ, Wald LL. Blipped-controlled aliasing in parallel imaging for simultaneous multislice echo planar imaging with reduced g-factor penalty. Magn Reson Med 2012 May 1; 67(5):1210-1224.
7 Barth M, Breuer F, Koopmans PJ, Norris DG, Poser BA. Simultaneous multislice (SMS) imaging techniques. Magn Reson Med 2016 Jan; 75(1):63-81.
8 Feinberg DA, Setsompop K. Ultra-fast MRI of the human brain with simultaneous multi-slice imaging. J Magn Reson 2013; 229:90-100.
9 Fritz J, Fritz B, Zhang J, Thawait GK, Joshi DH, Pan L, Wang D. Simultaneous multislice accelerated Turbo Spin Echo magnetic resonance imaging comparison and combination with in-plane parallel imaging acceleration for high-resolution magnetic resonance imaging of the knee. Invest Radiol 2017; 52:529-537.
10 Poser BA, Anderson RJ, Guerin B, Setsompop K, Deng W, Mareyam A, Serano P, Wald LL, Stenger VA. Simultaneous multislice excitation by parallel transmission. Magn Reson Med 2014; 71:1416-1427.
11 Gagoski BA, Bilgic B, Eichner C, Bhat H, Grant PE, Wald LL, Setsompop K. RARE/Turbo Spin Echo imaging with simultaneous multislice wave-CAIPI. Magn Reson Med 2015; 73:929–938.
12 Benali S, Johnston PR, Gholipour A, Dugan ME, Heberlein K, Bhat H, Bixby SD. Simultaneous multi-slice accelerated turbo spin echo of the knee in pediatric patients. Skeletal Radiol 2018 Jun; 47 (6):821-831.
13 Fritz J, Fritz B, Thawait GG, Meyer H, Gilson WD, Raithel E. Three-Dimensional CAIPIRINHA SPACE TSE for 5-Minute High-Resolution MRI of the Knee. Invest Radiol 2016; 51:609-617.
14 Fritz J, Ahlawat S, Fritz B, Thawait GK, Stern SE, Raithel E, Klyce W, Lee RJ. 10-min 3D Turbo Spin Echo MRI of the knee in children: arthroscopy-validated accuracy for the diagnosis of internal derangement. J Magn Reson Imaging 2018; doi: 10.1002/jmri.26241. epub ahead of print.

Contact

Sarah D. Bixby, M.D.
Associate Professor of Radiology
Department of Radiology
Boston Children's Hospital
300 Longwood Avenue,
Main Building, 2nd Floor
Boston, MA 02115
USA
Tel.: +1 857 218 4006
sarah.bixby@childrens.harvard.edu

15 Fritz J, Raithel E, Thawait GK, Gilson W, Papp DF. Six-fold acceleration of high-spatial resolution 3D SPACE MRI of the knee through incoherent k-space undersampling and iterative reconstruction – first experience. Invest Radiol 2016; 51:400–409.
16 Fritz J, Ahlawat S, Thawait GK, Raithel E, Gilson W, Lee RJ. 3D MRI of knee in pediatric patients with CAIPIRINHA SPACE: diagnostic performance assessment with arthroscopic correlation. Proc Intl Soc Mag Reson Med 2017; 25:1151.
17 Kalia V, Fritz B, Johnson R, Gilson WD, Raithel E, Fritz J. CAIPIRINHA accelerated SPACE enables 10-min isotropic 3D TSE MRI of the ankle for optimized visualization of curved and oblique ligaments and tendons. Eur Radiol 2017; 27:3652–3661.
18 Del Grande F, Delcogliano M, Guglielmi R, Raithel E, Stern SE, Papp DF, Candrian C, Fritz J. Fully automated 10-minute 3D CAIPIRINHA SPACE TSE MRI of the knee in adults. A multicenter, multireader, multifield-strength validation study. Invest Radiol 2018; 53:689-697.
19 Breuer FA, Blaimer M, Heidemann RM, Mueller MF, Griswold MA, Jakob PM. Controlled aliasing in parallel imaging results in higher acceleration (CAIPIRINHA) for multi-slice imaging. Magn Reson Med 2005 Mar 1; 53(3):684-691.
20 Jaimes C, Kirsch KE, Gee MS. Fast, free-breathing and motion-minimized techniques for pediatric body magnetic resonance imaging. Pediatr Radiol 2018; 48:1197-1208.
21 Rofsky NM, Lee VS, Laub G, Pollack MA, Krinsky GA, Thomasson D, Ambrosino MM, Weinreb JC. Abdominal MR imaging with a volumetric interpolated breath-hold examination. Radiology 1999; 212:876-884.
22 Lee VS, Lavelle MT, Krinsky GA, Rofsky NM. Volumetric MR imaging of the liver and applications. Magn Reson Imaging Clin N Am 2001; 9(4):697-716.
23 Krinsky GA, Lee VS, Theise ND, Weinreb JC, Rofsky NM, Diflo T, Teperman LW. Hepatocellular carcinoma and dysplastic nodules in patinets with cirrhosis: prospective diagnosis with MR imaging and explanation correlation. Radiology 2001; 219(2):445-54.
24 Chandarana H, Block TK, Rosenkrantz AB, Lim RP, Kim D, Mossa DJ, Babb JS, Kiefer B, Lee VS. Free-breathing radial 3D fat-suppressed T1-weighted gradient echo sequence. A viable alternative for contrast-enhanced liver imaging in patients unable to suspend respiration. Invest Radiol 2011; 46:648-653.
25 Chandarana H, Block KT, Winfeld MJ, Lala SV, Mazori D, Giuffrida E, Babb JS, Milla SS. Free-breathing contrast-enhanced T1-weighted gradient-echo imaging with radial k-space sampling for paediatric abdominopelvic MRI. Eur Radiol 2014; 24:320-326.
26 Vasanawala SS, Iwadate Y, Church DG, Herfkens RJ, Brau AC. Navigated abdominal T1-W MRI permits free-breathing image acquisition with less motion artifact. Pediatr Radiol 2010; 40:340-344.
27 Young PM, Brau AC, Iwadate Y, Vasanawala S, Daniel BL, Tamrazi A, Herfkens RJ. Respiratory navigated free breathing 3D spoiled gradient-recalled echo sequence for contrast-enhanced examination of the liver: diagnostic utility and comparison with free breathing and breath-hold conventional examinations. Am J Roentgenol AJR 2010; 195:687-691.
28 Azevedo RM, Campos ROP, Ramalho M, Heredia V, Dale BM, Semelka RC. Free-breathing 3D T1-weighted gradient echo sequence with radial data sampling in abdominal MRI: preliminary observations AJR Am J Roentgenol 2011; 197:650-657.
29 Kim KW, Lee JM, Jeon YS, Kang SE, Baek JH, Han JK, Choi BI, Bang Y-J, Kiefer B, Block KT, Ji H, Bauer S, Chin K. Free-breathing dynamic contrast-enhanced MRI of the abdomen and chest using a radial gradient echo sequence with K-space weighted image contrast (KWIC). Eur Radiol 2013; 23:1352–1360.
30 Kaltenbach B, Roman A, Polkowski C, Gruber-Rouh T, Bauer RW, Hammerstingl R, Vogl TJ, Zangos S. Free-breathing dynamic liver examination using a radial 3D T1-weighted gradient echo sequence with moderate undersampling for patients with limited breath-holding capacity. Eur J Radiol 2017; 86:26-32.

Improving patient experience

Redefining the MRI experience with Innovision

siemens-healthineers.com/innovision

Noisy and monotonous MRI exams are a thing of the past. Redefine the MRI experience with Innovision[1], the revolutionary in-bore infotainment solution. Patients are greeted by an impressive audio and video experience as soon as they lie on the table. The patient display keeps patients informed about the remaining scan time and displays predefined or custom content. Furthermore, the patient display makes the bore appear virtually larger, preventing a claustrophobic feeling. Innovision includes comfort pillows made of memory foam and specialized ear plugs that reduce scan noise and deliver clear audio signals to the patient. With Innovision, patients can hear their favorite music and voice commands from the technologist in excellent sound quality.

All benefits of Innovision at a glance:

- Enhance the patient experience with customizable video content
- Reduce claustrophobia and anxiety with a patient display that creates a virtually larger bore
- Keep the patient informed by displaying the remaining scan time
- Exceptional sound quality for voice commands and entertainment
- Effective noise reduction with a unique memory foam pillow and specialized ear plugs

[1]*Innovision is still under development and not yet commercially available. Its future availability cannot be guaranteed.*

SIEMENS Healthineers

Performance of Compressed Sensing Cardiac Cine Imaging in Children: Initial Experience

Davide Curione[1]; Paolo Ciliberti[2]; Dolores Ferrara[3]; Teresa Pia Santangelo[1]; Paolo Ciancarella[1]; Carmela Napolitano[1]; Aurelio Secinaro[1]

[1]Advanced Cardiovascular Imaging Unit – Imaging Department, Bambino Gesù Children's Hospital IRCCS, Rome, Italy
[2]Pediatric Cardiology and Cardiac Surgery Department, Bambino Gesù Children's Hospital IRCCS, Rome, Italy
[3]Department of Advanced Biomedical Sciences, Federico II University, Naples, Italy

Abstract

The aim of our study was to compare conventional segmented balanced steady-state free precession (bSSFP) and real-time Compressed Sensing (CS) cardiac cine imaging in a small group of pediatric patients[1]. 20 subjects with either cardiomyopathy or congenital heart disease treated with biventricular repair were included. Examinations were carried out on our MAGNETOM Aera 1.5T (Siemens Healthcare, Erlangen, Germany) using both retrospectively cardiac-gated Cartesian conventional bSSFP and real-time CS cardiac cine sequences with whole coverage of the ventricles in the short-axis plane. Quantification of ventricular volumes was performed in all cases by two clinical cardiac MRI specialists in consensus. They were blinded to patient diagnosis and type of sequence, and correlated values with phase-contrast flow measurements. CS cardiac cine imaging showed good diagnostic quality and performance. It had slightly lower spatial and temporal resolution but there were no significant differences between ventricular volumes compared to conventional bSSFP sequences. We believe that real-time CS cardiac cine definitely has potential for the pediatric population. However, more work is needed to assess its performance and overcome its current limitations.

Parameters	bSSFP	CS
TR/TE (ms)	2.92/1.21	2.66/1.1
Temporal resolution (ms)	37.44	39.90
FOV (mm)	340	360
Rectangular FOV (%)	75	75
Matrix	256 x 192	208 x 156
Spatial resolution (mm)	1.5 x 1.5 x 7	1.7 x 1.7 x 7
Flip angle (°)	73	55
Bandwidth (Hz/pixel)	930	962
GRAPPA	x2	–
CS	–	x9.9
Cardiac gating	Retrospective	ECG-triggered
Trajectory	Cartesian	Cartesian
Reconstructed cardiac phases	25	20
Number of slices	~15 (12–18)	~15 (12–18)
Breath-hold time (s)	~10 (6.8–13.5) / 2 slices	~20 (17–25)
Total SAX acquisition time (s)	~160 (130–190)	~20 (17–25)
Total reconstruction time (s)	~immediate	~120 (100–150)

Table 1: Sequence parameters.
bSSFP = balanced steady-state free precession; CS = Compressed Sensing; FOV = field of view; GRAPPA = generalized autocalibrating partially parallel acquisition; SAX = short axis; TE = echo time; TR = repetition time

Introduction

Compressed Sensing (CS) is a relatively novel magnetic resonance imaging (MRI) technique based on *k*-space incoherent subsampling paired with a noise-reduction algorithm employing sparse representation in a nonlinear iterative reconstruction process. The aim is to drastically speed up acquisition without significantly degrading image quality [1]. In recent years, CS has become increasingly popular in cardiac MRI. This is especially true for cine imaging in adults, where CS has shown itself to be accurate and reproducible, allowing for fast and reliable scanning even in difficult patients [2, 3]. Compared to conventional segmented balanced steady-state free precession (bSSFP) cine sequences, the major advantages of real-time CS cardiac cine are the decreased scan duration and the relative insensitivity to motion such as irregular heart rhythms and breathing [4]. These features account for most of its appeal in pediatric cases, where patient cooperation is often limited. Moreover, in contrast with classic real-time cine imaging using parallel imaging, CS cardiac cine yields higher spatial and temporal resolution, closer to that of conventional segmented bSSFP [5]. Nevertheless, the smaller anatomical structures and higher heart rates typically found in children can still be a concern. Additionally, congenital heart disease (CHD) can significantly subvert the usual cardiac anatomy and multiple lesions can exist simultaneously. This leads to complex ventricular geometry and flow-volume calculations, and therefore requires a high degree of definition and accuracy. A disadvantage of CS is the relatively long reconstruction times [3], which could impact exam planning and limit clinical implementation. However, recent experiences investigating CS in children and CHD are encouraging, showing feasibility and good agreement with conventional cine imaging [6]. In this context, we present results from our initial experience of how real-time CS cardiac cine performs in comparison with conventional segmented bSSFP cine in a small group of pediatric patients.

Methods

Between January and March 2019, we studied 20 patients who had either cardiomyopathy or CHD treated with biventricular repair and who were referred for cardiac MRI. Informed written consent for additional research scans was obtained from all individuals/guardians. All procedures were in accordance with the ethical standards of the responsible committee on human experimentation and with the Declaration of Helsinki and its later amendments.

All imaging was performed on a 1.5-Tesla MRI scanner (MAGNETOM Aera, Siemens Healthcare, Erlangen, Germany). We used the Body 18 matrix coil and the spine coil incorporated into the scan table. A vector electrocardiographic system was used for cardiac-gating. Ventricular volume assessment was performed with both conventional bSSFP and real-time CS cardiac cine sequences in the ventricular short-axis (SAX) plane using sufficient contiguous slices for gapless imaging to ensure whole coverage of both ventricles. Conventional bSSFP cine imaging involved a multi-slice retrospectively cardiac-gated Cartesian sequence, with two slices acquired during every breath-hold. Spatial resolution was 1.5 x 1.5 x 7 mm and temporal resolution was ~37 ms. Real-time CS cardiac cine imaging employed a multi-slice cardiac-gated Cartesian sequence, with the whole volume obtained during a single breath-hold or during free-breathing if breath-holding was not feasible. The acquisition duration was two R-R intervals per slice; the first heartbeat was a non-imaging "dummy" used to reach the steady state, and the second heartbeat was used for data acquisition. Spatial resolution was 1.7 x 1.7 x 7 mm (8 mm in two cases) and temporal resolution was ~40 ms. Full sequence parameters are shown in Table 1.

Quantification of ventricular volumes was performed in all cases by two clinical cardiac MRI specialists in consensus (FD with 6 months and CD with 5 years of experience, respectively), blinded to patient diagnosis and type of sequence, in a random order, and using a commercially available software (cvi[42], Circle Cardiovascular Imaging Inc., Calgary, Canada). The end-diastolic and end-systolic phases were identified for each ventricle through simultaneous visual inspection of all SAX cine images. The endocardial borders of all slices at end-diastole and end-systole were traced manually and included papillary muscles and trabeculation in the blood pool volume. End-diastolic volume (EDV), end-systolic volume (ESV), stroke volume (SV = EDV − ESV), and ejection fraction (EF = SV/EDV × 100) were calculated, correlating SV with aortic and pulmonary valve phase-contrast flow measurements.

Normally distributed continuous data were reported as mean ± standard deviation. Categorical variables were reported as numbers and percentages. Student's independent t-test was used to compare continuous variables. A p-value of less than 0.05 indicated a significant difference.

[1]MR scanning has not been established as safe for imaging fetuses and infants less than two years of age. The responsible physician must evaluate the benefits of the MR examination compared to those of other imaging procedures. Note: This disclaimer does not represent the opinion of the authors.

Results

The mean patient age was 14.57 ± 4.92 years (range: 7–21). 10 patients (50%) were male. 11 had CHD, while the rest had suspected or known cardiomyopathy. The mean heart rate was 80.89 ± 14.48 bpm (range: 55–110 bpm). Demographic details and diagnoses are provided in Table 2.

Our preliminary results showed that there were no statistically significant differences ($p > 0.05$) in EDV, ESV, SV, or EF for left ventricular and right ventricular measurements using either bSSFP or CS sequences. Although not significant, for CS there was a small tendency toward underestimation of all volumes (which was more evident for the RV), and toward overestimation of EF. Ventricular measurements obtained with both sequences are summarized in Table 3. Notably, mean reconstruction time was quite long for CS, with an approximate mean time of 120 ± 15 seconds (range: 100–150) to complete the whole volume.

Characteristics	Mean ± SD (range)
Male/Female	10/10
Age (years)	14.57 ± 4.92 (7–21)
Height (cm)	147.76 ± 17.21 (110–178)
Weight (kg)	48.4 ± 17.09 (26–72)
BSA (m^2)	1.46 ± 0.33 (0.9–2)
Heart rate (bpm)	80.89 ± 14.48 (55–110)
Cardiomyopathy	8
Aortic coarctation	3
Aortic stenosis	2
Tetralogy of Fallot (repaired)	2
Transposition of the great arteries (repaired)	2
Aortopathy	1
Congenitally corrected transposition of the great arteries	1
Myopericarditis	1

Table 2: Patient demographics and diagnoses.
BSA = body surface area; SD = standard deviation

Discussion

In our study, real-time CS cardiac cine imaging showed good diagnostic quality and performance, with slightly lower spatial and temporal resolution (Figs. 1, 2) but no significant differences between calculated ventricular volumes compared to conventional segmented bSSFP sequences. In some cases where irregular heart rhythm or difficulties in breath-holding caused mild motion artifacts on bSSFP images, free-breathing CS cardiac cine provided visually more robust images for volume quantification (Fig. 3). From a clinical point of view, reproducible ventricular quantification is paramount, irrespective of differences in image quality, as significant biases may impact clinical decision making [6, 7]. However, poorer edge definition and myocardial blood pool contrast still posed a major challenge for accurate ventricular segmentation with CS. This aspect might also vary depending on the type of CS sequence employed, with spiral *k*-space trajectories showing better reported results compared to Cartesian acquisition [3, 6]. However, we believe that this difficulty was substantially mitigated by the use of phase-contrast imaging to obtain stroke volume reference values. Although not specifically evaluated, our impression was that the straightforward analysis of CS images without phase-contrast correlation might not yield the same results, as minor but frequent adjustments were required to achieve values that were in accordance with flow measurements. End-diastolic volumes would probably be slightly underestimated and end-systolic volumes would

Measurements	bSSFP	CS	p
LV EDV (mL)	135.8 ± 48.1	133.2 ± 50.2	0.87
LV ESV (mL)	53.5 ± 24.9	52.7 ± 27.6	0.91
LV SV (mL)	82.5 ± 25.5	80.7 ± 25.3	0.82
LV EF (%)	61.6 ± 7.0	61.9 ± 7.4	0.9
RV EDV (mL)	140.2 ± 39.9	134.6 ± 37.3	0.6
RV ESV (mL)	59.5 ± 21.6	55.9 ± 19.6	0.58
RV SV (mL)	80.9 ± 21.2	74.3 ± 24.2	0.36
RV EF (%)	58.5 ± 6.4	59.1 ± 6.7	0.79

Table 3: Ventricular measurements obtained with bSSFP and CS cine imaging.
bSSFP = balanced steady-state free precession; CS = Compressed Sensing; EDV = end-diastolic volume; EF = ejection fraction; ESV = end-systolic volume; LV = left ventricular; RV = right ventricular; SV = stroke volume
Ventricular measurements are expressed as mean ± standard deviation.

probably be slightly overestimated otherwise, due to blood pool being excluded from the contours in diastole and to myocardial mass being included in systole, particularly for the right ventricle [6]. The decision to employ phase-contrast correspondence was made because we normally use it in our everyday clinical practice and it is frequently described in children and CHD [8]. Nevertheless, it is clearly a major limitation of our study. A further drawback of CS was the long total reconstruction time [3]. In some cases, it reached several minutes, even though images of the first few slices were generally visible after about 20 seconds. Regardless, while not unacceptable, this could be a significant obstacle to adopting CS in everyday clinical practice. Another limitation of our study is the small and heterogeneous population considered. The group contained both cardiomyopathies and CHD, and there were

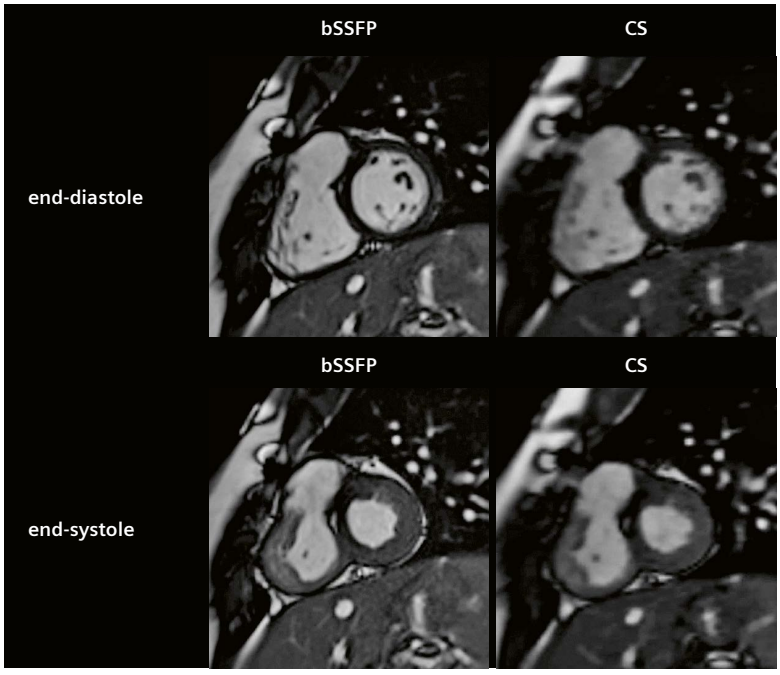

1 End-diastolic (top row) and end-systolic (bottom row) frames of conventional segmented balanced steady-state free precession (left column) and real-time Compressed Sensing cardiac cine sequences (right column) in a 13-year-old patient affected by tetralogy of Fallot treated with transannular patch and ventricular septal defect closure. The chemical shift artifact at the antero-basal interventricular septum corresponds to the area of ventricular septal defect repair.

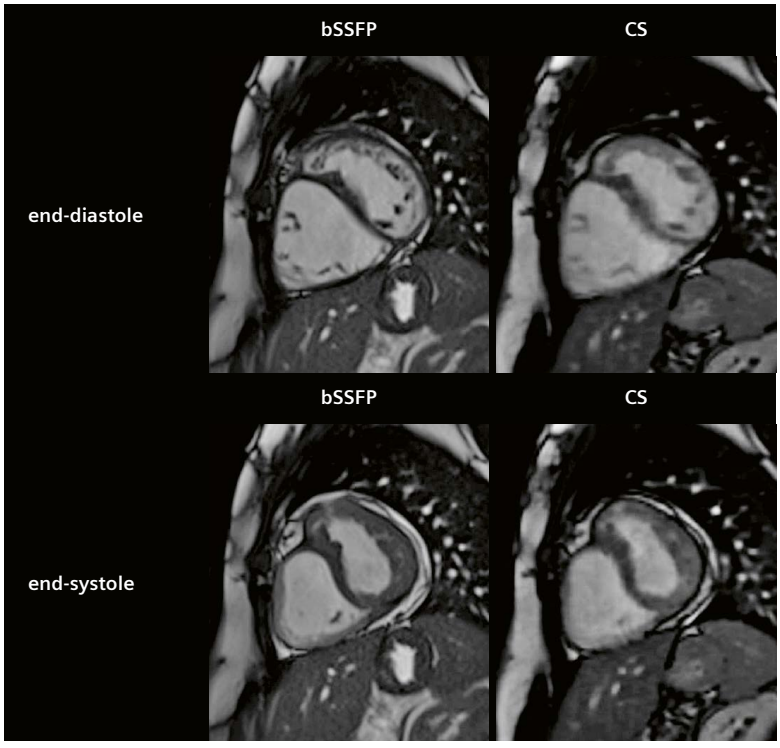

2 End-diastolic (top row) and end-systolic (bottom row) frames of conventional segmented balanced steady-state free precession (left column) and real-time Compressed Sensing (right column) cardiac cine sequences in a 15-year-old patient with congenitally corrected transposition of the great arteries. The anterior chamber is the subpulmonary left ventricle, which is dilated due to the presence of an ostium secundum interatrial defect. The posterior chamber is the hypertrophied systemic right ventricle.

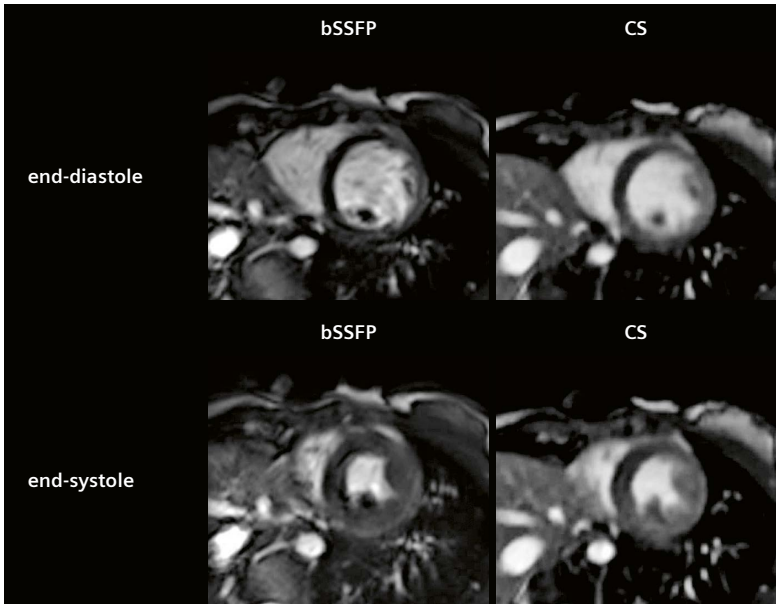

3 End-diastolic (top row) and end-systolic (bottom row) frames of conventional segmented balanced steady-state free precession (left column) and real-time Compressed Sensing (right column) cardiac cine sequences in a 9-year-old girl with sporadic ventricular ectopic beats and occasional difficulty performing breath-holds. Conventional bSSFP images show mild motion artifacts.

technical differences in two cases (slice thickness of 8 mm instead of 7 mm). Moreover, we did not calculate ventricular mass. Finally, the evaluation by two readers in consensus made it impossible to assess intra- and interobserver agreement. Future studies on larger and more homogeneous groups of patients could provide more robust results and evaluations of observer agreement.

In conclusion, we believe that CS definitely has potential for use in the pediatric population. However, more work is needed to assess its performance and to overcome its current limitations.

References

1 Lustig M, Donoho D, Pauly JM. Sparse MRI: the application of compressed sensing for rapid MR imaging. Magn Reson Med. 2007;58(6):1182–95.
2 Kido T, Kido T, Nakamura M, Watanabe K, Schmidt M, Forman C, et al. Compressed sensing real-time cine cardiovascular magnetic resonance: accurate assessment of left ventricular function in a single-breath-hold. J Cardiovasc Magn Reson. 2016;18(1):50.
3 Haji-Valizadeh H, Rahsepar AA, Collins JD, Bassett E, Isakova T, Block T, et al. Validation of highly accelerated real-time cardiac cine MRI with radial k-space sampling and compressed sensing in patients at 1.5T and 3T. Magn Reson Med. 2018;79(5):2745–51.
4 Goebel J, Nensa F, Schemuth HP, Maderwald S, Quick HH, Schlosser T, Nassenstein K. Real-time SPARSE-SENSE cine MR imaging in atrial fibrillation: a feasibility study. Acta Radiol. 2017;58(8):922–8.
5 Voit D, Zhang S, Unterberg-Buchwald C, Sohns JM, Lotz J, Frahm J. Real-time cardiovascular magnetic resonance at 1.5 T using balanced SSFP and 40 ms resolution. J Cardiovasc Magn Reson. 2013;15:79.
6 Steeden JA, Kowalik GT, Tann O, Hughes M, Mortensen KH, Muthurangu V. Real-time assessment of right and left ventricular volumes and function in children using high spatiotemporal resolution spiral bSSFP with compressed sensing. J Cardiovasc Magn Reson. 2018;20(1):79.
7 Oosterhof T, van Straten A, Vliegen HW, Meijboom FJ, van Dijk APJ, Spijkerboer AM, et al. Preoperative thresholds for pulmonary valve replacement in patients with corrected tetralogy of Fallot using cardiovascular magnetic resonance. Circulation. 2007;116(5):545–51.
8 Fratz S, Chung T, Greil GF, Samyn MM, Taylor AM, Valsangiacomo Buechel ER, et al. Guidelines and protocols for cardiovascular magnetic resonance in children and adults with congenital heart disease: SCMR expert consensus group on congenital heart disease. J Cardiovasc Magn Reson. 2013;15:51.

Contact

Aurelio Secinaro, M.D.
Bambino Gesù Children's Hospital IRCCS
Department of Imaging
Piazza Sant'Onofrio 4
00146 Rome
Italy
Phone: +39 06 68592790
Fax: +39 06 68594561
aurelio.secinaro@opbg.net

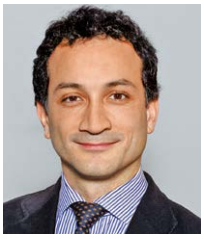
Aurelio Secinaro


Davide Curione

4-Dimensional Phase Contrast Imaging in Congenital Heart Disease: How We Do it

Timothy C. Slesnick, M.D.; Sassan Hashemi, M.D.

Emory University School of Medicine, Children's Healthcare of Atlanta, Atlanta, GA, USA

Introduction

The field of phase contrast (PC) imaging has expanded greatly in the last 30 years. The fundamental principle that a moving nuclei will experience a phase shift when subjected to a magnetic field gradient that is proportional to the flow velocity, and thus measurement of this phase shift can allow measurement of the velocity of the nuclei [1, 2], has transformed our approach to flow quantification. Today, cardiac magnetic resonance (CMR) is the gold standard for quantification of vascular flows [3, 4]. Though initially confined to 2-dimensional (2D) measurements of either through plane or in-plane flow, the development of 4-dimensional phase contrast imaging (4D flow) was first applied to central nervous system vasculature in the late 1980's [5] and subsequently to cardiovascular blood flow in the late 1990's [6] and has opened new avenues and insights.

Two-dimensional phase contrast imaging is now a routine part of most CMR studies in pediatric and adult patients with congenital heart disease (CHD). Though options exist for both breath held and free breathing 2D PC sequences, our lab, like most, prefers to use free breathing techniques with multiple signal averages (NSA). Assessment of flow in the aorta (Ao) and main pulmonary artery (MPA) allows for quantification of systemic (Qs) and pulmonary blood flow (Qp). Flow in the right pulmonary artery (RPA) and left pulmonary artery (LPA) allows quantification of differential pulmonary blood flow, as well as validation of the MPA flow.

In the present work, we delineate our current practices with 4D flow imaging in children[1] and young adults with CHD, with a focus on practical tips for users to bring this technology to their programs and their patients. Illustrative cases are given with some of the ever-expanding array of applications for this technology. Finally, several recent advances are highlighted which promise to continue to evolve this new technique.

Works in progress 4D Flow

The fundamental tenants of 4D flow are flow encoding in all three directions (x, y, z-axes). True 4D flow sequences obtain a 3D volume, with the fourth dimension representing time. The works in progress (WIP) 4D flow pulse sequence[2] we currently utilize is WIP 785A, first released in January of 2016 (Figures 1A and 1B, Clip 1 – to access the .avi's please visit www.siemens.com/4Dflow). The sequence utilizes 3D Cartesian sampling with flow encoding and generalized auto-calibrating partially parallel acquisition (GRAPPA) acceleration where the reference lines are acquired separately (aka ePAT). Acceleration can be applied in both phase encoding and the partition encoding directions since the dataset is a true 3D volume, with the expected decrease in signal to noise (SNR) of square root of each of the acceleration factors. When acceleration is applied in both phase encoding and partition encoding directions, SNR is decreased by the product of those

[1] MR scanning has not been established as safe for imaging fetuses and infants less than two years of age. The responsible physician must evaluate the benefits of the MR examination compared to those of other imaging procedures. Note: This disclaimer does not represent the opinion of the authors.

[2] WIP, the product is currently under development and is not for sale in the US and in other countries. Its future availability cannot be ensured.

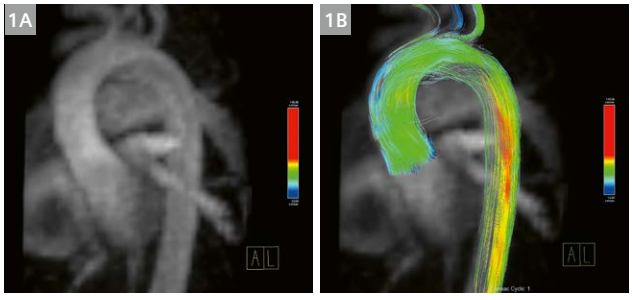

1 4D flow magnitude **(1A)** image of an aortic arch obtained using WIP 785A, as well as particle trace image **(1B)**.

factors, but the resultant change in the geometry factor, which also influences signal to noise loss, is less pronounced than if all acceleration is performed in one direction, so acceleration of 2 x 2 does result in less signal loss than 4 x 1. One final point on acceleration is that running 4D flow sequences post-contrast will obviously result in more signal, and thus more acceleration can be applied without loss of data integrity. On our 1.5 Tesla scanner, we typically run our 4D flow sequences post contrast (if contrast is given during the routine exam), and apply ePAT in either the phase encoding direction alone with a factor of 3 or in both the phase and partition encoding directions with factors of 2 for each (2 x 2). If no contrast is given to the patients during routine exam, we typically run the 4D flow sequence applying parallel imaging with a factor of 2 in the phase encoding direction alone.

In order to obtain this quantity of data, even for a small slab of coverage, requires substantial *k*-space sampling, far longer than is possible in a breath held study. In order to minimize respiratory motion, a respiratory navigator is typically employed (though as delineated below in the product section free breathing techniques with multiple signal averages can also be used). A cross-beam respiratory navigator is positioned on the dome of the diaphragm, and an acceptance window of ± 3–5 mm is typically used (± 3 mm for smaller children, ± 4–5 mm for larger children and young adults). Some users have reported using larger respiratory navigator windows, up to ± 8 mm, with acceptable degree of motion artifacts, but we do not have personal experience with this broad a range of respiratory navigated acceptance.

The WIP sequence can be run with either prospective or retrospective gating. In patients with an irregular heart rate, it is possible to use prospective ECG gating with a reduced acquisition window to avoid data acquisition spanning into the early systolic phase of the following heartbeat. In our experience, however, we find that even with optimal modifications to the 4D flow sequences, the validity of the data due to the inherent fluctuations in the hemodynamics of patients with significant arrhythmias continues to be challenging, and typically we choose not to perform 4D Flow imaging in these patients.

Using retrospective gating, the number of reconstructed phases ("Calculated phases") can be set by the user (Figure 2). Caution should be employed, however, that the reconstructed phases will be interpolated from the true number of cardiac phases acquired, which is determined by the heart rate and the repetition time. For example, we typically acquire 3 segments per heart beat per cardiac phase, which results in a TR of 58.2 msec. In a patient with a heart rate of 75 beats per minute (bpm), and a resultant cardiac cycle of 800 msec, this would yield 13 true cardiac phases. Though the interface allows the user to set the number of reconstructed phases to any desired value, our experience has shown that using slightly less than double the number of true phases produces values which correlate well with 2D PC data. We therefore typically calculate the actual number of phases for a given patient and sequence prescription, double the value, and then decrease slightly to allow all reconstructed phases to have some component of unique data.

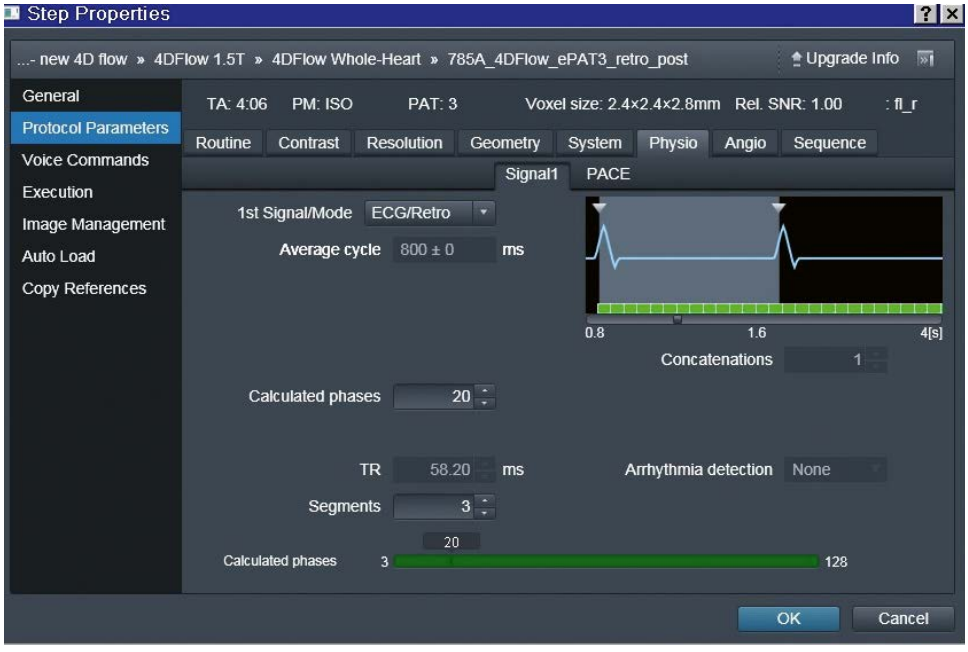

2 Screen shot demonstrating the Physio tab on the user interface where the number of "Calculated Phases" can be adjusted and the number of true phases can be calculated (cardiac cycle length divided by the TR).

Though this manipulation may seem a bit cumbersome, it allows the user to tailor the sequence and results to the individual patient. For smaller children with faster heart rates, it may be necessary to decrease the number of segments to 2 to allow a shorter TR and thus more reconstructed phases. Conversely, in older patients with slower heart rates (< 50–55 bpm) we will often increase segments to 4 to speed up the acquisition without compromising the number of reconstructed phases. Since each change to the number of segments has a direct correlation to the scan length, these manipulations must be made very thoughtfully. Increasing from 3 to 4 segments will cut acquisition time by 25%, while decreasing from 3 to 2 segments will require 50% longer. For most of our scans, we aim to reconstruct 16–25 phases, adjusting the parameters as needed.

As with any 3D dataset, obtaining isotropic voxels is advantageous as it allows the user to reformat/slice the data in any plane without loss of resolution. With the 4D Flow WIP, we typically decrease the phase and slice encoding direction percentages, so the actual obtained voxels are not quite isotropic, but the reconstructed voxels are. The user must remember that the voxel size is determined by the field of view (FOV), matrix (base resolution), and the slice thickness. FOV and matrix can be changed, but this does affect the in plane resolution and the SNR. The sequence will allow decreasing slice thickness to 1.5 mm, though in our lab we typically run the sequence at 2 mm isotropic.

Slice coverage is prescribed based on the anatomy of interest. For aortic pathology, simply covering the aortic arch (with care taken that the entirety of the aortic root, which is typically the largest portion of the thoracic aorta, is fully covered) is often sufficient. Aligning the plane in a sagittal oblique geometry along the long axis of the arch allows maximal coverage in a minimum number of slices. Depending on the child's (and aorta's) size, this can often be accomplished in as few as 12–14 slices, though with more dilated aortas 16–20 slices may be necessary. For alternative underlying pathologies, coverage may be needed for the entire ventricular volumes (when heart failure or inflow/outflow assessment is desired), branch pulmonary arteries (for TOF and single ventricle [SV] patients), or systemic or pulmonary veins (particularly in patients with anomalous returns). These cases often require wider coverage and thus more slices, so the balance between voxel size and acquisition time is paramount when planning these scans. For most 4D Flow datasets, we prescribe a straight or oblique sagittal plane of some type. Axial geometries can be used if only branch PA flow is desired, but coverage in the z-direction with axial slices is often quite limited unless large slabs are obtained. Coronal orientations are also possible, but will require phase encoding in the left-right direction (as opposed to anterior-posterior in sagittal or axial oblique geometries), so FOV and acquisition duration will be increased. Additionally, some analysis platforms have difficulties processing coronal 4D Flow datasets, though this can be overcome with manipulation on the user interface.

The final component we prescribe is our velocity encoding upper limits (VENC). As explained in the case examples below, we routinely set the VENC at the highest velocity value within the imaging prescription of interest to avoid aliasing. For most aortic and pulmonary artery studies we use either 150 or 200 cm/sec, unless there is known stenosis of a valve or great artery. For single ventricle studies where the bidirectional Glenn (BDG) or Fontan circuit are the primary area of interest, either 100 or 120 cm/sec is used, with the knowledge that aliasing may occur in the aorta but that is outside the primary vessels of interest (if quantification in the aorta is desired in an SV patient, then 150 or 200 cm/sec is used).

Product 4D Flow options

True 3D datasets

The current software platforms for Siemens Healthineers magnets allow the user to prescribe a 4D Flow dataset with a true 3D volume and flow encoding in all three directions using the product sequences alone (Figures 3A and 3B, Clip 2). This derivation must start with a base product sequence which utilizes prospective ECG triggering (more on this in a moment). On our magnet (MAGNETOM Avanto^{fit} on software platform *syngo* MR E11B), we have built this option from the underlying, "BEAT_FQ" sequence, though other options are possible. On *syngo* MR E11B, the current product sequence will not support a 3D acquisition when parallel imaging with GRAPPA and reference lines obtained using "GRE/separate" (aka ePAT) is employed, so

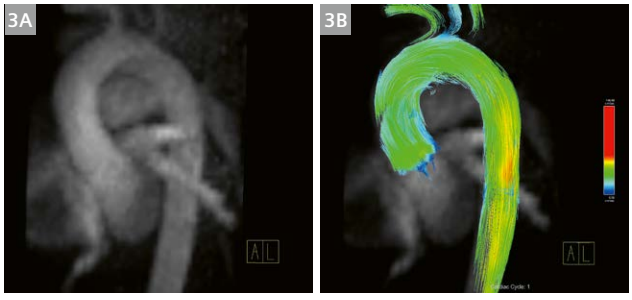

3 4D flow magnitude **(3A)** image of an aortic arch obtained using the product 4D flow derivative, as well as particle trace image **(3B)**.

under the Resolution tab, iPAT subtab, "Integrated" must be selected to change to iPAT parallel imaging (Figure 4). On the *syngo* MR E11C and subsequent platforms 3D acquisitions are possible with ePAT image acceleration. For the product 3D acquisition, parallel imaging can only be used in the phase encoding direction. We typically run the sequence with 3 fold acceleration and perform it post-contrast to ensure adequate signal. Next, under the Sequence card, Part 1 subtab, the Dimension can be changed from 2D to 3D (for *syngo* MR E11B this option will not be available until the parallel imaging is changed from ePAT to iPAT) (Figure 5). This change will automatically convert the flow direction from "Single dir" to "Single vel" (which results in flow encoding in all three directions, represented as F>>H, Throughplane, and A>>P in a sagittal geometry) (Figure 6).

Product phase contrast sequences do not have an option for a respiratory navigator, and since data acquisition is far too long for an individual breath-hold, free breathing techniques with multiple signal averages

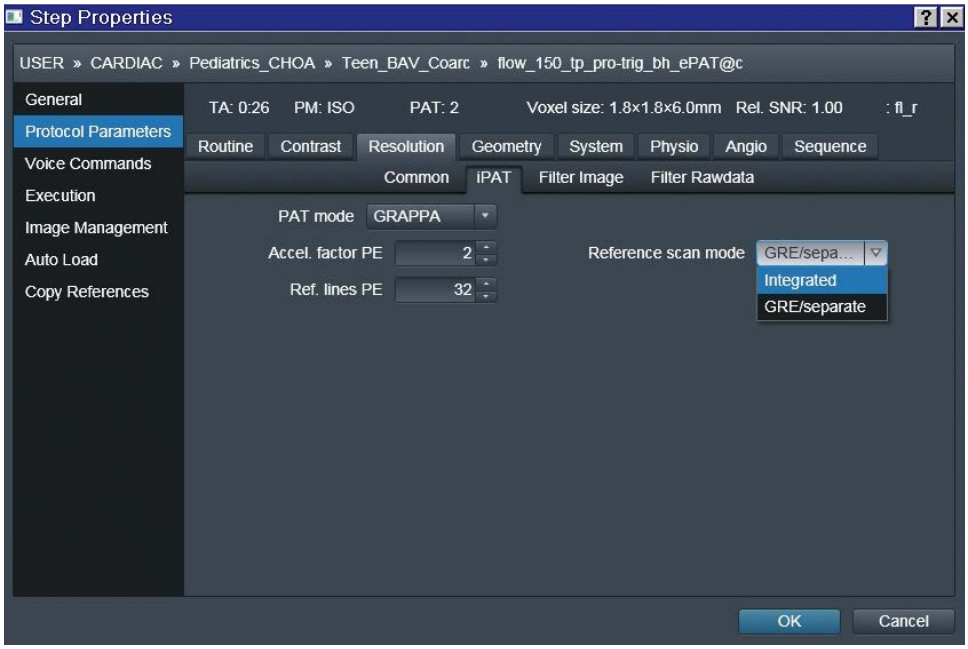

4 Screen shot illustrating how the reference line acquisition must be changed from "GRE/separate" to "Integrated" (aka ePAT to iPAT) in order to convert the sequence as described in the text.

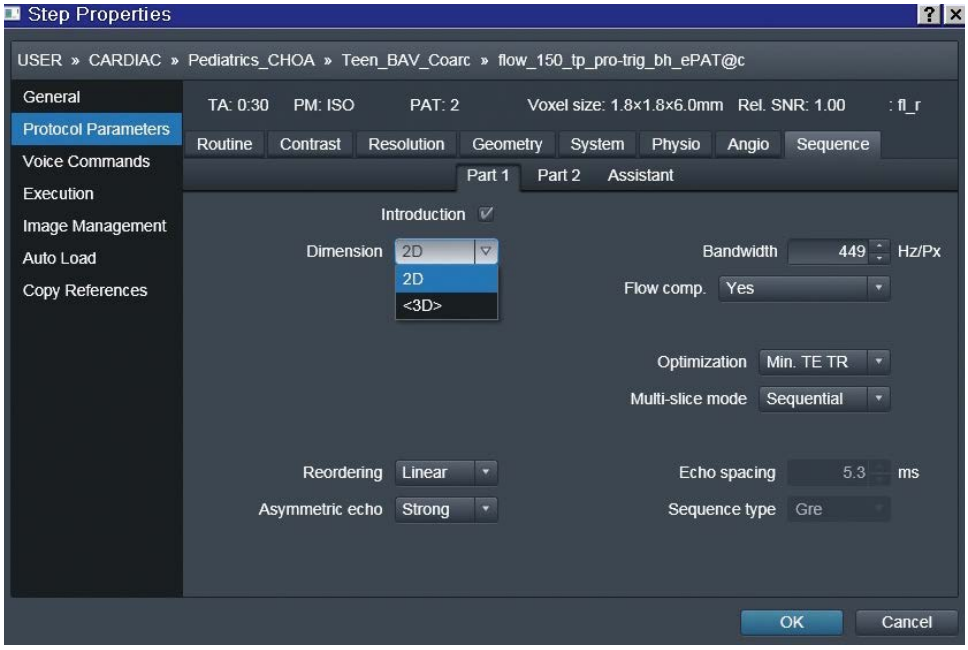

5 Screen shot illustrating how the 2D product phase contrast sequence can be changed to a 3D volume under the Sequence tab, Part 1.

are needed. Since this variant does produce a true 3D volume, it is less respiratory motion sensitive, so we typically acquire 2 NSA.

Slice thickness can be as thin as 1 mm, though again we typically run this variant at 2–2.5 mm in the interest of acquisition time. FOV and matrix are adjusted to ensure isotropic voxels. Slice orientation and number are set to cover the regions of interest. The VENC is set as described above.

The largest difference in this variant of 4D Flow is that the Siemens Healthineers current product sequence does not support retrospective gating for 3D volumes. This fact has three important consequences. First, the end of diastole cannot be captured, and thus the sequence represents only a large portion (not the entirety) of the cardiac cycle. Second, unexpected pronounced heart rate variability result in challenges with data sampling both in mistiming at the end of the cardiac cycle and missed acquisition on the beats following shorter cardiac intervals. Finally, with prospective gating, the number of phases is fixed at the

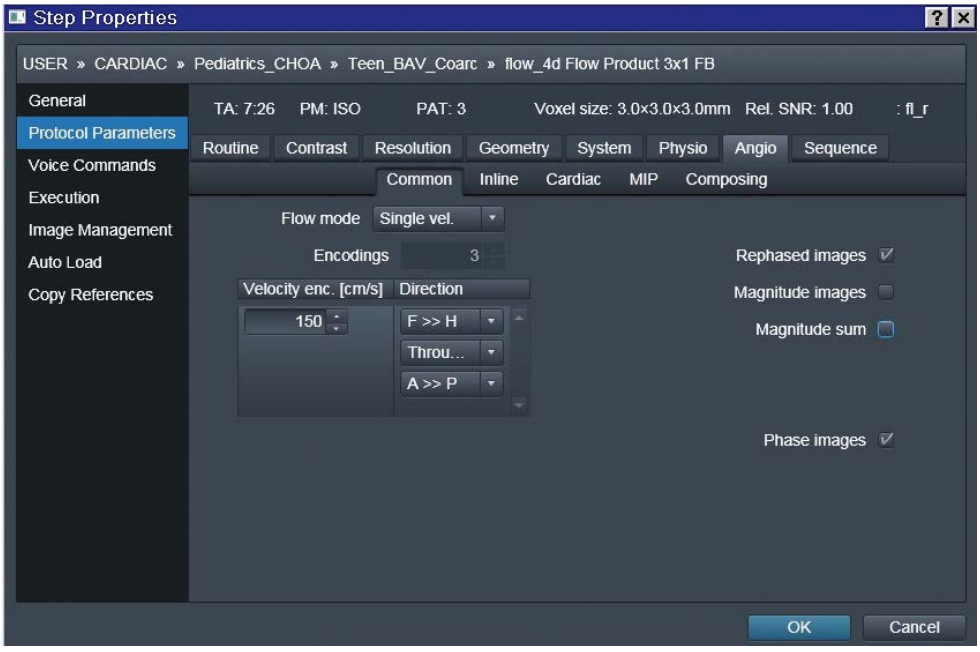

6 Screen shot illustrating the change to the "Single vel" option with velocity encoding in all three directions (F>>H, Throughplane, and A>>P) under the Angio tab.

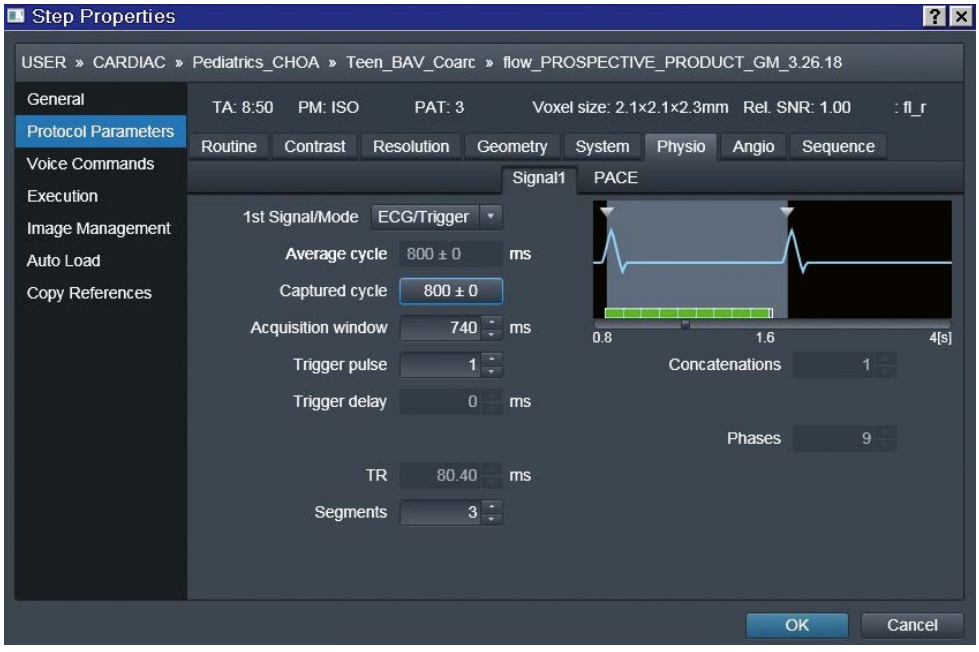

7 Screen shot demonstrating the Physio tab on the user interface where the number of phases is displayed on the right hand side. Note, that compared to the WIP version, there is no input for "Calculated Phases" since this sequence is prospectively gated.

true number of acquired phases and cannot be interpolated to yield more reconstructed phases. Thus for this product 4D Flow sequence on a patient with an average heart rate of 75 bpm, a resultant cardiac cycle of 800 msec, the repetition time would be 80.4 msec (assuming 3 segments are selected) and there will only be 9 phases produced (Figure 7). If the user desires more phases, the number of segments must be reduced (with resultant increased acquisition time).

"Pseudo 4D Flow": Contiguous stack of 2D slices

An additional alternative to the product 4D Flow described above is acquisition of a contiguous stack of 2D slices, each with flow encoding in all three directions, which in summation represent a 3D volume (Figures 8A and 8B, Clip 3). The sequence can again be built starting with the base "BEAT_FQ" sequence. It is important when setting up the multiple 2D slices to utilize no slice gap (aka "Distance factor") (Figure 9). Parallel imaging can remain with "GRE/separate", and similar to the true 3D product sequence, acceleration is only possible in the phase encoding direction. We typically run the sequence post-contrast with 3 fold acceleration.

Since there is no option for respiratory navigator on the product flow sequences, again multiple signal averages are employed. As opposed to the variant described above, 2D slices are more motion sensitive, so we typically utilize 3 NSA with the patient free breathing (though with small patients and very shallow respirations, we have utilized 2 NSA with this variant).

With a contiguous stack of 2D slices, minimum slice thickness is 2.8 mm, which means that even with FOV and matrix optimization, the isotropic voxel size is larger than on other 4D flow variants. Typically, we run this variant with 3 mm isotropic voxels, which does result in decreased resolution which is readily apparent on the magnitude images (Figures 10A and 10B), but as explained below, still produces reasonable data for flow visualization and hemodynamic analysis.

Under the Angio tab, "Flow mode" can be manually changed from the standard "Single dir" to the "Single vel" (Figure 6). The VENC is set to an appropriate value.
The contiguous stack of 2D slices variant does have the advantage that it, like the WIP, can be run with retrospective gating, and thus the number of reconstructed phases can be set by the user (Figure 11). As described above, we do not recommend setting the total phases greater than twice the number of actual phases as

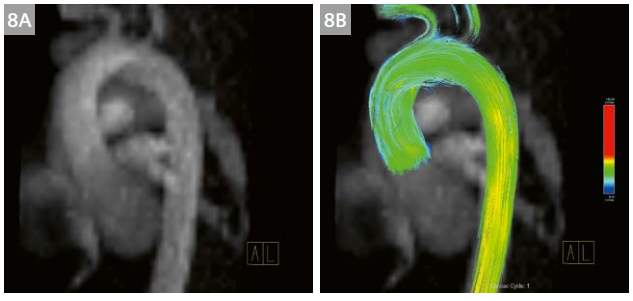

8 4D flow magnitude **(8A)** image of an aortic arch obtained using the product "pseudo 4D flow" stack of 2D slices derivative, as well as particle trace image **(8B)**.

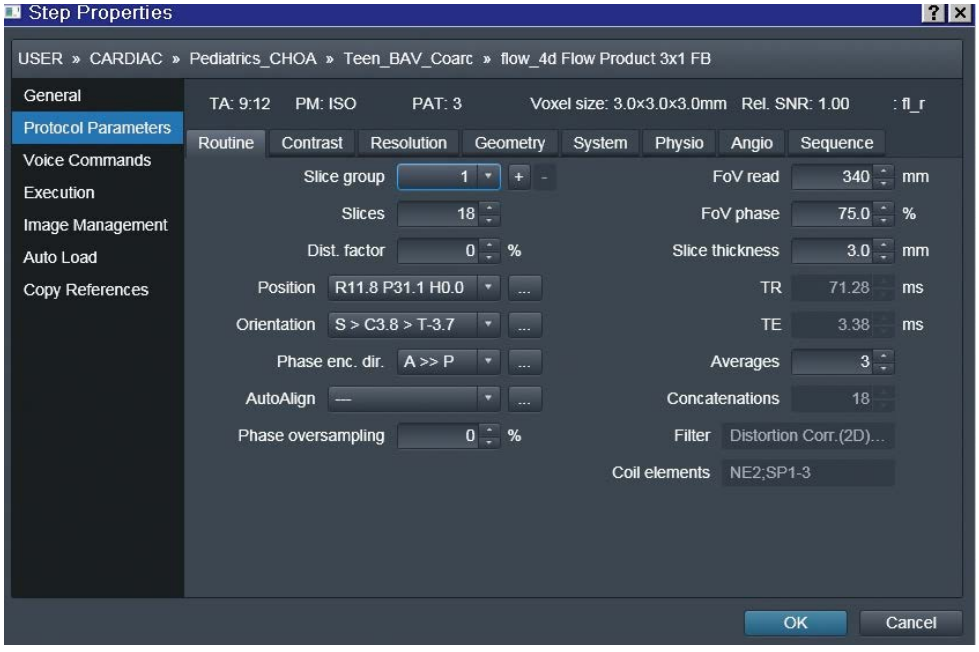

9 Screen shot of the Routine tab where the stack of slices are composed with no gap ("Distance Factor").

determined by the repetition time and the heart rate, but you can achieve improved temporal resolution compared to the other product variant (where prospective gating is the only option).

In our experience, for similar patient's conditions and imaging data size, the continuous stack of 2D slices technique requires a shorter acquisition time than the true 3D volume product variant. This time saving does come at a price of worse spatial resolution, but offers the user improved temporal resolution compared to the other product option and also does allow retrospective gating. As described below, for flow visualization and simple quantification, we have found the resolution of this technique to be sufficient.

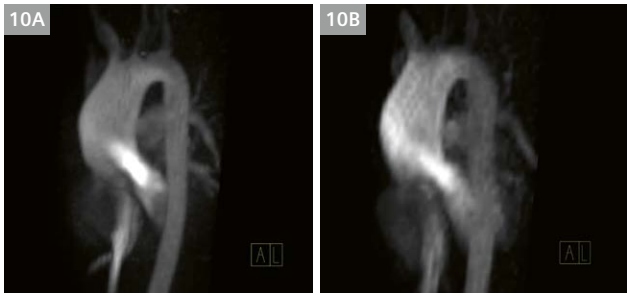

10 Comparison of imaging on the same patient with both WIP **(10A)** and product pseudo 4D flow images **(10B)**. Note that the spatial resolution is not as good with the latter technique.

Analysis of data

Currently, we use prototype Siemens Healthineers "4Dflow v2.4" software for the majority of our 4D flow post-processing. In its current form, it is a work-in-progress software intended only for research which is equipped with good visualization and analytic options. User interface is simple and familiar since it uses the same format as in other MRI software packages in the Siemens Healthineers *syngo* ecosystem. It is divided into six consecutive tabs which guide the user from loading the data to visualization of 4D flow.

There is no PACS integration available at this time and 4D flow data should be loaded from a local disk. After loading the study ("Study Load" tab), the user can navigate between different phases and slices to find the desired structure and check for gross aliasing in different velocity encoding directions. You can also crop the dataset in phase and frequency encoding directions retrospectively (Crop Box). This helps to minimize the use of processing resources by the software, provides more accurate background phase correction and also reduces noise during visualization.

The second tab, "Corrections", provides background phase correction, anti-aliasing and motion tracking. Background phase correction extracts the stationary tissue by looking at the variance of velocities in each voxel which is deemed to be the lowest for stationary tissue. The resultant velocities in each slice are corrected so that the stationary tissue has zero velocity. As mentioned previously, cropping the dataset in the previous tab helps to eliminate wrap and ghosting artifacts which may

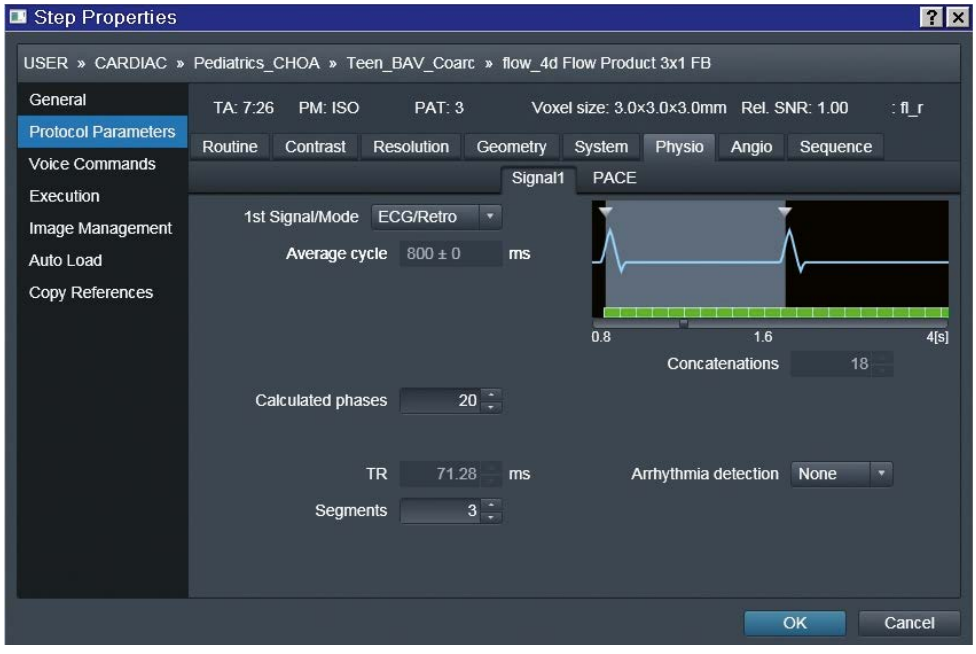

11 Similar to Image 2, the Physio tab on the user interface with the stack of 2D slices technique gives the user the ability to input the number of "Calculated Phases".

interfere with stationary tissue extraction. The anti-aliasing algorithm looks for very large opposite jumps in the velocity-time curve for each voxel and removes the wrap introduced by insufficient velocity range. Finally, motion tracking uses a symmetric deformable registration technique to track the segmented anatomy, analysis planes and particle seeds over time. Note that motion tracking requires at a minimum of 16 slices to function properly, per the Siemens Healthineers user manual. We recommend utilizing all three correction techniques to provide the most robust data.

Before proceeding to the next tab, we adjust the "segmentation threshold" from the tools tab in the bottom toolbox. This slider controls the threshold-based segmentation according to the signal intensity. The goal is to find the balance between including the desired anatomy without going beyond vessel boundary (Figure 12). After adjusting the threshold, the mesh transparency can be adjusted or turned off from the display tab if desired.

Since the majority of our 4D flow patients have complex and abnormal flow patterns (e.g. eccentric and helical flow in ascending aorta in stenotic bicuspid aortic valve or low velocity and opposing flow directions in Fontan circuit), we have opted not to use centerline and vessel model extraction available in "Segmentation" tab and skip to "Flow evaluation". These are options within the software platform and can streamline the workflow for patients with laminar flow, but for the majority of our cases this aspect of the software often produces unreliable results (Figure 13).

Next, under the "Flow evaluation" tab, there are different functions located under sub-tabs: "Planes" and "Calc". Under Planes, the user can draw contours along the vessel(s) of interest for flow quantification and particle seeding for visualization. We recommend setting the overlay to "none" for easier recognition of the anatomy (Figure 14). One can then navigate through the vessel in the 3D viewer on the left hand side of the screen. Note that contours can only be drawn in the left upper window, marked by a red border. Therefore, the red orthogonal line should always be perpendicular to the flow at the desired location. Once a contour is drawn, the flow-time curve will be automatically shown in the lower section of the screen. After all contours are added, user can switch to calculation tab to get detailed flow quantification (e.g. net flow, velocities, regurgitation fraction) through each contour. This is a valuable option to cross-examine 2D phase contrast flow data with 4D flow, especially in cases when 2D flow data quality is suboptimal (Figure 15).

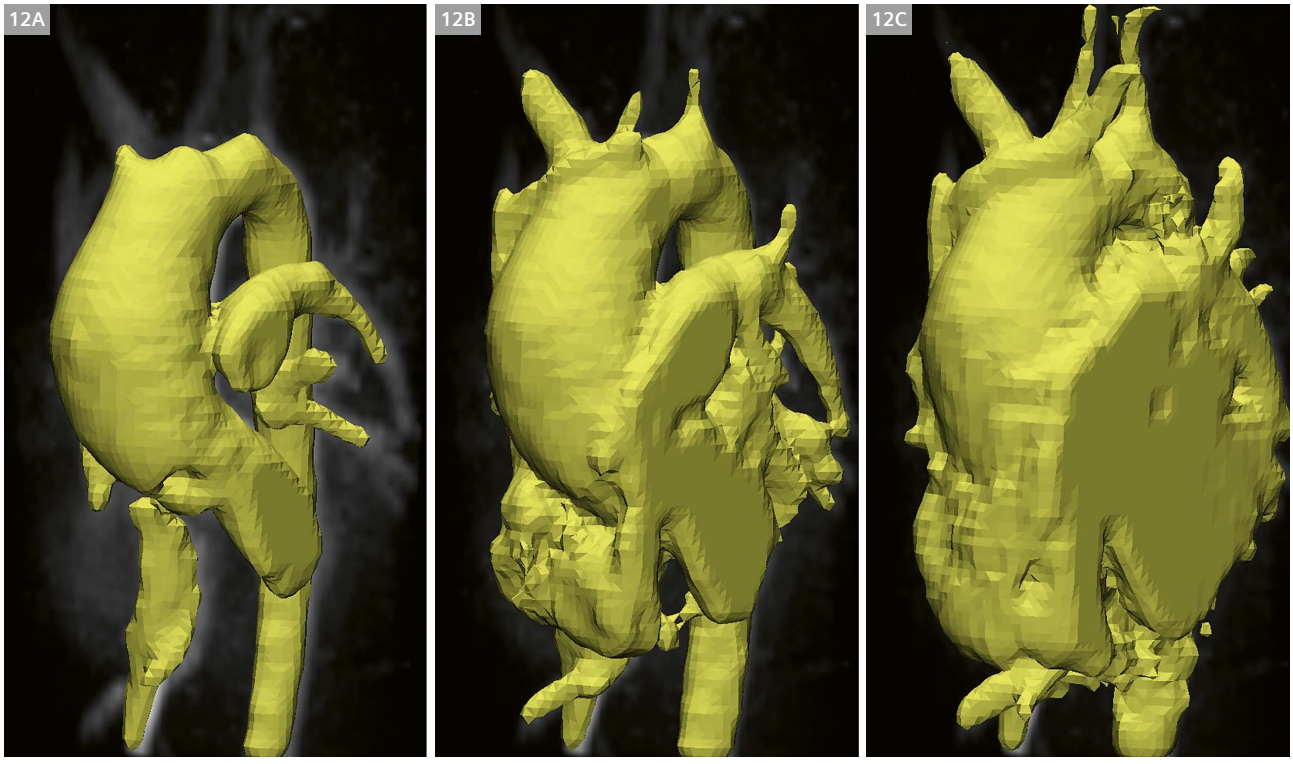

12 Segmentation with the Threshold slider: inadequate **(12A)**, adequate **(12B)**, excessive **(12C)** threshold.

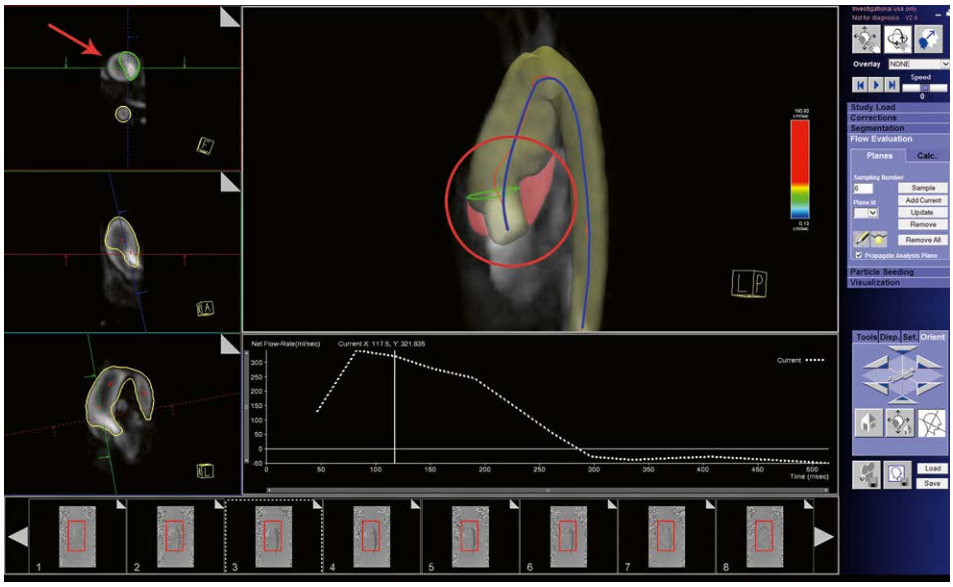

13 Unsuccessful centerline extraction and volume segmentation in a patient with bicuspid aortic valve. The true centerline (blue) and unsegmented aortic volume (bright red) are shown. Arrow points to the unsegmented ascending aortic lumen in axial plane.

14 Switching the overlay preset to "none" makes for easier navigation of the anatomy in the left panel (arrow).

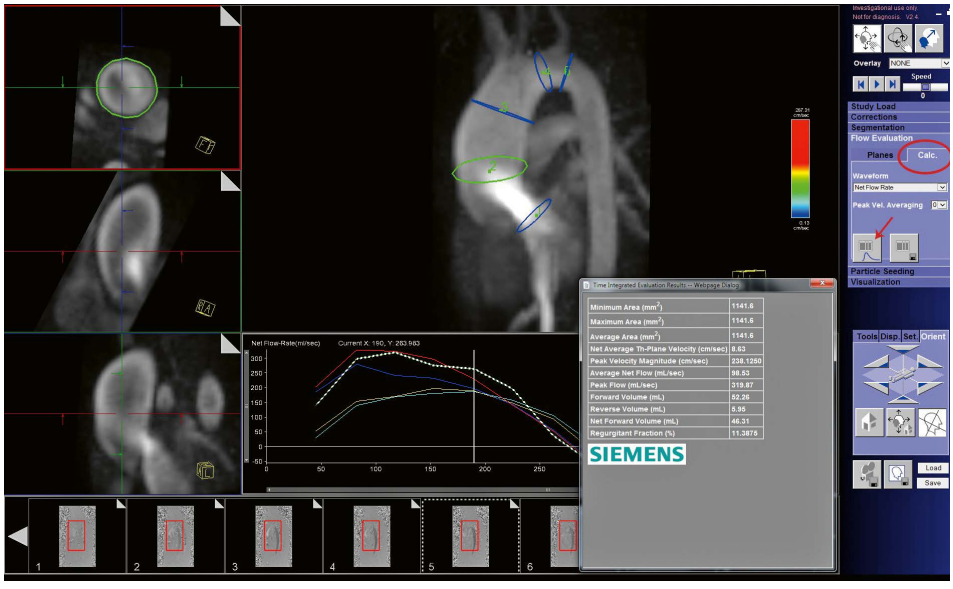

15 Flow quantification through the desired contour by switching to the "Calc" tab in flow evaluation.

The focus of the last two tabs is visualization of 4D flow. The "Particle seeding" tab allows the user to seed each contour drawn in the previous step with either the same or different colors (up to 4 colors). In cases where there are multiple inflows, the user can assign different colors to better visualize flow contribution and behavior during mixing (e.g. color coding SVC and IVC in Fontan circuit or pulmonary veins and mitral regurgitation jet in mitral valve disease). The user can also choose between seeding the drawn contours or the entire segmented volume by switching between volume and planes in the drop down menu. There are options to control the density of particle seeds, intervals in which they are emitted and the number of cardiac cycles they are visualized throughout. In our lab, we typically only change particle density for better visualization. In general, we use higher density in cases with larger voxel size (50–60% for 2–2.5 mm voxels and 70–80% for 2.6–3 mm voxels).

The final tab offers three visualization options. "Vector Field" illustrates the velocity vectors summation in the segmented planes or volume for each voxel over the cardiac cycle. "Particle Traces" continuously creates time-resolved pathlines originating from the seed planes to visualize the dynamic change in trajectory and velocity. "Streamlines" captures the instantaneous 3D velocity vector field in each cardiac phase. Unlike "Particle Traces", it does not represent temporal evolution of flow in the vessel (Figure 16). We prefer to visualize our 4D flow data with "Particle Traces" since subjectively it is more easily understood (and has good agreement with "Streamline" visualization). Finally, the user can export desired images or movie clips or save the workflow (segmentation, centerline and contours) for future use.

Case examples

Our most common patient population in which we utilize 4D flow imaging is those with various forms of Aortopathies. Bicuspid aortic valve patients frequently have abnormal flow jets in the ascending aorta, and in extreme examples can have a left hand helix pattern (Figure 17, Clip 4). Those with genetic syndromes, such as Turner syndrome, may have vortex formations in atypical locations, such as at the base of the left subclavian artery at the terminal end of an elongated transverse arch (Figure 18, Clip 5). There is work underway to assess these abnormal flow patterns and the resultant effect on wall integrity, rate of vascular dilation, and propensity to dissection [7–9]. Using the tools we have described above, flow dynamics can be visualized and basic assessment of hemodynamics can be obtained. Calculation of wall shear stress can also be performed. In our lab, when patients are found to have altered flow patterns in various forms of Aortopathy, the frequency of their follow up is often increased, and consideration is given for how these insights help predict their risk of cardiovascular events in the scope of surgical timing and planning.

The next most common patient population is those with repaired tetralogy of Fallot (TOF). Regardless of whether a transannular patch is used at the time of TOF repair, the pulmonary valve is virtually always non-functional by the time patients reach adolescence, and severe pulmonary insufficiency (coupled often with some degree of residual obstruction) is nearly universal. Visualization of the flow in the RVOT, both stenotic and regurgitant, is very helpful to understand the progression of the disease (Figure 19, Clip 6). Flow within the main and branch PA's, with quantification of vortices, can be

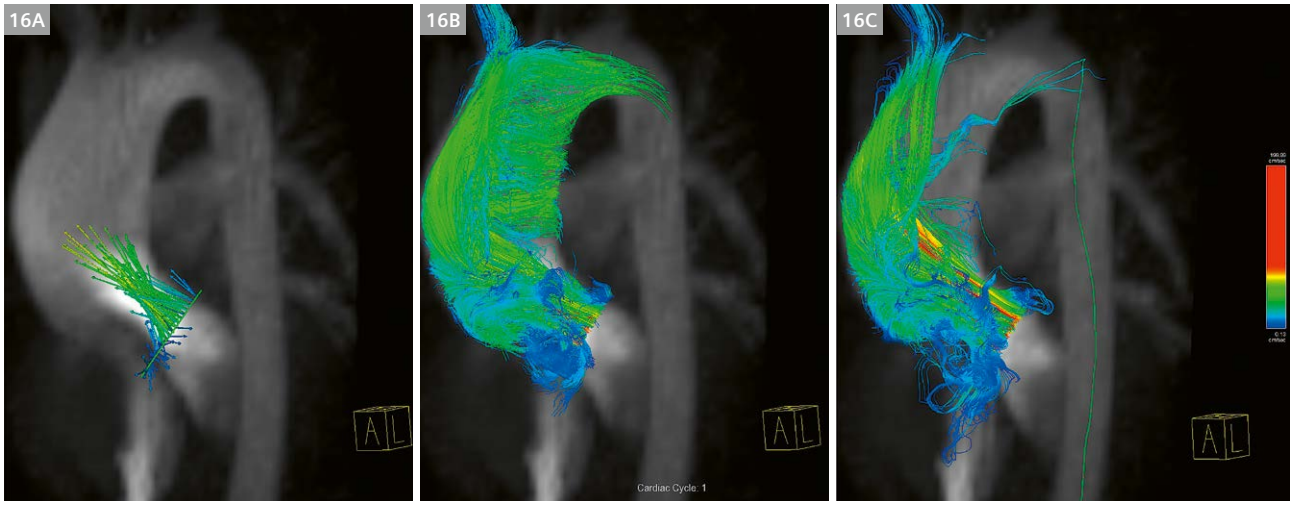

16 Visualization options: vector field **(16A)**, particle traces **(16B)** and Steamlines **(16C)**.

studied and correlated with presence and rate of RV dilation [10–12]. In those with irregular main and branch pulmonary artery architecture, such as those with pseudoaneurysm formation, these abnormal flow patterns are even more pronounced (Figure 20, Clip 6).

In our opinion, one of the most helpful patient subgroups for 4D flow imaging are those with single ventricle anatomies. A heterogeneous group, ranging from variants such as tricuspid atresia with a single left ventricle, to those with hypoplastic left heart syndrome with a single

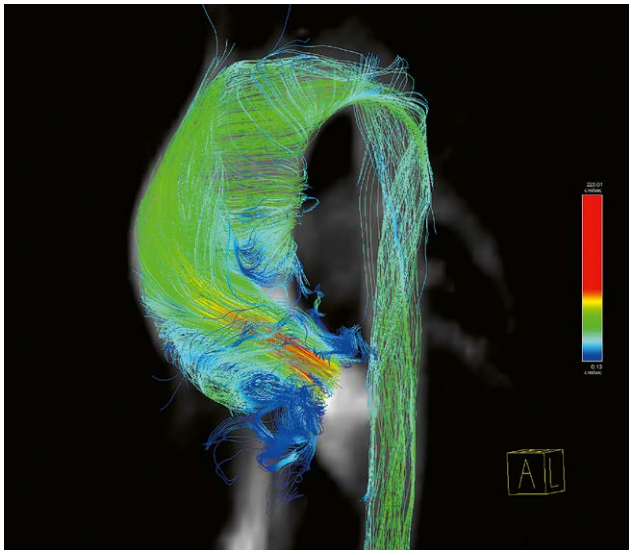

17 Patient with a bicuspid aortic valve and a left hand helical pattern in the ascending aorta.

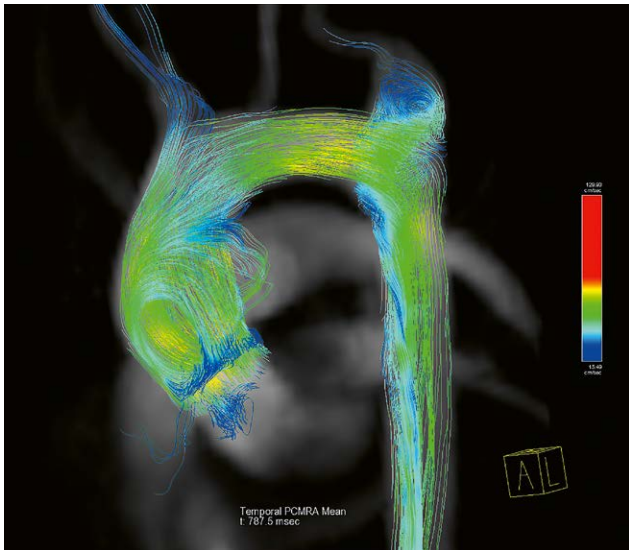

18 Patient with Turner syndrome, no evidence of coarctation of the aorta, but with a prominent vortex formation at the base of the left subclavian artery.

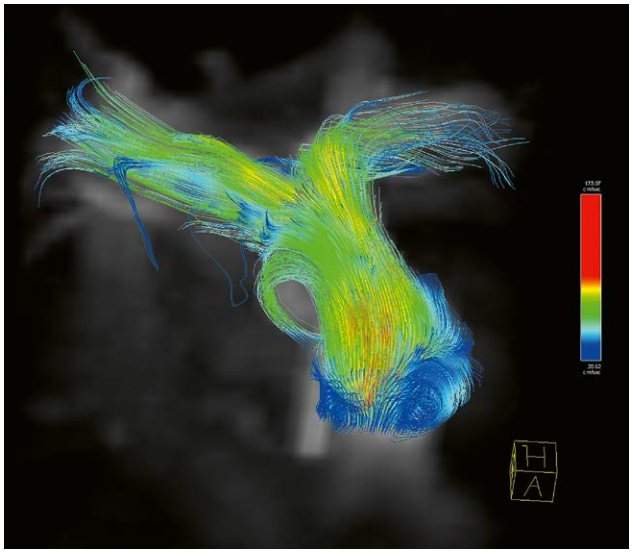

19 Patient with repaired tetralogy of Fallot and turbulent flow noted in the main and branch pulmonary arteries.

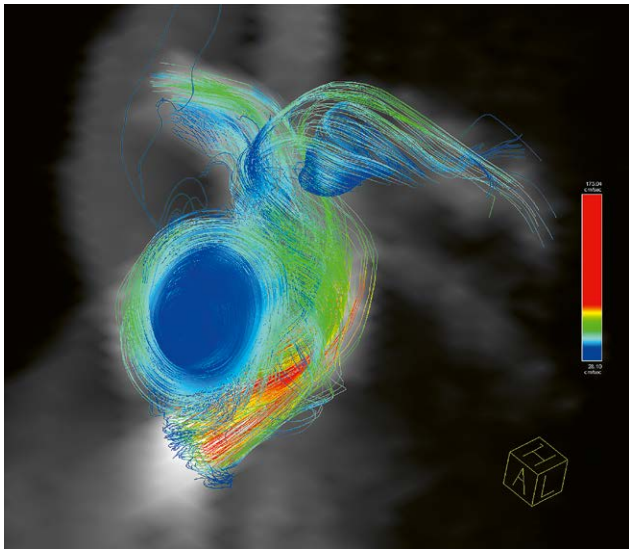

20 Different patient with repaired tetralogy of Fallot and a pseudoaneursym on the anterior surface of the main pulmonary artery. Note the prominent vortex within the pseudoaneurysm.

right ventricle, to those with heterotaxy syndrome with a myriad of systemic and pulmonary venous anomalies on top of their intracardiac defects, these patients truly represent the extreme end of complexity in the field of congenital heart disease. The unifying feature for these patients is the series of staged palliations they undergo, culminating in a Fontan procedure. With only a single functional ventricle which must be used to pump blood to the body, the Fontan circulation relies on passive systemic venous return into the pulmonary arteries by anastomosing the superior vena cava (SVC) (Figure 21, Clip 7) directly to the PA and connecting the inferior vena cava (IVC) to the PA as well (Figure 22, Clip 8), via either an intracardiac tunnel or a separate conduit.

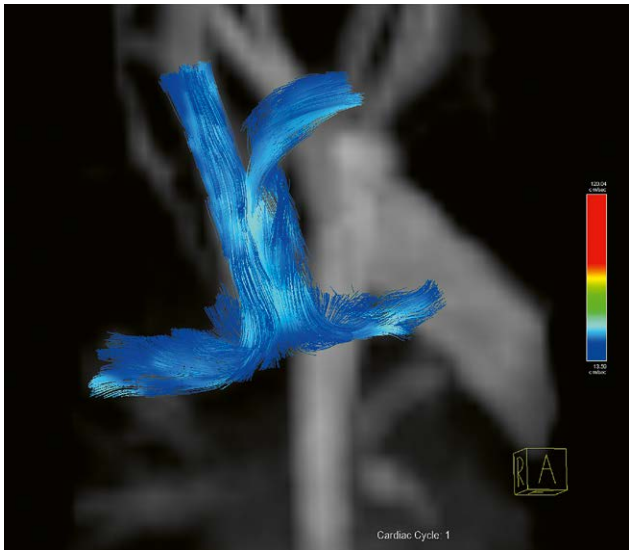

21 Flow from the superior vena cava into the branch pulmonary arteries in a patient with single ventricle anatomy who has undergone a bidirectional Glenn anastomosis.

In patients who have undergone a Fontan completion, altered flow hemodynamics within their circuit can lead to several clinical issues. One of the most difficult to assess is formation of pulmonary arteriovenous malformations (PAVM), thought to be due to lack of a component of hepatic blood flow (termed "hepatic factor") to reach the pulmonary capillary bed in affected lung segments. Knowledge of the streaming of the inferior systemic venous return, therefore, is of paramount importance in assessing these patients' risk for development of PAVM's [13]. Traditional 2D flow imaging can assess total volumes of flow into the RPA and LPA, but cannot quantify how much of each lung's arterial supply comes from the IVC versus the SVC. While the Siemens Healthineers software mentioned above does not have specific features to quantify flow volumes produced only from select vessels, we have developed an in-house MATLAB code which allows us to perform these calculations.

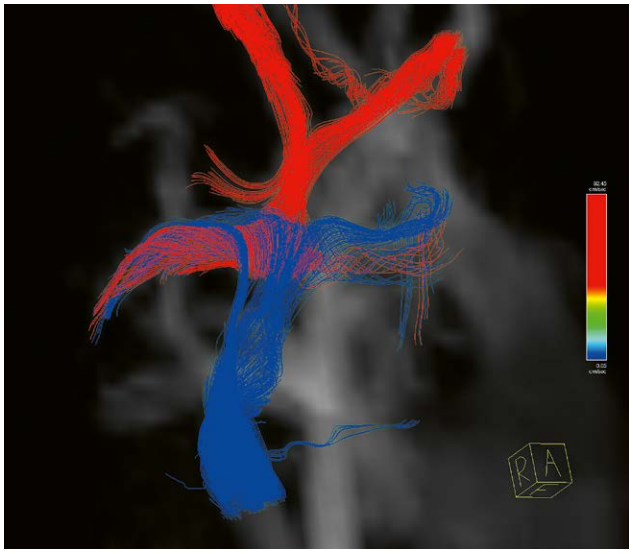

22 Flow from the superior vena cava (colored red) and inferior vena cava (labeled blue) into the branch pulmonary arteries in a patient with single ventricle anatomy who has undergone a bidirectional Glenn anastomosis and subsequent Fontan completion. In this patient's case, there was a small fenestration placed in the Fontan baffle, seen by the blue streamlines heading rightward on the image near the lower margin of the Fontan.

23 Patient with Ebstein's anomaly of the tricuspid valve, with flow across the superior aspect of the tricuspid valve labeled blue and across the inferior aspect labeled red, so that the abnormal flow in the right ventricle based on portion of tricuspid inflow can be visualized.

One final application that we are increasingly using 4D flow to assess is intraventricular flow dynamics in patients with heart failure or abnormal ventricular loading. While in adult patients, this topic is much more common in those with a structurally normal heart and heart failure from ischemic cardiac disease [14], in pediatric patients many forms of native and palliated congenital heart disease lead to long-term heart failure. Labs have looked at both left and right ventricular mechanics, including in patients with repaired TOF [15] and single ventricle patients [16, 17]. An additional, less studied disease type is patients with Ebstein's anomaly, where marked tricuspid insufficiency results in very abnormal flow patterns in the right ventricle (Figure 23, Clip 9). Performing 4D flow allows visualization of these hemodynamics, which may lead to better understanding of the mechanism of ventricular dilation and dysfunction for many of these patients.

Future directions

One limitation of 4D flow is the long acquisition times required. With the addition of compressed sensing and other image acceleration techniques, data acquisition times continue to shrink, allowing increases in spatial and temporal resolution in the datasets. Many vendors and labs are now working towards a vision of having 4D flow represent a "one stop shop" for congenital cardiac magnetic resonance imaging. One can imagine that if the spatial resolution can be decreased to roughly one millimeter voxels, then full anatomic reconstructions including short axis cine stacks can be extracted from the 4D datasets for analysis. If the temporal resolution can be improved to match current 2D flow methodologies (typically 30 phases per cardiac cycle), and retrospective gating acquisitions are used, then the 4D flow data would obviate the need for additional 2D phase contrast imaging. Thus, a high spatial and temporal resolution 4D flow dataset would provide all of the anatomic, functional, and flow data on a given patient, without need for acquiring separate double oblique 2D planes. This approach also has the advantage of being much easier for a technologist to acquire, as it is not patient specific / anatomy dependent for accurate image plane set up.

There are, however, several existing challenges to such an approach. Full chest coverage with millimeter voxels requires a large quantity of data, and this is amplified by the desire for high temporal resolution increasing the number of phases. For example, in many adolescent size patients, in order to cover the whole chest in a sagittal geometry with 1 mm slices, 100–150 slices are needed. If temporal resolution of 30 phases per cycle is desired, this will produce between 12,000 and 18,000 images. This vast array of data takes substantial time for reconstruction, made even more computationally demanding when iterative reconstruction is used with compressed sensing. Computational power and processors continue to improve, but most labs that are currently taking this type of approach to 4D flow imaging the reconstruction is done off-line and takes several hours before the data is ready.

Another challenge to this approach to 4D flow imaging is ensuring consistent, uniform signal throughout the study. As discussed above, while 4D flow sequences can be obtained with or without contrast, performing these sequences post-contrast allows increased SNR and CNR as well as higher degrees of parallel imaging acceleration. In the past, blood-pool gadolinium contrast agents such as Gadofosveset trisodium were used in several pediatric labs for performance of contrast enhanced MR angiography and 4D flow imaging [18], but this agent is no longer commercially available in the United States. Another option is non-gadolinium based contrast agents, such as ferumoxytol, which has been used for neonatal and pediatric CMR studies, though our lab does not have personal experience with this approach. Ferumoxytol has a different risk profile than gadolinium based agents, but there is data that for select patient groups these techniques can decrease the need for sedation/anesthesia (which also carries its own inherent risks) [19].

Conclusions

Application of 4D flow imaging to patients with congenital heart disease is an exciting new avenue for greater understanding of patient specific hemodynamics. Both prototype sequences as well as derivations of product pulse sequences allow acquisition of 4D flow datasets, with strengths and weaknesses in each technique. In our lab, we utilize a combination of these sequences, tailored to the individual patient anatomy, size, heart rate, and time limitations on the study. While several third party analysis platforms are available, at the current time the majority of our experience is with the Siemens 4D flow software, and we find that both the 3D visualization and quantification potential on this platform allows comprehensive use of these 4D flow data for our patients.

To access the .avi clips please visit

www.siemens.com/4Dflow

Abbreviations

2D	2-dimensional	**GRAPPA**	Generalized auto-calibrating partially parallel acquisition	**Qp**	Pulmonary blood flow
4D flow	4-dimensional phase contrast imaging			**RPA**	Right pulmonary artery
Ao	Aorta	**IVC**	Inferior vena cava	**PC**	Phase contrast
bpm	Beats per minute	**LPA**	Left pulmonary artery	**TR**	Repetition time
BAV	Bicuspid aortic valve	**MPA**	Main pulmonary artery	**SNR**	Signal to noise ratio
BDG	Bidirectional Glenn	**NSA**	Number of signal averages	**SV**	Single ventricle
CMR	Cardiac magnetic resonance imaging	**PAVM**	Pulmonary arterio-venous malformations	**SVC**	Superior vena cava
				Qs	Systemic blood flow
CHD	Congenital heart disease			**TOF**	Tetralogy of fallot
FOV	Field of view	**PA**	Pulmonary artery	**VENC**	Velocity encoding
				TOF	Tetralogy of fallot
				VENC	Velocity encoding

References

1 P. R. Moran. "A flow velocity zeugmatographic interlace for NMR imaging in humans". Magn Reson Imaging, 1, 197-203, 1982.
2 M. O'Donnell. "NMR blood flow imaging using multiecho, phase contrast sequences". Med Phys, 12, 59-64, 1985.
3 A. J. Powell and T. Geva. "Blood flow measurement by magnetic resonance imaging in congenital heart disease". Pediatr Cardiol, 21, 47-58, 2000.
4 K. K. Whitehead, K. S. Sundareswaran, W. J. Parks, M. A. Harris, A. P. Yoganathan and M. A. Fogel. "Blood flow distribution in a large series of patients having the Fontan operation: a cardiac magnetic resonance velocity mapping study". J Thorac Cardiovasc Surg, 138, 96-102, 2009.
5 C. L. Dumoulin, S. P. Souza, M. F. Walker and W. Wagle. "Three-dimensional phase contrast angiography". Magn Reson Med, 9, 139-149, 1989.
6 H. G. Bogren and M. H. Buonocore. "4D magnetic resonance velocity mapping of blood flow patterns in the aorta in young vs. elderly normal subjects". J Magn Reson Imaging, 10, 861-869, 1999.
7 L. Mirabella, A. J. Barker, N. Saikrishnan, E. R. Coco, D. J. Mangiameli, M. Markl and A. P. Yoganathan. "MRI-based Protocol to Characterize the Relationship Between Bicuspid Aortic Valve Morphology and Hemodynamics". Ann Biomed Eng, 43, 1815-1827, 2015.
8 N. Saikrishnan, L. Mirabella and A. P. Yoganathan. "Bicuspid aortic valves are associated with increased wall and turbulence shear stress levels compared to trileaflet aortic valves". Biomech Model Mechanobiol, 14, 577-588, 2015.
9 Y. Shan, J. Li, Y. Wang, B. Wu, A. J. Barker, M. Markl, C. Wang, X. Wang and X. Shu. "Aortic shear stress in patients with bicuspid aortic valve with stenosis and insufficiency". J Thorac Cardiovasc Surg, 153, 1263-1272 e1261, 2017.
10 J. Geiger, M. Markl, B. Jung, J. Grohmann, B. Stiller, M. Langer and R. Arnold. "4D-MR flow analysis in patients after repair for tetralogy of Fallot". Eur Radiol, 21, 1651-1657, 2011.
11 C. J. Francois, S. Srinivasan, M. L. Schiebler, S. B. Reeder, E. Niespodzany, B. R. Landgraf, O. Wieben and A. Frydrychowicz. "4D cardiovascular magnetic resonance velocity mapping of alterations of right heart flow patterns and main pulmonary artery hemodynamics in tetralogy of Fallot". J Cardiovasc Magn Reson, 14, 16, 2012.
12 D. Hirtler, J. Garcia, A. J. Barker and J. Geiger. "Assessment of intracardiac flow and vorticity in the right heart of patients after repair of tetralogy of Fallot by flow-sensitive 4D MRI". Eur Radiol, 26, 3598-3607, 2016.
13 P. Bachler, I. Valverde, N. Pinochet, S. Nordmeyer, T. Kuehne, G. Crelier, C. Tejos, P. Irarrazaval, P. Beerbaum and S. Uribe. "Caval blood flow distribution in patients with Fontan circulation: quantification by using particle traces from 4D flow MR imaging". Radiology, 267, 67-75, 2013.
14 J. Zajac, J. Eriksson, P. Dyverfeldt, A. F. Bolger, T. Ebbers and C. J. Carlhall. "Turbulent kinetic energy in normal and myopathic left ventricles". J Magn Reson Imaging, 41, 1021-1029, 2015.
15 P. Sjoberg, S. Bidhult, J. Bock, E. Heiberg, H. Arheden, R. Gustafsson, S. Nozohoor and M. Carlsson. "Disturbed left and right ventricular kinetic energy in patients with repaired tetralogy of Fallot: pathophysiological insights using 4D-flow MRI". Eur Radiol, 2018.
16 V. P. Kamphuis, A. A. W. Roest, J. J. M. Westenberg and M. S. M. Elbaz. "Biventricular vortex ring formation corresponds to regions of highest intraventricular viscous energy loss in a Fontan patient: analysis by 4D Flow MRI". Int J Cardiovasc Imaging, 34, 441-442, 2018.
17 J. Wong, R. Chabiniok, S. M. Tibby, K. Pushparajah, E. Sammut, D. S. Celermajer, D. Giese, T. Hussain, G. F. Greil, T. Schaeffter and R. Razavi. "Exploring kinetic energy as a new marker of cardiac function in the single ventricle circulation". J Appl Physiol (1985), 2018.
18 A. Tandon, S. Hashemi, W. J. Parks, M. S. Kelleman, D. Sallee and T. C. Slesnick. "Improved high-resolution pediatric vascular cardiovascular magnetic resonance with gadofosveset-enhanced 3D respiratory navigated, inversion recovery prepared gradient echo readout imaging compared to 3D balanced steady-state free precession readout imaging". J Cardiovasc Magn Reson, 18, 74, 2016.
19 L. M. Lai, J. Y. Cheng, M. T. Alley, T. Zhang, M. Lustig and S. S. Vasanawala. "Feasibility of ferumoxytol-enhanced neonatal and young infant cardiac MRI without general anesthesia". J Magn Reson Imaging, 45, 1407-1418, 2017.

Contact

Timothy C. Slesnick, M.D.
Director, Cardiac MRI
Children's Healthcare of Atlanta
Associate Professor
Department of Pediatrics
Emory University School of Medicine
1405 Clifton Road North East
Atlanta, GA 30322
USA
Tel: +1 404-256-2593
SlesnickT@kidsheart.com

Deep Cervical Infantile Hemangioma Identified by Time-Resolved Magnetic Resonance Angiography

Nicole Seyfried[1]; Vikas Gulani[2]; Verena Carola Obmann[3]

[1] School of Medicine, Case Western Reserve University, Cleveland, OH, USA
[2] Case Western Reserve University and University Hospitals Case Medical Center, Cleveland, OH, USA
[3] Department of Diagnostic, Interventional and Pediatric Radiology (DIPR), Inselspital, Bern University Hospital, University of Bern, Switzerland

Abstract

Infantile hemangiomas are the most common benign vascular tumors of infancy. We present a case report of a 5-month-old[1] female presenting with a posterior neck mass that was later diagnosed as an infantile hemangioma. We describe the application of time-resolved MR angiography in the evaluation of a pediatric vascular anomaly.

Introduction

Infantile hemangiomas (IHs) are common, benign tumors of vascular origin. Often arising shortly after birth, these lesions demonstrate a proliferative phase followed by an involution phase that may last several years [1]. Although generally self-limited in nature, potential complications of IH include scarring and disfigurement, airway obstruction, congestive heart failure and vision loss [2]. The majority of infantile hemangiomas may be diagnosed clinically, although deep lesions and those presenting without cutaneous involvement warrant further investigation to rule out other vascular malformations, especially high flow lesions that may require different treatment [1]. Furthermore, due to the risks of complications such as airway obstruction, imaging is indicated for suspected pediatric vascular anomalies of the head and neck [3]. Ultrasound imaging with spectral Doppler plays a strong role in imaging vascular anomalies in pediatric patients [4]. MRI including T1 and T2-weighted images and MR angiography are used for diagnosis and to evaluate the extent of the lesion [5]. Time-resolved MR angiography with technologies such as 3D time-resolved imaging of contrast kinetics (TRICKS) or contrast-enhanced time-resolved MR angiography (MRA) with interleaved stochastic trajectories (TWIST) technique allows dynamic evaluation of pediatric head and neck vascular anomalies

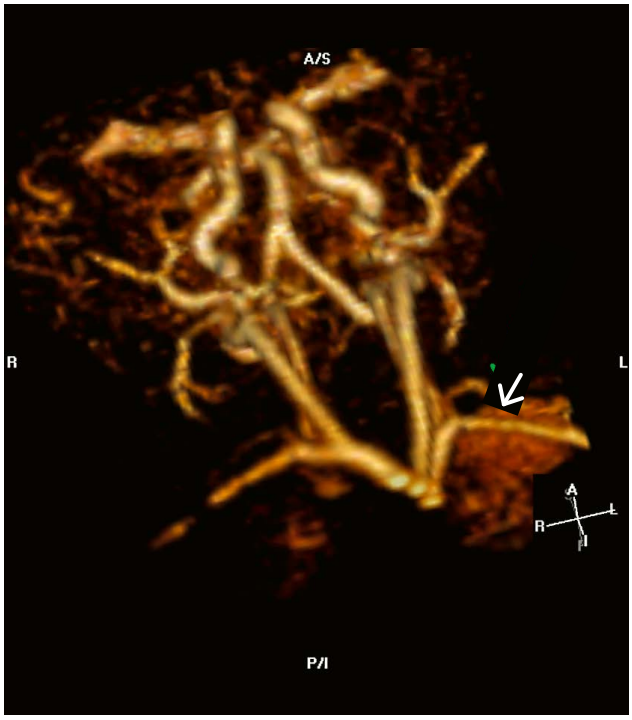

1 Capture from a rotated arterial phase MIP from a frame showing the tortuous vessel filling the lesion in this phase of enhancement. *Access the .avi clip at: www.siemens-healthineers.com/TWIST*

[1] *MR scanning has not been established as safe for imaging fetuses and infants less than two years of age. The responsible physician must evaluate the benefits of the MR examination compared to those of other imaging procedures. Note: This disclaimer does not represent the opinion of the authors.*

while preserving both temporal and spatial resolution and eliminating the need for breath-holds and specific timing of the contrast bolus [3, 6, 7, 8]. A Keyhole-like acceleration scheme is employed [9]. Central portions of *k*-space are updated more often, while peripheral portions of *k*-space are updated less frequently, sharing information across multiple frames. This allows dynamic contrast imaging with a high frame rate that is governed principally by the update rate of the center of *k*-space. Very small boluses of gadolinium can be employed along with a dynamic free breathing acquisition, allowing imaging of even very small children[1] without general anesthesia.

Case report

A 5-month-old[1] female patient presented in 2009 with a left posterior shoulder mass. The mass had been enlarging in size since one month of age. Additionally, a right lateral brow cyst was present since birth and had been noted to be enlarging in proportion to the patient. There were no other peripheral anomalies and past medical history was otherwise unremarkable. Evaluation was performed to determine the extent of the lesion and to assess whether this was a high flow abnormality. Images were obtained with a 3 plane localizer, a contrast-enhanced 4D dynamic time-resolved MRA technique using the TWIST sequence, and coronally reconstructed and axially reconstructed fat-saturated 3D VIBE pre- and post-contrast. Imaging was performed on a 3T MAGNETOM Verio (Siemens Healthcare, Erlangen, Germany). Slice thickness was 1.1 mm, frame rate was 2 seconds per frame, FOV was 195 x 272, resolution 1.1 x 1.1 x 1.1 mm^3, FA 25 degrees, GRAPPA factor 2 x 2, for a total acceleration of 4. The central "A" region of *k*-space that is updated with every frame was set at 14% and the 33% of the outer "B" region was updated with each frame. Dynamic subtraction images along with time-resolved subtraction MIPs in three planes were obtained, along with 3-dimensional reformats from selected planes. The patient received moderate sedation with the assistance of the Pediatric Sedation Unit at our institution, which specializes in sedation of children. General anesthesia was not administered. Per a protocol developed at our institution for dynamic imaging of very small children, a small amount of Propofol was hand-injected into the intravenous line just prior to injection of Gadolinium contrast, in order to minimize patient motion in response to contrast injection. 1.2 ml of gadolinium-based contrast (Magnevist, Bayer, Leverkusen, Germany) and a subsequent saline flush were hand-injected. Imaging revealed a 3.5 x 2.0 x 2.1 cm mass in the posterior cervical soft tissue. The mass demonstrated high signal intensity in T2-weighted images and low signal intensity in T1-weighted images. On dynamic post-contrast imaging the lesion was observed to fill in the arterial phase from a tortuous vessel arising from the proximal left subclavian artery (Fig. 1). Venous phase imaging demonstrated two draining veins, which fed into the distal left subclavian vein (Fig. 2). Time resolved subtracted MIP images, as well as single frame movies from the arterial phase and venous phase are also shown. *To access the .avi's please visit www.siemens-healthineers.com/TWIST*.

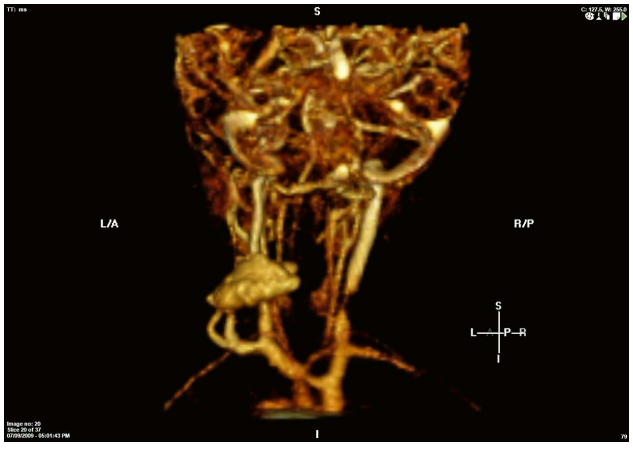

2 Capture from a venous phase MIP showing the two veins draining from the lesion.
Access the .avi clip at: www.siemens-healthineers.com/TWIST

One month after imaging revealed the vascular lesion, the patient was referred to plastic surgery for evaluation of both the right lateral brow cyst, thought to be a dermoid cyst, and the left cervical vascular lesion. On physical exam, the cervical lesion was compressible and non-tender. Cardiac and pulmonary findings were unremarkable. The decision was made to schedule a surgical excision of both the lateral brow cyst and the cervical vascular lesion. Due to the well-circumscribed nature of the lesion, this was attempted without additional radiologic intervention. The surgery was performed when the patient was 10 months of age. The entire cervical vascular lesion was surgically excised and sent to pathology for evaluation. Immunostaining for GLUT1 was positive and an infantile hemangioma was diagnosed.

Discussion

Brief case summary

A 5-month-old female patient with a left posterior cervical mass and a right lateral brow cyst presented for imaging evaluation. Contrast-enhanced 4D dynamic time-resolved MRA using the TWIST sequence was performed, revealing a vascular lesion in the deep cervical soft tissue with prominent arterial filling of a feeder vessel originating from the proximal subclavian artery and two draining veins leading into the left subclavian vein. Surgical excision of the infantile hemangioma was performed 6 months later with good results.

Infantile hemangioma:
Etiology, diagnosis and treatment

Infantile hemangioma is an extremely common vascular tumor of infancy. The incidence has been shown to be 4–5%. The lesions consist mainly of capillaries and endothelial cells and may be superficial, deep or compound [1]. The etiology of IH is not well understood, although several theories have been considered. Associated risk factors for IH include low birth weight, female gender, Caucasian race and advanced maternal age. Familial associations have also been reported [10]. Mechanisms of pathogenesis have been debated and one suggested mechanism is that tissue hypoxia, which results in an upregulation in transcription of genes including GLUT1, contributes to endothelial proliferation and formation of IH [10]. GLUT1 immunostaining has been shown to be positive in 95% of IHs. Normal vascular endothelial cells do not express GLUT1 [12].

Diagnosis of infantile hemangioma can be made clinically in 93% of cases. Clinical diagnosis is made using the classification system of Mulliken and Glowacki, which distinguishes hemangiomas from vascular malformations [13]. Further classification has been delineated by the International Society for the Study of Vascular Anomalies (ISSVA) [3]. The 7% of cases of IH that cannot be diagnosed clinically warrant further investigation, including ultrasonography or MRI [5]. Additionally, imaging may be used in cases of soft tissue vascular anomalies in order to determine the extent of the lesion. Multiple MRI sequences are typically used to evaluate the lesion. T1-weighted images show anatomic detail while T2-weighted images with fat saturation demonstrate the lesion. Gadolinium-based contrast is often administered and post-contrast sequences are obtained. Time-resolved MR angiography can be utilized in order to visualize dynamic filling of the lesion in the arterial phase and the venous phase [5]. Time-resolved MR angiography with interleaved stochastic trajectories (TWIST) has many advantages in the imaging diagnosis of pediatric soft tissue vascular lesions. Dynamic contrast-enhanced images can be acquired with a high spatial resolution in a short period of time as described above. This eliminates the need for specific timing of the contrast bolus, a challenge in the pediatric population. High spatial and temporal resolution allows for significant anatomic detail of vessels. The necessity of cessation of breathing during imaging acquisition is negated, allowing for the imaging of pediatric patients for which a breath-hold is not possible. TWIST has been shown to have a higher sensitivity and a comparable specificity to conventional contrast-enhanced MRI in the diagnosis of infantile hemangioma [3, 14]. Many additional applications of time-resolved MR angiography have been described [8, 14].

Infantile hemangiomas often do not require treatment and will involute over time. High risk lesions may be treated with oral or topical beta blockers [2]. Surgical resection has been argued to be a first line treatment to prevent permanent disfigurement caused by rapid and unpredictable high rates of growth of these lesions [15].

Conclusion

Infantile hemangioma is a common benign vascular tumor of infancy. IHs are often diagnosed clinically and are self-limiting in nature, however lesions localized to the head and neck warrant further investigation with imaging to rule out malignant causes and to evaluate risk of complications. Time-resolved MR Angiography with stochastic interleaved trajectories (TWIST) provides a non-invasive imaging modality for evaluation of IH while allowing for dynamic visualization of the lesion with high temporal and spatial resolution.

To access the .avi clips please visit
www.siemens-healthineers.com/TWIST

References

1 Adams DM, Ricci KW. Infantile Hemangiomas in the Head and Neck Region. Otolaryngol Clin North Am. 2018 Feb;51(1):77-87. doi: 10.1016/j.otc.2017.09.009. Review. PubMed PMID: 29217069.

2 Smith CJF, Friedlander SF, Guma M, Kavanaugh A, Chambers CD. Infantile Hemangiomas: An Updated Review on Risk Factors, Pathogenesis, and Treatment. Birth Defects Res. 2017 Jul 3;109(11):809-815. doi: 10.1002/bdr2.1023. Epub 2017 Apr 12. Review. PubMed PMID: 28402073; PubMed Central PMCID: PMC5839165.

3 Higgins LJ, Koshy J, Mitchell SE, Weiss CR, Carson KA, Huisman TA, Tekes A. Time-resolved contrast-enhanced MRA (TWIST) with gadofosveset trisodium in the classification of soft-tissue vascular anomalies in the head and neck in children following updated 2014 ISSVA classification: first report on systematic evaluation of MRI and TWIST in a cohort of 47 children. Clin Radiol. 2016 Jan;71(1):32-9. doi: 10.1016/j.crad.2015.09.006. Epub 2015 Oct 21. PubMed PMID: 26474946.

4 Johnson CM, Navarro OM. Clinical and sonographic features of pediatric soft-tissue vascular anomalies part 1: classification, sonographic approach and vascular tumors. Pediatr Radiol. 2017 Aug;47(9):1184-1195. doi: 10.1007/s00247-017-3885-y. Epub 2017 Aug 4. Review. PubMed PMID: 28779195.

5 Navarro OM. Magnetic resonance imaging of pediatric soft-tissue vascular anomalies. Pediatr Radiol. 2016 May;46(6):891-901. doi: 10.1007/s00247-016-3567-1. Epub 2016 May 26. Review. PubMed PMID: 27229506.

6 Korosec Fr, Frayne R, Grist TM, Mistretta CA. Time-resolved contrast-enhanced 3D MR angiography. Magn Reson Med 1996; 36:345-351.

7 Laub G. Kroeker R. *syngo* TWIST for dynamic time-resolved MR angiography. MAGNETOM Flash 2006; 3;92-95.
8 Blackham KA, Passalacqua MA, Sandhu GS, Gilkeson RC, Griswold MA, Gulani V. Applications of time-resolved MR angiography.AJR Am J Roentgenol. 2011 May;196(5):W613-20. doi: 10.2214/AJR.10.4227. Review. PubMed PMID: 21512053.
9 Van Vaals J, Brummer M, Dixon W, et al. 'Keyhole' method for accelerating imaging of contrast agent uptake. J Magn Reson Imaging 1993; 3:671-5.
10 Castrén E, Salminen P, Vikkula M, Pitkäranta A, Klockars T. Inheritance Patterns of Infantile Hemangioma. Pediatrics. 2016 Nov;138(5). pii: e20161623. Epub 2016 Oct 12. PubMed PMID: 27940781.
11 Janmohamed SR, Madern GC, de Laat PC, Oranje AP. Educational paper: Pathogenesis of infantile haemangioma, an update 2014 (part I). Eur J Pediatr. 2015 Jan;174(1):97-103. doi: 10.1007/s00431-014-2403-6. Epub 2014 Aug 26. Review. PubMed PMID: 25156689.
12 van Vugt LJ, van der Vleuten CJM, Flucke U, Blokx WAM. The utility of GLUT1 as a diagnostic marker in cutaneous vascular anomalies: A review of literature and recommendations for daily practice. Pathol Res Pract. 2017 Jun;213(6):591-597. doi: 10.1016/j.prp.2017.04.023. Epub 2017 Apr 27. Review. PubMed PMID: 28552538.
13 MacFie CC, Jeffery SL. Diagnosis of vascular skin lesions in children: an audit and review. Pediatr Dermatol. 2008 Jan-Feb;25(1):7-12. doi: 10.1111/j.1525-1470.2007.00573.x. Review. PubMed PMID: 18304145.
14 Obmann VC, Chalian M, Mansoori B, Sanchez E, Gulani V. Advantages of time-resolved contrast-enhanced 4D MR angiography in splenic arterial steal syndrome. Clin Imaging. 2018 May - Jun;49:169-173. doi: 10.1016/j.clinimag.2018.03.003. Epub 2018 Mar 7. PubMed PMID: 29558712.
15 Boyd VC, Bui D, Naik B, Levy ML, Hicks MJ, et al. Surgery: The Treatment of Choice for Hemangiomas. Seminars in Plastic Surgery. 2006 August; 20(3):163-168.

Contact

Vikas Gulani, M.D.
Department of Radiology
Case Western Reserve University
University Hospitals Case Medical Center
11100 Euclid Ave
Bolwell Building, Room B120
Cleveland, OH 44106
USA
vxg46@case.edu


Vikas Gulani


Nicole Seyfried


Verena Obmann

Fetal MR Imaging: An Overview

Xianyun Cai[1]; Xin Chen[1]; Cong Sun[1]; Tuantuan Wang[1]; Hong Tang[1]; Jinxia Zhu[2]; Guangbin Wang[1]

[1]Department of MR, Shandong Medical Imaging Research Institute, Shandong University, China
[2]Siemens Healthineers, MR Collaboration, Beijing, China

The primary objective of prenatal diagnosis is to obtain genetic, anatomical, biochemical, and physiological information about the fetus that will allow the detection of any abnormalities that may have implications for the fetal and postnatal periods. This will make it possible to offer the family information, genetic counseling, and therapeutic alternatives. The main imaging method used for routine fetal examinations is ultrasonography (US). It is noninvasive, inexpensive, widely available, and can provide real-time studies without ionizing radiation. However, in cases of advanced gestational age, patient obesity, oligohydramnios, improper fetal position, and interposition of intestinal gas or pelvic acoustic shadows, US might have technical limitations and be unable to confirm findings. In our department, we consider using MRI when the US findings are equivocal or when the US images are difficult to interpret due to factors such as late pregnancy or an inaccessible fetal position. Fetal MR imaging[1] is regarded as a valuable adjuvant imaging tool for dedicated cases at field strengths of 3T or less. In general, with appropriate sequence adaptations, examinations of the fetus at 3T are comparable with images obtained at 1.5T. Also, because of the higher image resolution and signal-to-noise ratio (SNR), finer structures and lesions can be delineated at 3T. However, a major drawback is that examinations at 3T are more prone to artifacts, which complicates imaging the fetus for traditional referrals (maternal obesity, polyhydramnios). It is therefore important to decide which system might be better suited to address certain indications [1]. Investigation of normal organ development with fetal MRI has been described by Prayer et al. [2]. Maturational processes in utero are characterized by changes in the shape, size, and content/composition of organs, and by their relationship to each other.

In our institution, all the MRI examinations were performed on a 1.5T MAGNETOM Amira (Siemens Shenzhen Magnetic Resonance, Shenzhen, China) with spine and body array coils positioned over the lower pelvic area. Since our department introduced fetal MRI in June 2006, a total of 15,000 pregnant women with various anomalies (screened by ultrasonography) have been referred for fetal MRI examinations at our institution. The cases include brain, spine, chest, and abdominal anomalies. A placental MRI scan was performed for the first time in 2009, and 1,102 such scans have been performed to date. A total of 235 fetal spine scans have been performed since 2015, when susceptibility-weighted imaging (SWI) – a technique developed by Siemens [3], which conventionally uses the BOLD mechanism to generate venograms of the brain and to quantify venous oxygenation levels [4] – was first modified for fetal spine imaging with fast data acquisition by Robinson et al. [5]. In recent years, the development of MR sequences has led to major changes in fetal MRI imaging in our unit.

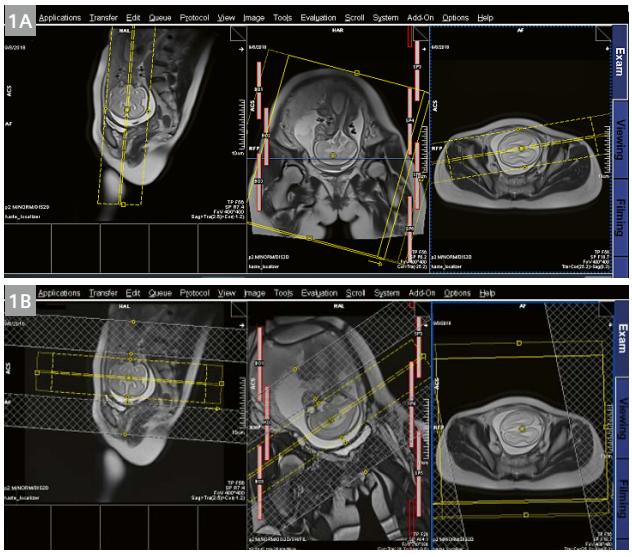

1 Sagittal and coronal localizer images of the fetal brain.

[1]*MR scanning has not been established as safe for imaging fetuses and infants less than two years of age. The responsible physician must evaluate the benefits of the MR examination compared to those of other imaging procedures. Note: This disclaimer does not represent the opinion of the authors.*

The rise and development of fetal magnetic resonance imaging

Origins

Since fetal MR imaging was first used in 1983 [6], no consistent or convincing evidence has emerged to suggest that briefly exposing a fetus to the changing electromagnetic fields of MR imaging has any harmful effects. In the early days, however, the acquisition time was too long and the motion artifacts were severe, which resulted in poor image quality and hindered the development of fetal MRI. With the development of ultrafast sequences in the 1990s, such as single-shot steady-state free precession (SSFP), half-fourier acquisition single-shot turbo spin echo (HASTE), fast T1-weighted gradient echo, and echo planar imaging, MR imaging became a noninvasive modality that could complement US in detecting fetal abnormalities, establishing prognoses, and assisting in perinatal management.

Safety

With fetal MRI, safety considerations such as exposure times, gradient field switching, noise, and radiofrequency power deposition should be kept in mind while following established guidelines [5–9]. No documented indications exist for using contrast agents in fetal MR imaging. Generally speaking, fetal MR imaging should be avoided in the first trimester, since the fetal cells are rapidly dividing and differentiating, and the influence of MRI on organogenesis is still unclear. Also, it is difficult to obtain good-quality images in very young fetuses.

Another important issue to consider in fetal MRI concerns gadolinium-based intravenous contrast media. These agents have been shown to cross the placenta and may appear in the fetal bladder, which means they are reabsorbed from the amniotic fluid by swallowing. The use of gadolinium-based contrast agents for MR imaging in pregnant women remains controversial. Recently, an animal experiment was conducted to determine whether gadolinium remains in juvenile nonhuman primate tissue after maternal exposure to intravenous gadoteridol during pregnancy. The study concluded that gadoteridol could cross the placenta. Given the similarities between human and nonhuman primate placental physiology, the study suggests there could be relatively little deposition in human fetal tissues after maternal gadoteridol injection. However, the long-term risk of such low levels of gadolinium deposition is still unknown. At our institution, no intravenous injection (of gadolinium agents or sedation agents) was used for any of the examinations, and specific absorption rate limits were in keeping with departmental protocols.

Moreover, maternal indications for prenatal MRI also need to be taken into account.

Fetal MR imaging

All the patients were imaged in supine or left-lateral position, depending on what was most comfortable. Fetal images are obtained in three orthogonal planes in the mother to plan the sagittal, coronal, and axial views of the fetus. The last sequence is used as a reference for planning the next sequence to compensate for fetal movement. All sequences are performed in all three planes through the fetus. Additional imaging planes, such as oblique sagittal or coronal positions, were obtained as needed. An axial T2-weighted sequence may be performed through the fetal brain for purposes of gestational dating. In recent years, ultrafast MR imaging sequences have provided short image acquisition times and usually prevent fetal motion from degrading image quality.

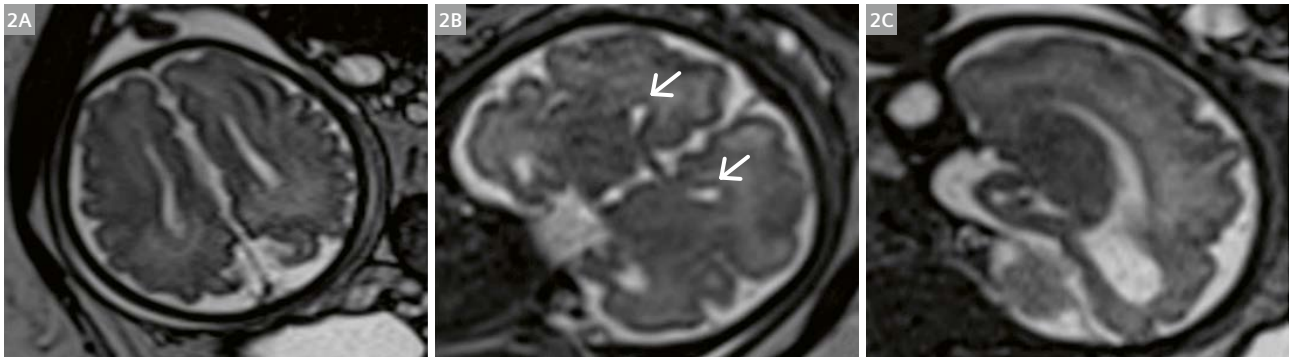

2 **Corpus callosum agenesis**
Sagittal HASTE **(2C)** shows complete absence of the corpus callosum. Axial TrueFISP **(2A)** shows parallel orientation of lateral ventricles. Coronal TrueFISP **(2B)** shows steer-horn-shaped frontal horns (arrows) resulting from the impression of Probst bundles.

1. **T2-weighted sequences**
   T2-weighted imaging (T2WI) includes single-shot, and half-Fourier single shot turbo spin echo (SSTSE, HASTE) T2-weighted sequences, and balanced sequences such as true fast imaging with steady-state precession (TrueFISP), which produces high tissue contrast and highlights the hyperintense amniotic fluid. At our institution, T2 HASTE and T2 TrueFISP were the most frequently used sequences for evaluating fetal anatomy. The TrueFISP sequence also allows vascular studies that require no intravenous contrast agent and can reveal hyperintense fetal vessels (vessels appear hypointense on SSTSE T1-weighted and T2-weighted images).

2. **T1-weighted sequences**
   T1-weighted imaging (T1WI), including 3D dual gradient echo (GRE), 2D fast spoiled GRE (FISP), and 3D liver acquisition and volume acquisition (3D VIBE), show less tissue contrast than T2WI sequences. T1WI sequences are primarily used to identify subacute bleeding, calcification, and lipoma, which appear as hyperintense loop structures in studies of congenital diaphragmatic hernia (CDH). T1WI sequences are also used to assess the presence and distribution of meconium, which enables accurate diagnosis of gastrointestinal abnormalities, reveals the size and location of the fetal liver, and can identify fetal, placental, or maternal hemorrhage.

3. **Susceptibility-weighted imaging**
   Susceptibility-weighted imaging (SWI) uses the intrinsic nature of local magnetic fields to enhance image contrast and thereby improve the visibility of various susceptibility sources and facilitate diagnostic interpretation [7]. It is worth mentioning that calcification is strongly diamagnetic and therefore decreases the magnetization in bone compared to the applied magnetic field. The technique results in a high contrast between bone and soft tissue, but a low contrast between different types of soft tissue. The low-signal bone is therefore easily distinguishable from the surrounding soft tissue.

4. **Diffusion-weighted imaging**
   As well as being used to diagnose cerebral infarction, diffusion-weighted imaging (DWI) sequences are currently being developed for fetal applications. The technique is already being used to study the maturity of lung parenchyma.

Fluid-sensitive short T1 inversion recovery (STIR), intravoxel incoherent motion imaging (IVIM), MR hydrography, and other sequences are not part of the routine fetal protocol but may be performed in specific cases where necessary.

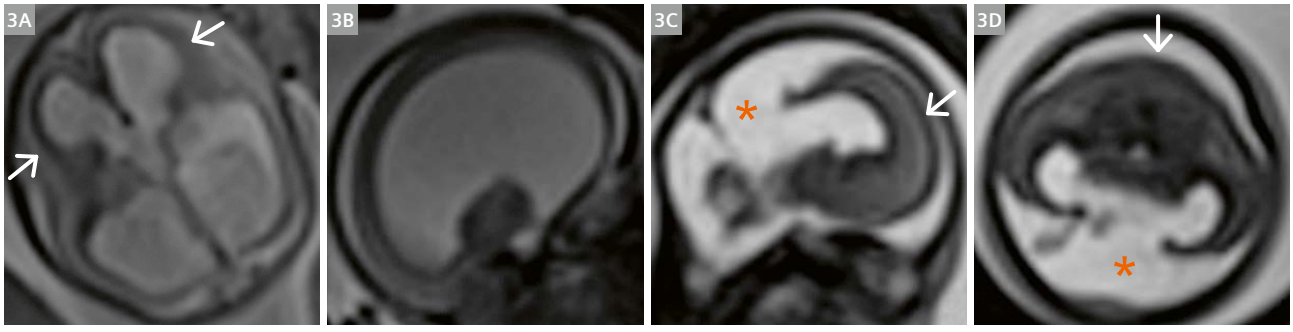

3 **Severe hydrocephalus (3A, B) and alobar holoprosencephaly (3C, D)**
Axial and coronal **(3A)** T2 HASTE imaging shows the marked dilation of the cerebral bilateral ventricle stenosis with only a thin mantle of overlying cerebral cortex (arrows). Sagittal **(3C)** and coronal **(3D)** T2 TrueFISP imaging shows only minimal frontal cerebral mantle (white arrows in 3A and B) and replacement of the majority of the brain with CSF (star). Coronal **(3C)** and axial **(3D)** T2 TrueFISP show a complete absence of falx, an interhemispheric fissure, and corpus callosum. Also visible is a horseshoe-shaped monoventricle communicating with a dorsal cyst (star).

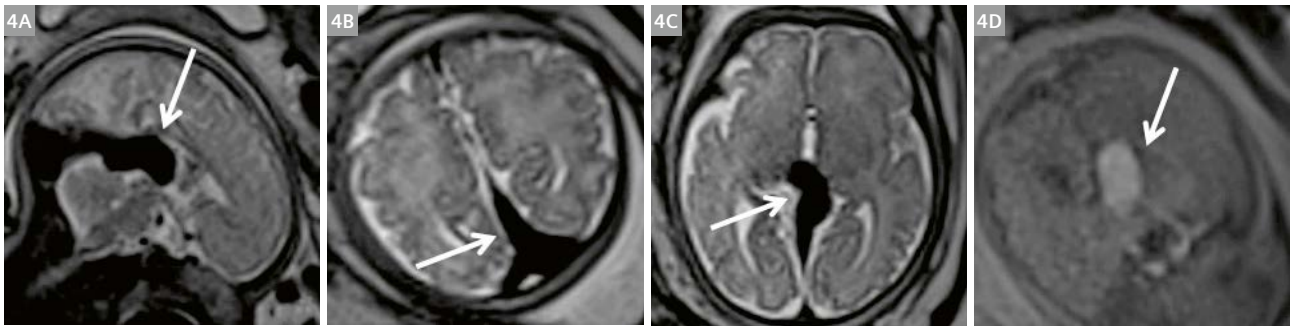

4 Galen vein malformation
Sagittal **(4A)** and coronal and axial **(4B)** T2 HASTE show a large varix (arrow) replacing the Galen vein, which exhibits hyperintensity on T1WI (**4D**, arrow).

The anatomy and anomalies in fetal MRI

Brain and spine

Imaging the central nervous system (CNS) anatomy and relevant pathology is clinically important for the early identification of cranial and spinal malformations and anomalous development. Fetal MRI has been shown to have higher contrast resolution and SNR than ultrasonography when it comes to illustrating the morphological changes in cranial and spinal brain abnormalities [8]. Most of the literature describing the results of MRI in large series of fetuses with CNS abnormalities deals with cerebral pathology. Spinal anomalies are usually described using examinations of smaller groups of patients or in case reports.

MR images of the developing fetal brain reflect changes in histogenesis and myelination. Subsequent changes are seen in the brain volume, surface configuration (sulcation), and internal configuration. Detailed information provided by MRI is necessary to evaluate the differentiation of white and gray matter, migration and myelination disorders, brain morphology and pathologies, and cranial posterior fossa and midline structures. Here, localizer brain scans (Fig. 1) provide the basis for images demonstrating different developmental deformities (Figs. 2–4).

The spinal canal and cord anomalies are among the CNS abnormalities which occur as a result of disruptions in formation and maturation. During the first three to five weeks of gestation (neurulation period), the neural tube, notochord, spine, and cranium develop. Disorders that occur at this stage of gestation (i.e., most spinal canal defects) are called "dorsal induction abnormalities". The dysraphic spinal canal and spinal cord disorders are divided into three groups: open dysraphic abnormalities, occult dysraphic abnormalities, and latent dysraphic abnormalities (e.g., diastematomyelia, hydromyelia, syringomyelia, dorsal dermoid sinus, teratoma, hamartoma, lipoma, dermoid/epidermoid cyst, and caudal regression syndrome).

Congenital anomalies of the spine occur at four to six weeks of gestation due to abnormal vertebral development that causes asymmetric growth of the spine. Anomalies in the ossification center of the fetal vertebral body result in bony defects such as hemivertebrae, butterfly vertebrae, and block vertebrae, which cause congenital scoliosis. MRI of fetuses diagnosed with osseous anomalies of the spine remains largely unexplored. Recently, we adapted and improved a clinically available SWI sequence for fetal spine imaging to evaluate vertebral malformations and anomalous vertebral development (in bony structures). We also typically used T2 TrueFISP and HASTE sequences to evaluate the recognition of the fetal spinal canal and spinal cord pathologies, as described in previous studies [9].

For MR imaging of the fetal spine, the protocol first involved a scout imaging sequence to gather information about the orientation of the fetus. Subsequent routine clinical sequences included T1WI, DWI, HASTE, T2-weighted TrueFISP, and SWI sequences. The HASTE, TrueFISP, and SWI sequences were obtained in the axial, coronal, and sagittal planes. The axial plane is best for assessing the neural arches, the coronal plane allows an additional assessment of the ribs and of pedicular widening in cases of spina bifida, and the sagittal plane is best for assessing the whole spine lengthways. The SWI sequence is best run immediately after routine HASTE or TrueFISP sequences, depicting the required anatomy by simply copying the slice parameters and thereby minimizing the time between sequences and reducing the chance of fetal motion. Here, localizer spine scans (Fig. 5) provide the basis for demonstrating various developmental deformities as follows (Figs. 5–9).

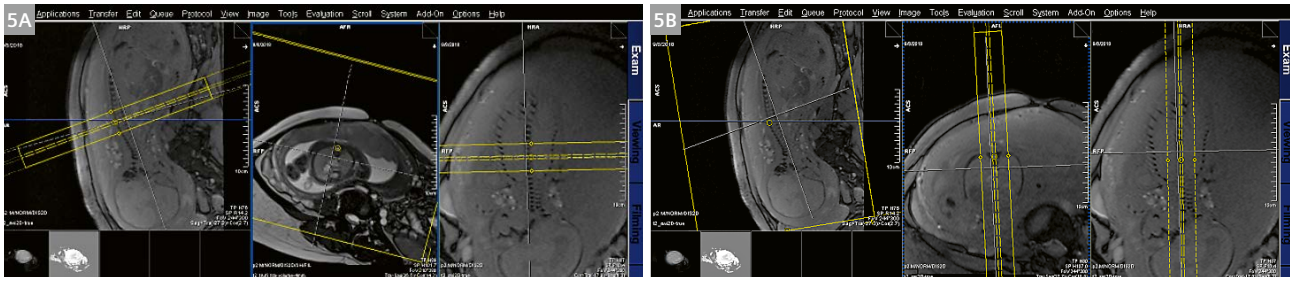

5 Axial, sagittal, and coronal localizer images of the fetal spine.

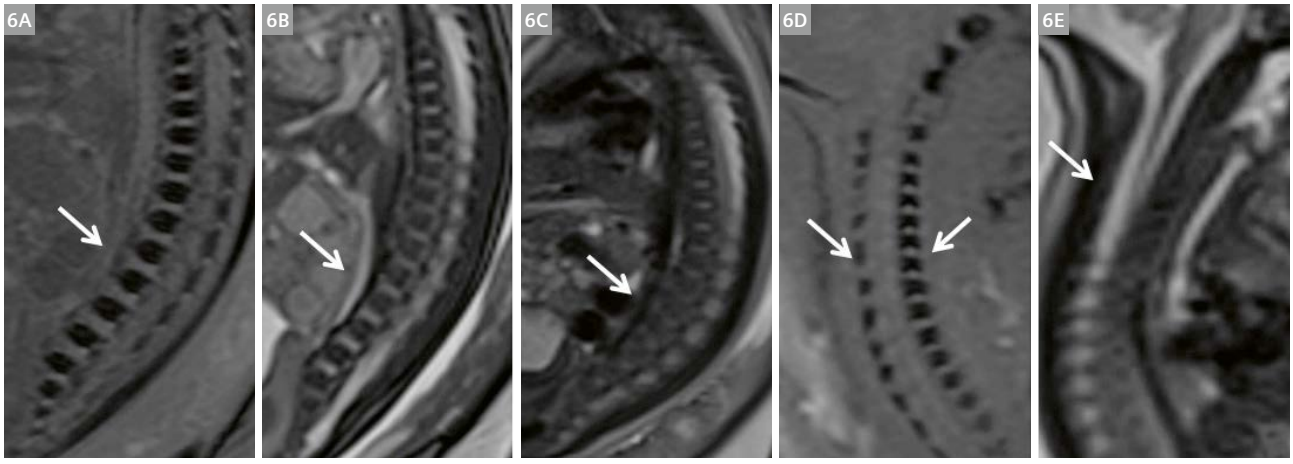

6 Images at 32 weeks' gestation (6A–C) and 26 weeks' gestation (6D–E) with normal fetal spine structures. Sagittal view of the thoracolumbar spine, MR images including SWI (6A), TrueFISP (6B), and HASTE (6C). The SWI **(6A, D)** clearly shows the vertebral bodies and the posterior elements (arrows). On a similar plane in the same position using TrueFISP **(6B, E)** and HASTE **(6C)**, the vertebral column (arrows) is shown poorly but could reveal the structures of the intraspinal canal.

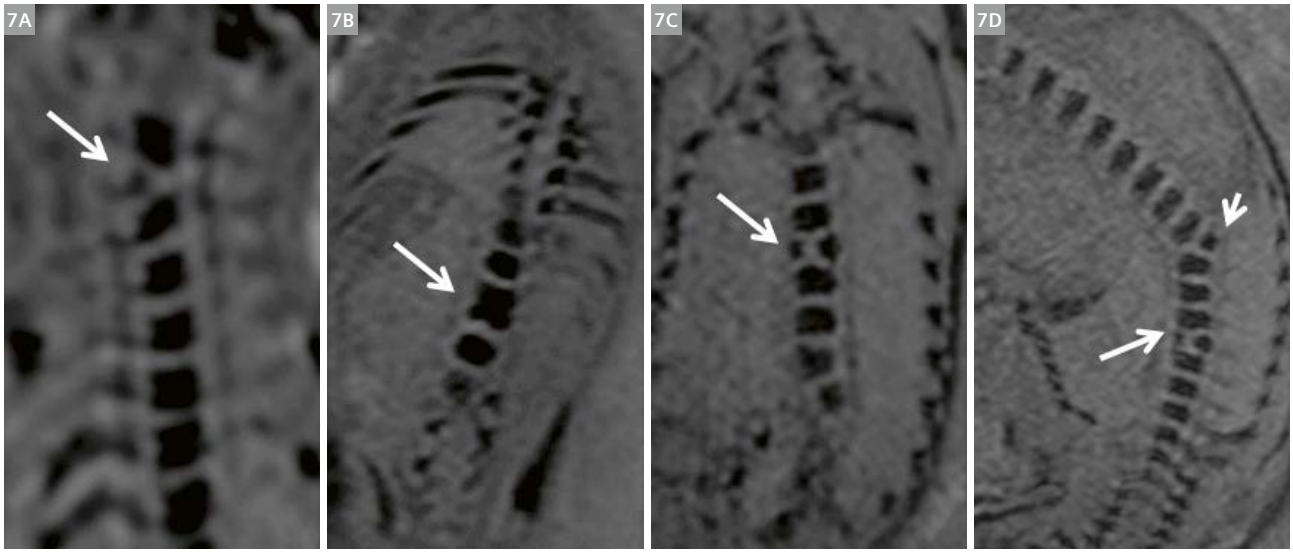

7 SWI images at 26 weeks' gestation (7A), 25 weeks (7B), 33 weeks (7C), and 34 weeks with fetal vertebral anomalies. Coronal views of the cervical **(7A)**, lumbar **(7B)**, and thoracic **(7C)** spine show hemivertebrae, block vertebrae, and butterfly vertebrae. Multiple vertebral anomalies with hemivertebrae (short arrows) and butterfly vertebrae (long arrows) are clearly visible in coronal 2D SWI **(7D)**.

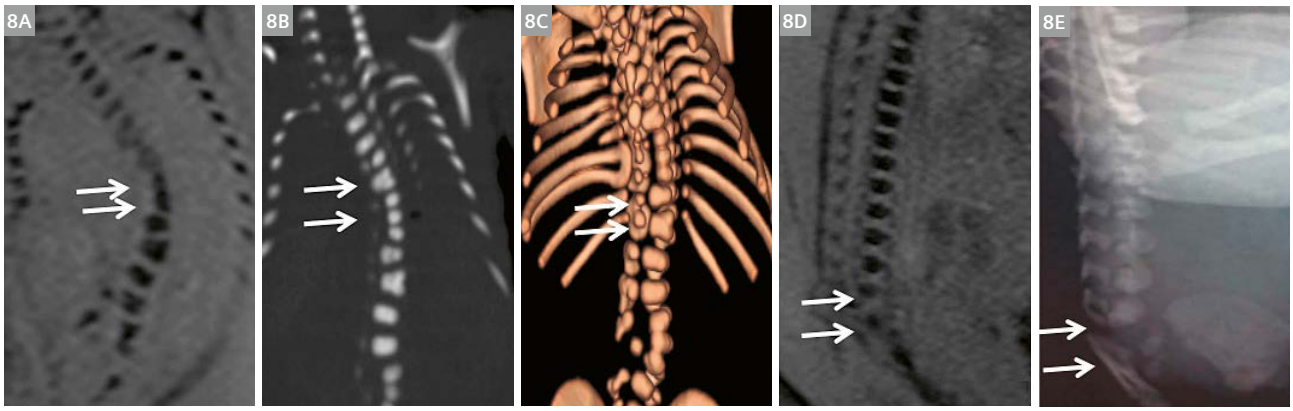

8 Images at 24 weeks' gestation (8A–E) with multiple vertebral anomalies (8A–C) and at 32 weeks' gestation (8D–E) with caudal regression syndrome. SWI **(8A)** shows multiple vertebral anomalies (arrows) that were consistent with the postmortem CT (**8B**, **C**, arrows). SWI shows dysplasia of the sacrococcygeal vertebrae (arrows) that was consistent with the postmortem X-ray (**8E**, arrows).

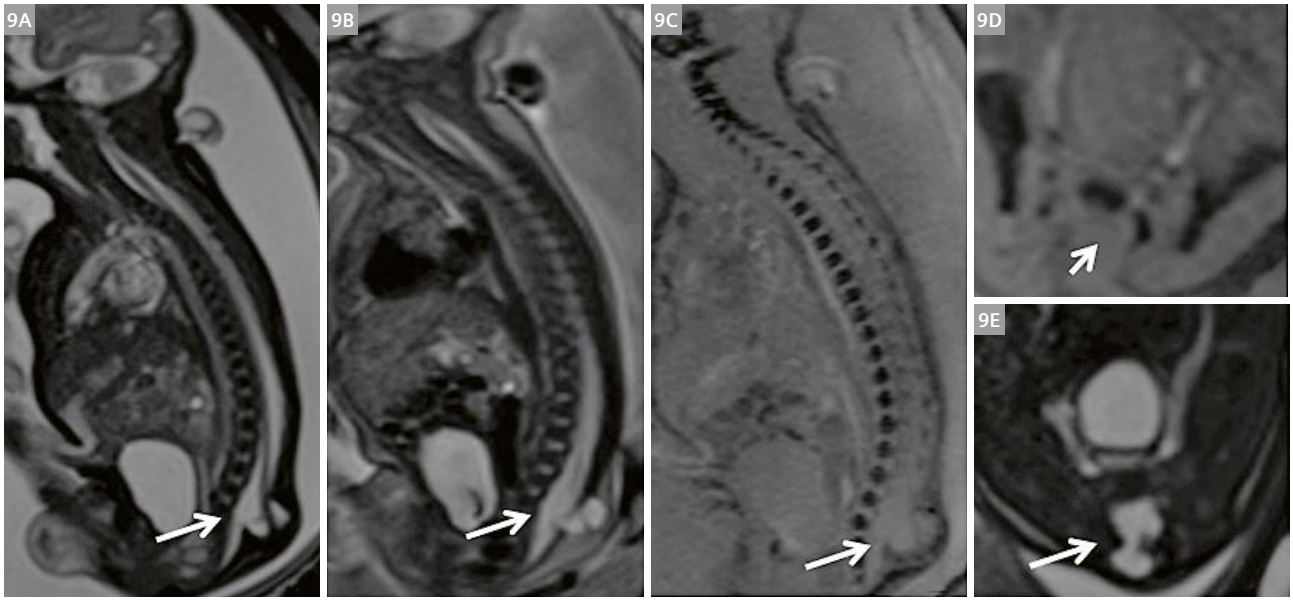

9 Images at 32 weeks' gestation with spinal dysraphism (9A–E). Sagittal view of the MR images include HASTE **(9A)**, TrueFISP **(9B, E)**, and SWI **(9C, D)**. The pocket-like processes protruding from the sacrococcygeal spinal canal were all visible, and the spinal cord was found to extend from the spinal canal to the dilated dural capsule (9A, B, E, long arrow), which could not be seen with SWI (9C, D). However, SWI showed excellent osseous spinal structures and demonstrates the pedicular widening (9C, long arrow; 9D, short arrow).

Chest

At present, ultrasound and MRI are the only diagnostic tools that can examine fetal lungs noninvasively. MRI provides additional biochemical and functional information that cannot be obtained by ultrasound as well as detailed structural information. This therefore makes it a valuable diagnostic adjunct for assessing fetal lung development [10]. Congenital chest malformations can range from small and asymptomatic entities to large, space-occupying masses that require immediate surgical treatment. An understanding of fetal chest masses is essential for appropriate monitoring during pregnancy, and for treatment recommendations and delivery management. The most common congenital chest anomalies include congenital cystic adenomatoid malformation (CCAM), congenital diaphragmatic hernia (CDH), bronchopulmonary sequestration (BPS), congenital hydrothorax, and congenital lobar emphysema. Less common entities include congenital high airway obstruction syndrome (CHAOS), congenital bronchogenic cyst, bronchial atresia, pulmonary arteriovenous malformation (PAVM), congenital pulmonary lymphangiectasia, pulmonary hypoplasia-aplasia, mediastinal teratoma, and mediastinal lymphangioma. These pulmonary abnormalities are not mutually exclusive; they frequently occur together as hybrid conditions.

The MRI sequences used to evaluate the fetal chest include HASTE, fast single-shot echo, and TrueFISP. In our unit, HASTE and TrueFISP images are the most useful for evaluating the lung anatomy. The lungs typically contain a significant amount of alveolar fluid, which is homogeneously hyperintense relative to the chest wall muscle on T2-weighted images.

Congenital diaphragmatic hernia and extralobar pulmonary sequestration were demonstrated as follows (Figs. 10, 11).

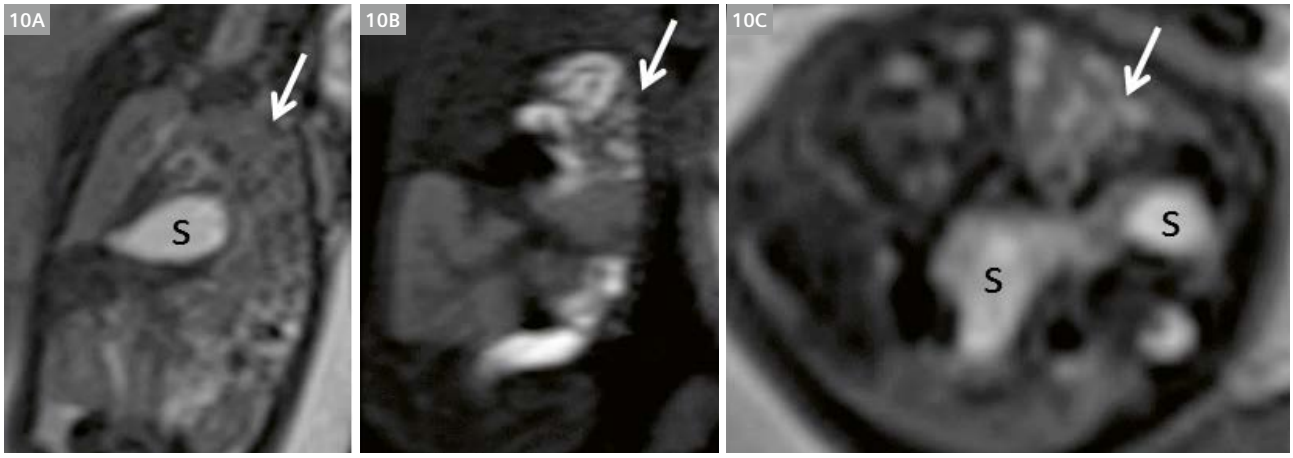

10 Congenital diaphragmatic hernia at 28 weeks' gestation
Coronal **(10A)** and axial **(10C)** T2 HASTE, and T1w imaging **(10B)** show herniated content (arrow) displacing the heart and compressing the unilateral lung and portions of the bowel (10B, arrow) and stomach (S) occupying the unilateral hemithorax.

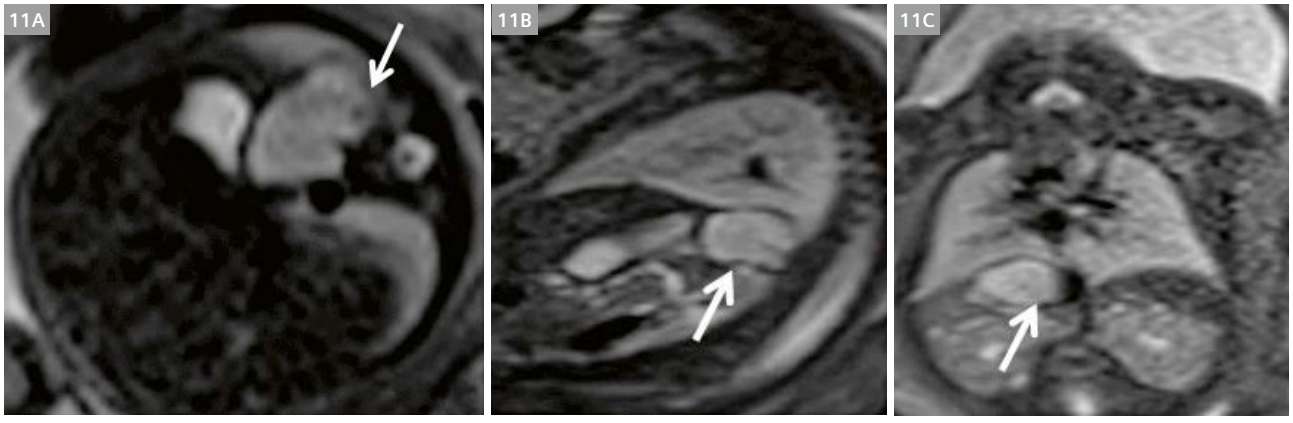

11 Extralobar pulmonary sequestration at 32 weeks' gestation
Axial **(11A)**, sagittal **(11B)**, and coronal **(11C)** T2 HASTE show a homogeneous, high T2WI signal between the left subphrenic space and left kidney with a clear boundary (arrow). Postnatal CT (not shown) enhancement shows a vascular shadow connected to the aorta.tions of the bowel (10B, arrow) and stomach (S) occupying the unilateral hemithorax.

Abdominal abnormalities and tumors

Fetal abdominal deformities and tumors vary in their location, and can be derived from the gastrointestinal tract, liver, kidney, and retroperitoneum. Congenital tumors are defined as those that are present during the fetal stage or at birth. In some cases, MRI can provide important information and even add important findings to prenatal US for perinatal management by visualizing fetal tumors with common tumor-related complications and other exceptional congenital abnormalities [11]. Common indications for fetal gastrointestinal (GI) MRI include suspected esophageal, small bowel, and large bowel obstruction, bowel malrotation, and bowel perforation resulting in meconium peritonitis or meconium pseudocyst. MRI is also particularly useful for evaluating rare GI abnormalities, such as megacystis microcolon intestinal hypoperistalsis syndrome (MMIHS), cloacal exstrophy, and cloacal malformation. Although US remains the modality of choice for investigating fetal anomalies, the findings are often nonspecific and may relate to transient normal variants [12]. In addition, urine and fluid in the colon beyond 24 weeks may have a similar sonolucent appearance on US and opposite appearances on MR images, allowing better identification and discrimination. In our department, a T1-weighted breath-hold sequence is completed in the coronal plane and, if necessary, in the sagittal and axial planes.

Different developmental deformities in the abdomen were demonstrated as follows (Figs. 12–16).

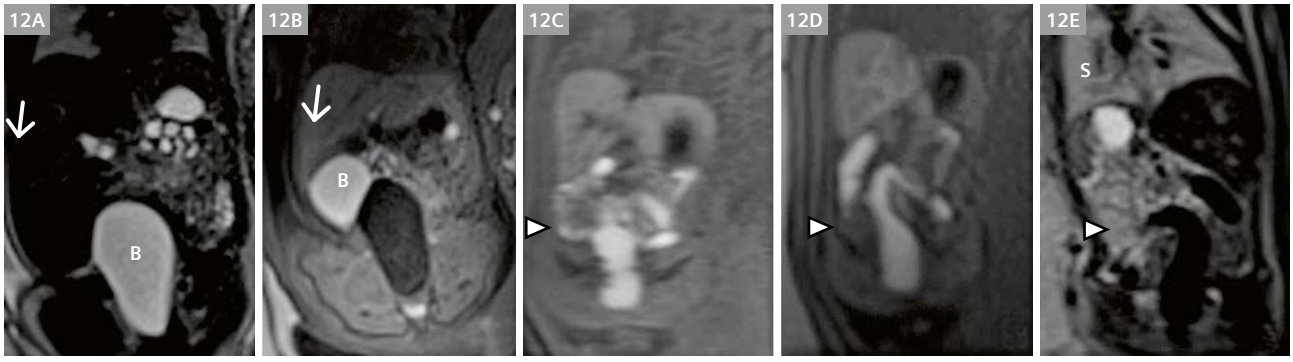

12 **Localized intestinal dilatation at 30+4 weeks' gestation, and imperforate anus at 28 weeks' gestation**
Coronal T2 HASTE **(12A)** and T1w **(12B)** images show the dilated loops of one part of the gastrointestinal tract. It is markedly hyperintense on T1WI (arrow) and hypointense on T2WI (arrow). Coronal T1WI **(12C, D)** and T2 TrueFISP **(12E)** images show a prominent rectum (arrowhead) with high T1 signal intensity and low T2 signal intensity. The abnormality of the large bowel was identified and diagnosed as rectal atresia during a postnatal physical examination. B = urinary bladder, S = stomach.

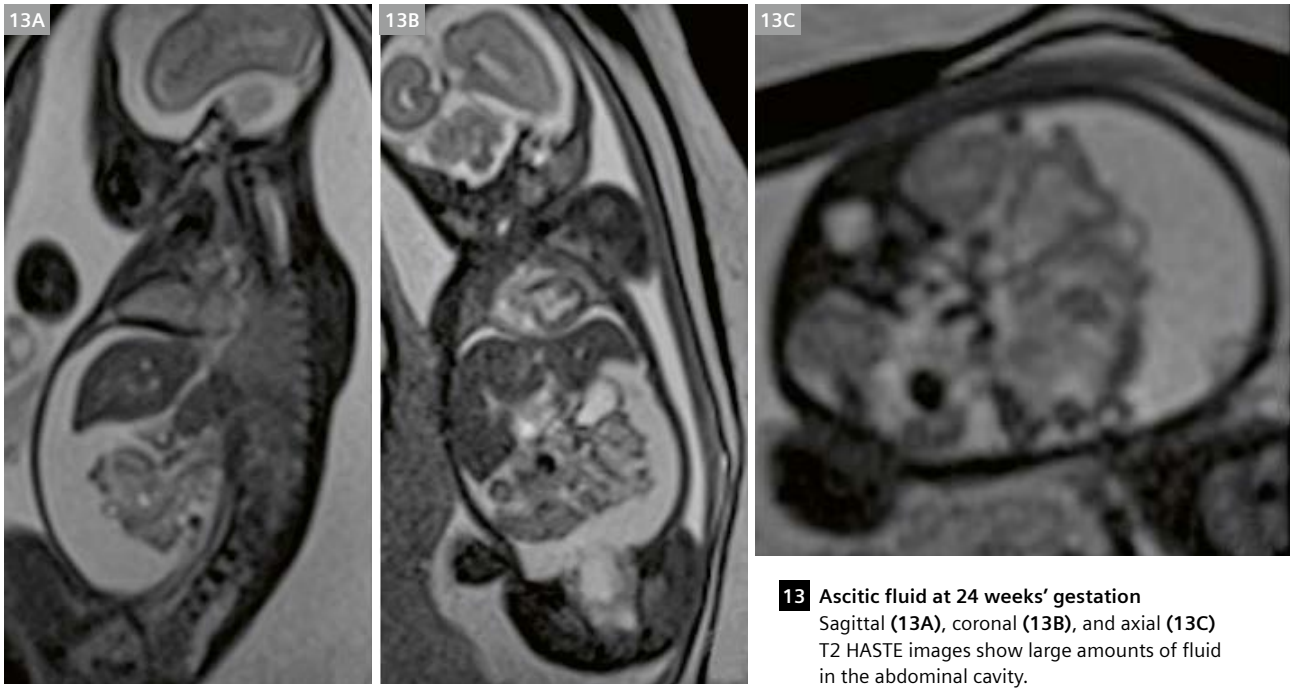

13 **Ascitic fluid at 24 weeks' gestation**
Sagittal **(13A)**, coronal **(13B)**, and axial **(13C)** T2 HASTE images show large amounts of fluid in the abdominal cavity.

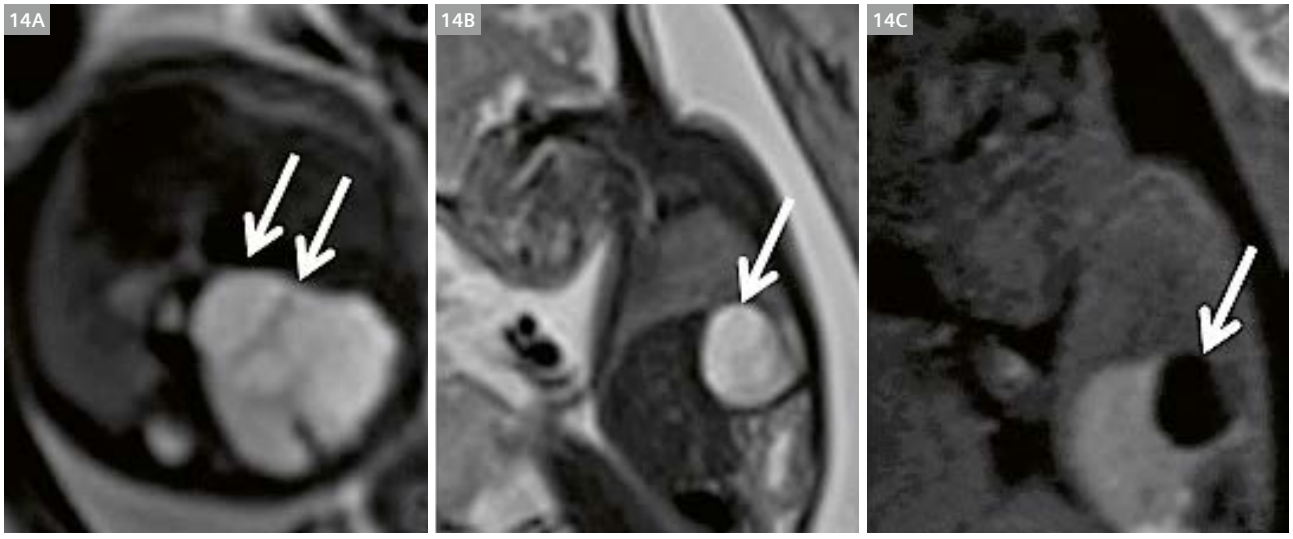

14 Neuroblastoma at 28 weeks' gestation
Axial **(14A)**, sagittal **(14B)**, and coronal **(14C)** T2 HASTE images show a solid mass with a clear boundary above a lateral kidney that is hyperintense on a T2-weighted sequence (arrow) and was found to be neuroblastoma after birth.

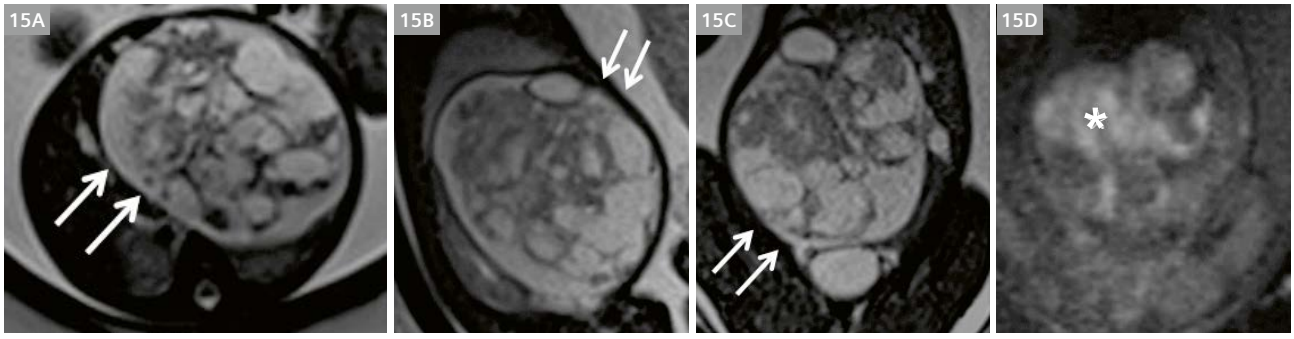

15 Teratoid tumors at 30 weeks' gestation
Axial T2 HASTE **(15A)**, sagittal **(15B)**, and coronal **(15C)** T2 TrueFISP images show a heterogeneous solid cystic mass with a high-intensity heterogeneous signal (arrows), and surrounding tissue that was markedly squeezed. The giant lesions showed restricted diffusion with DWI (**15D**, star). A histopathological diagnosis of teratoid tumors was made after birth.

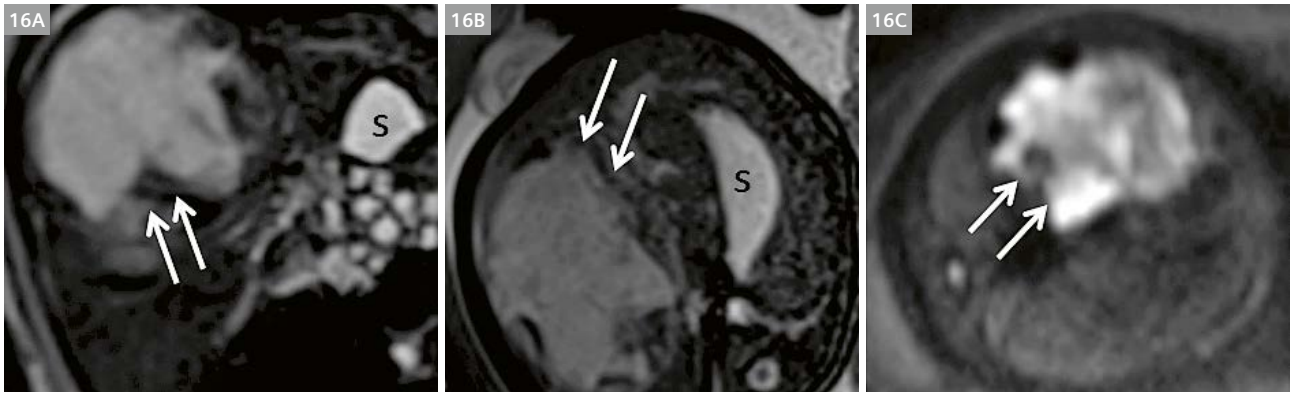

16 Hepatic hemangioendothelioma at 32 weeks' gestation
Coronal T2 HASTE **(16A)** and axial T2 TrueFISP **(16B)** images show a large heterogeneous and high-signal mass in the liver parenchyma, and highly restricted diffusion with DWI **(16C)**. A histopathological diagnosis of hepatic hemangioendothelioma was made after birth.

Maternal indications for prenatal MRI

In addition to fetal indications, there are several maternal indications for prenatal MR imaging. They include the possibility of uterine rupture, the need to differentiate between placenta accreta and percreta, a large myoma interfering with the pregnancy, and MR pelvimetric measurements. In our unit, the technique of placental MRI and the diagnostic level are increasingly convincing and compelling.

Abnormal invasive placenta (AIP) is a disease with a spectrum of severity characterized by abnormal, firmly adherent placental implantation into the uterus at varying depths. It is typically referred to as placenta accreta, increta, and percreta [13]. When AIP occurs, the placenta may not be completely separated from the uterus at the time of delivery, resulting in potentially life-threatening intrapartum or postpartum massive hemorrhage and associated morbidity such as multisystem organ failure, disseminated intravascular coagulation, and even death. Placenta percreta (PP) is the most dangerous type of AIP. It is characterized by trophoblasts fully penetrating the myometrium and in some cases extending to or breaching the serosa and even invading surrounding structures [14]. An accurate prenatal diagnosis of PP is therefore imperative.

In 2017, our team published an article on placenta accreta [15] that aimed to identify specific MRI features for differentiating PP from placenta accreta (PA), and to characterize the features of invasive placenta previa. Our studies showed a series of MRI features, including myometrial thinning, interrupted myometrium, loss of the placental-myometrial interface, marked placental heterogeneity, dark intraplacental bands, abnormal intraplacental vascularity, abnormal uterine bulge, placental bulge (type I and type II, Fig. 2), uterine serosal hypervascularity, bladder wall nodularity, and extrauterine placental extension. Our results suggest that type II placental bulge and uterine serosal hypervascularity are useful MRI features for differentiating PP from PA. Profoundly abnormal vessels are associated with greater blood loss during caesarean section. Our results could contribute to accurate prenatal diagnosis of PP and help minimize the risk of massive hemorrhage [15].

In our center, all the patients with suspected invasive placenta previa (IPP) were imaged in the supine or left-lateral position with bladders moderately full. T2-weighted HASTE and T2-weighted TrueFISP images were obtained without breath-hold in the axial, coronal, sagittal, and oblique sagittal planes. Additional imaging planes perpendicular to the placenta-uterus interface or uterus-bladder interface were obtained in the region of the suspected AIP.

Several placenta increta and placenta percreta were demonstrated as follows (Figs. 17–20).

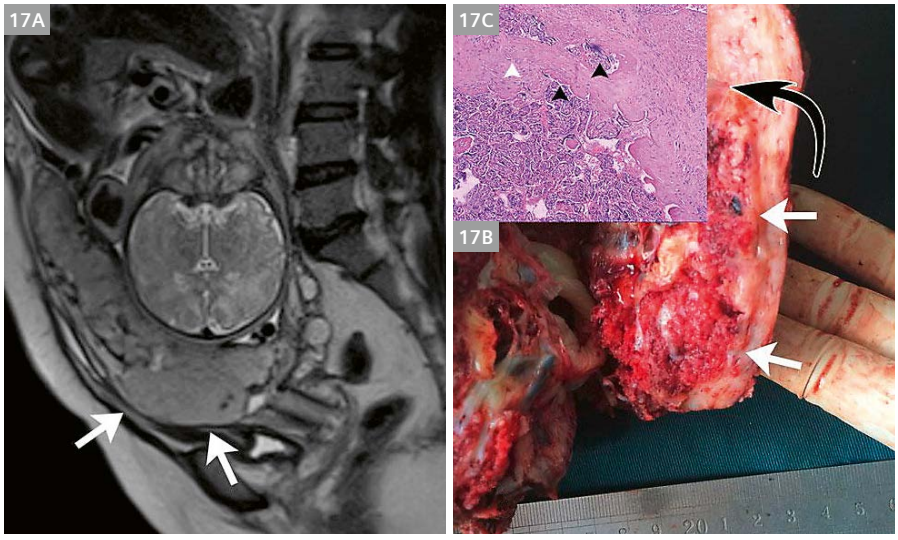

17 Placenta increta (PI) in a 40-year-old woman at 35 weeks' gestation
A sagittal T2 HASTE MR image **(17A)** demonstrates type I placental bulge (white arrows) with an intact uterine outline. A photograph **(17B)** of gross specimens after hysterectomy shows that the placenta has invaded the myometrium (white arrows) with intact uterine serosa, consistent with PI. A photomicrograph (**17C**, magnification x 400, hematoxylin and eosin stain) shows chorionic villi (black arrowheads) implanted in the myometrium (white arrowhead), consistent with PI.

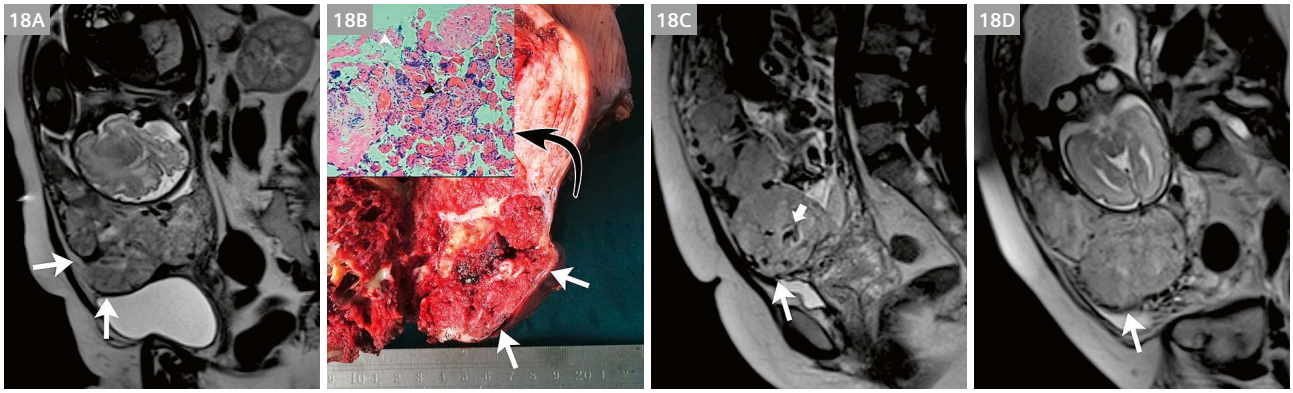

18 **Placenta percreta (PP, 18A, B) in a 39-year-old woman at 30 weeks' gestation**
A sagittal T2 HASTE MR image **(18A)** shows type II placental bulge (white arrows) protruding from the uterine outline. A photograph **(18B)** of gross specimens after hysterectomy shows placental invasion (white arrows) through the uterine wall, consistent with PP. A photomicrograph (magnification: x 400, hematoxylin and eosin stain) shows chorionic villi (black arrowhead) penetrating the myometrium (white arrowhead), consistent with PP. Sagittal T2 HASTE MR images show a type IIa placental bulge (long arrow, a focal outward bulge protruding from the uterine outline) with bridging vessels (short arrow) in a 31-year-old woman at 35 weeks' gestation with PP **(18C)** and type IIb placental bulge (long arrow) without bridging vessels in a 29-year-old woman at 32 weeks' gestation with PP **(18D)**.

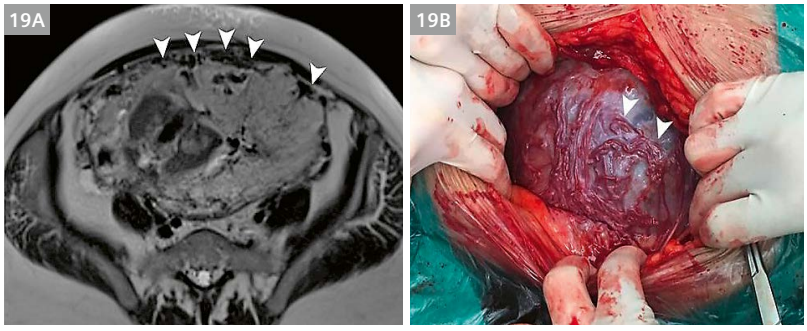

19 **Placenta percreta (PP) in a 35-year-old woman at 29 weeks' gestation**
An axial T2 HASTE image **(19A)** shows uterine serosal hypervascularity (arrowheads, tortuous and closely packed vessels along the uterine serosa) in the lower uterine segment.
A photograph **(19B)** taken during cesarean delivery shows the tortuous abnormal vessels in the uterine serosa (arrowheads), consistent with their appearance on MR images.

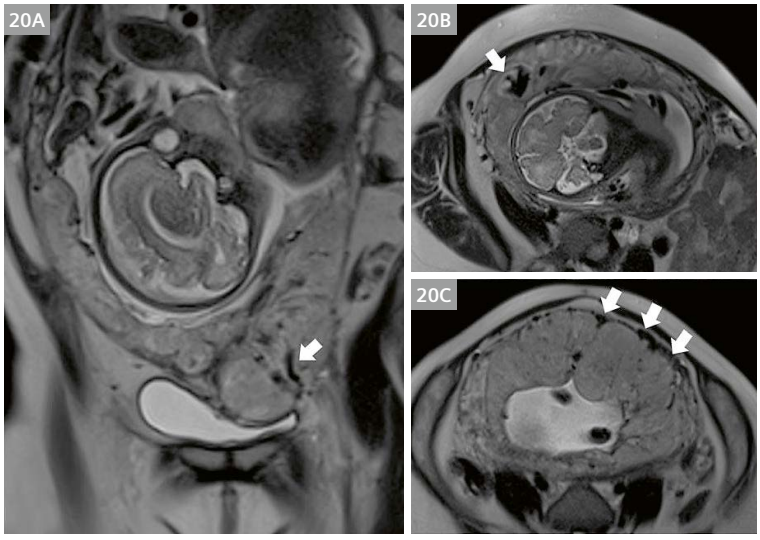

20 A coronal T2 HASTE MR image **(20A)** shows bridging vessels (arrow) through the bulging placenta in a 25-year-old woman at 32 weeks' gestation with placenta percreta (PP). An axial T2 HASTE MR image **(20B)** shows abnormal intraplacental vascularity (arrow) in a 28-year-old woman at 30 weeks' gestation with placenta increta (PI). An axial T2 HASTE MR image **(20C)** demonstrates uterine serosal hypervascularity (arrows) in a 34-year-old woman at 35 weeks' gestation with PP.

As outlined in this article, fetal MR imaging is playing an increasingly important role in prenatal diagnostics. Nevertheless, US will and should remain the first choice for prenatal screening due to its low cost, ease of availability, and superb safety profile. Advances in fetal MRI have given clinicians powerful tools to identify fetal pathologies. These can range from small and symptomatic abnormalities to large, space-occupying masses that require immediate surgical treatment. The information obtained with fetal MR imaging can be helpful and allow early planning of prenatal management.

References

1 Weisstanner C, Gruber GM, Brugger PC, et al. Fetal MRI at 3T – ready for routine use? Br J Radiol. 2017; 90(1069):20160362.
2 Prayer D, Brugger PC. Investigation of normal organ development with fetal MRI. Eur Radiol. 2007; 17(10):2458-2471.
3 Haacke EM, Xu Y, Cheng YC, et al. Susceptibility weighted imaging (SWI). Magn Reson Med. 2004; 52(3):612-618.
4 Reichenbach JR, Jonetz-Mentzel L, Fitzek C, et al. High-resolution blood oxygen-level dependent MR venography (HRBV): a new technique. Neuroradiology 2001; 43(5):364-369.
5 Robinson AJ, Blaser S, Vladimirov A, et al. Foetal "black bone" MRI: utility in assessment of the foetal spine. Br J Radiol. 2015; 88(1046):20140496.
6 Smith FW, Adam AH, Phillips WD. NMR imaging in pregnancy. Lancet. 1983; 1(8314-5):61-62.
7 Reichenbach JR, Venkatesan R, Schillinger DJ, et al. Small vessels in the human brain: MR venography with deoxyhemoglobin as an intrinsic contrast agent. Radiology. 1997; 204(1):272-277.
8 Coakley FV, Glenn OA, Qayyum A, et al. Fetal MRI: a developing technique for the developing patient. AJR Am J Roentgenol. 2004; 182(1):243-252.
9 Duczkowska A, Bekiesinska-Figatowska M, Herman-Sucharska I, et al. Magnetic resonance imaging in the evaluation of the fetal spinal canal contents. Brain Dev. 2011; 33(1):10-20.
10 Kasprian G, Balassy C, Brugger PC, et al. MRI of normal and pathological fetal lung development. Eur J Radiol. 2006; 57(2):261-270.
11 Nemec SF, Horcher E, Kasprian G, et al. Tumor disease and associated congenital abnormalities on prenatal MRI. Eur J Radiol. 2012; 81(2):e115-e122.
12 Veyrac C, Couture A, Saguintaah M, et al. MRI of fetal GI tract abnormalities. Abdom Imaging. 2004; 29(4):411-420.
13 Belfort MA. Placenta accreta. Am J Obstet Gynecol. 2010; 203(5):430-439.
14 Silver RM, Barbour KD. Placenta accreta spectrum: accreta, increta, and percreta. Obstet Gynecol Clin North Am. 2015; 42(2):381-402.
15 Chen X, Shan R, Zhao L, et al. Invasive placenta previa: Placental bulge with distorted uterine outline and uterine serosal hypervascularity at 1.5T MRI – useful features for differentiating placenta percreta from placenta accreta. Eur Radiol. 2018; 28(2):708-717.

Contact

Guangbin Wang
Department of MR
Shandong Medical Imaging Research Institute
Shandong University
324, Jingwu Road, Jinan
Shandong 250021
China
wgb7932596@hotmail.com

Guangbin Wang

Xianyun Cai

We are looking forward to hearing from you

Founded in 1993 the MAGNETOM Flash magazine has been around almost as long as MAGNETOM MRI scanners.

In times of online media and digitalization we would value your feedback to ensure that the magazine continues to fit your interests and professional needs.

Please take a moment to complete a brief reader survey at
www.siemens.com/magnetom-world

syngo Virtual Cockpit – Your Software for Remote Scanning Assistance and More Flexible Workforce Management

Petra Kraft; Janis Dummet

Siemens Healthineers, Forchheim, Germany

Growing financial pressure and increasingly assertive patients are pushing imaging providers toward finding ways to deliver high-quality care while at the same time keeping costs low. As a relevant cost and quality factor, healthcare personnel have a considerable bearing on tackling these challenges. But as qualified staff is expensive and hard to come by in some markets, optimal deployment of human resources is key to success. New working methods are required that will enable hospitals to deal with the increasing workload and quality expectations despite having a smaller workforce at their disposal.

syngo Virtual Cockpit[1], our new software solution, allows medical staff to connect remotely to scanner workplaces to assist personnel at a different location, especially where more sophisticated examinations are required. *syngo* Virtual Cockpit can be used with CT, MR, and MR PET scanners from Siemens Healthineers. The ability to deploy experienced technologists across multiple locations allows healthcare providers to manage their workforce more flexibly and thus ease tight human resources.

Connecting clinical teams beyond physical boundaries

For radiological examinations, experienced colleagues can "tune in" quickly and in real time via headsets, conference speakers, chat or video functions. That means that the steering technologists[2] can remain at their own location and provide guidance to the modality technologist[3] operating the scanner at another location, e.g., to adjust protocol parameters.

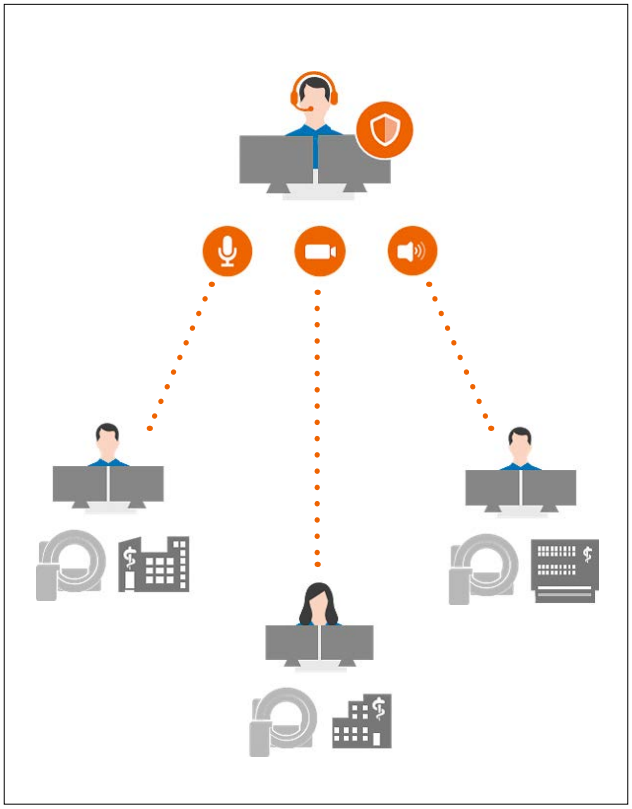

1 *syngo* Virtual Cockpit allows medical staff to provide comprehensive scanning assistance to imaging personnel via video, audio, and chat functions. Up to three scanners at different locations can be supported simultaneously by one steering technologist.

[1]*syngo Virtual Cockpit is not commercially available in all countries. For regulatory reasons, its future availability cannot be guaranteed. Precondition: Expert-i enabled modality from Siemens Healthineers.*
[2]*Steering technologist: An experienced technologist who works with syngo Virtual Cockpit and connects to modalities remotely.*
[3]*Modality technologist: A technologist who works locally at the modality site.*
[4]*The statements by Siemens Healthineers' customers presented here are based on results that were achieved in the customer's unique setting. Since there is no 'typical' hospital and many variables exist (e.g., hospital size, case mix, level of IT adoption), there can be no guarantee that other customers will achieve the same results.*

"We expect the use of syngo Virtual Cockpit to have a significant impact because we will save costs by not sending dedicated steering technologists from one site to the other. We will also be able to better utilize our scanner fleet. Our patients will also benefit, because they no longer have to go to a dedicated site in our network to get a special examination."[4]

Associate Professor Justus Roos, M.D., Head of Radiology and Nuclear Medicine
Lucerne Cantonal Hospital (LUKS), Switzerland

Improving workforce productivity

With this software tool, the steering technologist can perform scans at one location while offering remote support to up to three colleagues in parallel. This makes the best possible use of resources and can lead to an increase in the total number of scans performed. Having the support of a steering technologist on hand can also positively affect the efficiency of scan procedures. Experience from Alliar Médicos à Frente, a large radiology network in Brazil, showed that with *syngo* Virtual Cockpit, the scan time could be reduced by 33%. Furthermore, long commutes between different sites are no longer necessary as steering technologists can guide exams performed by on-site technologists with *syngo* Virtual Cockpit from anywhere, which in turn saves time and costs. Also, in this way it is easy to overcome bottlenecks due to vacation periods, sick leave, nightshifts or other reasons.

Achieving a higher level of standardization

Especially when it comes to complex examinations, expert knowledge is critical. With *syngo* Virtual Cockpit, less-experienced staff can always call on a colleague for live support. This remote collaboration helps reduce the number of unwarranted variations in reports, resulting in consistent image quality across the healthcare enterprise and more accurate diagnoses. With the introduction of *syngo* Virtual Cockpit Alliar Médicos à Frente in Brazil was able to reduce the number of rescans to less than 1% of cases.

Increasing patient satisfaction

Patient satisfaction is becoming an increasingly relevant factor in the reimbursement of healthcare services. *syngo* Virtual Cockpit can have a positive impact on the productivity of medical institutions. Furthermore, making

MR workplace

Chat window on additional PC (e.g., RIS client)

2 The modality technologist is sitting at the modality console. To start a supported session, the chat tool of *syngo* Virtual Cockpit can be opened on another Windows PC, for example, the PC used for the RIS.

expert knowledge available independent of location means that specialized examinations can be offered at any site in a healthcare network. As a result, patients receive appointments more quickly for examinations at their preferred location. In this way, *syngo* Virtual Cockpit improves patient convenience and provides access to healthcare to more patients, in particular those requiring complex examinations.

The *syngo* Virtual Cockpit workflow – easy and intuitive

Imagine a complex examination is planned at an MR scanner. Due to a lack of onsite knowledge, a decision is made to support the examination remotely.

Step 1: Establishing a connection between modality and steering technologist
The modality technologist is sitting at the MR workplace and logs onto the *syngo* Virtual Cockpit software at a Windows PC next to the modality console. In a chat window, the modality technologist can see a list of all available steering technologists. The modality technologist can now choose one of those colleagues and start a chat. Later the steering technologist can connect and assist remotely at the MR console.

Step 2: Logging on securely to the scanner workplace
To establish a connection via *syngo* Virtual Cockpit, the steering technologist needs to enter a one-time password provided by the modality technologist.

The modality technologist clicks the Expert-i icon on the modality workplace and a one-time password is displayed. The modality technologist types this password in the chat window of *syngo* Virtual Cockpit.

The steering technologist now has full access to the modality workplace. Two IP cameras can be set up at the modality to show e.g. the patient on the table and the monitor of the contrast injector.

Step 3: Performing the scan with remote assistance
The modality technologist positions the patient on the exam table. As soon as all workflow steps such as coil positioning have been completed, the modality technologist leaves the room.

Now the steering technologist assists in the scanning procedure. Both colleagues keep in constant contact by communicating via speakerphone, headset, or chat. If contrast media has to be injected, it is the task of the modality technologist to start injection on site. If a CT examination is being performed, it is also the modality technologist's task to start the radiation or move the table.

syngo Virtual Cockpit is compatible with most Siemens Healthineers scanners

syngo Virtual Cockpit software can be used with all MR systems equipped with software version MR VA or later that support Expert-i. For CT, *syngo* Virtual Cockpit is compatible with all Somaris 7-based scanners with software version VB20[5], all Somaris 5-based scanners with software version VC50, as well as all Somaris X-based scanners (.go platform) with software version VA30[5]. For details, please contact your local Siemens Healthineers organization.

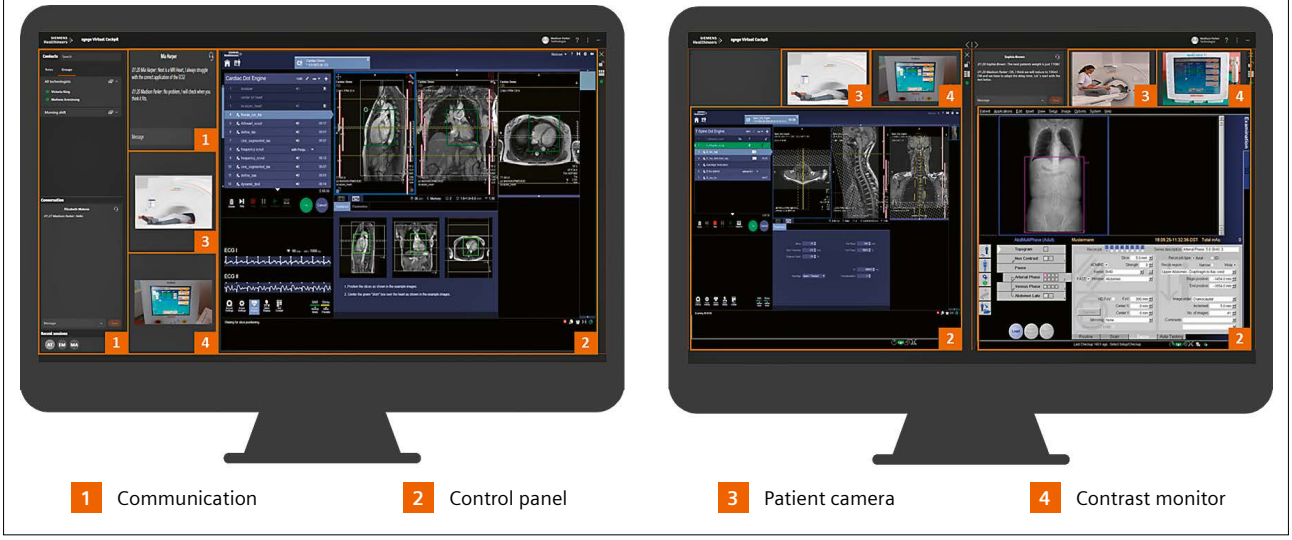

3 Each modality is displayed in a dedicated segment of the screen on the steering technologist's workplace with its own chat window. The steering technologist can see all the necessary information on his or her workplace: Contact list, chat, modality camera and contrast monitor overview. Moreover, the user name of each technologist is always visible.

"If you really have a shortage of technicians and you have to decide every morning whether you have to close a machine, yes or no, that's not really convenient. I mean we totally reduced that down to zero."[4]

Professor Michael Forsting, M.D., Director, Institute of Diagnostic and Interventional Radiology and Neurology, University Hospital Essen, Germany

Technical requirements for *syngo* Virtual Cockpit

syngo Virtual Cockpit requires the following hardware and software equipment:

- The steering technologist workplace requires one PC (Windows 10), two monitors, and a communication device.
- The modality technologist workplace needs to be equipped with one PC (Windows 7/8/10) with one monitor, one to two IP cameras, and a communication device (with headset or speakerphone).
- For a stable connection, a minimum bandwidth of 60 Mbps[6] is needed between the steering client and the modality.[7]

Summary

Our new software solution *syngo* Virtual Cockpit has been designed to assist scan procedures remotely from any location. By making expert knowledge available across sites in real time, *syngo* Virtual cockpit addresses the challenge of the shortage of experienced technologists while at the same time ensuring high-quality care.

[5] *Both software versions VB20 and VA30 are under development. Not available for sale. Future availability cannot be guaranteed.*
[6] *For connecting one scanner and no IP cameras.*
[7] *Server requirements can be stated only after the server has been implemented and after system testing results are known.*

Contact

Petra Kraft
Siemens Healthineers
DI SY M&S M
Siemensstr. 3
91301 Forchheim
Germany
+49 (174) 3144075
petra.kraft@siemens-healthineers.com

Petra Kraft

Janis Dummet

Meet Siemens Healthineers

Siemens Healthineers: Our brand name embodies the pioneering spirit and engineering expertise that is unique in the healthcare industry. The people working for Siemens Healthineers are totally committed to the company they work for, and are passionate about their technology. In this section we introduce you to colleagues from all over the world – people who put their hearts into what they do.

Hi there, my name is Stuart Calder

and I am an MRI applications specialist in Australia. I started my career over 30 years ago when I started studying diagnostic radiography in Edinburgh, Scotland. I graduated in 1991 and after almost four years of working in Edinburgh I went on an adventure to Australia, originally for a year – however 24 years later I'm still here! When I look back I think I was either crazy or brave to do such a thing. I don't think that I would have the nerve for such an adventure these days – having said that I haven't regretted my move. When you move country to work I think you make a real effort to be social and meet new people and as such it doesn't take long to create a group of friends and feel like home. Australia also didn't seem too foreign for a British person as the Queen is still on the money, they drive on the left side of the road, and they speak English.

Melbourne, Australia

How did you first come in contact with MRI?
Working as a radiographer in a private hospital in Melbourne gave me my first exposure to MR. Amazingly, when I left Scotland there were no clinical MRI machines – how times have changed. In 2000 I became an MRI Supervisor and in 2005 I became the MRI State Coordinator for the company I worked for. Over those years I worked on four different magnets across all vendors. I distinctly remember our double echo sequence for 19 transverse slices in the brain used to take 9:02 minutes and I also remember kneeling at the end of the scanner to manually tune the extremity coil before we could start scanning. The younger generation always laugh when I tell them such stories. In 2010 after 15 years of service at Epworth Hospital in Melbourne I felt I needed a change and hence started with Siemens.

What is most fascinating about your job?
I distinctly remember my first day with Siemens Australia. I was sent to Adelaide to shadow a colleague who was installing a MAGNETOM Trio. A staff member at this hospital asked how long I'd been with Siemens and I replied: „About 45 minutes". She laughed and said, „Excellent! It's my first day, too". Back then our MR applications team was very small, we had three applications specialists, a product specialist, and a marketing manager. Now, nine years later the success of the MR business in this region, its research possibilities, and the quality and support that Siemens offer speak for themselves. I find the main part of my role is to provide outstanding customer service. We get to ensure that the professionals we teach are well equipped and up-to-date on the use of their equipment. This ultimately filters down to the patient so they can have the best possible outcome with a high level of patient care.

Being an applications specialist has given me the opportunity to learn so much. Not only from the excellent courses we attend but also from a cross section of the radiographers we teach and the colleagues we get to work with. No two weeks are ever the same and most Mondays it feels like you're starting a new job with the fears of – what will the customers be like?; where should I park?; what are their expectations of me?; where's the toilet?; where's a good place for coffee?

What do you think are the most important developments in MRI and in healthcare?
MR is also far more accessible now than it was when I first started in MR. MRI used to only be available in major hospitals in major cities. People are living longer and with this aging population comes the need for more screening scans and therefore preventing diseases before they occur. Nowadays, even the smallest private practise often has an MR scanner and patients can now also have the convenience of not having to travel so far for an examination or wait so long for it. This of course has its own challenges as it gets more difficult to find experienced MRI radiographers to staff these scanners. Siemens have the ability

now however to utilize Siemens Remote Service (SRS) and provide assistance in real time. This again has been implemented since I started with Siemens – the Applications helpdesk in the Australia / New Zealand region is a full-time job which is shared between all of us.

The speed of MR development astounds me too. Again when I started we were on either *syngo* MR A or B software and worked on MAGNETOM Espree, Avanto, Trio, and Verio systems. Then along came *syngo* MR C, D, E software, *syngo*.via, and now *syngo* MR XA platforms. There's never a dull moment and with each software release R&D come up with better solutions for customer ease of use and the ability to scan more patients which ultimately leads to shorter waiting lists and a better outcome for the patient which is our main focus. SMS acceleration techniques are only just beginning. It's amazing how fast scanning is becoming maintaining excellent image quality.

Outside of work ...
Being an applications specialist is not just a job, it's a lifestyle. I have been able to see so much of Australia, New Zealand, China, and Europe working with Siemens. I think if I could have a month off I would still use it to travel. Travel is a passion of mine and always has been. Having said that priorities change and now that I'm partnered with 2 dogs I love staying at home. Perhaps with a month off we could hire a campervan and explore without heading to the airport!

Melbourne, Australia

I'm Emily Lucchese,

one of the MRI applications specialists in Australia. This February was my four-year anniversary with Siemens and I can't believe how quickly time has gone. I've learnt an incredible amount in this role – not only about MR physics and our *syngo* platforms, but about how best to teach individuals. Everyone learns differently and it's my job to teach the staff how to use the system to the best of its ability after I've gone – that's my aim at the end of handover applications. Finding the best way to do that can be challenging. I was exposed to a very passionate MRI mentor early on in my radiography career and I credit him for my love of the imaging modality. Not everyone is as lucky as I was, so educating people about MRI is something I love.

How did you first come in contact with MRI?
I began working in MRI in a private hospital in Melbourne on a very old GE scanner and then began working in a public hospital for less than a year, where I was introduced to Siemens' MAGNETOM Symphony and MAGNETOM Verio, before moving to a different private company and worked solely on Siemens scanners. I really loved where I worked and the people I worked with, but was looking for a challenge. When I heard about the job with Siemens at a Siemens user group meeting in Australia, it sounded like a great opportunity to meet new people, learn a lot, and travel the world – I was single and fairly free, so thought it was the perfect time for a change.

What is most fascinating about your job?
One of the best things about my job is the training that we receive at our headquarters in Erlangen, Germany. I've had many trips over and made friends with other MR application specialists all over the world. I've been able to learn from them how differently people around the world perform MRI and have shared different tips and tricks between us.

Being an applications specialist definitely comes with its challenges. Living in such a big country with a high number of magnets means that we spend a lot of time travelling. I've missed numerous family functions and birthdays over the last four years but thankfully, they still love me! Getting to know people for a short period and then moving on can be tough – I've become so fond of the customers I've come across and had such fun with them, it's sometimes hard to say goodbye.

What do you think are the most important developments in MRI?
Luckily, the good definitely outweighs the bad. I'm constantly learning new things about this job and MRI in general. The technology is growing so fast and it's exciting being a part of a company that is in the forefront of research and development. Compressed Sensing and its applications absolutely blows my mind. The quality we're able to achieve with images free of motion, even when the patient is breathing and then being able to achieve such fast temporal resolution is a game-changer. Not all patients are able to comply with our strict conditions and time constraints – acceleration techniques are now readily available to help with this, ensuring that all patients are able to receive the best care.

The entire editorial staff at Bambino Gesù Hospital (Rome, Italy), and at Siemens Healthineers extends their appreciation to all the radiologists, technologists, physicists, experts, and scholars who donate their time and energy – without payment – in order to share their expertise with the readers of MAGNETOM Flash.

MAGNETOM Flash – Imprint

Publisher:
Siemens Healthcare GmbH
Magnetic Resonance,
Karl-Schall-Str. 6, D-91052 Erlangen, Germany

Editor-in-chief:
Antje Hellwich
(antje.hellwich@siemens-healthineers.com)

Guest editor:
Paolo Tomà, M.D.
Professor of Pediatric Radiology
Bambino Gesù Hospital
Rome, Italy

Editorial Board:
Rebecca Ramb, Ph.D.; Sunil Kumar S. L., Ph.D.;
Wellesley Were; Gary R. McNeal, MS (BME)

Review Board:
Katja Böhm; Daniel Fischer;
Christian Geppert, Ph.D.; Berthold Kiefer, Ph.D.;
Heiko Meyer, Ph.D.; Christian Schuster, Ph.D.;

Copy Editing:
Sheila Regan, Jen Metcalf, UNIWORKS,
www.uni-works.org
(with special thanks to Kylie Martin)

Layout:
Agentur Baumgärtner,
Friedrichstr. 4, D-90762 Fürth, Germany

Production:
Norbert Moser,
Siemens Healthcare GmbH

Printer:
G. Peschke Druckerei GmbH,
Taxetstr. 4, D-85599 Parsdorf b. Munich, Germany

MAGNETOM Flash is sent free of charge to Siemens Healthineers MR customers, qualified physicians, technologists, physicists and radiology departments throughout the world. It includes reports in the English language on magnetic resonance: diagnostic and therapeutic methods and their application as well as results and experience gained with corresponding systems and solutions. It introduces from case to case new principles and procedures and discusses their clinical potential. The statements and views of the authors in the individual contributions do not necessarily reflect the opinion of the publisher.

The information presented in these articles and case reports is for illustration only and is not intended to be relied upon by the reader for instruction as to the practice of medicine. Any health care practitioner reading this information is reminded that they must use their own learning, training and expertise in dealing with their individual patients. This material does not substitute for that duty and is not intended by Siemens Healthcare to be used for any purpose in that regard. The drugs and doses mentioned herein are consistent with the approval labeling for uses and/or indications of the drug. The treating physician bears the sole responsibility for the diagnosis and treatment of patients, including drugs and doses prescribed in connection with such use. The Operating Instructions must always be strictly followed when operating the MR system. The sources for the technical data are the corresponding data sheets. Results may vary.

We welcome your questions and comments about the editorial content of MAGNETOM Flash. Please contact us at
magnetomworld.team@siemens-healthineers.com

Manuscripts as well as suggestions, proposals and information are always welcome; they are carefully examined and submitted to the editorial board for attention. MAGNETOM Flash is not responsible for loss, damage, or any other injury to unsolicited manuscripts or other materials. We reserve the right to edit for clarity, accuracy, and space. Include your name, address, and phone number and send to the editors, address above.

MAGNETOM Flash is also available online:

www.siemens.com/magnetom-world

Not for distribution in the US

On account of certain regional limitations of sales rights and service availability, we cannot guarantee that all products included in this brochure are available through the Siemens sales organization worldwide. Availability and packaging may vary by country and is subject to change without prior notice. Some/All of the features and products described herein may not be available in the United States.

The information in this document contains general technical descriptions of specifications and options as well as standard and optional features which do not always have to be present in individual cases, and which may not be commercially available in all countries.

Due to regulatory reasons their future availability cannot be guaranteed. Please contact your local Siemens organization for further details.

Siemens reserves the right to modify the design, packaging, specifications, and options described herein without prior notice. Please contact your local Siemens sales representative for the most current information.

Note: Any technical data contained in this document may vary within defined tolerances. Original images always lose a certain amount of detail when reproduced.

Siemens Healthineers Headquarters
Siemens Healthcare GmbH
Henkestr. 127
91052 Erlangen, Germany
Phone: +49 9131 84-0
siemens-healthineers.com

Published by Siemens Healthcare GmbH · Order No. A91MR-1000-138M-7600 · Printed in Germany · 7183 04190.5 ·

siemens.com/magnetom-world